Modelling linear electron transport with particular reference to thylakoid structure

Ira Tremmel

A thesis submitted for the degree of

Doctor of Philosophy

of The Australian National University

Environmental Biology Group
Research School of Biological Sciences
Australian National University

April 2003

Statement

Except where otherwise indicated, the work contained within this thesis is my own.

I. G. Tremmel (April 2003)

Some results and methods presented in the present thesis are presented or submitted for publication:

Tremmel, I., Kirchhoff, H., Farquhar, G.D. and Weis, E. Micro–organisation of thylakoids and the control of whole chain photosynthetic electron transport. Presented as selected speaker at *The 12th International Congress on Photosynthesis*, August 2001, Brisbane, Australia.

Tremmel, I., Kirchhoff, H., Farquhar, G.D. and Weis, E. Dependence of plastoquinol diffusion on the shape, size, and density of integral thylakoid proteins. *Biochim. Biophys. Acta*, submitted.

Environmental Biology
Research School of Biological Sciences
Institute of Advanced Studies
The Australian National University

Acknowledgments

Completing a PhD is not possible without a great deal of support, both personal and related to the research. Therefore, I wish to take the opportunity to thank the many people that have guided me through this time.

First, I wish to thank my supervisors Professor Graham Farquhar and Professor Engelbert Weis for their flexibility and for having given me the opportunity to complete a somewhat unusual PhD, involving a cooperation across continents. I wish to thank Graham Farquhar for taking me on as a student despite my research being outside his usual area of interest. As well for the many interesting discussions and for polishing my English. Thanks very much as well to Engelbert Weis for stimulating discussions and having always been approachable.

Furthermore, I wish to thank my advisors, Dr Helmut Kirchhoff, Professor Jan Anderson and Dr Fred Chow. All of them have been very approachable and I had stimulating discussions with them. Special thanks to Helmut for support with the experiments and to Fred for proof–reading the thesis.

I wish to thank Professor Klaus Tenberge for the opportunity to use his lab and equipment for the embedding of the samples for electron microscopy. Further I thank Marianne Johannsen, Dr Udo Mays, Dr Sally Stowe and Dr Cheng Huang for their patience and good advice related to embedding, staining, sectioning and all other steps leading to the micrographs.

Thanks also to Marilyn Ball for allowing me to use a computer in her lab when I was running out of computing time. I also wish to thank Dr John Shaw for his help with the manuscript.

For support in the lab in Münster I thank Ute Mukherrjee. Many thanks to Werner Lamkemeyer for nourishing the spinach and his always friendly nature.

In the administration I wish to thank Marlene in der Stroth and Michelle McCarthy for always being willing to help and particularly Cris Carey for 'proov–readink' the thesis.

Special thanks to Barbara Cather for giving me the opportunity to live in Graduate House and for her help in various everyday matters.

However, apart from administration and research it is important to have friends for moral support. In Australia, thanks particularly to Dr Katharina Siebke: She endured patiently all my ups and downs and we also had many interesting discussions about a variety of biological and other topics.

In Germany, thanks to my lab, in particular to Mark Schöttler, Julia Maurer and all those who contributed to a good atmosphere with good mood. Thanks to Mark and Julia in many ways: They contributed much to my physical wellbeing by supplying me with sandwiches when I did not have time to have proper lunch in the 'Mensa'. Additionally they helped me with supplying my worn out nerves with the necessary amount of theobromine ;-)

Last but not least however, I wish to thank my family. Most of all, of course, thanks to my husband Dr Thomas Strauß. He was a strong support with his love and encouragement. With him I could discuss all the algorithms in my program. He was a great help particularly in the parameterising of the protein shapes, the profiling and the general software architecture. Without you I wouldn't have stayed the course. Thanks so very much!

Thesis Abstract

There are five integral proteins and two mobile redox carriers involved in electron transport. The former are the light–harvesting complexes, photosystem II, cytochrome *bf*, photosystem I and the ATP–synthase, whereas the mobile carriers are plastoquinone and plastocyanin. Only the concerted action of all of these components leads to an optimal light usage. A variety of structural data on the integral proteins and thylakoid structure is available. However, although a great deal is known about the single steps of electron transfer and the proteins involved in photosynthesis only little is known about the interplay of the single components.

Classical theoretical approaches to whole chain electron transport are reductionistic models that attempt to understand reaction chains by quantifying the single components. These models typically do not take into account how the single components are spatially organised. Recently, however, evidence has arisen that organisational aspects may have a high impact on linear electron flow in thylakoids [26, 111, 93, 109, 92, 96]. Lavergne, Joliot and co–workers [111, 93, 109, 92] and Kirchhoff and co–workers [96] suggest that the high protein density in thyalkoids may restrict the migration of plastoquinone. Further evidence that a plastoquinone pool shared by all photosystem II may be an over–simplification is presented in the present work. Perhaps for whole chain electron transport it holds that, as Aristotle put it: *"The whole is more than the sum its parts."*.

In this work a Monte Carlo simulation is developed and the diffusion coefficient of plastoquinone diffusion between the integral proteins acting as obstacles is examined. Using obstacles exhibiting a realistic shape, derived from structural analysis of the integral photosynthetic proteins, it is found that plastoquinone diffusion in thylakoids is severely restricted. The area occupied by integral proteins is close to the percolation threshold beyond which the obstacles form closed domains within which plastoquinone can diffuse freely but cannot leave. Slight changes in the protein arrangement lead to pronounced changes in diffusion behaviour under such conditions. Therefore, factors are investigated that may influence the protein arrangement and,

hence, plastoquinone diffusion. It was found that boundary lipids and the mobility of the integral proteins may play an important role in plastoquinone migration.

Further, the role of protein–protein interactions on the organisation of proteins within thylakoids is examined. It is found that diffusion limitation can be promoted by interaction energies. On the other hand by reducing the excluded volume clustering of some particles increases the available free space for non–interacting particles. This may prevent the obstruction of binding sites that may occur when purely random distribution of proteins is assumed.

Finally, whole chain electron transport is simulated with the Monte Carlo simulation. Two different binding mechanisms for plastoquinone at the oxidising site of cytochrome *bf*, which is the rate limiting step, are investigated: a collisional mechanism and a tight binding mechanism. The former assumes immediate electron transfer at a successful encounter while the latter assumes irreversible binding at cytochrome *bf* before the slow reaction takes place. The two mechanisms cannot be distinguished *in vitro* since diffusion limitation does not occur. It is found that in thylakoids, however, the two mechanisms result in different electron transport characteristics. Rate constants used in the simulation are varied to match experimental data on P700 re–reduction kinetics. From the results it is concluded that the measured data can best be matched when severely restricted plastoquinone diffusion and a tight binding mechanism are assumed.

Contents

Abbreviations

aqua dest.	distilled water
ATP	adenosine triphosphate
BBY	**B**erthold and **B**abcock and **Y**ocum [23]
Chl	chlorophyll
cyt bf	cytochrome bf complex
cyt b_h	cytochrome b_6 high potential chain
cyt b_6hp	as cyt b_h, both notations are common in the literature
cyt b_l	cytochrome b_6 low potential chain
cyt b_6lp	as cyt b_l, both notations are common in the literature
cyt f	cytochrome f
DCMU	3-(3,4-dichlorophenyl)-1,1-dimethylurea
DGDG	digalactosyldiacylglycerol
DLVO	**D**eryagin and **L**andau [41], and **V**erwey and **O**verbeek [177] theory of colloid aggregation
DMBQ	2,5-dimethyl-p-benzoquinone
e^-	electron
EDTA	ethylene-diamine-tetra-acetic acid
ETC	electron transport chain
Fd	ferredoxin
FeS	Rieske iron sulfur cluster
FNR	ferredoxin–NADP–reductase
FRAP	**f**luorescence **r**ecovery **a**fter **p**hotobleaching
HEPES	4-(2-hydroxyethyl)-1-piperazinethansulfonic acid
J_e	electron flow from water to a terminal acceptor beyond P700
LHC	light–harvesting complex
MGDG	monogalactosyldiacylglycerol
MES	2-(N-morpholino)ethanesulphonic acid
MV	methyl viologen

NADPH	reduced nicotinamide adenine dinucleotide phosphate
NNDA	nearest neighbour distribution analysis
OEC	oxygen evolving complex
P680	primary electron donor in PS II (chl a–dimer)
P700	primary electron donor in PS I (chl a–dimer)
PC	plastocyanin
PCA	pair correlation analysis
PG	phosphatidylglycerol
Pheo	pheophytin
PQ	plastoquinone
PQH_2	plastoquinol, the reduced form of plastoquinone
PS	photosystem
QA	primary acceptor at PS II
Q_B	Q_B binding site at PS II
Q_o	oxidising binding site at cyt *bf*
Q_r	reducing binding site at cyt *bf*
SET	steady-state electron transport
SQDG	sulfoquinoldiacylglycerol
TEM	transmission electron microscope
tricine	N[tris-(hydroxymethyl)methyl]glycine
Tyr 161	tyrosine 161
V_A	acceptor pool (P700, and following electron acceptors)
$V_{\text{cyt } b}$	cytochrome b pool (low potential chain: cyt b_l, cyt b_h)
V_D	donor pool (water, carriers of the OEC, P680)
V_{PC}	plastocyanin pool (includes the high potential chain: FeS, cyt *f*, PC, P700)
V_{PQ}	plastoquinol pool

$\{C_{V_{PQ}}\}$	capacity of the electron storing pool V_{PQ}
$\{cyt\ bf\}$	concentration of cyt *bf* relative to that of cyt *bf* = 1
{PC}	concentration of PC relative to that of cyt *bf*
$\{PQH_2\}$	concentration of PQH_2 relative to that of cyt *bf*
{PS I}	concentration of PS I relative to that of cyt *bf*
{PS II}	concentration of PS II relative to that of cyt *bf*
$\{V_{PC}\}$	electrons stored in the plastocyanin pool, relative to that of cyt *bf*
$\{V_{PQ}\}$	electrons stored in the plastoquinol pool, relative to that of cyt *bf*

List of Figures

List of Tables

Chapter 1

Introduction

Contents

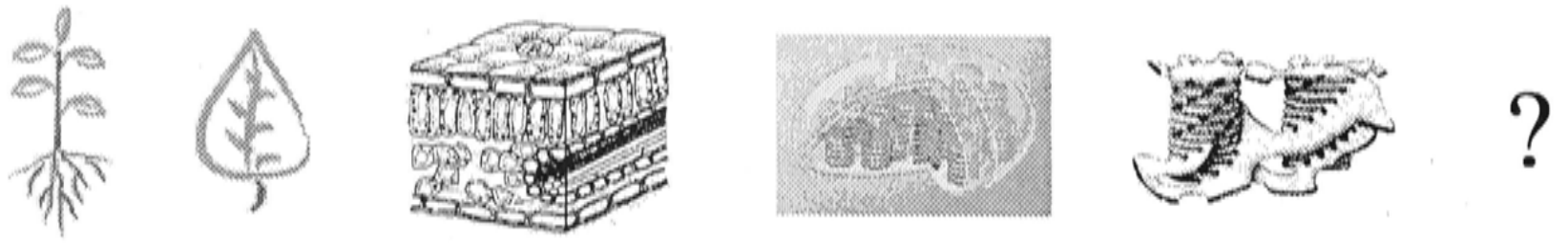

The present work examines photosynthetic electron transport with particular reference to the organisation of thylakoid membranes. Thylakoid membranes are the site of photosynthesis where light energy is converted into chemical energy. The thylakoid membranes of higher plants are highly structured. Stacked membrane regions, called grana thylakoids, can be distinguished from unstacked membranes, called stroma thylakoids. The differentiation between stacked and unstacked membranes also occurs at the protein level. The protein composition of grana and stroma thylakoids is different and it has been suggested that this spatial differentiation reflects different biochemical functions (for more detail see Section 1.2). In the course of photosynthesis electrons are transported between the photosynthetic proteins. Two different types of electron flow can be distiguished: cyclic electron flow and linear electron flow. Cyclic electron flow leads to chemically stored energy in the form of ATP whereas linear flow leads to the formation of ATP and NADPH. ATP and NADPH are both needed for carbon fixation. Cyclic electron flow is suggested to be located in the stroma thylakoids whereas the grana are the site of the linear electron transport.

In addition to large more or less immobile proteins, small diffusible electron carriers are involved in photosynthetic electron transport. One of them is the lipophilic plastoquinone that moves between the larger proteins within the thylakoid membrane. It has been argued that the abundant integral proteins may act as obstacles for plastoquinone diffusion. However, little is known about the arrangement of the photosynthetic proteins in the membrane and how this may influence plastoquinone diffusion and consequently electron transport. In order to get a better understanding of the photosynthetic electron flow, we need to understand more about the organisation of the involved complexes. Accordingly, the work presented here focusses on the role of the thylakoid architecture in photosynthetic electron transport. The investigations concentrate particularly on grana thylakoids and plastoquinone diffusion between photosynthetic proteins within the grana core.

1.1 Photosynthetic electron transport in higher plants

Photosynthetic electron transport leads to two important products: ATP and NADPH (reducing equivalent). In the course of electron transport from water to $NADP^+$ a pH–gradient across the thylakoid membrane is built up. The proton electrochemical potential gradient between the stroma and the lumen is used to conserve energy. Energy set free by protons leaving the lumenal space along the gradient is converted to chemical energy, ATP, via the ATP–synthase according to the chemiosmotic theory of Mitchell [123, 78]. Between the initial donor, H_2O, and the final electron acceptor, $NADP^+$, is a potential difference of more than 1.2 V. This energy is provided by the absorption of light.

After absorption of a photon by the light–harvesting antenna, energy is transferred to the reaction centre of a photosystem (PS) as an exciton. The excitation of the reaction centres leads to a charge separation. Electrons are then transferred to acceptors with a higher (i.e. less negative) redox potential. Electron flow in higher plants involves several electron transfer steps (for a schematic diagram of intermolecular electron transfer see Figure 1.1, for intramolecular transfer see Figure 1.2, Figure 1.3 and Figure 1.4).

With the exception of the lipid–like plastoquinone all of the components involved in electron transport are embedded in proteins. Light capturing proteins are the photosystems PS I (ca. 20 subunits) [165] and PS II (600 kDa, consisting of more than 25 subunits) [143]. They are associated with light–harvesting complexes (LHC) I and LHC II, respectively. On the other hand, there are components only transferring electrons and/or protons. Amongst them is the large membrane spanning cytochrome (cyt) *bf* complex (242 kDa), consisting of 11 different subunits [184] as well as smaller mobile monomeric proteins such as plastocyanin on the lumen side (10 kDa) [67] and ferredoxin on the stroma side (11 kDa) [99].

The reduced form of plastoquinone (PQ) is plastoquinol (PQH_2). In contexts equally relevant for PQ and PQH_2 (e.g. diffusion properties) the term plastoquinone is used for both.

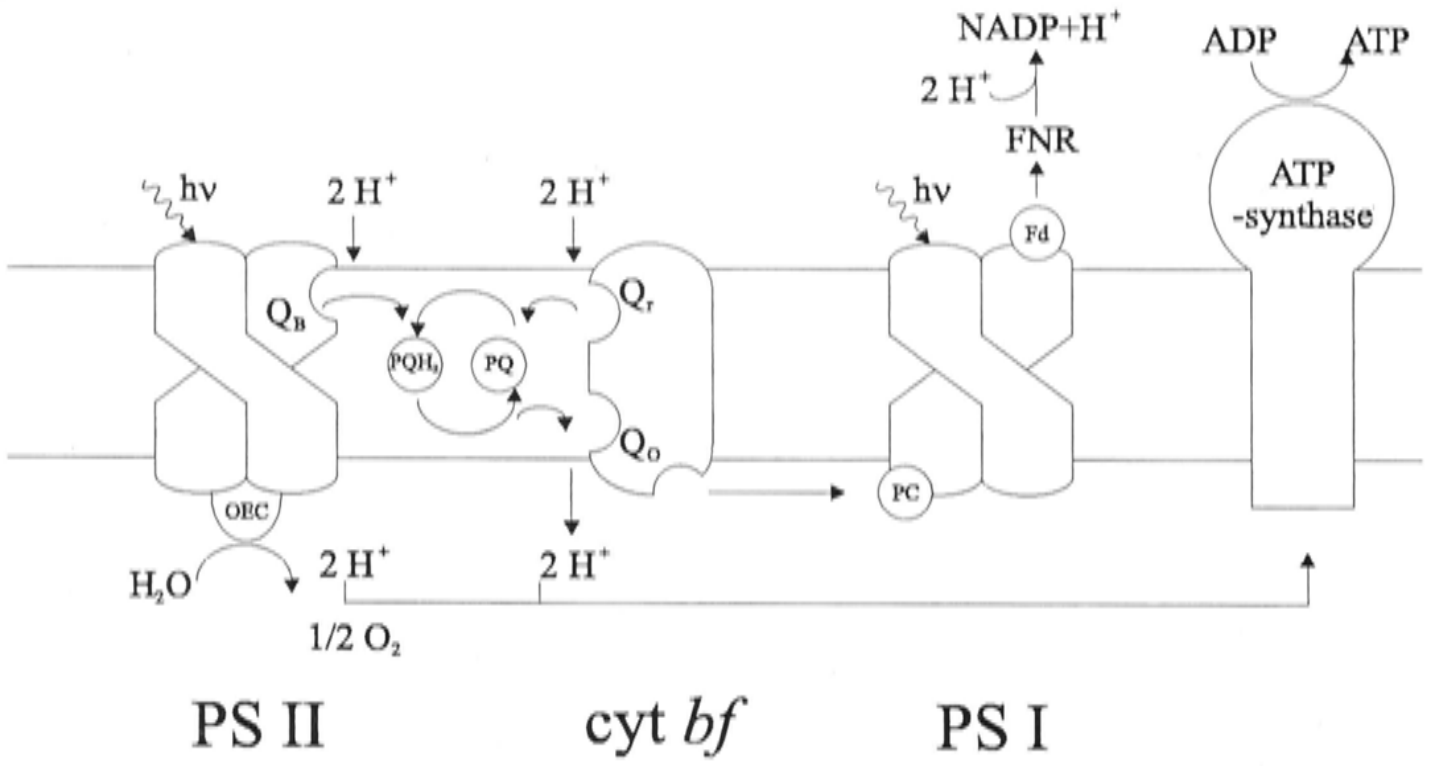

Figure 1.1: *Schematic diagram of intermolecular electron transport in higher plants. Abbreviations: OEC: oxygen evolving complex, Q_B: secondary electron quinone–acceptor of PS II, PQ: plastoquinone, PQH_2: plastoquinol (i.e. reduced plastoquinone), Q_o and Q_r: oxidising and reducing binding site on cyt bf, respectively, PC: plastocyanin, Fd: ferredoxin, FNR: ferredoxin–NADP–reductase.*

1.1.1 Light absorption and exciton transfer

The absorption of light initiates the electron transport processes. To increase the cross–section for absorption about 200–300 chlorophylls are associated with one reaction centre in higher plants [118]. Some 50–80% of the chlorophylls are localized in the LHC.

Light absorbed by a chlorophyll molecule leads to an excited state. According to the energy of the absorbed light quantum, different excited states can be occupied. States higher than the first excited singlet state S_1 are very unstable and relax quickly to the S_1 state. Thus, the energy of this transition cannot be used for the much slower photosynthetic processes. Only the energy difference between the first excited singlet state S_1 and the ground state S_0 can be used for photosynthesis.

Once a chlorophyll molecule has absorbed a light quantum the excitation can be transferred to other molecules as an exciton. Only if the exciton reaches the reaction centre in the core complex can the energy be used for photochemistry. To avoid competing reactions leading to an energy loss, two conditions have to be accounted for:

- fast transfer times of the excitons
- high rate of primary charge separation

These conditions are provided in the photosystems. The transfer time for an exciton between adjacent chlorophyll molecules is one of the fastest processes in nature occuring within some 100 fs [175]. The time between the absorption of a light quantum and stabilized charge separation (trapping time) is 60–90 ps for PS I [173] and some 100 ps for PS II [175]. This is faster than the rate constants for competing reactions leading to an energy loss.

There are two models describing exciton transfer in a pigment system associated with a photosystem (see [175, 148] as a review). The delocalized exciton coupling is restricted to systems with highly overlapping orbitals. Above a threshold of about 2 nm distance between the molecules, exciton transfer can be described with the Förster theory [148]. The Förster theory describes exciton transfer for weakly coupled systems i.e. the electron orbitals of molecules involved are only slightly overlapping. In both cases the rate of exciton transfer is correlated with the distance between adjacent pigments. Therefore, it is important that pigments involved in exciton transfer are close enough in the protein to ensure high rates of transfer. Similarly, energetically coupled proteins need to be located close to each other in the membrane to allow exciton transfer between them.

1.1.2 Photosystem II

Transfer of an exciton to the reaction centre of PS II leads to electron transfer from the primary donor, P680, to the primary acceptor pheophytin (Pheo) (see Figure 1.2). The so called radical pair is formed: $P680^+/Pheo^-$. From pheophytin the electron is then transferred to Q_A, a tightly bound quinone. From Q_A the electron is transferred to the terminal acceptor of PS II, the plastoquinone (PQ) located in the Q_B pocket. Q_B is a two electron gate. After receiving a second electron

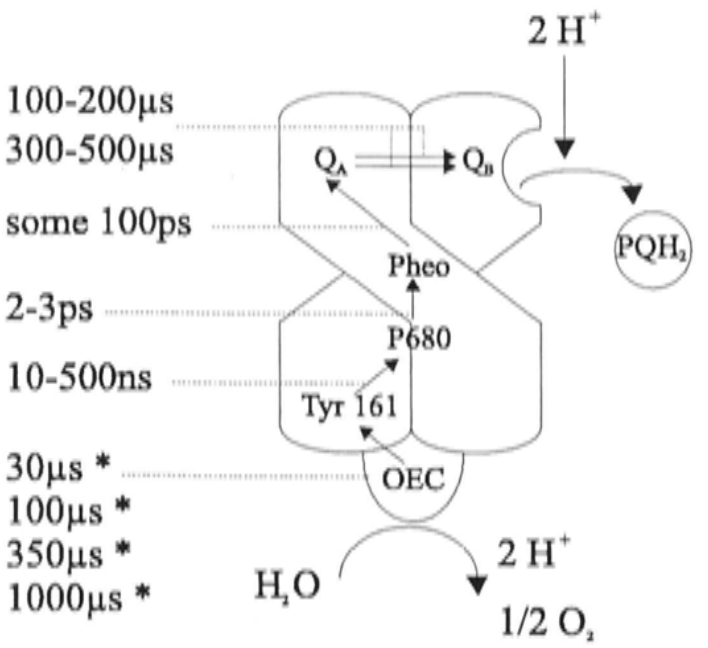

Figure 1.2: *Schematic diagram of intramolecular electron transport in PS II. Abbreviations: OEC: oxygen evolving complex, Tyr 161: tyrosine 161, P680: Chl a–dimer, reaction centre of PS II, Pheo: pheophytin, Q_A and Q_B primary and secondary quinone–acceptor, respectively. Values are from Diner et al. [42], values denoted with a* are from Britt [32].*

the reduced PQ picks up two protons from the stroma side and leaves the Q_B binding site as the neutral diol form (PQH_2). The dissociation constant (PQ–PS II $\rightleftharpoons$ PQ + PS II) of this diol form as well as that of the neutral ketoform is high (1–2 mM [43]). In comparison the dissociation constant of the intermediate semiquinol is thought to be 2000 fold lower [43]. This matches with the experimental finding that the Q_B^- state is very stable [39]. This is interpreted as coulomb forces stabilizing the semiquinone form in the Q_B pocket. Only the neutral forms of plastoquinone (PQ) and plastoquinol (PQH_2) can leave the Q_B pocket easily.

On the donor side the oxidised form of the primary donor, $P680^+$, is reduced by an electron from the oxygen evolving complex (OEC) mediated by the tyrosine 161[a] located on the D1 subunit of the PS II [42]. The active centre of the OEC is formed by four manganese ions, in the ground state coordinated with one (maybe two) water molecules. The concerted action of the OEC synchronizes the one electron step to P680 with the four electron steps leading to the evolution of one molecule oxygen (O_2) out of two water molecules. This synchronization may help avoiding the development of highly reactive oxygen radicals. The OEC is stabilized by extrinsic subunits protruding into the lumen [190, 45].

[a]tyrosine 161 is sometimes called tyrosine Z.

The PS II complexes are heterogeneous. Around 35% of PS II (termed PS II_β) appear to have a two–fold smaller antenna size than PS II_α and are organised in isolated units i.e. they are not energetically connected to each other [13, 11, 172, 110]. In contrast PS II_α are energetically connected via their large antennae. PS II_α usually appear as dimers.

In addition to the photochemical heterogeneity there is also a spatial heterogeneity [14, 11, 164, 20, 1, 2]. About 85–90% of the PS II are located in the grana whereas only 10–15% of the PS II are located in the stroma. The PS II situated in the stroma is considered to belong to the PS II_β type. From these numbers it can be concluded that there might be a significant part of PS II_β in the grana too (see Section 1.2.1). It was suggested by Albertson and co–workers that the PS II_α are localized in the centre of the grana whereas PS II_β are situated in the grana margins [4, 110].

1.1.3 Cytochrome *bf* complex

Electrons are transferred from PS II to the membrane–bound cytochrome *bf* complex by the small, lipophilic plastoquinol diffusing within the membrane (see Figs. 1.1 and 1.3).

There is a strong structural and functional similarity between the cytochrome *bf* of higher plants and the cytochrome *bc* of mitochondria and bacteria. Cytochrome *bc* complexes in crystals exist as a closely interacting dimer, suggesting that the dimer is a functional unit [187]. It is unclear whether this holds also for the cyt *bf* complexes. There is some evidence that cyt *bf* exists as a dimer (see e.g. [80, 85, 38]). However, it is still not clear whether the two cyt *bf* monomers in a dimer interact with each other, and if they do, in which way they interact [66, 129, 133, 146, 65, 162].

Electron transfer at cytochrome *bf*: The Q–cycle

The electron transfer in the cyt *bf* complex is assumed to follow a Q–cycle. The Q–cycle was postulated first for the cyt *bc* complex in mitochondria by Mitchell (1976) [123]. According to the Q–cycle one electron from the PQH_2 is transferred to the oxidised Rieske FeS centre after binding at the Q_o binding site[b]. From there

[b]The nomenclature of the binding sites on the cyt *bf* complex is not uniform. Here the designation Q_o for oxidising is used for the binding site at which PQ is oxidised. Other names found in

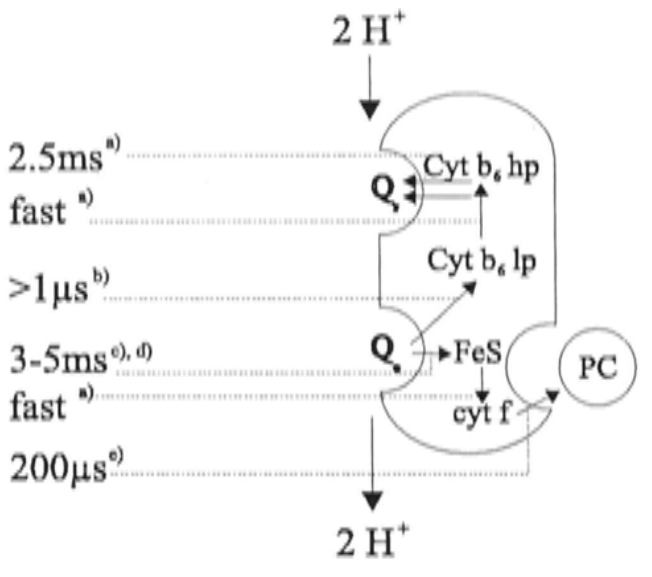

Figure 1.3: *Schematic diagram of intramolecular electron transport in cyt bf. Abbreviations: Q_o and Q_r: plastoquinol and plastoquinone binding sites, respectively, FeS: Rieske iron sulfur cluster, cyt f: cytochrome f, PC: plastocyanin, cyt $b_6$lp: cytochrome b_6 'low potential', cyt $b_6$hp: cytochrome b_6 'high potential'. Sources for transfer rates: a) Hope et al. [81], b) Link [112], c) Cramer et al. [38], d) Hauska et al. [78], and e) Haehnel et al. [72].*

the electron flows very quickly to the oxidised cytochrome f [81] and leaves the cyt bf via a plastocyanin bound at the lumen side leaving a semiquinol at the Q_o pocket. The formation of a semiquinol at the Q_o site establishes the conditions for electron transfer to the low potential cyt b (cyt b_l or cyt b_6lp) [112]. From cyt b_l the electron flows quickly to the high potential cyt b (cyt b_h or cyt b_6hp) [81]. During the electron transfer two protons are released on the lumen side. The sequence is repeated when another PQH_2 binds at the Q_o binding site. From cyt b_h the electron is transferred to PQ at the Q_r binding site. After the second cycle two electrons are transferred to PQ eventually leading to the formation of PQH_2 by the uptake of two protons from the stroma side. The PQH_2 can leave the Q_r binding site and enter the plastoquinol pool.

Altogether the binding of two PQH_2 at the Q_o binding site leads to two electrons flowing to plastocyanin via the Rieske FeS centre and two electrons reducing a PQ at the Q_r pocket mediated by cytochrome b. This PQH_2 can now be oxidised at the Q_o binding site. As a consequence there are two additional protons shuttled to the lumen. The ratio of shuttled protons to transferred electrons is thereby increased from 8 H^+/4 e^- to 12 H^+/4 e^- [36].

---

the literature are Q_p for positive or Q_o for outside. Correspondingly the site of PQH_2 reduction is here called Q_r for reducing. Other names used in the literature being Q_n for negative or Q_i for inside

The Q–cycle seems to be permanently operative in cytochrome *bc* complexes [78] but data for the cytochrome *bf* complex are contradictory. For example stoichiometries of protons per transported electron differing from 3:1 are found in uncoupled thylakoids for some pH values [142] or for varied light intensities in coupled thylakoids [21]. However, there seems to be general agreement in the literature that the Q–cycle is obligatory also for the cyt *bf* complex [112, 21]. Stoichiometries different from 3:1 might be explained by additional proton channels [21]. Such channels are also proposed by Joliot and Joliot, based on measurements of the electrochromic shift of the membrane proteins [90].

1.1.4 Photosystem I

Photosystem (PS) I resembles PS II in many ways. Apart from a remarkable structural similarity [144, 143] analogies in functional aspects can be found. In particular the first steps of electron flow from the reaction centre show similarities.

The primary donor of PS I is P700, a Chl *a*–dimer. After trapping of an exciton it donates an electron to a chlorophyll from which it is transferred to phylloquinone [75] (compare electron transfer in PS II 1.1.2). The terminal acceptor is ferredoxin that is located at the stroma side. Ferredoxin is a mobile electron carrier and carries its electron to the ferredoxin–$NADP^+$ reductase[c]. On the donor side the oxidised form of the primary donor $P700^+$ is reduced by the small diffusible, protein plastocyanin, shuttling electrons within the lumen space from cyt *bf* to PS I.

As with PS II, PS I is heterogeneous [170]: PS I_α is located in the grana margins whereas PS I_β is found in the stroma thylakoids (see Sections 1.2.1 and 1.2.2). Similar to PS II_α, the PS I_α type centres have larger antenna (about 30–40% larger) [1]. The additional antenna of grana PS I_α form a special pool of LHC II that is attached to PS I and functionally coupled to it [16].

The reactions in the PS I and PS II can be considered as fast in relation to the plastoquinol oxidation at the cyt *bf* complex, which is considered to be the slowest step in the electron transport chain [71].

---

[c]The ferredoxin–$NADP^+$ reductase was recently suggested to be part of the cytochrome *bf* complex [189]

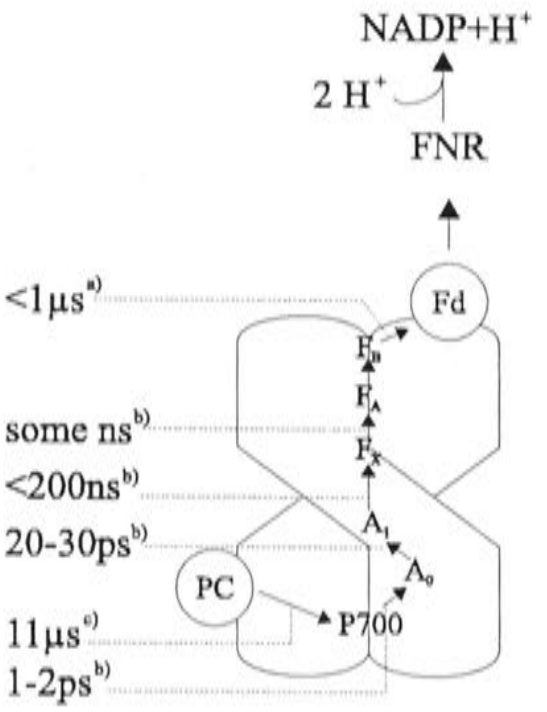

Figure 1.4: *Schematic diagram of intramolecular electron transport in PS I. Abbreviations: PC: plastocyanin, P700: Chl a–dimer, reaction centre of PS I, A_0: chlorophyll a, A_1: phylloquinone, F_x, F_A, and F_B: iron sulfur cluster, Fd: ferredoxin, FNR: ferredoxin–NADP oxidoreductase. Sources for transfer rates: a) Haehnel et al. [73], b) Malkin [113], and c) Haehnel [71].*

1.1.5 Intramolecular electron transport

In the case of PS I, PS II, and cyt *bf* intramolecular electron transport has to be considered. Intramolecular electron transport is characterized by fixed positions of the redox active components. Thus, the path of the electron is strongly determined. The rate of electron transfer at a redox centre site is described by the Marcus theory of electron transfer [115] (see [53] for a review). According to this theory, the rate constant depends on the thermodynamic driving force (ΔG_0), the reorganisation energy (λ), and the overlap of the orbitals of the electron donor and acceptor species involved. The thermodynamic driving force (ΔG_0) is expressed as the difference between the mid–point potentials of the redox components. The reorganisation energy (λ) consists of two components: (1) the outer reorganisation energy; and (2) the inner reorganisation energy. The former is connected with changing orientation of solvent molecules whereas the latter is determined by changes of binding distances and angles of the reactants themselves. From the Marcus theory, the activation energy of a reaction will equal zero, and hence the reaction will occur without any loss, if ΔG_0 equals λ. This leads to extremly high transfer rates. For increasing ΔG_0 the rate constant decreases again and transfer reactions get less efficient and slower for very high ΔG_0.

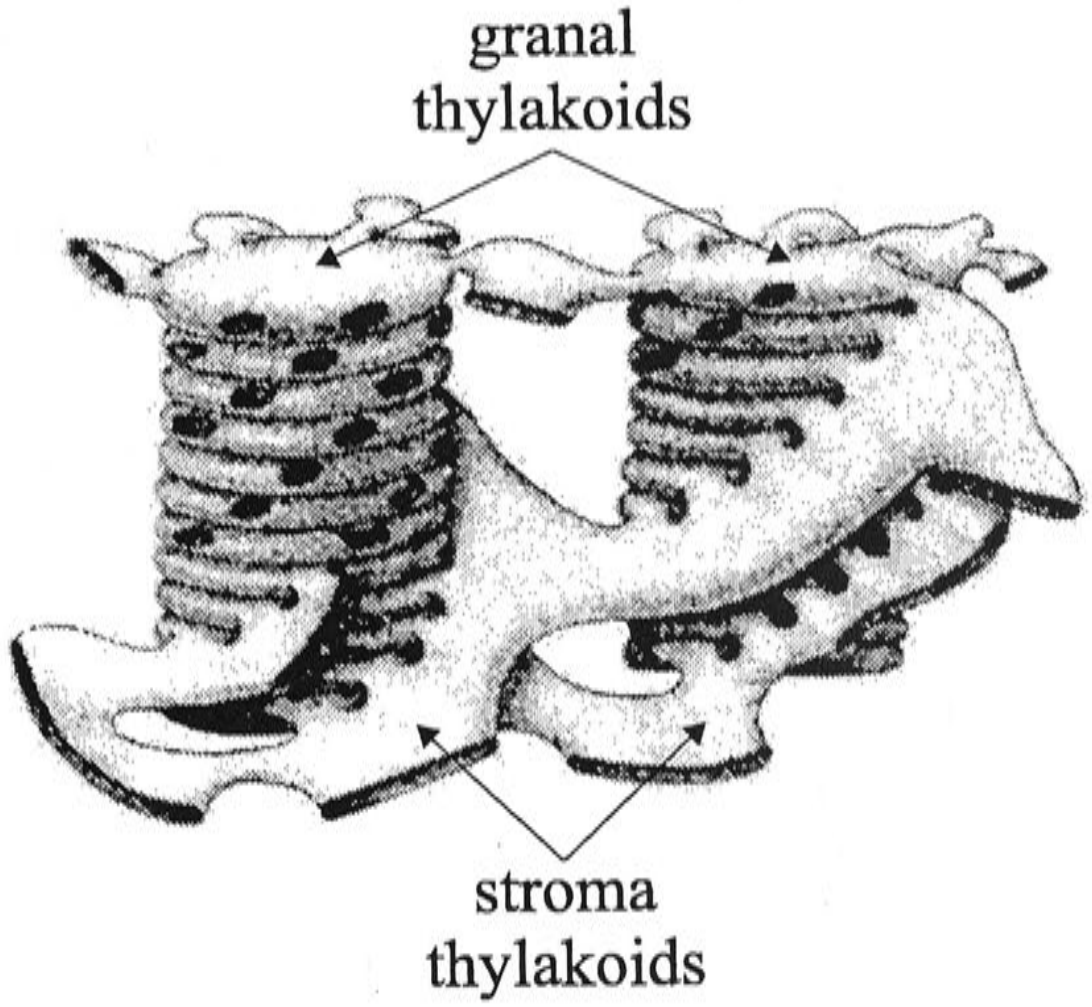

Figure 1.5: *Model of the thylakoid membrane. From Staehelin and van der Staay [165].*

1.2 Architecture of the thylakoids

While CO_2 fixation takes place in the chloroplast stroma, the thylakoid membranes are the site of electron transport. The structure of the thylakoid membrane was mainly resolved with the help of electron microscopy (for a review see [165]) and is shown in Figure 1.5. The thylakoid membrane network consists of a single membrane enclosing the lumen space. It is divided into stacked regions (granal thylakoids) and unstacked regions (stroma thylakoids) [1, 2].

A typical grana stack is composed of two to about twenty grana discs depending on the growth conditions. In each grana disc two to twelve stroma thylakoids are inserted. The stroma membrane is connected to the different grana discs in one grana stack in junctions that form a right handed helix [165, 17].

A granum consists of a central core with appressed membranes forming the grana stack, and a peripheral domain that consists of the margins, and two end membranes [1]. In contrast to the appressed grana core membranes, the margins, the end membranes, and the stroma lamellae are stroma–exposed. These regions are distinguished from each other by their biochemical composition and thus their function (see Figure 1.6, Table 1.1).

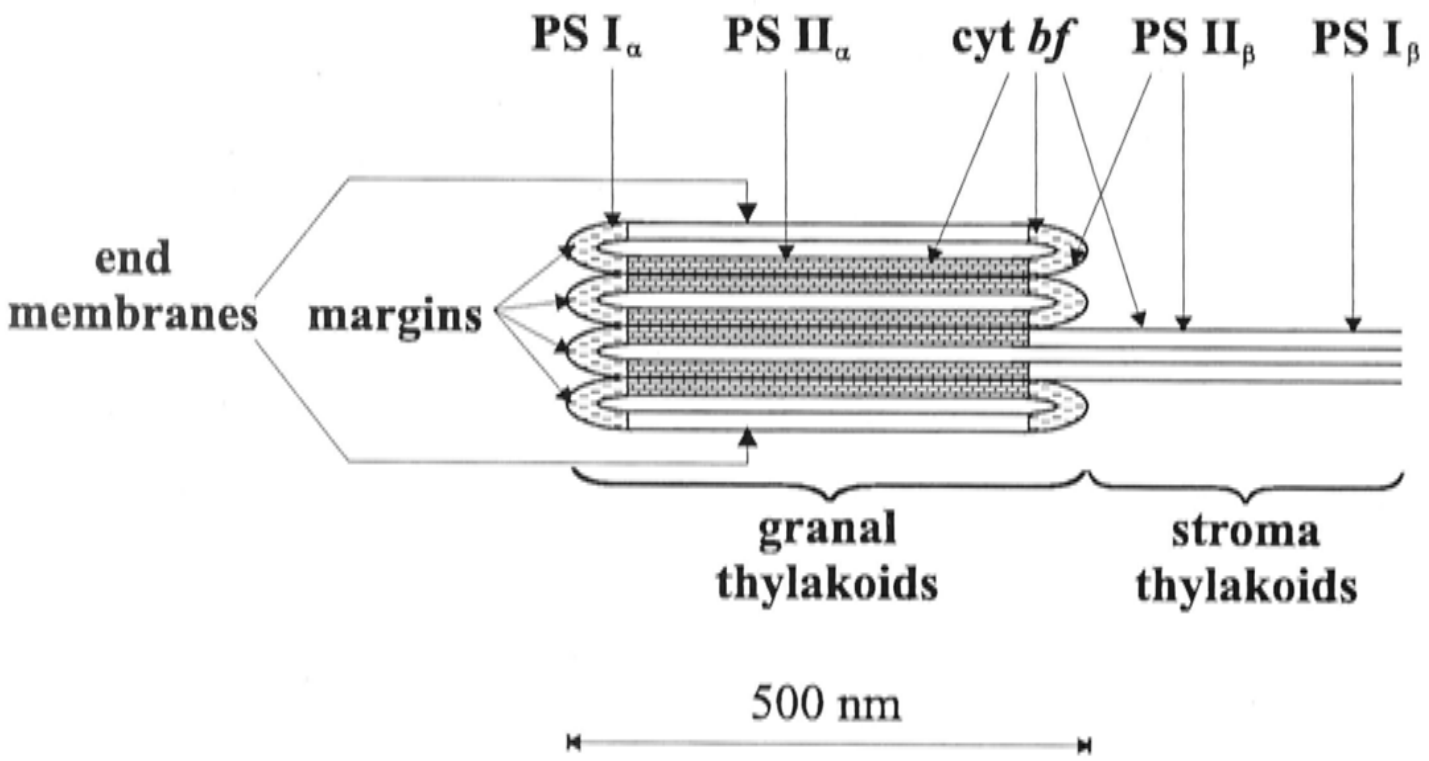

Figure 1.6: *Schematic diagram illustrating the different domains of the thylakoid membrane according to Wollenberger et al. [182]. LHC and ATP–synthase not shown.*

1.2.1 The grana thylakoids

Despite the complexity and plasticity of the thylakoid membrane, there is a certain regularity in the structure of the thylakoid systems of plants grown under normal conditions. Viewed from above, the grana stacks are circular in shape with a diameter that is generally between 400–500 nm. Garab and Mustárdy [63] suggest that the diameter of the grana disks, the multilayer arrangement of the thylakoids, and the internal organisation of stacked membranes 'homogenize' the light absorption in the granum. According to their hypothesis the granum would behave as an optical unit or a resonator involving complex interference pattern and multiple internal reflections [63]. The number of stacked membranes per granum is about 5–20 and the chlorophyll *a*/*b* is 3.0±0.5. A high consistency is found in different plants. The relative amount of granal membranes (ca. 75–85%), and stroma membranes (ca. 15–25%) is highly conserved among different plants. This may be of functional significance [1].

The grana core

The grana core membranes are enriched in PS II_α type centres [13] and contain the highest concentration of cyt *bf* complexes compared to the other thylakoid domains [1]. Both plastoquinone and plastocyanin occur in the grana core [124] whereas PS I cannot be found [110] (see Figure 1.6).

The abundance of light–harvesting complexes (LHC) II in the grana suggests that these antenna complexes also play a structural role. The fact that in all LHC II–containing plants the two photosystems are segregated between the granal and stromal membranes suggests that the LHC II may be involved not only in stacking but also in the lateral separation of PS II and PS I [63]. Further, it has been shown that LHC II complexes, when embedded in lipids, spontaneously form large stacked lamellae with dimensions commensurate with the grana [157].

The grana margins

The margins cover about 40% of the circular grana [1] (i.e. a 60 nm annulus for a granal membrane that is 500 nm in diameter). They contain PS II_β, cyt *bf* complexes, PS I_α, and ATP–synthase [1] (see Figure 1.6). The concentration of cyt *bf* in the margins is the lowest of all thylakoid regions [182]. Probably the circular border

component	grana	stroma	reference
PS II	85%	15%	[165]
PS I	68%	32%	[3]
cyt *bf*	85%	15%	[3]
plastocyanin			
darkness	40%	60%	[73]
illuminated	55%	45%	[73]
plastoquinone	77%	22%	[34]

Table 1.1: *Distribution of photosynthetic components in the different regions of the thylakoids.*

between the PS II_α–containing and the PS I_α–containing domain is not sharp and there might be some intermixing [1].

Albertson proposed that linear electron transport is carried out between the PS II_α centres in the grana and the PS I_α centres in the margins. Thus, long–range electron transport by the diffusible electron carriers (plastoquinone and plastocyanin) over more than 250 nm (the diameter of a granum) is not necessary [1].

1.2.2 The stroma thylakoids

The stroma thylakoids, which might be the site of cyclic electron flow [1], contain PS II_β, cytochrome *bf*, PS I_β, and ATP synthase [1] (see Figure 1.6). There may be a heterogeneity between the cyt *bf* complexes found in the stroma and those found in the grana, similar to the situation for PS II and PS I [1].

The organisation of PS II and PS I in different domains could avoid wasteful 'spill over' between the two photosystems [10].

Interestingly only the ATP–synthase and PS I, which are both absent from the grana centres, possess protein subunits projecting from the membrane into the stroma [181]. As a consequence these complexes cannot penetrate the stacked membrane region because of steric obstruction. The same holds for the LHC I that binds to PS I.

Recently it was suggested by Ford and co–workers [61] that further segregation exists within the grana itself. They studied the structure of isolated granal membranes by cryo–electron microscopy on native crystals. From their data they conclude that LHC II and PS II are located in seperate lipid bilayers in the grana–stack. Participation of the isolated LHC II in photosynthesis would require efficient exciton transfer between adjacent grana stacks. However, the distance between the membranes is in the order of a few Å and this will probably decrease the efficiency of exciton transfer. Furthermore the model does not account for cytochrome *bf*. One possible interpretation of the model would be that cyt *bf* cannot be found in the inner grana membranes. This is in contradiction to the findings of Wollenberger and co–workers [182] and Albertson [1]. Further this would require extremely fast long–range diffusion of plastoquinone; this in turn is in contradiction to investigations of plastoquinone diffusion (see e.g. [111, 93, 109, 92]). Another possible interpretation of the model is that the native crystals that were investigated might not be representative for the thylakoids. Nevertheless, the existence of native crystals is very interesting and their investigation may lead to important findings.

1.2.3 Lipids

Interestingly the thylakoid membrane shows an unusual lipid composition (see Table 1.2): The galactolipids listed in Table 1.2, and SQDG are found solely in thylakoid membranes, whereas phosphatidylglycerol (PG) — typical for many membranes — is rare in thylakoids. Sterols are not found at all [178].

Due to the content of sulfolipids and phosphatidylglycerol, the lipid matrix of the thylakoids has a negative surface charge at physiological pH. The functional importance of the lipid composition for photosynthetic electron transport and ATP–formation is not yet clear [178]. Caused by its wedge shape monogalactosyldiacylglycerol might play a role in the filling of gaps between the lipid matrix and the integral proteins. This is of importance for the development of a proton gradient over the thylakoid membrane that is necessary for ATP formation. The role of

lipid type	**relative amount**
monogalactosyldiacylglycerol (MGDG)	50%
digalactosyldiacylglycerol (DGDG)	30%
phosphatidylglycerol (PG)	10–20%
sulfoquinoldiacylglycerol (SQDG)	5–10%

Table 1.2: *Lipid composition of the thylakoid membrane. The given numbers are typical values. The actual composition may vary in different species depending on the growth conditions [178].*

digalactosyldiacylglycerol could be in grana stacking by the formation of specific lipid–ion complexes [179, 119, 169]. Additionally it was shown that lipids play an important role in the aggregation of LHC II [158] and there is evidence that PG stabilizes the trimeric form of the LHC II [178] and promotes the formation of PS II dimers [103]. Boundary lipids can exert a strong influence on the functionality and mobility of integral proteins [156]. Hence, it appears that lipids ensure a well ordered array of the complexes, yet allowing significant structural flexibility [63].

A large variety of different lipid types is obtained by diverse fatty acid residues that can be of different length with a variable number of double bonds (zero to three) [178]. This variety is specific for a species but can be influenced by the growth conditions as well. The growth temperature plays an especially important role for the lipid composition of membranes [178].

1.2.4 Models for thylakoid stacking

In all higher plants and many green algae thylakoid membranes form stacked regions (grana) that can be distiguished from unstacked regions (stroma) [11, 169]. In isolated thylakoids stacking of grana lamellae is induced by addition of cations whereas

the absence of cations leads to destacking. Destacking in turn causes mixing of the photosystems and quenching of PS II fluorescence [125]. Thus, stacking seems to be of functional importance [11].

In this Section the two most important hypotheses explaining grana stacking are introduced.

The surface–charge theory

According to the surface charge theory developed by Barber [19], two membrane lamellae are attracted by van der Waal's type forces and repelled by electrostatic forces. The latter are screened by counterions, thus resulting in the prevalence of the attractive forces. This theory is essentially an application of the DLVO (Deryagin and Landau [41], and Verwey and Overbeek [177]) theory of colloid aggregation.

Following this theory, phosphorylation of membrane proteins increases the negative charge on their surface, and phosphoproteins migrate out of the stacked regions or, in other words, create additional unstacked regions.

However this theory can not explain the observation that stacking of thylakoids and segregation of photosystems are two independent phenomena caused by two different ion–dependent mechanisms [183, 169].

The surface–charge theory was extended by the idea of entropy–assisted grana formation by Chow [35]. Chow suggested that the overall entropy of the system might be increased by membrane stacking. Entropy as a source of ordering is somewhat counter–intuitive but the loss of entropy associated with orientational ordering might be more than compensated by the gain in free volume where smaller particles can diffuse [132, 44, 35].

The molecular recognition theory

Allen [5] proposed an alternative hypothesis based mainly on molecular recognition between proteins. Stacking of grana is achieved by specific interaction between proteins. The molecular recognition theory does not specify the proteins responsible for stacking, but quite generally phosphorylation of proteins will alter their structure and consequently change the binding specificity and thus cause destacking.

This theory does not attempt to explain the ion–dependent events in stacking and photosystem segregation. Thus, only the surface charge theory and the molecular

recognition theory together are able to explain known properties of the thylakoid membrane [169].

1.2.5 Diffusion processes

As discussed above (Section 1.1) there are two mobile carriers involved in linear electron transport: plastocyanin and plastoquinone. They have to travel distances of up to 200–250 nm from the PS II in the centre of the grana stack to PS I in the grana margins. Both diffusible carriers are found throughout the thylakoids (see Table 1.1). Thus, it is not clear which is responsible for long range transport.

Plastoquinol is a small lipid–soluble molecule that transports electrons on its surface. It has a high diffusion coefficient. Because of this it has been the favorite candidate for the long range mobile carrier [1]. However, one has to take into account that the membrane in which it is diffusing is crowded with proteins that may act as obstacles (see e.g. [151, 111, 96]). First evidence for this arose from estimations of the diffusion coefficient for PQ in phosphatidylcholine lipid vesicles [26]. The diffusion coefficient is about a factor of ten lower if 20% of the membrane are occupied by proteins. More recent measurements in thylakoids using fluorescence quenching of pyrene yielded a coefficient between 0.1–3 $\cdot 10^{-9}$ cm^2/s which is 100 times slower than the coefficient in artificial lipid vesicles without proteins [24].

Functional investigations of plastoquinol diffusion revealed that the photo–reduction of plastoquinone by photosystem II is biphasic [93]. Furthermore, cyt b_h reduction is also heterogeneous [92]. Both results can be interpreted in terms of a restricted PQ diffusion and that there are two pools of PQ and cyt bf. One pool can be assigned to the stroma region the other can be assigned to the grana region [93, 92].

According to Joliot, Lavergne and Béal [93] restricted diffusion of PQ also appears on a finer scale. Evidence for this arises from measurements of the apparent equilibrium constant between Q_A and PQ. Values of 1–5 [93] are obtained which is much lower than that expected by considering the midpoint potential (≥ 70). This can be explained by a further compartmentation of quinone diffusion domains within the grana. Thus, the accumulation of Q_A^- does not express a global equilibrium, but rather indicates total reduction in micro–domains where the PQ/Q_A ratio is small [93].

Following these findings Joliot, Lavergne and coworkers developed the micro–domain theory. According to this theory the crowding of the membrane by integral proteins results in a network of barriers to diffusion [93, 109, 92]. This theory is based on a percolation effect (see also Section 1.2.6). In this case the lateral diffusion coefficient (D) may be distance dependent ($D(r)$) [151]. Furthermore, the diffusion coefficient is dependent on the concentration of obstacles (c), thus leading to $D(r, c)$. Under the assumption of a random walk of a point tracer in the presence of immobile point obstacles[d] on a triangular lattice, Saxton [151] found a threshold of 50% ($c = 0.5$) occupation of lattice sites. Above this threshold $D(r, 0.5)$ approaches zero at some finite r. The physical or biological meaning of this is, if there are too many obstacles in the diffusion space, the tracer will get 'caught' between the obstacles so that it can not leave a certain area, thus leading to a diffusion coefficient of zero outside this area ($D(r_{outside}, c_p) = 0$) but much higher within the area $D(r_{inside}, c_p) \geq 0$. Thus, micro–domains are regions in the thylakoids within which PQ can diffuse freely but which it can not leave on a short time scale[e]. The micro–domains are bounded by membrane proteins acting as obstacles to PQ diffusion. It follows that only PS II and cyt *bf* complexes localized in the same micro–domain are connected on a fast time scale.

The concentration of proteins in the grana is indeed very high. It is thought to be well above 60% (stroma: ca. 40%) [159, 163, 126], and thus might meet the threshold conditions that allow the formation of diffusion domains. However the exact value of the percolation threshold depends strongly on many factors e.g. the shape of the obstacles. Furthermore for the estimation of the percolation threshold of 0.5 Saxton used a homogeneous distribution of the obstacles and no obstacle–obstacle interaction. This probably does not hold for the proteins in the thylakoid membrane. The interplay of the percolation threshold with factors influencing the thylakoid architecture is one aspect investigated in the present study. In contrast to

[d]point obstacle are assumed to occupy exactly one site on the lattice.

[e]It has to be taken into account that the obstacles are not completely immobile as assumed for the determination of the percolation threshold. The membrane proteins are undergoing Brownian motion and thus moving albeit very slowly compared to the small PQ.

PQ, plastocyanin is a small water–soluble protein that carries its redox group well protected within the protein matrix. Fast electron transfer ($\leq$ 10 μs) proceeds as intramolecular transfer after tight binding to specific docking sites on either cyt *bf* or PS I. Thus dissipative and short circuit reactions during long range electron transport could be minimal.

The possibility of free plastocyanin diffusion is controversal in the literature. The lumenal space is quite narrow and the two inner opposing membranes come even closer together during illumination caused by protonation of carboxylate groups on protein surfaces. Protruding hydrophilic loops of the membrane proteins further narrow the diffusion space [1]. Furthermore from older measurments of the reaction kinetics of P700 and cytochrome *f* following partial inhibition of PC by potassium cyanide (KCN), it was concluded that the mobility of PC in the lumenal space is severely restricted (see [71] as a review). However more recent investigations lead to different results that are compatible with a fast and freely diffusible PC. The earlier results are attributed to artifacts in the measurements that were eliminated in the recent experiments [47].

1.2.6 Percolation theory

As described in Section 1.2.5 PQ diffusion in thylakoids may be severely restricted due to the integral proteins acting as obstacles. Restricted diffusion between obstacles can be described by percolation theory.

Percolation deals with the arrangement of randomly distributed particles in an (infinite) lattice. Particles in the lattice may occupy neighbouring sites and thus form clusters, where 'clusters' are defined as groups of neighbouring occupied sites. All sites within one cluster are thus connected to each other by an unbroken chain of neighbour–links from one occupied site to the next. Percolation theory now deals with the number and properties of these clusters [166].

The formation of clusters is dependent on the fraction of occupied lattice sites, p. Above a certain threshold (*percolation threshold*, p_c, with 'c' standing for 'critical') one cluster extends through the whole lattice like water *percolates* through a coffee machine. Here it has to be noted that the term 'cluster' as it is often used in the percolation theory corresponds to the free space in the work presented here[f]. For

[f]Depending on the usage of the term 'cluster' for free space or for the obstacle–clusters the threshold may be p_c or (1-p_c).

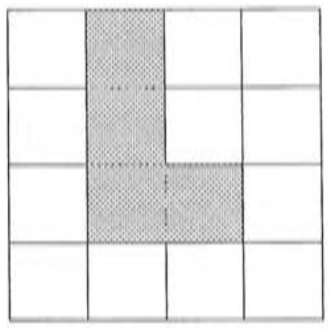

Figure 1.7: *Schematic diagram depicting 'site percolation' versus 'bond percolation'. According to the 'site percolation' the size of the cluster (grey) is four whereas it contains three bonds.*

$p < p_c$ there is no percolating cluster and for $p > p_c$ there is (at least) one percolating cluster. Thus at $p = p_c$, and only there, something peculiar happens: for the first time a path of neighbouring occupied sites on the lattice expands through the whole lattice. Thus the percolation threshold (also referred to as 'critical point') marks a phase transition where the system changes its behaviour qualitatively for one particular value of a continuously varying parameter, p.

The descriptions above are related to 'site percolation'. Its counterpart is called 'bond percolation' and is defined as follows. If lines are drawn between neighbouring lattice sites then each line can be an open bond with probability p, or a closed bond with probability $(1 - p)$. A cluster is a group of sites connected by open bonds (see also Figure 1.7).

However, despite both its success and its mathematical ground, percolation theory has resisted exact calculations. Most known data are numerical estimates, from both Monte Carlo simulations and series expansions [62, 166]. In particular, analytic calculation of percolation thresholds has proven to be a rather difficult task. For instance, twenty years or so were necessary to prove the numerical estimate of $p_c = 1/2$ for the square bond percolation threshold [171]. The bond threshold is also known exactly for the two–dimensional honeycomb and triangular lattices [171]. The situation is even worse in the case of site percolation. Indeed, thresholds are known exactly only in the cases of two–dimensional triangular and Kagomé lattices [171]. At a dimension higher than two, no thresholds were determined exactly. From simulations, percolation thresholds are found to depend on both the space dimension d and the coordination number q (describing the number of nearest neighbours).

Historically, percolation theory goes back to Flory [60] and to Stockmayer [168] who used it to describe how small branching molecules form larger and larger macromolecules if more and more chemical bonds are formed between the origi-

nal molecules. However, usually, the start of percolation theory is associated with a 1957 publication of Broadbent and Hammersley which introduced the name and dealt with it in a more mathematical way [33]. Today there is a large variety of applications of percolation theory as for example animal migration, bush fires, evaluating the distribution of oil or gas inside porous rocks in oil reservoirs, diffusion processes etc. For an overview on diffusion in membranes see Almeida and Vaz [9].

1.2.7 Monte Carlo Algorithm $M(RT)^2$

One focal point of the present work is a Monte Carlo simulation that is developed to study the organisation of proteins within the thylakoid membrane.

The Monte Carlo algorithm was developed in the present form by Metropolis, Ulam, and Neumann during their work on the Manhatten project (study of neutron diffusion). The name 'Monte Carlo' was first used by Metropolis and Ulam [121]. Instead of calculating many dimensional integrals to calculate the properties of the system, the Monte Carlo method consists of simply integrating over a sample of random states.

Considering a canonical ensemble (i.e. a system in which the number of particles, system volume, and temperature are constraints) the probability for the system to be in state s with the energy E_s is:

$$p_{eq}(s) = \frac{1}{f} exp(\frac{-E_s}{kT}). \tag{1.1}$$

The factor f is a normalisation factor to ensure that the sum over all probabilities is one:

$$\sum_s p_{eq}(s) = 1 \Leftrightarrow f = \sum_s exp(\frac{-E_s}{kT}). \tag{1.2}$$

For large systems the distribution of the probabilities $p_{eq}(E)$ is concentrated around a mean energy $\langle E \rangle$. Even for states with energy differing only slightly from $\langle E \rangle$ the probability is close to zero.

The expected value $\overline{V}$ of a state s is

$$\overline{V} = \sum_s V(s) \cdot p_{eq}(s). \tag{1.3}$$

According to the classical Monte Carlo algorithm one would sum over a random sampling of states instead of summing over the whole space. However, for large systems one would hereby waste a lot of time by calculating coefficients equal to zero, due to the concentration of probabilities around the mean energy. Therefore Metropolis and co–workers [120] suggested a modified approach, the $M(RT)^2$–algorithm. Instead of first randomly choosing a configuration and then weighting the configuration with its probability, they chose configurations with the probability exp(-E/kT) and then weighted them evenly.

The procedure is as follows:

1. A random configuration is chosen.
2. An arbitrary step is suggested (each step is only dependent on the former configuration: Markov–process).
3. **a)** The suggested step is accepted when $\Delta E < 0$,

   b) If $\Delta E > 0$ the step is only accepted with the probability $e^{-\Delta E/kT}$.
4. Starting the loop again with 2).

Thus the probability of choosing a probable configuration (high $exp(-E/kT)$) is increased and the system will move to equilibrium.

Today the name 'Monte Carlo' stands for numerical algorithms using random numbers to find an approximate solution of a complex system. It is often used for stochastic problems that are too complex to be solved analytically. The Monte Carlo method has been extended to a broad range of physical and biological systems. It has also been applied to diffusion in biomembranes (as examples see [150, 151, 124, 48]).

Most published simulations of diffusion between obstacles are restricted to spherical obstacles and of more general nature. The Monte Carlo approach carried out in the present work, uses different shapes of obstacles, representing integral membrane proteins, to simulate domain formation for plastoquinone diffusion in grana.

1.3 Research Objectives

In the present work different mathematical and experimental approaches are presented to elucidate whole chain electron flux and factors that may influence it.

Although a variety of structural data of the photosynthetic proteins and their aggregation in thylakoids is available, little is known about the functional consequences. Most models of linear electron transport do not take into account any information about the structural organisation of thylakoid membranes. Therefore in the present work the following steps are taken to get a better understanding of linear electron flow:

- a mathematical model of electron flow is developed, based on differential equations and assuming a shared plastoquinone pool.
- the limits of models that do not take into account spatial aspects are pointed out.
- a model of thylakoids is developed that incorporates spatial information to get insight into the functional consequences of the membrane organisation.
- structural factors are examined that may influence electron transport and those factors that need to be investigated (experimentally) in more depth for a better understanding of electron transport are pointed out.
- using available information about thylakoid structure linear electron transport is modelled.

Chapter 2

Mathematical model of electron flux assuming a common plastoquinone pool

Contents

2.1 Introduction

The photosynthetic electron transport chain of the thylakoid membrane from higher plants and green algae consists of three integral protein complexes: photosystem (PS) II, the cytochrome (cyt) *bf* complex, and PS I. Between these complexes electrons are transferred by two mobile carriers: plastoquinone (PQ), which connects PS II with cyt *bf*, and plastocyanin (PC) connecting cyt *bf* with PS I (see also Section 1.1 and Figure 1.1).

As a first approach to gaining a better understanding of whole chain electron transport from PS II to PS I a simple mathematical model, based on differential equations, is developed[a]. In experiments the proton–gradient, which is built up during electron transport, is often uncoupled by chemicals like nigericin, leading to a degradation of the pH gradient. The advantage of uncoupling the pH gradient is to get better defined, albeit artificial, conditions. Thus, the model simulates electron transport under saturating light and uncoupled conditions for a given stoichiometry of the components involved.

The model enables the calculation of the rates of electron transport and the concentration of electrons stored in the different redox centres. The pH of the surrounding medium is varied to compare the predictions of the model with experimental data.

The considerations are started with the description of the general concept followed by the listing of the general assumptions. Next, a minimal model is presented. This model only considers the PQ reduction at the Q_B binding site on PS II and oxidation of PQH_2 at the Q_o binding site on cyt *bf*. With the minimal model data from the literature are fitted. The minimal model is then extended to account for the reactions at the Q_r site on cyt *bf*. As with the minimal model, data from the literature are fitted and the obtained time constants discussed.

2.2 Background and general concepts

The model includes the Q–cycle of electrons associated with the cytochrome *bf* complex (see Section 1.1.3). It permits a quantitative description of the character-

[a]It has to be noted that shortly after this model was developed Berry and Rumberg published a much more exhaustive model of whole chain flux that incorporates proton translocation [22].

istic dependencies of the electron flow to PS I (J_e) on the pH inside and outside the thylakoids.

The slowest step during the transport of an electron from water to NADPH is the oxidation of plastoquinol at the Q_o–site of the cytochrome *bf* complex. Thus, to describe the operation of the whole electron transport chain (ETC), one should characterize the steps having rates comparable to that of plastoquinol oxidation.

Transport steps that are relatively fast are grouped together in this approach (see Figures 2.1 and 2.5). This is in analogy to the model proposed by Dubinskii [50]. Carriers between which the electron transport is relatively fast ($\leq$1 ms) constitute an electron storing 'pool'. As an example electron transport between the Rieske cluster and cyt *f* up to P700 can be considered to be relatively fast [81, 72], and thus the components involved in that flux are grouped into to the same pool. Whereas transport of electrons within a pool is fast, transport between carriers belonging to different pools is relatively slow. Hence plastoquinone and the Rieske centre between which electron transport is relatively slow (3–5 ms [38, 78]) belong to different pools.

2.3 General assumptions applied in the model

1. Fast electron transfer within electron storing pools, slow interconversion between the pools.

2. Within each pool electrons are immediately and completely transferred to the redox components with the highest redox potential. That means a consecutive filling of the pools.

3. Unlimited capacity of the electron source (water) and the terminal acceptor (e.g. methyl viologen).

4. Light saturation corresponds to 10 quanta/ms (per PS II).

5. Obligatory Q–cycle (see also Section 1.1.3).

6. No diffusion limitation for PQ and PQH_2 and no dissociation before the reaction takes place. That means if there is a molecule available for binding at the reaction site it will bind.

2.4 A minimal model assuming very fast PQ reduction at the Q_r site of cyt *bf* complex

2.4.1 Electron storing pools

The steps considered to be slow in this model are the excitation of the reaction centres of both photosystems (at least in low light when the time interval between the arrival of successive light quanta is long), the protonation of quinones at the Q_B–site of PS II and the plastoquinol oxidation at the Q_o–site of the cyt *bf* comlex.

Accordingly the following pools can be identified (see also Figure 2.1):

- The plastoquinol pool (V_{PQ}). Once the quinones are reduced, electrons are carried from the PS II to the cyt *bf* quite quickly i.e. no diffusion limitation is assumed. The electron storage capacity of the pool is two times the concentration of plastoquinones in the pool since each PQ can carry two electrons.

- The high potential pool (V_{hp}). This pool includes the high potential chain, i.e. the Rieske centre (FeS), cytochrome *f*, plastocyanin (PC), and the P700 reaction centre of the PS I.

- The acceptor pool (V_A). To this pool belong carriers connected with the PS I as well as the terminal acceptor, ferredoxin (Fd). In most experiments artificial acceptors are used and in this case the pool can be considered as an ideal acceptor with unlimited capacity.

- The donor pool (V_D). This pool includes water as the electron source for the ETC, carriers of the water splitting complex, and P680, the reaction centre of PS II. The water filling the thylakoid lumen makes this pool a practically inexhaustible electron donor.

Strictly speaking another pool should be considered that is located between the potentially slow arrival of light quanta at P680 (light intensity dependent) and the quinone protonation at the Q_B pocket of the PS II (pH–dependent). However, the model assumes that the state of the PS II does not influence the proton and electron fluxes and therefore will not be specifically identified.

Slow transport reactions between the different pools are the reactions at the Q_B and Q_o–binding site. How many electrons can be stored in each pool depends

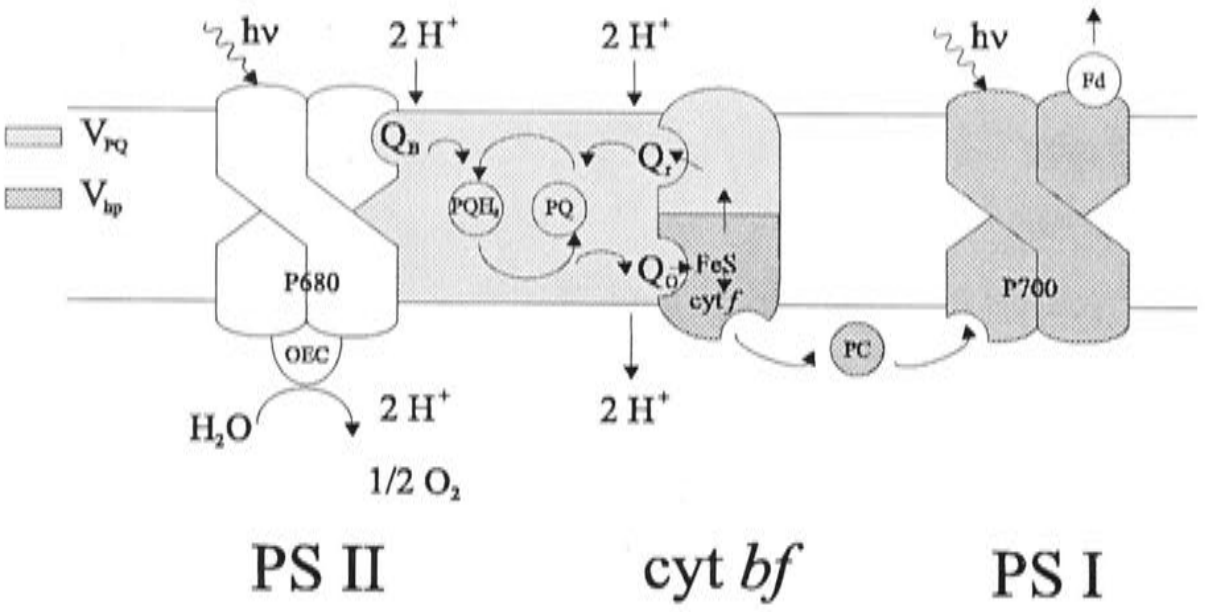

Figure 2.1: *Schematic diagram showing the two electron storing pools in the photosynthetic electron transport chain. Light grey: the plastoquinol pool V_{PQ}, medium grey: the high potential pool V_{hp}, grey: the acceptor pool V_A and the donor pool V_D. Abbreviations: OEC: oxygen evolving complex, P680: Chl a dimer, reaction centre of PS II, QB: binding site for PQ reduction, PQ: plastoquinone, PQH_2: plastoquinol, Qo and Qr: oxidising and reducing binding site on cyt bf, respectively, FeS: Rieske iron sulfur cluster, cyt f: cytochrome f, PC: plastocyanin, P700: Chl a dimer, reaction centre of PS I, Fd: ferredoxin.*

on the stoichiometry between the different electron carriers {PS II} : {PQH_2} : {cyt *bf*} : {PC} : {PS I}. As the electron transport through cytochrome *bf* is rate limiting, the amount of cyt *bf* is taken as the basis for the stoichiometry i.e. the concentrations of the components per cyt *bf* is considered.

2.4.2 The differential equations

The following set of differential equations describes the electron transfer from one pool to another (see Figure 2.2). Thus it contains the relatively slow steps in the ETC.

$$\frac{d\{V_{\mathrm{PQ}}\}}{dt} = 2 \cdot J_B - J_o, \tag{2.1}$$

$$\frac{d\{V_{hp}\}}{dt} = J_o - J_{\mathrm{P700}}, \tag{2.2}$$

where the braces {} denote the concentration, relative to that of cyt *bf* in the membrane. $\{V_{\mathrm{PQ}}\}$ is the concentration of electrons stored in plastoquinol

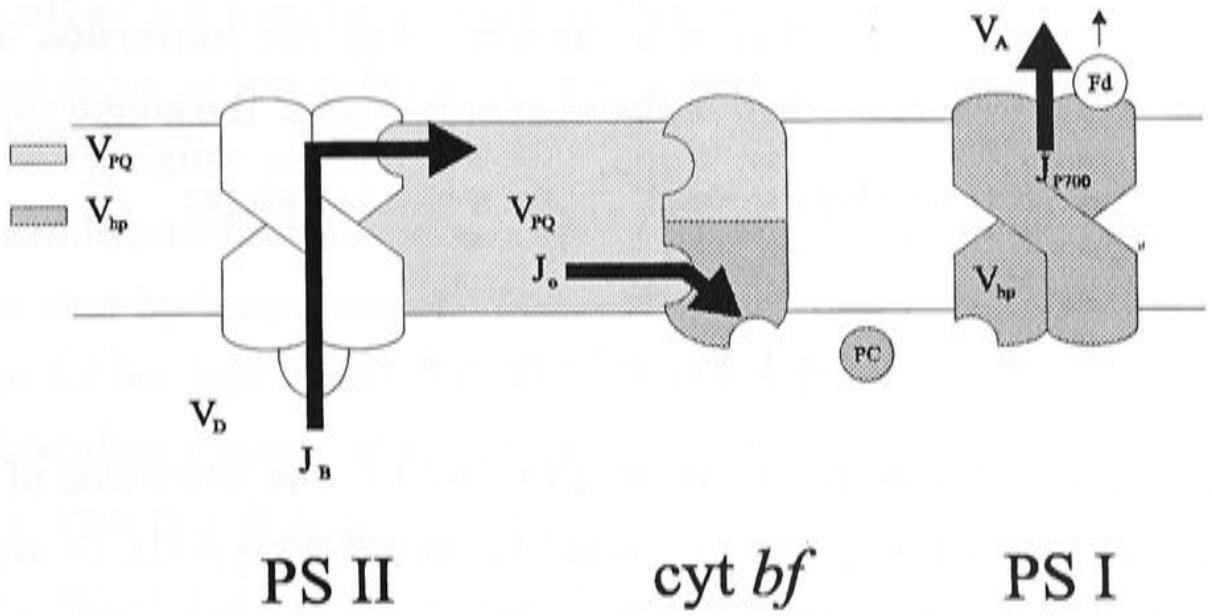

Figure 2.2: *Schematic diagram showing the fluxes between the two electron storing pools in the photosynthetic electron transport chain. Shades as in Figure 2.1.* J_B *electron flux into the PQ pool according to equation (2.5),* J_o *as in equation (2.8), and* J_{P700} *as in equation (2.9).*

molecules (PQH_2) relative to that of cyt *bf*. E.g. 24 electrons if a stoichiometry of {PS II} : {PQ} : {cyt *bf*} = 2 : 12 : 1 is assumed. $\{V_{hp}\}$ is the concentration of electrons bound at carriers belonging to the high potential pool (e.g. 5 electrons for a stoichiometry of {cyt *bf*} : {PC} : {PS I} = 1 : 2 : 1, because 1 e^- can be stored in each of the components within this pool: FeS, cyt *f*, PC, and P700). The system does not contain equations for the donor pool and the acceptor pool as they are idealised not to limit the overall flux J_e.

J_B and J_o are the rates of PQ reduction at the Q_B–binding site of the PS II and the oxidation of PQH_2 at the Q_o–binding site of the cyt *bf* complex, respectively. J_{P700} is the rate of electron transfer from P700 to the terminal acceptor. The factor of 2 times J_B takes into account that the redox conversion of one PQ molecule is associated with the transfer of two electrons, whereas the outflux of the pool is only associated with the transfer of one electron because the second electron is recycled via the Q–cycle.

2.4.3 Electron fluxes at the different reaction sites

Following [51], the rate of redox conversion is calculated using:

$$J = \frac{\{R\}}{\tau}, \tag{2.3}$$

where $\{R\}$ is the concentration of molecules ready for conversion and τ is the necessary time for the reaction, and is the sum of times for the single steps involved.

For J_B this reaction involves several time consuming steps:

$$\tau_B = 2 \cdot \tau_{L_2} + 2 \cdot \tau_{\text{PS II}} + \tau_{Q_B}. \tag{2.4}$$

At the Q_B–site a two electron transfer is involved in the formation of PQH_2. The first term $(2 \cdot \tau_{L_2})$ describes the time needed for two light quanta to arrive at P680 to initialize the transport of two electrons. The second term $(\tau_{\text{PS II}})$ denotes the time for the charges to travel from water over the PS II carriers to the Q_B–binding site ($\tau_{\text{PS II}} \approx 0.5$ ms per electron [50]). The last term (τ_{Q_B}) is the time for Q_B^{2-} protonation. This reaction does not take long in the pH range studied, so that it is possible to neglect this term [50].

The flux at the Q_B–binding site J_B is proportional to the concentration of quinones bound to the Q_B–binding site divided by the time necessary for the reaction:

$$J_B = \frac{\{Q_B\}}{\tau_B}, \tag{2.5}$$

with $\{Q_B\}$:= the concentration of Q_B sites with bound plastoquinone (PQ) relative to that of cyt bf.

To determine the time needed for the reactions at the Q_o site one has to take into account that the reactions show a strong pH–dependency. A bell shaped relationship between the rate coefficient k_{QF} for the oxidation of decyl PQH_2 at the Q_o site and the pH was found by Hope and co–workers [83]. The bell–shape can be interpreted as meaning that two states have to be in favourable conditions for the reaction to take place e.g. one reaction partner has to be protonated whereas the other one has to be unprotonated. These two conditions each lead to a pK value (pK_a and pK_b) thus determining the bell–shape [83]. Correspondingly Hope and co–workers used the following equation to fit their data:

$$k_{QF} = \frac{k_{max} \cdot K_b \cdot [H^+]}{(1 + K_a \cdot [H^+])(1 + K_b \cdot [H^+])}. \tag{2.6}$$

A good fit was obtained by Hope and co–workers for pK values of 6.1 and 8.9 [83]. The value of pK=6.1 was interpreted to reflect quinone radical anion formation

for which a pK of 6.0 was determined by Hauska co–workers [77]. The protonation of the radical anion at low pH leads to a more positive redox potential of the couple $QH^{\bullet}/Q$ than at higher pH thus slowing down the cyt b reduction at the Q_o site. Another possible interpretation could be by analogy with the cyt bc_1 complex where it was found that hydroquinone oxidation requires that a group on the bc_1–complex with a pK of 6.5 be deprotonated [30]. The higher pK of 8.9 could be related to the pK of the histidine ligands of the oxidised Rieske cluster where the hydroquinone binds. This histidine ligand in cyt bc_1 has a pK of 9.2 [30]. An interpretation proposed by Hope and co–workers is that an irreversible[b] alkaline effect on the cyt b or the Rieske subunit could lead to a diminution of the quinol oxidation rate–coefficient [83].

The rate constants found by Hope and co–workers for Decyl PQH_2 oxidation (k_{QF}) were not true second order rate–constants but were given in relative units. Following that, instead of using $\tau_o \hat{=} 1/k_{QF}$ for the transfer of an electron to cyt f and the deprotonation of PQ, the model considered here uses a time constant that is proportional to that value ($\tau_o = \tau_{min}/k_{QF}$). An additional pH–independent time step is introduced considering the time involved in the second electron transfer reaction following the binding on the Rieske cluster and the time needed for the travelling of the electrons within the cyt bf complex, thus leading to:

$$\tau_o = \frac{\tau_{min_o} \cdot ((1 + K_a \cdot [H^+]) \cdot (1 + K_b \cdot [H^+]))}{K_b \cdot [H^+]} + \tau_{BF}, \tag{2.7}$$

$$\begin{aligned} \text{with} \quad pK_a &= 6.1 \\ pK_b &= 8.9. \end{aligned}$$

Thus J_o can be calculated according to:

$$J_o = \frac{\{QH_{2,o}\} \cdot \{FeS_{ox}\}}{\tau_o}, \tag{2.8}$$

with $\{QH_{2,o}\}$:= the concentration of Q_o sites with bound plastoquinol (PQH_2) relative to that of cyt bf,

$\{FeS_{ox}\}$:= the concentration of oxidised Rieske clusters ready for electron uptake relative to that of cyt bf.

[b] Maybe denaturating [83].

Finally, J_{P700} can be calculated according to:

$$J_{\mathrm{P700}} = \frac{\{\mathrm{P700}_{red}\}}{\tau_{\mathrm{PS\,I}}}, \tag{2.9}$$

with $\{\mathrm{P700}_{red}\}$:= the concentration of reduced P700 relative to that of cyt *bf*,

$\tau_{\mathrm{PS\,I}}$:= the time needed for an electron transfer from P700 to the terminal acceptor.

2.4.4 Redox state of the electron carriers

To calculate the electron fluxes at the different sites, the concentrations of binding sites with bound redox carriers relative to cyt *bf* have to be determined. As noted above each PQ can store 2 electrons; thus the concentration of $\mathrm{PQH_2}$ molecules relative to that of cyt *bf* (and consequently to the concentration of Q_o sites) is $V_{\mathrm{PQ}}/2$, which is half of the concentration of electrons stored in the pool (V_{PQ}). Now assuming that there is no diffusion limitation and all available $\mathrm{PQH_2}$ binds at the Q_o site (see Section 2.3), it follows that:

$$\begin{aligned}
&\text{if} && \{V_{\mathrm{PQ}}\}/2 > 1 \\
&\Leftrightarrow && \{\mathrm{PQH_2}\} > \{\text{cyt } bf\} \\
&\Rightarrow && \{\mathrm{QH}_{2,o}\} = 1, \\
&\text{if} && \{V_{\mathrm{PQ}}\}/2 \leq 1 \\
&\Leftrightarrow && \{\mathrm{PQH_2}\} \leq \{\text{cyt } bf\}, \\
&\Rightarrow && \{\mathrm{QH}_{2,o}\} = \{V_{\mathrm{PQ}}\}/2.
\end{aligned} \tag{2.10}$$

with $\{\mathrm{PQH_2}\}$:= the concentration of $\mathrm{PQH_2}$ relative to that of cyt *bf*.

For the calculation of the concentration of PQ per cyt *bf*, one has to know the capacity of the plastoquinone pool ($\{\mathrm{C}_{V_{\mathrm{PQ}}}\}$) which is twice the concentration of PQ per cyt *bf*. The difference between the maximum concentration of electrons that can be stored in the pool ($\{\mathrm{C}_{V_{\mathrm{PQ}}}\}$) and the concentration of electrons stored in

the pool divided by two gives the concentration of unreduced PQ per cyt *bf*. It follows that

$$\{\mathrm{PQ}\} = (\{C_{V_{\mathrm{PQ}}}\} - \{V_{\mathrm{PQ}}\})/2. \tag{2.11}$$

Similar to the above and according to Section 2.3, if enough PQ is available (PQ≥PS II) all Q_B binding sites are assumed to be occupied. Otherwise (PQ<PS II), the Q_B binding site will be occupied according to the concentration of available PQ. Thus for the portion of PQ bound at the Q_B site, the following conditions hold:

$$\begin{array}{lrcl} \text{if} & \{V_{\mathrm{PQ}}\} & \leq & \{C_{V_{\mathrm{PQ}}}\} - 2 \cdot \{\mathrm{PS\ II}\} \\ \Leftrightarrow & \{\mathrm{PS\ II}\} & \leq & \{\mathrm{PQ}\} \\ \Rightarrow & \{Q_B\} & = & \{\mathrm{PS\ II}\}, \end{array} \tag{2.12}$$

$$\begin{array}{lrcl} \text{if} & \{V_{\mathrm{PQ}}\} & > & \{C_{V_{\mathrm{PQ}}}\} - 2 \cdot \{\mathrm{PS\ II}\} \\ \Leftrightarrow & \{\mathrm{PS\ II}\} & > & \{PQ\} \\ \Rightarrow & \{Q_B\} & = & \{\mathrm{PS\ II}\} \cdot (\{C_{V_{\mathrm{PQ}}}\} - \{V_{\mathrm{PQ}}\})/2 \end{array}$$

with $\{\mathrm{PS\ II}\}$:= the concentration of PS II (thus Q_B sites) relative to that of cyt *bf*,

$\{Q_B\}$:= the concentration of Q_B sites with bound PQ relative to that of cyt *bf*.

Because of its negative charge an electron is transferred from redox components with a lower redox potential to those with a higher potential. Thus in order to find the redox states of the carriers belonging to the high potential pool (V_{hp}), a consecutive reduction of the components belonging to this pool is assumed (see equation (2.13)). First P700, the component with the highest redox potential within the pool is reduced, followed by PC and cyt *f*, and finally FeS with the lowest redox potential. That is a simplifying assumption and not necessarily true. The simplification becomes more realistic the greater the difference in the redox potentials of the various components — and hence as the equilibrium constant for electron transitions becomes greater. The following equations are used for the determination of the redox state of FeS and P700:

$$\begin{aligned}
&\text{if } \{V_{hp}\} > 4 \Rightarrow \{\text{FeS}_{ox}\} = 5 - \{V_{hp}\},\\
&\text{if } \{V_{hp}\} \leq 4 \Rightarrow \{\text{FeS}_{ox}\} = 1,\\
&\text{if } \{V_{hp}\} > 1 \Rightarrow \{\text{P700}_{red}\} = 1,\\
&\text{if } \{V_{hp}\} \leq 1 \Rightarrow \{\text{P700}_{red}\} = \{V_{hp}\}.
\end{aligned} \tag{2.13}$$

The first two conditions describe how FeS will only be reduced if all the other components in the pools are already reduced — according to the assumptions above. The latter two conditions are the formulation of the assumption that as soon as there is an electron stored in the PC pool it will immediately be transferred to the P700.

2.4.5 Summary of the assumptions

The general assumptions for the model are described in Section 2.3. In addition the following assumptions are introduced for the minimal model:

1. The protonation of PQ at Q_B is fast and can thus be neglected.
2. pH–dependency of PQ oxidation is mainly caused by the importance of reaction groups being protonated or unprotonated.

2.4.6 Fitting literature data with the model

A program was written in the computer language C to fit experimental data of Rumberg and Siggel [147] according to the mathematical formulation described above. In this publication the pH–dependency of the re–reduction of P700 after switching off the saturating light was measured. In the model presented here, the stoichiometry is assumed to be $\{\text{PS II}\} : \{\text{PQ}\} : \{\text{cyt } bf\} = 2 : 12 : 1$.

To fit the data the time needed for a photon to arrive at P680 is assumed as $\tau_{L_2} = 10$ ms. As shown in Figure 2.3 a good fit is obtained. The fitted time constants for the reactions at the Q_o are:

$$\begin{aligned}
\tau_{min_o} &= 4.1 \text{ ms},\\
\tau_{BF} &= 9.3 \text{ ms}.
\end{aligned}$$

τ_{min_o} describes the pH–dependent reactions whereas τ_{BF} describes the pH–independent reactions. The sum of the errors squared is 56.8 s^{-2}. The interpretation of the time constants will be discussed in the following Section.

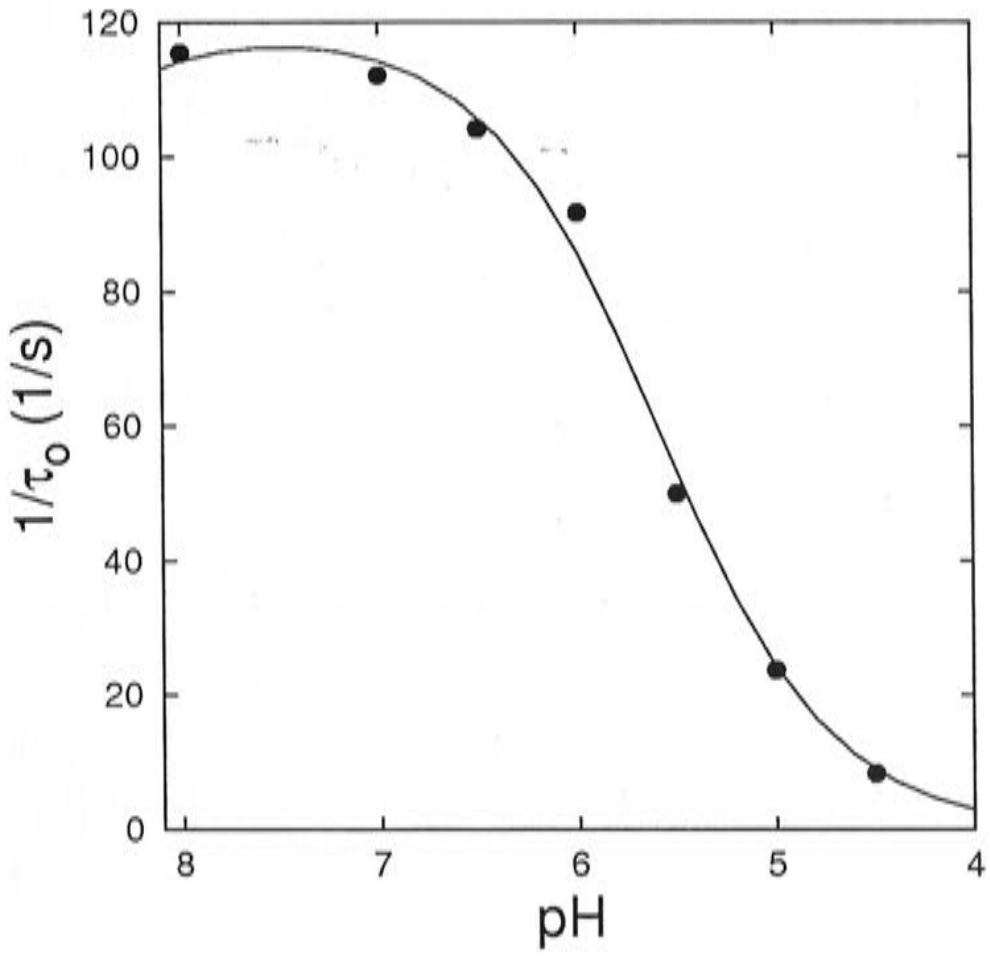

Figure 2.3: *pH–dependency of P700 re–reduction. Circles: experimental data of Rumberg and Siggel [147], the line shows the best fit to the data according to the 'minimal model'.* $\tau_{min_o} = 4.1$ *ms,* $\tau_{BF} = 9.3$ *ms, sum of errors squared: 56.8* s^{-2}*. Note that the pH–values on the x–axis are in descending order from left to right; this is for easier comparison with the original work of Rumberg and Siggel.*

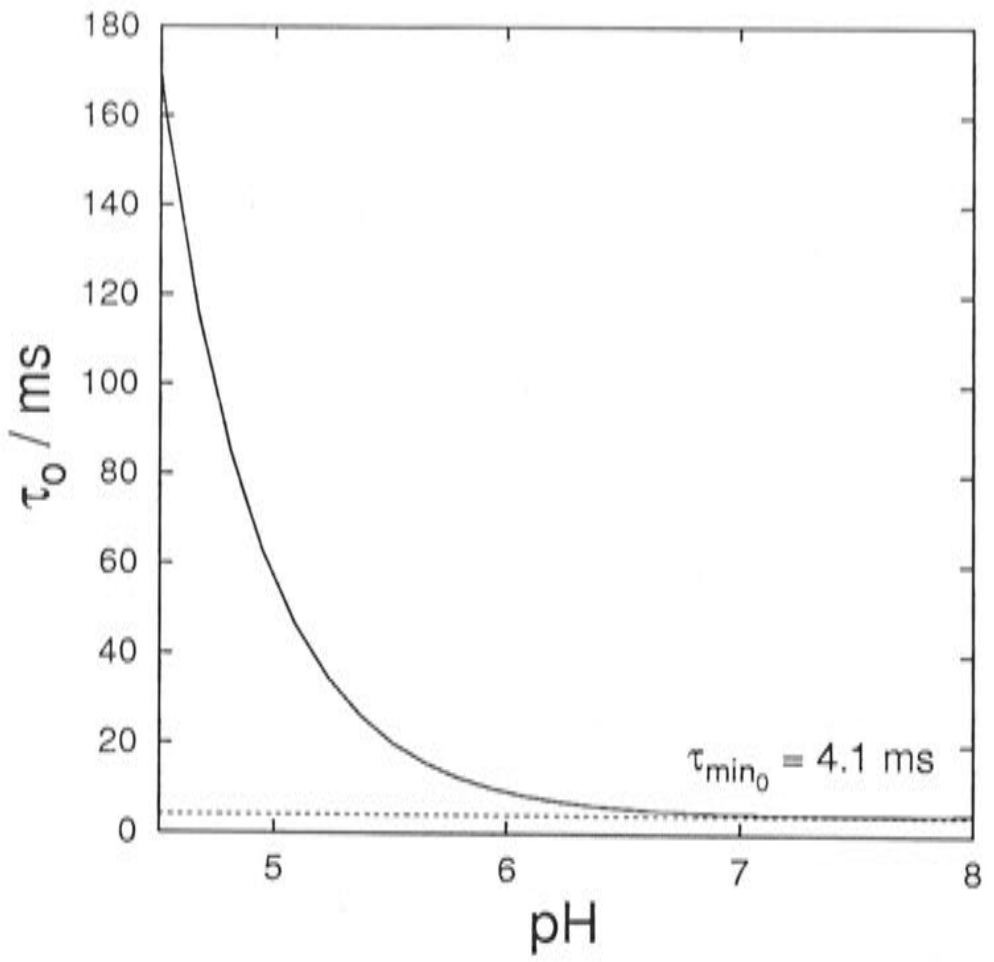

Figure 2.4: *Relationship between the pH–dependent part of τ_o and τ_{min_o}, according to equation (2.7).*

2.4.7 Discussion of the 'minimal model'

It can be seen from Figure 2.3 that good fits are obtained by fitting the results of the simulation to the experimental data of Rumberg and Siggel [147]. To understand the meaning of the results obtained one has to insert τ_{min_o} into equation (2.7). For illustration the relationship between the pH–dependent part of τ_o and τ_{min_o} is shown in Figure 2.4. Using equation (2.7) for $\tau_{min_o} = 4.1$ it follows, that at optimal conditions (pH=7.5) the pH–dependent part of τ_o is 4.47 ms.

However, one has to be careful with the interpretation of the fitted parameters because it depends on the interpretation of the reasons for the bell–shaped pH–dependency of the PQH_2 oxidation. Following the interpretation by Link, deprotonation of the quinol and the binding of the deprotonated quinol to the Rieske cluster are the pH–dependent steps described by τ_o [112]. In contrast to this τ_{BF} describes the pH–independent reactions following the binding of the deprotonated quinol. According to Hope and co–workers [83] protonation of the quinole radical anion causes the decrease of the rate constant for the cyt *b* reduction at low pH. Hence the pH–dependent part of τ_o would describe the reactions leading to cyt *b* reduction, whereas τ_{BF} would describe pH–independent reactions that could include reactions following the binding at the Rieske cluster and preceeding the cyt *b* reduction.

The pH–dependent part of τ_o (4.47 ms at pH 7.5) found here is in good agreement with the time for electron transfer from PQH_2 to the Rieske cluster of 3–5 ms determined by Hauska and co–workers.[c] [78] thus matching the interpretation by Link [112].

However, rate constants for cyt b_h re–oxidation determined by Hope and co–workers are in the order of 350–407 s^{-1} [82, 81] which is in the same order of magnitude as the reactions at the Q_o site as well as the τ_{BF} determined here. Accordingly, the reactions at the Q_r site should be taken into account in the model. It should be noted, however, that in their experiments Hope and co–workers applied very short light flashes (15 ns) at 0.2 Hz. Due to the very low frequency, relaxation processes can take place between the flashes thus reducing the amount of PQH_2 available for the reactions at the Q_o sites. Recent findings on the crystal structure of the cyt bc_1 complex, however, suggest that the cyt bc_1 acts as a functional dimer [187]. The reactions on one monomer of the dimer might be driven by the reactions on the other dimer [65]. Hence a restricted availability of PQH_2 could strongly influence the rate of the cytochrome bc_1 reactions. Because of the strong similarity to the cytochrome *bf* complex the same might hold for the latter and consequently lead to an underestimation of the rate for cyt b_h re–oxidation when measured in conditions where not enough PQH_2 is available (e.g. in oxidizing conditions)[d].

Whereas τ_{min_o} is related to the pH–dependent part of the time needed for the PQH_2 oxidation at the Q_o site (τ_o), the pH–independent τ_{BF} represents all pH–independent reactions, hence it implicitly may contain times involved in the PQ reduction at the Q_r site. Because the reactions at the Q_r site are not considered explicitly in the model, nothing can be said about their influence on τ_{BF}. Because of that and the reasons discussed above a more complex model is developed in order to find what time constants can be estimated when the reactions at Q_r are introduced explicitly.

---

[c]The electron transfer between the Rieske cluster and cyt *f* takes only a fraction of a millisecond and can thus be neglected.

[d]The fact that for reducing conditions a good fit of the rate constants involved in the Q–cycle was obtained in reference [82] by considering a monomeric operation of the cytochrome whereas in oxidizing conditions the predicted maximum of cyt b_h disagreed, might possibly be explained by a dimeric operation of the cytochrome complex.

2.5 A model explicitly including reactions at the Q_r site on the cyt *bf* complex

2.5.1 Electron storing pools

In addition to the steps considered in Section 2.4, now the protonation of quinones at the Q_r–site of the cyt *bf* comlex is explicitly taken into account. Hence one additional pool is introduced (see Figure 2.5).

According to that the following pools have to be identified:

- The plastoquinol pool (V_{PQ}).
- The cytochrome *b* pool ($V_{\mathrm{cyt}\ b}$). Cytochrome b_l (cyt b_l) and cytochrome b_h (cyt b_h) constitute this pool. Thus its capacity for electron storage equals two, since each of the cytochromes *b* can accept one electron. The electron transport from cytochrome b_l to cytochrome b_h is fast.
- The high potential pool (V_{hp}).
- The acceptor pool (V_A).
- The donor pool (V_D).

It should be noted that in these pools components are grouped together according to the rates of electron flux. The grouping is not necessarily related to the spatial organization of the components. The different redox carriers of cytochrome *bf* complex for example belong to different pools: FeS belongs to the high potential pool (V_{hp}) whereas cyt b_l belongs to the cytochrome *b* pool ($V_{\mathrm{cyt}\ b}$).

2.5.2 The differential equations

Now three differential equations are needed to describes the electron transfer from one pool to another (see Figure 2.6).

$$\frac{dV_{\mathrm{PQ}}}{dt} = 2 \cdot (J_B + J_r - J_o), \tag{2.14}$$

$$\frac{dV_{\mathrm{cyt}\ b}}{dt} = J_o - 2 \cdot J_r, \tag{2.15}$$

$$\frac{dV_{hp}}{dt} = J_o - J_{\mathrm{P700}}. \tag{2.16}$$

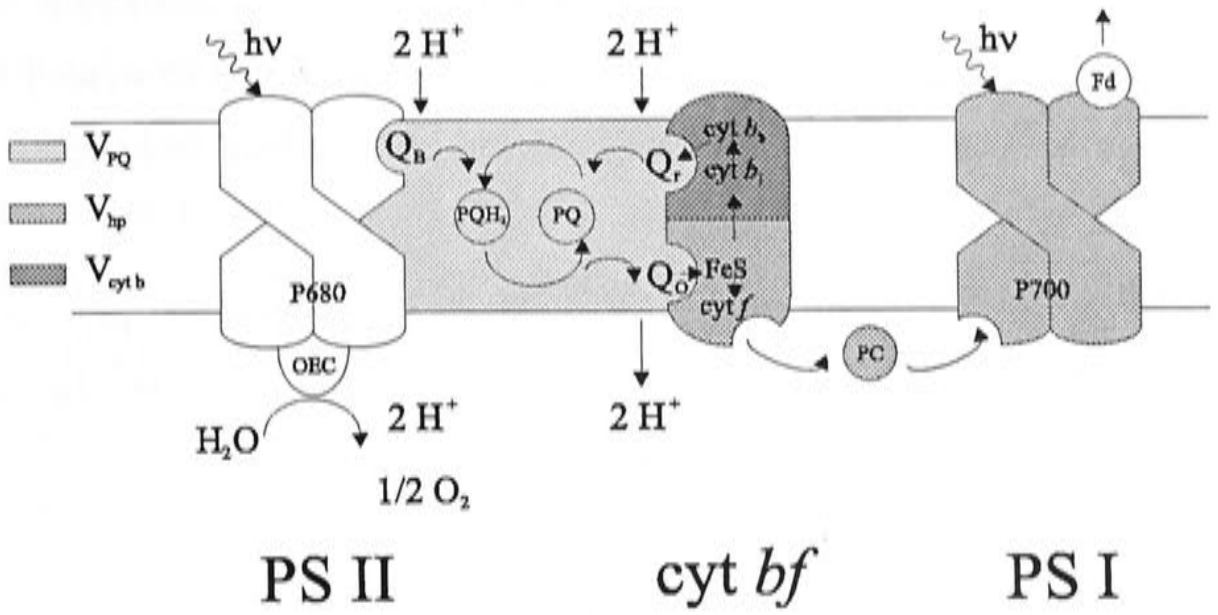

Figure 2.5: *Schematic diagram showing the three electron storing pools in the photosynthetic electron transport chain. Light grey: the plastoquinol pool V_{PQ}, medium grey: the high potential pool V_{hp}, dark grey: the cyt b pool $V_{cyt\ b}$, and grey: the acceptor pool V_A and the donor pool V_D. Abbreviations: OEC: oxygen evolving complex, P680: Chl a dimer, reaction centre of PS II, QB: binding site for PQ reduction, PQ: plastoquinone, PQH_2: plastoquinol, Qo and Qr: oxidising and reducing binding site on cyt bf, respectively, FeS: Rieske iron sulfur cluster, cyt f: cytochrome f, cyt b_l: cytochrome b 'low potential', cyt b_h: cytochrome b 'high potential', PC: plastocyanin, P700: Chl a dimer, reaction centre of PS I, Fd: ferredoxin.*

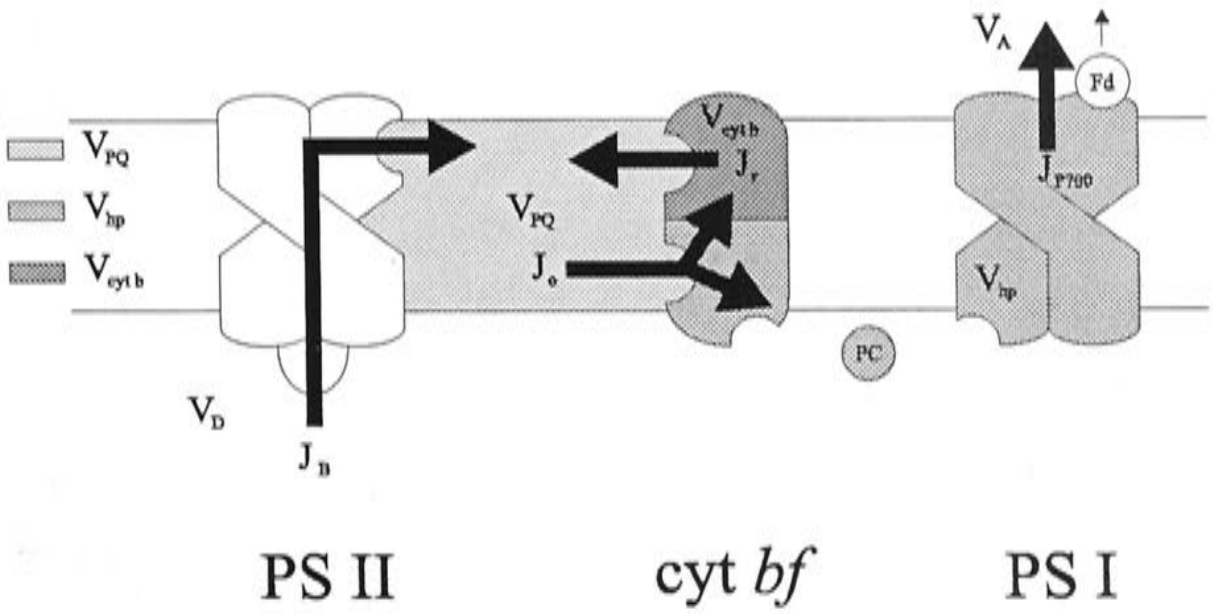

Figure 2.6: *Schematic diagram showing the fluxes between the three electron storing pools in the photosynthetic electron transport chain. Shades as in Figure 2.5. J_B electron flux into the PQ pool according to equation (2.5), J_o as in equation (2.17), J_r as in equation (2.20), and J_{P700} as in equation (2.9).*

V_{PQ} is the concentration of electrons stored in plastoquinol molecules (PQH_2), $V_{cyt\ b}$ is the concentration of electrons stored in the cyt b of the cytochrome b pool, and V_{hp} is the concentration of electrons bound at carriers belonging to the high potential pool, each relative to cyt bf.

J_r is the influx of electrons into the plastoquinone pool (V_{PQ}) caused by the formation of PQH_2 at the Q_r–binding site of the cyt bf complex, J_B, J_o, and J_{P700} are as in the model described in the Section 2.4.

2.5.3 Electron fluxes at the different reaction sites

The electron fluxes at the Q_B site and at P700 are the same as in Section 2.4.3. The flux at the Q_o site is very similar to that in Section 2.4.3 but now it has to be taken into account that for the transfer of the two electrons the FeS as well as the cyt b_l have to be oxidised, leading to:

$$J_o = \frac{\{QH_{2,o}\} \cdot \{FeS_{ox}\} \cdot (1 - \{\text{cyt } b_l^-\})}{\tau_o}. \tag{2.17}$$

This is in accordance with the experimental findings by Snyder and co–workers [161] who investigated spectroscopically the reduction kinetics of cyt c_1 and cyt b isolated from Yeast.

To describe the flux at the Q_r site, the analysis again starts with the time necessary for the reaction. Because the pH–dependency of the reactions involved in the PQ reduction is not clear yet, two different pH–dependencies are tested:

1. Reactions inversely proportional to the proton concentration:

$$\tau_r = \tau_{min_r} \cdot \frac{10^{-7}}{[H^+]}. \tag{2.18}$$

   This takes into account that the protonation should slow down when the pH is high and hence protons available for the reaction are limited.

2. Reaction pH–independent:

$$\tau_r = \tau_{min_r}. \tag{2.19}$$

   This will be the case if the protonation itself is rather fast and thus not rate limiting. This is given e.g. for the reactions at the Q_o site where the pH–dependency is determined by the protonation state of the binding sites involved rather than the protonation step itself. A pH–dependency caused by

the protonation state would not lead to a bell shaped pH–dependency but to a monotonically increasing rate with decreasing pH.

The number of molecules ready for conversion at the Q_r–binding site is the product of the concentration of Q_r–binding sites with bound quinones ($\{Q_r\}$) times the concentration of reduced cyt b_h, and cyt b_l each relative to the concentration of cyt bf. The latter term is included to take into account the fact that two electrons are transferred.

Thus J_r can be calculated according to:

$$J_r = \frac{\{Q_r\} \cdot \{\text{cyt } b_h^-\} \cdot \{\text{cyt } b_l^-\}}{\tau_r}. \tag{2.20}$$

2.5.4 Redox state of the electron carriers

The value for $\{Q_o\}$ is determined as described in Section 2.4.4. The concentrations of $\{Q_B\}$ and $\{Q_r\}$ relative to that of cyt bf are estimated in a manner analogous to that described in Section 2.4.4 assuming an equal probabilty for a PQ to bind at the Q_B or the Q_r site.

Thus the calculation of the redox state of the redox components is carried out as follows (compare Section 2.4.4):

$$\begin{aligned}
&\text{if} \quad \{V_{\text{PQ}}\} > 2 \cdot (\{C_{V_{\text{PQ}}}\} - (\{\text{PS II}\} + \{\text{cyt}\})) \\
&\Rightarrow \quad \{Q_B\} = \{\text{PS II}\} \cdot \tfrac{\{C_{V_{\text{PQ}}}\} - \{V_{\text{PQ}}\}}{2 \cdot (\{\text{PS II}\} + \{\text{cyt}\})}, \\
&\Rightarrow \quad \{Q_r\} = \{\text{cyt}\} \cdot \tfrac{\{C_{V_{\text{PQ}}}\} - \{V_{\text{PQ}}\}}{2 \cdot (\{\text{PS II}\} + \{\text{cyt}\})},
\end{aligned} \tag{2.21}$$

$$\begin{aligned}
&\text{if} \quad \{V_{\text{PQ}}\} \leq 2 \cdot (\{C_{V_{\text{PQ}}}\} - \{\text{PS II}\}) \\
&\Rightarrow \quad \{Q_B\} = \{\text{PS II}\}, \\
&\Rightarrow \quad \{Q_r\} = \{\text{cyt}\},
\end{aligned}$$

with $\{\text{cyt}\}$:= concentration of cyt bf (thus Q_r sites) per cyt bf (equal to 1).

$\{Q_r\}$:= the concentration of Q_r sites with bound PQH_2 relative to that of cyt bf.

To find the redox state of the carriers belonging to the newly introduced cyt b pool a consecutive reduction first of cyt b_h, then of cyt b_l is assumed, similar to the assumption described in Section 2.4.4. In contrast to the estimation of the redox state of the carriers forming the PC pool this assumption is quite reliable in this case because the difference in the redox potentials (and thus the equilibrium constant for electron transitions) is quite high (100 mV). It accords with the finding that cyt b_l did not give any reduction signal in experiments of Nitschke and co–workers [128]. The redox states are calculated according to the following equations:

$$\begin{aligned}
&\text{if } \{V_{\text{cyt } b}\} > 1 \Rightarrow \{\text{cyt } b_{l_{ox}}\} = 2 - \{V_{\text{cyt } b}\},\\
&\text{if } \{V_{\text{cyt } b}\} \leq 1 \Rightarrow \{\text{cyt } b_{l_{ox}}\} = 1,\\
&\text{if } \{V_{\text{cyt } b}\} > 1 \Rightarrow \{\text{cyt } b_{h_{red}}\} = 1,\\
&\text{if } \{V_{\text{cyt } b}\} \leq 1 \Rightarrow \{\text{cyt } b_{h_{red}}\} = \{V_{\text{cyt } b}\}.
\end{aligned} \tag{2.22}$$

The first two conditions describe that cyt b_l will only be reduced when cyt b_h is reduced. The latter two conditions are the formulation of the assumption that as soon as there is an electron stored in the cyt b pool it will be transferred to cyt b_h immediately.

The calculation for the components of the PC pool is the same as in Section 2.4.4.

2.5.5 Summary of the assumptions

In addition to the general assumptions described in Section 2.3 the following assumptions are introduced for the model described above:

1. Protonation at Q_B is fast and can thus be neglected.
2. pH–dependency of PQ oxidation is mainly caused by the importance of reaction groups being protonated or unprotonated.
3. An average time constant for the first and second reduction step at Q_r is assumed.

2.5.6 Fitting literature data with the model

The equations in the program are changed according to the mathematical formulation described above. The stoichiometry is assumed to be {PS II} : {PQ} : {cyt bf}

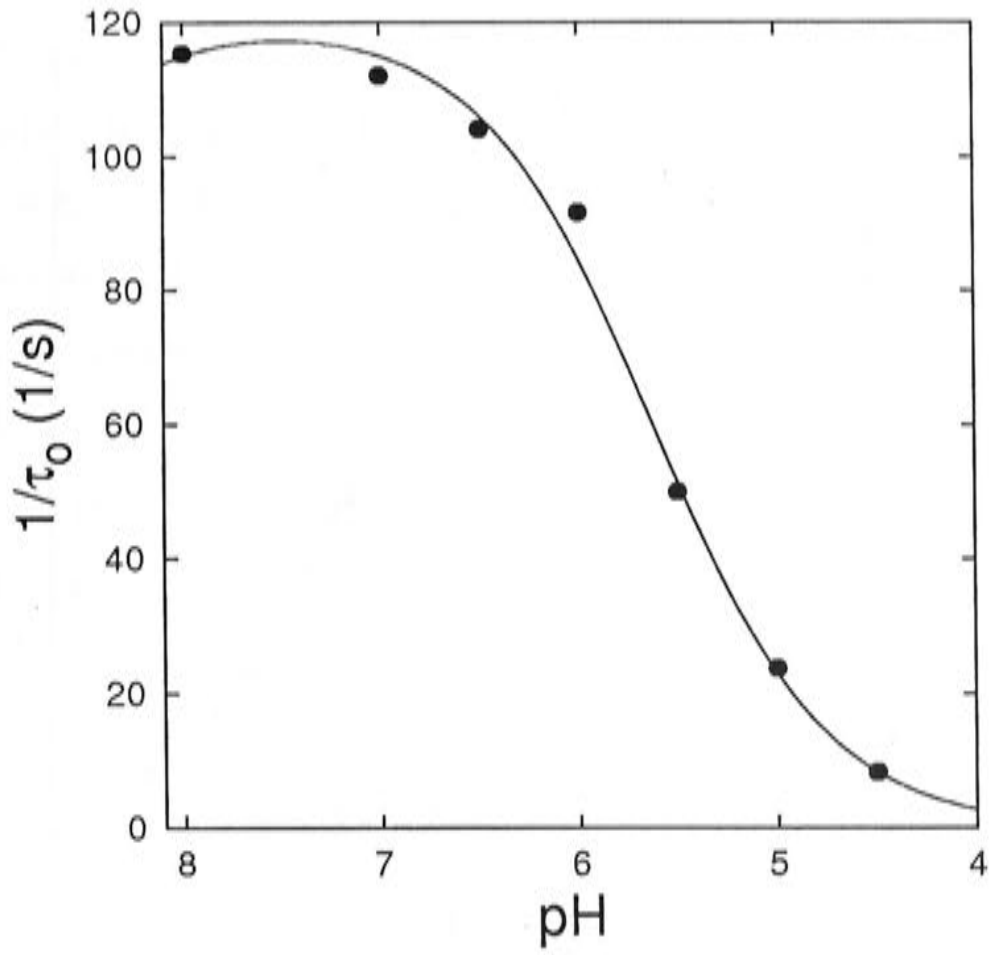

Figure 2.7: *pH–dependency of P700 re–reduction as in Figure 2.3. The line shows the best fit to the data according to the model implicitly taking into account the PQ reduction at the Q_r site. The reactions at Q_r are assumed to be pH–dependent. τ_{min_o} = 4.4 ms, τ_{BF} = 8.8 ms, $\tau_r = 1.5 \cdot 10^{-5}$, sum of errors squared: 66.31 s^{-2}.*

$= 2 : 12 : 1$. As shown in Figure 2.7 and Figure 2.8 a reasonable fit is obtained for pH–dependent as well as for pH–independent reactions at the Q_r site.

1. pH–dependent reactions at the Q_r site

For the pH–dependent reactions at the Q_r site described in equation (2.18) the best fit is obtained with:

$$\begin{aligned} \tau_{min_o} &= 4.4 \text{ ms}, \\ \tau_{BF} &= 8.8 \text{ ms}, \\ \tau_{min_r} &= 1.5 \cdot 10^{-5} \text{ ms}. \end{aligned}$$

τ_{min_o} is as described in Section 2.4.7. According to the interpretation of the bell–shaped pH–dependency by Link [112] τ_{BF} stands now for the pH–independent reactions following the binding of PQH_2 at Q_o but this time without containing implicitly the reactions at the Q_r site. The sum of the errors squared is 66.31 s^{-2}.

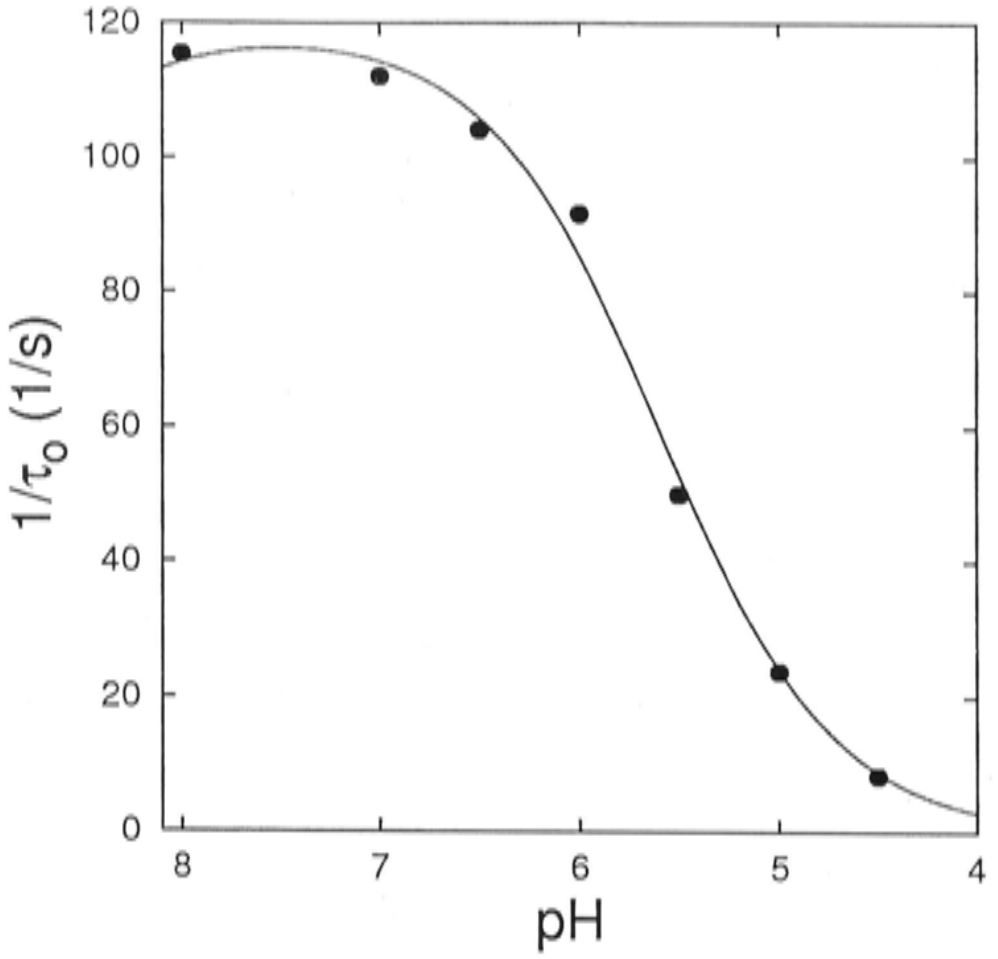

Figure 2.8: *pH–dependency of P700 re–reduction as in Figure 2.3. As Figure 2.7. But here, the reactions at Q_r are assumed to be pH–independent. $\tau_{min_o} = 3.9$ ms, $\tau_{BF} = 8.1$ ms, $\tau_r = 1.1 \cdot 10^{-1}$, sum of errors squared: 59.30 s^{-2}, $x = 9$.*

2. pH–independent reactions at the Q_r site

For the pH–independent reactions at the Q_r site described in equation (2.19) the best fit is obtained with:

$$\begin{aligned} \tau_{min_o} &= 3.9 \text{ ms}, \\ \tau_{BF} &= 8.1 \text{ ms}, \\ \tau_{min_r} &= 1.1 \cdot 10^{-1} \text{ ms}. \end{aligned}$$

The sum of the errors squared is 59.30 s^{-2}. τ_{min_r} here describes the pH–independent reactions at the Q_r site, τ_{min_o}, and τ_{BF} are as described above.

2.5.7 The influence of higher binding affinity at the Q_r site

The analysis is extended to take into account a different affinity for PQH_2 at Q_r compared to Q_B. This is assumed because equal binding properties on the two different proteins are quite improbable. Now, a higher binding affinity at the Q_B site, especially at high light, would accelerate the reduction of the PQ pool while the

Q–cycle would be slowed down because of the shortage of unreduced PQ. When the Q–cycle is disturbed at the Q_r site the cytochrome b pool will be more reduced and consequently slow down the PQH_2 oxidation at Q_o. Hence, this situation could lead to a harmful overreduction of the PQ pool and a 'jam' caused by the highly reduced cytochrome b pool. In contrast to this, a lower binding affinity at the Q_B site would slow down the PQ reduction at PS II in favour to an undisturbed Q–cycle[e].

Assuming that the affinity at Q_r for PQH_2 is x times greater than at Q_B, the calculation of the redox state $\{Q_B\}$ and $\{Q_r\}$ changes to.

$$
\begin{aligned}
\text{if} \quad \{V_{PQ}\} &> 2 \cdot (\{C_{V_{PQ}}\} - (\{\text{PS II}\} + \{\text{cyt}\})) \\
\Rightarrow \quad \{Q_B\} &= \{\text{PS II}\} \cdot \tfrac{\{C_{V_{PQ}}\} - \{V_{PQ}\}}{2 \cdot (\{\text{PS II}\} + x \cdot \{\text{cyt}\})}, \\
\Rightarrow \quad \{Q_r\} &= x \cdot \{\text{cyt}\} \cdot \tfrac{\{C_{V_{PQ}}\} - \{V_{PQ}\}}{2 \cdot (\{\text{PS II}\} + x \cdot \{\text{cyt}\})}, \qquad (2.23) \\
\text{if} \quad \{V_{PQ}\} &\leq 2 \cdot (\{C_{V_{PQ}}\} - \{\text{PS II}\}) \\
\Rightarrow \quad \{Q_B\} &= \{\text{PS II}\}, \\
\Rightarrow \quad \{Q_r\} &= \{\text{cyt}\},
\end{aligned}
$$

For the pH–dependent reaction best fits are obtained for

$$
\begin{aligned}
\tau_{min_o} &= 4.2 \text{ ms}, \\
\tau_{BF} &= 9.2 \text{ ms}, \\
\tau_{min_r} &= 2.1 \cdot 10^{-4} \text{ ms}, \\
x &= 7/3, \\
\text{sum of errors squared} &= 57.65 \ s^{-2}.
\end{aligned}
$$

Whereas for the pH–independent reaction best fits are obtained for

$$
\begin{aligned}
\tau_{min_o} &= 4.2 \text{ ms}, \\
\tau_{BF} &= 9.1 \text{ ms}, \\
\tau_{min_r} &= 1.0 \cdot 10^{-1} \text{ ms}, \\
x &= 9/1, \\
\text{sum of errors squared} &= 57.73 \ s^{-2}.
\end{aligned}
$$

[e]However, it has to be mentioned that in crystals PQ could not be found at the Q_o site. This suggests that the binding affinity for PQ at that site is quite low [187]

However, the fits including different binding affinities are not much better than those found for equal binding affinity and the time constants obtained are the same order of magnitude. Only for the pH–dependent case one of the parameters obtained was different: τ_{min_r} is tenfold higher if a 7/3 fold higher binding affinity for PQ at Q_r is assumed than for an equal binding affinity. On the other hand, this time constant is very fast and therefore not limiting.

2.5.8 Discussion of the model

For both pH–dependencies good fits are obtained.

1. pH–dependent reactions at the Q_r site

If a pH–dependency of the PQ reduction is introduced, the time constant for this reaction is very small ($3.6 \cdot 10^{-4}$ ms). Looking at the measured data, it is obvious that the re–reduction time of P700 is not slowing down at high pH (see e.g. Figure 2.3). This contrasts with equation (2.18) for the assumed rate for the PQ reduction. The latter decreases with increasing pH, reflecting the need for protons for the reaction to take place. Hence, if a pH–dependency as given above is introduced, the measured data can only be explained by non–limiting reactions at the Q_r site. If the reactions at this site were slow, this would cause an increase of the re–reduction time (decrease of $1/\tau$) at high pH. Thus it is reasonable that quite short reaction times are obtained in the fit. That again would endorse the assumption in the minimal model (see Section 2.4) and raises the question of whether it is necessary to explicitly formulate the reactions at the Q_r site.

2. pH–independent reactions at the Q_r site

However in the model of Hope and co–workers [81] no pH–dependency of the cyt b_h re–oxidation could be found. The interpretation of the results when considering pH–independent reactions is more complicated. The best fits resulted in relatively short reaction times for the pH–independent reaction at Q_r. This would be in agreement with the assumptions of the minimal model but in contradiction to the relatively slow re–oxidation of cyt b_h found by Hope and co–workers. However, the slow value found in their experiments might be an artifact of the flash light conditions as discussed in Section 2.4.7.

Now the reactions at the Q_o site are considered. Again the time constant related to the pH–dependent step τ_{min_o} agrees quite well with literature data for electron transfer from PQH_2 to the Rieske cluster. This would match the interpretation of the pH–dependency by Link [112]. According to the interpretation by Hope and

co–workers the pH–dependent time constant relates to the reduction of cyt b [83] that should be rather fast [112] in contrast to the result obtained here.

Looking at τ_{BF} it has to be noted that in contrast to the 'minimal model' in this model τ_{BF} does not contain implicitly reactions at the Q_r site. It only contains pH–independent reactions at the Q_o site. According to Link's interpretation of the bell–shaped pH–dependency of the quinone oxidation [112] these are the reactions following the binding at the Rieske cluster. That includes (1) the electron transfer to cyt b_l, (2) travelling times for the electrons within the complex, and (3) the time until the oxidised PQ is available to enter the PQ pool. The first step should be a rather quick reaction, in the order of 10^6/s [112]. The second reaction has to be considered to be fast too, according to the big difference in the redox potentials of cyt b_l and cyt b_h. PQ could not be found at the Q_o site in crystals. This suggests that the binding affinity for PQ at that site is quite low [187] and consequently the unbinding should be rather quick. It follows that τ_{BF} should be small but a reasonable fit could not be obtained omitting τ_{BF}, neither with pH–dependent reactions at Q_r nor with pH–independent reactions. However, the time required for an electron to be transferred from cyt b_h certainly depends on the availability of PQ. On the other hand following the interpretation of the bell–shaped pH–dependency by Hope and co–workers [83] τ_{BF} also contains the reactions at the Q_o site preceding the cyt b_l reduction. That could be (1) the deprotonation of PQH_2 to PQH^- which is considered to precede the oxidation because the midpoint potential for quinol oxidation is much too positive ($> +900$ mV [136]), (2) the transfer of the first electron to FeS, and (3) the second deprotonation step. According to this interpretation the time constant obtained for the reactions preceding the cyt b reduction is sensible whereas the time constant for the the cyt b reduction and the following reactions found here is too high.

2.5.9 Comparison between the numerical and the analytical solution for the special case of a highly oxidised system

To evaluate the numerical solution of the differential equations, the analytical solution for a special case (highly oxidised system) was determined. Several different states of the system arise because of the assumption of a consecutive filling of the pools. Some of them can be solved easily while others result in a complex system of coupled differential equations. Therefore only one of the simplier cases is chosen as an example.

The V_{PQ} pool can be in three different states:

(1) $0 < \{V_{\mathrm{PQ}}\} < 2$,

(2) $2 < \{V_{\mathrm{PQ}}\} < \{\mathrm{C}_{V_{\mathrm{PQ}}}\}$ - ($\{$PS II$\}$+$\{$cyt $bf\}$),

(3) $\{\mathrm{C}_{V_{\mathrm{PQ}}}\}$ - ($\{$PS II$\}$+$\{$cyt $bf\}$) $< \{V_{\mathrm{PQ}}\}$.

(1) refers to an oxidised system, where the concentration of $\{(\mathrm{QH}_2)_Z\}$ is limited at the Q_o site on cyt bf. (2) reflects the situation where enough PQ is available for both, the Q_B site and the Q_r site. At the same time enough PQH_2 is available for the Q_o site. In contrast (3) describes a reduced system where PQ is limited.

Similarly, the $V_{\mathrm{cyt}\ b}$ pool can be in two states:

(1) $0 < \{V_{\mathrm{cyt}\ b}\} < 1$,

(2) $1 < \{V_{\mathrm{cyt}\ b}\} < 2$,

Assuming a stoichiometry of ($\{$cyt $bf\}$: $\{$PC$\}$: $\{$PS I$\}$) = (1 : 2 : 1), the V_{hp} pool can be in three different states:

(1) $0 < \{V_{hp}\} < 1$,

(2) $1 < \{V_{hp}\} < 4$,

(3) $4 < \{V_{hp}\} < 5$,

This results in 18 possible different states of the system. The analytical description of some of these states can be solved simply. However, some result in a coupled system of non–linear differential equations that cannot easily be solved analytically. The analytical solution presented here is restricted to the simple case of an oxidised system.

The electron fluxes are:

$$J_B = \{Q_B\}/\tau_B, \tag{2.24}$$

$$J_r = \{Q_r\} \cdot \{\text{cyt } b_h^-\} \cdot \{\text{cyt } b_l^-\}/\tau_r, \tag{2.25}$$

$$J_o = \{\mathrm{QH}_{2,o}\} \cdot \{\mathrm{FeS}_{ox}\} \cdot (1 - \{\text{cyt } b_l^-\})/\tau_o, \tag{2.26}$$

$$J_{\mathrm{P700}} = \{\mathrm{P700}_{red}\}/\tau_{\mathrm{PS\ I}}, \tag{2.27}$$

From the assumption that all pools are in state 1, it follows that

$$\{Q_B\} = \{\text{PS II}\}, \tag{2.28}$$
$$\{Q_r\} = 1, \tag{2.29}$$
$$\{(\text{QH}_2)_Z\} = \{V_{\text{PQ}}\}/2, \tag{2.30}$$
$$\{\text{cyt } b_l^-\} = 0, \tag{2.31}$$
$$\{\text{cyt } b_h^-\} = \{V_{\text{cyt } b}\}, \tag{2.32}$$
$$\{\text{FeS}_{ox}\} = 1, \tag{2.33}$$
$$\{\text{P700}_{red}\} = \{V_{hp}\}. \tag{2.34}$$

Correspondingly in the oxidised state the fluxes are as follows:

$$J_B = \{\text{PS II}\}/\tau_B, \tag{2.35}$$
$$J_r = 0, \tag{2.36}$$
$$J_o = \{V_{\text{PQ}}\}/(2 \cdot \tau_o), \tag{2.37}$$
$$J_{\text{P700}} = \{V_{hp}\}/\tau_{\text{PS I}}, \tag{2.38}$$

Thus, from equation (2.14)–(2.16) for the set of differential equations in the oxidised state, it follows:

$$\dot{x} = a - 2bx, \tag{2.39}$$
$$\dot{y} = bx, \tag{2.40}$$
$$\dot{z} = bx - cz, \tag{2.41}$$

where $x := \{V_{\text{PQ}}\}$,
$y := \{V_{\text{cyt } b}\}$,
$z := \{V_{hp}\}$,
with $a := 2 \cdot \{\text{PS II}\}/\tau_B$,
$b := 1/(2 \cdot \tau_o)$
$c := 1/\tau_{\text{PS I}}$

For the first equation (2.39), the homogeneous solution is

$$x_H = A \cdot e^{-2bt}. \tag{2.42}$$

Variation of parameters leads to:

$$x_I = A(t) \cdot e^{-2bt}. \tag{2.43}$$

Insertion of this function into the differential equation (2.39) leads to a differential equation in $A(t)$.

$$\frac{dA}{dt} = ae^{2bt}. \tag{2.44}$$

Inserting the solution of this differential equation into equation (2.43) leads to the inhomogeneous solution. The linear combination of the homogeneous and the inhomogeneous solution span the space of general solutions of the differential equation.

It follows that

$$x = a/2b + Ce^{-2bt}. \tag{2.45}$$

with C being the integration constant.

Together with the starting condition ($\{V_{\mathrm{PQ}}\}(\mathrm{t}{=}0) = 0$) and inserting a, b, c, and x this leads to the solution:

$$\{V_{\mathrm{PQ}}\} = \frac{2\{\mathrm{PS\ II}\}\tau_o}{\tau_B}(1 - e^{-t/\tau_o}). \tag{2.46}$$

Inserting this function into the differential equation (2.40) leads to

$$y = \frac{a}{2}(t + \frac{1}{2b}e^{-2bt}) + D. \tag{2.47}$$

with D being the integration constant.

Using the starting condition ($\{V_{\mathrm{cyt}\ b}\}(\mathrm{t}{=}0) = 0$) and inserting a, b, and c the solution of the differential equation (2.40) is

$$\{V_{\mathrm{cyt}\ b}\} = \frac{\{\mathrm{PS\ II}\}}{\tau_B}(t + \tau_o(e^{-t/\tau_o} - 1)). \tag{2.48}$$

Differential equation (2.41) is solved by insertion of the solution of differential equation (2.39). This leads to:

$$\dot{z} + cz = \frac{a}{2}(1 - e^{-2bt}). \tag{2.49}$$

The derivative is:

$$\ddot{z} + c\dot{z} = abe^{-2bt}. \tag{2.50}$$

This equation is solved with the following approach:

$$\dot{z} = \lambda(t)e^{-2bt}. \tag{2.51}$$

Inserting this into equation (2.50) leads to the differential equation

$$\dot{\lambda} + (c - 2b)\lambda = ab. \tag{2.52}$$

Again, this can be solved by finding the homogeneous solution and variation of the constant of the homogeneous solution. The homogeneous solution is:

$$\dot{\lambda}_H = Ae^{(2b-c)t}. \tag{2.53}$$

Variation of A in time ($A(t)$), inserting in equation (2.52) leads to a differential equation in $A(t)$. The solution of this equation is then inserted into the inhomogeneous equation. The linear combinations of this solution and that of the homogeneous equation gives all solutions for λ:

$$\lambda = \frac{-ab}{2b - c} + Ee^{(2b-c)t}. \tag{2.54}$$

with E being the integration constant.

The boundary condition to determine the integration constant is ($\dot{z}(t = 0) = 0$). This follows from equation (2.41), using $x(0) = 0$ and $z(0) = 0$. It leads to

$$\dot{z} = \frac{ab}{2b - c}(e^{-ct} - e^{-2bt}). \tag{2.55}$$

This can be easily integrated. Using the starting condition ($\{V_{hp}\}$(t=0) = 0) yields:

$$z = \frac{ab}{2b - c}(\frac{1}{2b}e^{-2bt} - \frac{1}{c}e^{c}t) + \frac{a}{2c} \tag{2.56}$$

$$\tag{2.57}$$

$$\Leftrightarrow \{V_{hp}\} = \frac{\tau_{\text{PS I}}\{\text{PS II}\}}{\tau_B(\tau_{\text{PS I}} - \tau_o)}(\tau_o e^{\frac{-1}{\tau_o}t} - \tau_{\text{PS I}} e^{\frac{-1}{\tau_{\text{PS I}}}t}) + \frac{\tau_{\text{PS I}}}{\tau_B} \tag{2.58}$$

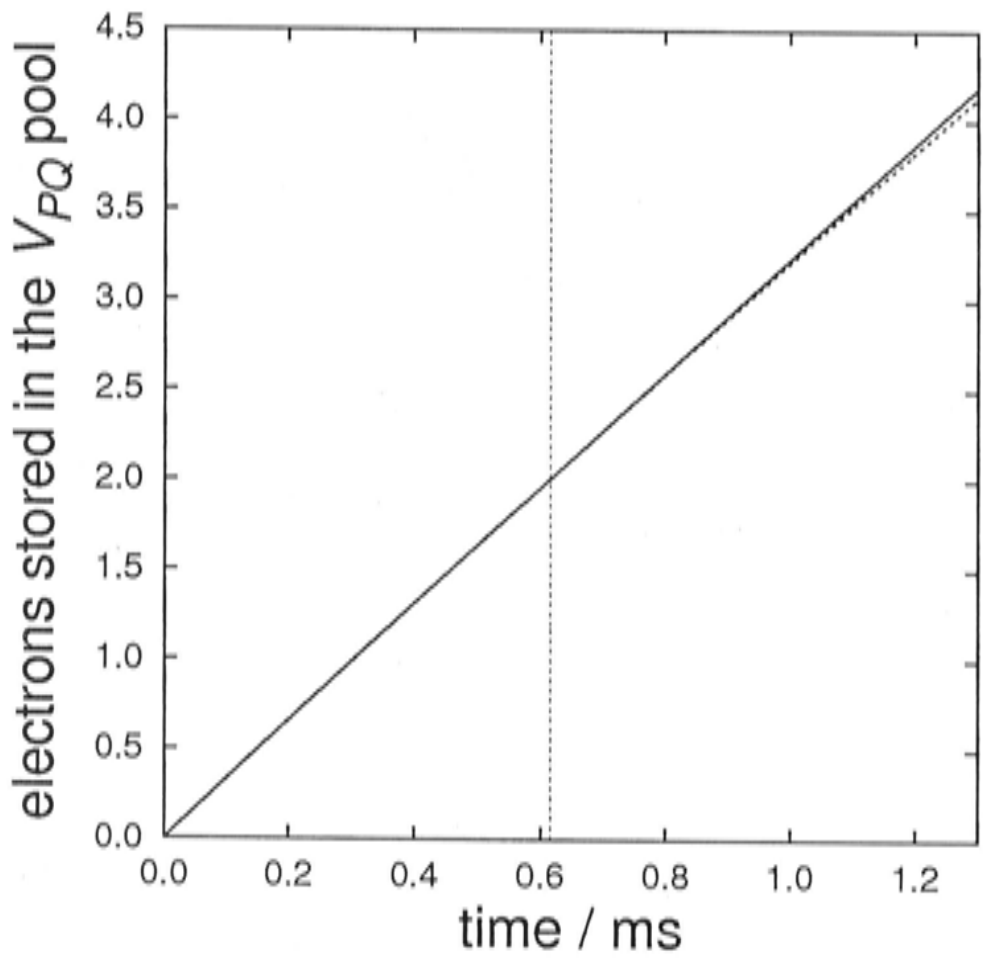

Figure 2.9: *Comparison of the analytical solution with the numerical solution for the V_{PQ} pool. The solid line shows the values obtained from the analytical solution, the dashed line (mostly hidden by the nearly identical solid line) shows the computed values. Time constants are those of the best fit for the pH–dependent reactions at the Q_r site. The dashed vertical line shows the limit of the analytical solution. After the indicated time of 0.615 ms the V_{PQ} pool is larger than 2 for all tested pH values ($pH = 5$, 6, and 7) and thus the assumptions of the analytical solution are no longer valid. Only results for $pH = 7$ are shown as the values for $pH = 6$ and $pH = 5$ are nearly identical.*

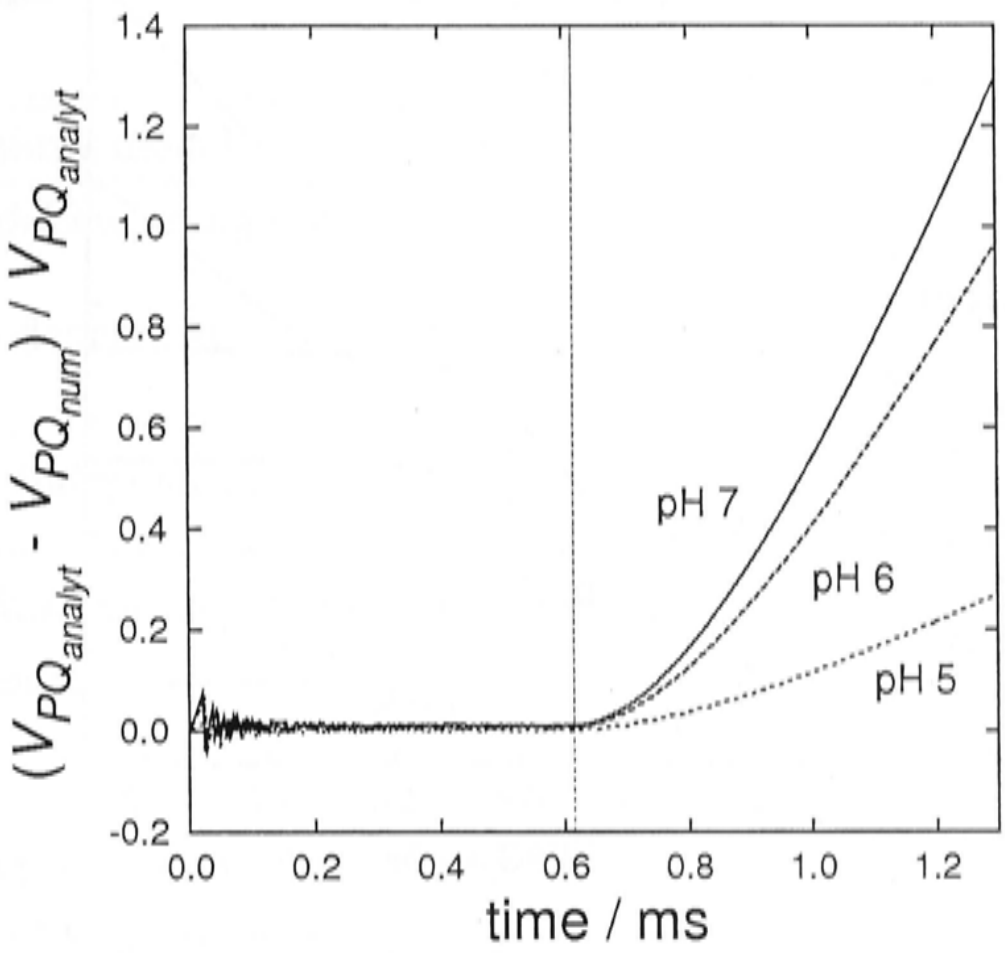

Figure 2.10: *Similar to Figure 2.9 but here the y–axis shows the difference between the analytical solution and the numerical solution for the V_{PQ} pool in %.*

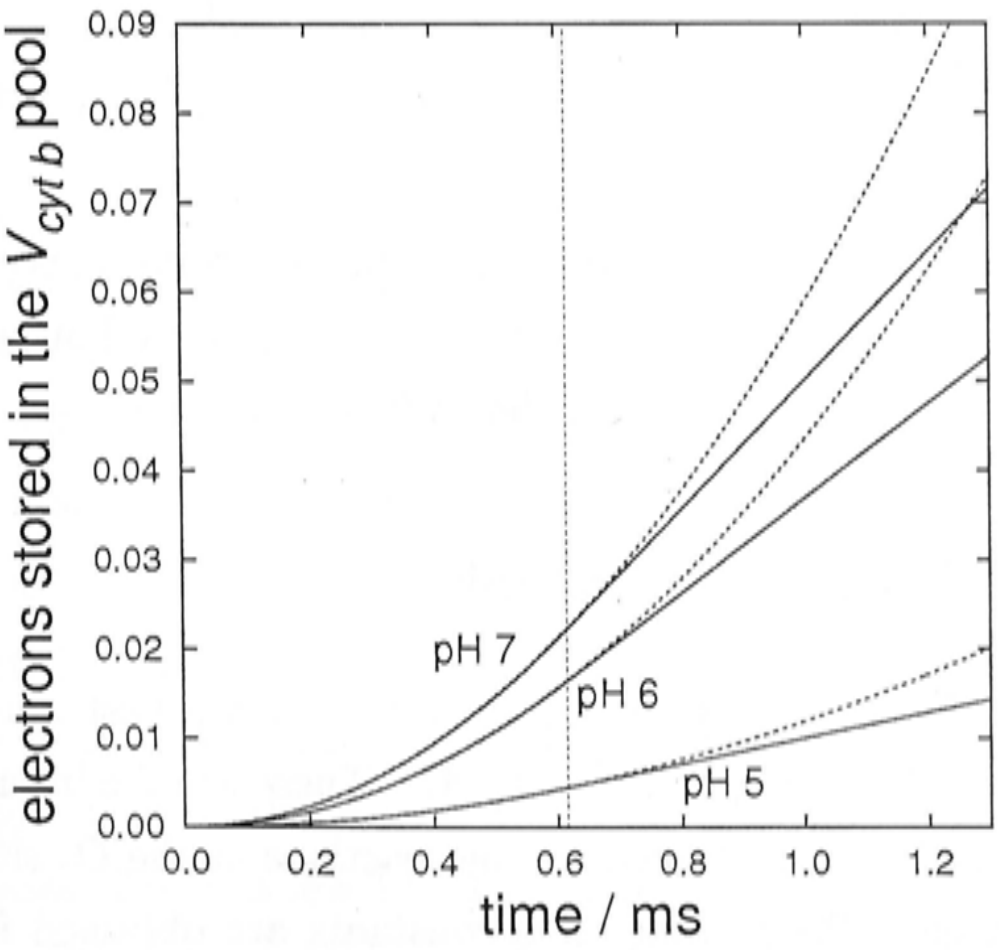

Figure 2.11: *Comparison of the analytical solution with the numerical solution for the $V_{cyt\,b}$ pool. Similar to Figure 2.9. Here, results for all tested pH values are shown.*

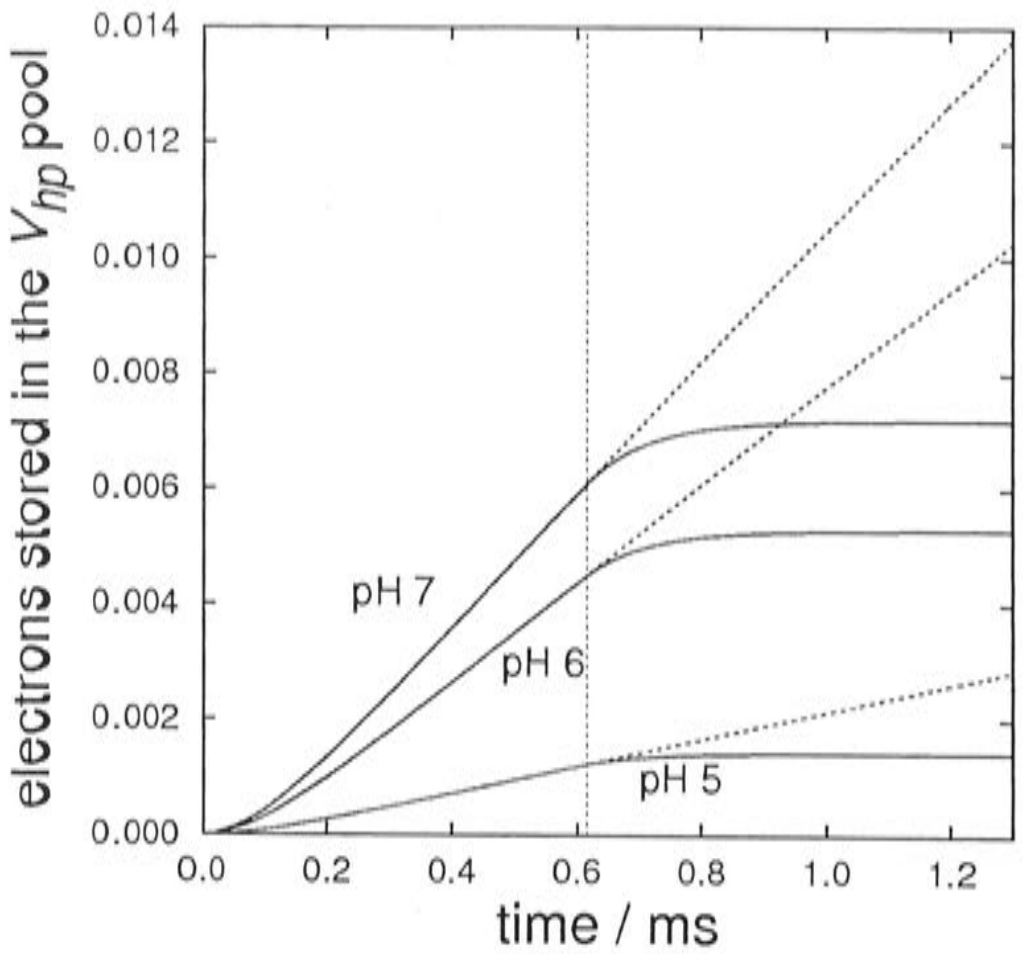

Figure 2.12: *Comparison of the analytical solution with the numerical solution for the V_{hp} pool. As Figure 2.11.*

The solution presented here is compared with the electron concentration in the electron storing pools obtained from numerical integration for the pH–dependent case. The parameters leading to the best fit are used ($\tau_{min_o} = 4.4$ ms, $\tau_{BF} = 8.8$ ms, $\tau_r = 1.5 \cdot 10^{-5}$). Solutions are compared for pH=5, pH=6, pH=7 (see Figures 2.9–2.12).

It can be seen in Figures 2.9–2.12 that the numerical solution is extremely similar to the analytical solution. However, the comparison is carried out only for the case of very oxidised conditions and the pH–dependent reaction at Q_r.

2.5.10 Conclusion and Outlook

In summary of the three models presented here two are best able to explain the experimental data of Rumberg and Siggel [147]. These are the 'minimal model' and the model explicitly taking into account the reactions at the Q_r site assuming pH–independent reactions. Reasonable time constants are obtained for the reactions considered (see Table 2.1). However all models result in relatively fast reactions at the Q_r site: $1.5 \cdot 10^{-5} - 2.1 \cdot 10^{-4}$ ms for the pH–dependent reactions, and ca. 10^{-1} ms for the assumption of pH–independent reactions. This is in contradiction to the low rate constants for cyt b_h re–oxidation (350–407 s^{-1}) [82, 81].

model	binding affinity Q_r/Q_B	rate constants/ms τ_{min_o}	τ_{BF}	τ_{min_r}
minimal model	equal	4.1	9.3	–
model including Q_r				
pH–dependent	equal	4.4	8.8	$1.5 \cdot 10^{-5}$
	7/3	4.2	9.2	$2.1 \cdot 10^{-4}$
pH–independent	equal	3.9	8.1	$1.1 \cdot 10^{-1}$
	9/1	4.2	9.1	$1.0 \cdot 10^{-1}$

Table 2.1: *Rate constants resulting from best fits to the experimental data using the differnt models.*

All models presented in this Chapter lead to very similar time constants and pH–dependencies of P700 re–reduction. To discriminate between the different models more data sets would be required. Since the models show the most difference in the values of τ_{min_r} data sets related to the flux at the Q_r would be needed for such a discrimination. However, data on the reactions at the Q_r site are difficult to obtain and most information is based on modelling work as e.g. [81].

Outlook

Now the model (including Q_r, pH–independent, equal binding affinity) is used to predict the control that PS II exerts on electron flux (see Figure 2.13). Experimentally the control PS II exerts on whole chain electron flux can be analyzed by titrating down PS II with DCMU and measuring the resulting electron flow to P700. Accordingly, Figure 2.13 shows the electron flux through P700 (J_{P700}) as a function of the percentage of active PS II.

The predicted curve is shown in Figure 2.13. If only few PS II are inhibited a slight increase in J_{P700} is found, followed by a steep decrease to zero for all PS II being inhibited. Due to the several times faster reactions at the Q_B site, J_{P700} does not decrease if only a few PS II are inhibited. Instead, the rise of the curve when only few PS II are inhibited reflects the competition between the Q_B site and the Q_r site since equal binding probabilities are assumed[f]. The steep decline

[f]With increasing binding affinity at the Q_r site the increase becomes less pronounced (data not shown).

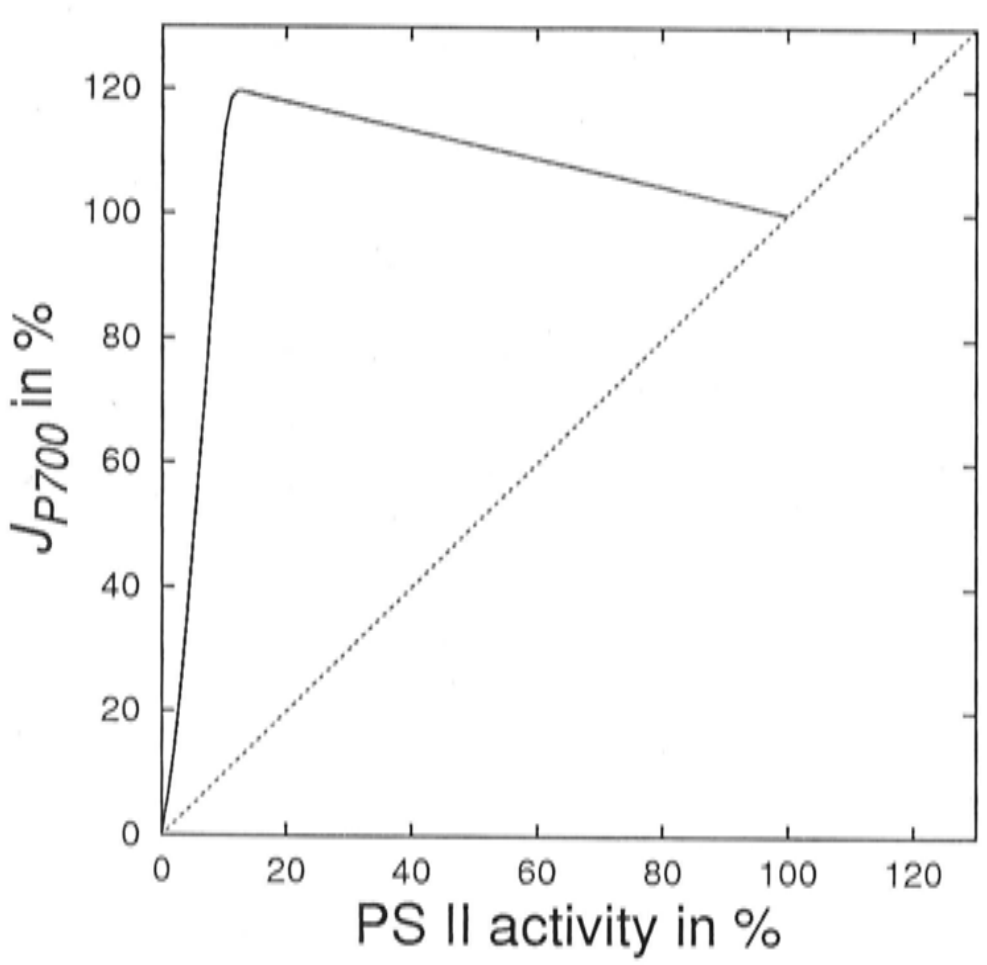

Figure 2.13: *Predicted curve of control on electron flux exerted by PS II using the pH–independent model including Q_r (equal binding affinity). 100 percent at the x–axis corresponds to the undisturbed system, i.e. no inhibition of PS II by DCMU. 100 percent on the y–axis correspond to the flux through P700 measured in the absence of DCMU.*

reflects the situation when the overcapacity of PS II is not sufficient to compensate PS II inhibition.

The predicted curve is somewhat unexpected and the question is whether it reflects the realistic situation or rather limitations of the model. Therefore the predictions will be tested against experimental data in the next Chapter. There measurements of the control, that PS II exerts on electron flux are analysed and discussed in the context with the predictions arising from the model presented here. Possible limitations of the model leading to the resulting curve will be discussed.

Chapter 3

Titration of PS II and its influence on whole chain electron flux

Contents

3.1 Introduction

As the electron flow through the cyt *bf* complex is known to be the slowest step in the electron transport chain, PS II should exert little control on the whole chain flux ($H_2O \rightarrow$ PS I) under saturating light (see also predicted curves (Figure 2.13) in Chapter 2). This was indeed what Kirchhoff and co–workers [96] found in destacked thylakoids, which exhibit a non–linear control curve: if PS II activity was titrated to 50% of its total activity, the whole chain flux, J_e, decreased only about 25%. In contrast to that, their flux control curve for stacked thylakoids was nearly linear, indicating that PS II exerts strong control on the overall electron flux. The data were interpreted by assuming that only in destacked membranes do a large number of PS II share a pool of diffusing PQ (see Figure 3.1A). Destacking was achieved by a decrease in the Mg^+ concentration, which leads to an general increase in the electrostatic repulsive forces between charged integral protein complexes. In this state, despite a high protein density, the rapidly diffusing PQ was suggested to weave its way through the complexes. In stacked thylakoids (see Figure 3.1B), rapid PQ diffusion to cyt *bf* was suggested to be restricted to small domains in the close vicinity of individual PS II centres [96]. Kirchhoff and co–workers proposed a dynamic protein network formed in grana stacks by specific interactions between PS II and LHC II. In this arrangement, cyt *bf* complexes may have access to photo–reduced PQ in the close vicinity of PS II only (see Figure 3.1B).

To test the model of electron transport presented in Chapter 2 and its limitations, PS II titration measurements were carried out for thylakoids from pea, spinach, and tobacco. Linear electron flow is then plotted versus PS II activity. It is found that the three species investigated show complex, s–shaped control by PS II of whole chain transport. This cannot be explained by the model of electron transport presented in Chapter 2 that is based on shared pools. Nor can the s–shape be explained by the micro–domain concept proposed by Kirchhoff and co–workers [96]. This concept would lead to either a linear relationship (small domains) or a simple curved relationship (large domains). Instead the complex curves are explained by an extended micro–domain concept and are fitted with a stochastical, mathematical model incorporating spatial aspects of protein organisation.

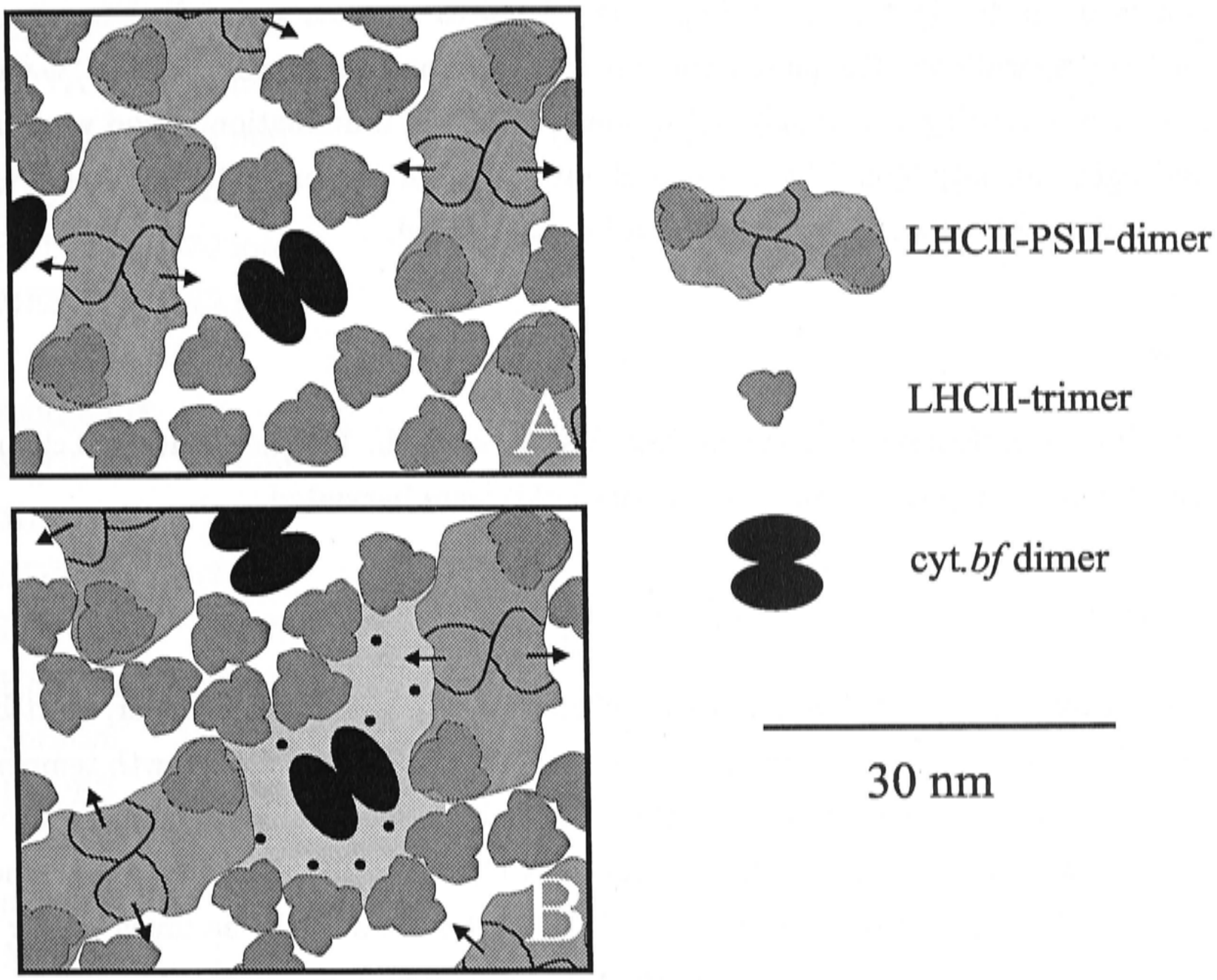

Figure 3.1: *Tentative representation of assembly of proteins in the thylakoid membrane. Destacked (A), and stacked (B). The light grey shaded area between the proteins represents one selected example of a PQ diffusion domain. Arrows show the direction of electron flux from the Q_B site. According to Kirchhoff et al. [96], modified.*

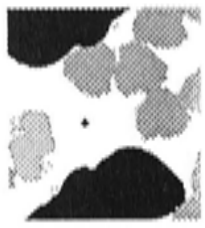

3.2 Methods and Material

3.2.1 Plant material

Spinach

Leaves of six to eight weeks–old spinach (*Spinacea oleracea* var. polka) were used for the preparations. The plants were grown hydroponically at about 13–16 °C with nutrients according to Randall and Bouma [141]. The illumination period was 10 h and light intensity (400–700 nm) was about 200 μmol photons m^{-2} s^{-1}). Care was taken that only leaves not shaded by others were used.

Pea

Pea (*Pisum sativum*) was grown as described for spinach. For the isolation of chloroplasts from pea, young sprouts (2–3 weeks old) were harvested.

Tobacco

Fully–expanded but still young leaves of tobacco (*Nicotiana tabacum* var. petit havanna) were used. Plants were grown on soil in a glasshouse. The growth temperature was ca. 22 °C but in summer time it may be higher. In the glasshouse plants were illuminated for 11 h with artificial light (100–250 μE). However, in summertime daylight is considerably longer and light intensities might be much higher as the sunblinds are controlled by temperature but not by light.

3.2.2 Solutions

Isolation media spinach

solution A:		
$MgCl_2$	1 mM	
$MnCl_2$	1 mM	
EDTA	2 mM	
KCl	50 mM	**pH 6.1 (KOH)**
KH_2PO_4	0.5 mM	
Sorbitol	330 mM	
MES	25 mM	

solution B:		
$MgCl_2$	1 mM	
$MnCl_2$	1 mM	
EDTA	2 mM	
KCl	10 mM	**pH 6.7 (KOH)**
KH_2PO_4	0.5 mM	
Sorbitol	330 mM	
HEPES	25 mM	

solution C:		
$MgCl_2$	1 mM	
$MnCl_2$	1 mM	
EDTA	2 mM	
KCl	60 mM	**pH 6.7 (KOH)**
KH_2PO_4	0.5 mM	
Sorbitol	330 mM	
HEPES	25 mM	

Isolation media pea

solution PeaA:		
EDTA	0.04 mM	
KCl	0.40 mM	**pH 7.8 (KOH)**
Sorbitol	330 mM	
HEPES	2 mM	

Isolation media tobacco

solution 1:		
$MgCl_2$	1 mM	
$MnCl_2$	1 mM	
EDTA	2 mM	
KCl	40 mM	**pH 6.1 (KOH)**
KH_2PO_4	0.5 mM	
Sorbitol	330 mM	
MES	40 mM	

BSA (added freshly before preparation): 0.2 % (w/w)

solution 2 (hypotonic):		
Tricine	20 mM	
KCl	50 mM	**pH 7.8 (KOH)**
$MgCl_2$	5 mM	

solution 2 (hypertonic):		
Tricine	20 mM	
KCl	50 mM	**pH 7.8 (KOH)**
$MgCl_2$	5 mM	
Sorbitol	660 mM	

solution 3:

HEPES	50 mM	
KCl	10 mM	**pH 7.5 (KOH)**
$MgCl_2$	7 mM	
Sorbitol	330 mM	

Assay media

solution D, hypotonic:

$MgCl_2$	7 mM	
KCl	80 mM	**pH 7.6 (KOH)**
HEPES	30 mM	

solution D, hypertonic:

$MgCl_2$	7 mM	
KCl	80 mM	**pH 7.6 (KOH)**
Sorbitol	600 mM	
HEPES	30 mM	

solution 4, isotonic:

$MgCl_2$	7 mM	
KCl	80 mM	**pH 7.6 (KOH)**
Sorbitol	300 mM	
HEPES	30 mM	

3.2.3 Preparation of thylakoids

Spinach

Intact chloroplasts were isolated as described in [108]. Leaves of spinach were harvested at the end of the dark period to minimize their starch content. Thereafter the leaves were washed twice in de–ionised water and the middle veins were removed. Afterwards the leaf material (ca. 15 g) was homogenized in a Waring Blendor for 12 s in 150 ml of solution A. The homogenized material was filtered through 4 layers of gauze and 1 layer of nylon cloth (pore diameter: 20 μm). The suspension was centrifuged in four tubes with 1400 g for 60 s to deposit the chloroplasts. The pellet

was washed in 5 ml solution B per tube and another centrifugation step at 630 g was carried through for 45 s. The pellet was resuspended and washed a second time in 5 ml solution B per tube and centrifuged at 630 g for 35 s. After the last centrifugation step, the pellet was suspended in about 1 ml of solution C and stored in darkness on ice. All steps were carried out in a cold room (ca. 4 °C) on ice with cooled tubes, pipettes, and buffer.

It is advantageous to make measurements on thylakoids because they allow better access to chemicals than do chloroplasts with an intact envelope. Therefore thylakoids were freshly prepared from chloroplasts before every series of measurements. To obtain thylakoids, chloroplasts were shocked osmotically: chloroplasts were placed in solution D hypotonic (typical dilution of thylakoid suspension to solution D: 1:75). After 60 s an equal amount of solution D hypertonic was added to obtain an isotonic assay medium. Chlorophyll concentration was usually 10–20 μg/ml, if not indicated differently. This treatment leaves the thylakoid membrane system quite intact (as indicated by an extremely low proton leakage when protonmotive force is built up [95]). Typical whole chain electron transport rates were 1150 $\mu mol_{e^-}\ h^{-1}\ mg_{Chl}^{-1}$ (287 $mmol_{e^-}\ s^{-1}\ mol_{Chl}^{-1}$). PS II activity was usually around 2300 $\mu mol_{e^-}\ h^{-1}\ mg_{Chl}^{-1}$ (573 $mmol_{e^-}\ s^{-1}\ mol_{Chl}^{-1}$).

Pea

After harvesting, the pea sprouts were immediately placed in a bag of two layers of gauze and cooled in a beaker with iced de–ionised water. Afterwards the peas (ca. 50 g) were homogenized in a Waring Blendor in 200 ml iced solution peaA. The homogenized material was filtered as described for spinach, distributed to four tubes and centrifuged for one minute at 1400 g. The chloroplast containing pellet was then resuspended with 5 ml solution peaA and the suspension was redistributed to two tubes. A second centrifugation at 1400 g for 40 s followed by resuspension in 5 ml solution peaA was carried out. The thylkaoids were placed in one tube and centrifuged a last time at 1400 g for 40 s. The sediment was resuspended in 1 ml solution C (same as for spinach) and stored on ice.

Thylakoids were prepared freshly for each measurement as described for spinach. The same media as for spinach were used. Typical whole chain electron transport rates were ca. 1280 $\mu mol_{e^-}\ h^{-1}\ mg_{Chl}^{-1}$ (320 $mmol_{e^-}\ s^{-1}\ mol_{Chl}^{-1}$). PS II activity was usually around 2400 $\mu mol_{e^-}\ h^{-1}\ mg_{Chl}^{-1}$ (600 $mmol_{e^-}\ s^{-1}\ mol_{Chl}^{-1}$).

Tobacco

Whereas young peas or spinach leaves after the dark period hardly contained starch, a high starch content was a big problem for the isolation of tobacco chloroplasts. Therefore instead of chloroplasts, thylakoids were isolated. First preparations only yielded a very low whole chain electron transport rate. Values below 400 $\mu mol_{e^-}\ h^{-1}\ mg_{Chl}^{-1}$ (100 $mmol_{e^-}\ s^{-1}\ mol_{Chl}^{-1}$) were usually obtained. PS II activity was between 1400 and 2000 $\mu mol_{e^-}\ h^{-1}\ mg_{Chl}^{-1}$ (349–498 $mmol_{e^-}\ s^{-1}\ mol_{Chl}^{-1}$). Therefore the procedure was optimized to the form described below. With this procedure thylakoids were obtained that usually yielded a whole chain electron transport rate between 580 and 780 $\mu mol_{e^-}\ h^{-1}\ mg_{Chl}^{-1}$ (144–194 $mmol_{e^-}\ s^{-1}\ mol_{Chl}^{-1}$) and a PS II activity between 1960 and 2400 $\mu mol_{e^-}\ h^{-1}\ mg_{Chl}^{-1}$ (488–598 $mmol_{e^-}\ s^{-1}\ mol_{Chl}^{-1}$).

The day before thylakoids were isolated, whole plants were stored overnight in darkness at room temperature to reduce the starch content at least somewhat. Ca. 15 g leaf material was used. Major veins were removed thoroughly with a razor blade after washing the leaves twice in de–ionised water. Afterwards the material was homogenized in a Waring Blendor for ca. 12 s in 150 ml of solution 1 and filtered through 4 layers of gauze and 1 layer of nylon cloth (pore diameter: 20 μm). After homogenization the suspension was placed in two tubes and centrifuged at 2000 g for 70 s. The resulting green pellet was surrounded by a white ring of starch. The pellet was resuspended in 2.5 ml solution 2 (isotonic, obtained by using equal amount of solution 2 hypotonic and solution 2 hypertonic) per tube. Resuspension was carried out carefully to avoid resuspension of starch together with the chloroplasts. After transferring the suspension into two clean tubes, the chloroplasts were shocked osmotically in 10 times the suspension volume (ca. 25 ml per tube) of solution 2 (hypotonic). After 30 s the same volume of solution 2 hypertonic was added to get an isotonic medium. The shocked chloroplasts were centrifuged again at 160 g for 60 s to suspend larger cell and/or chloroplast fragments and starch. The supernatant was centrifuged at 1400 g for 60 s to concentrate the thylakoids. The pellets of both tubes were resuspended in ca. 1 ml solution 3 and stored until used in darkness on ice.

As with spinach all steps were carried out in a cold room (ca. 4 °C) on ice with cooled tubes, pipettes, and buffer.

Determination of chlorophyll content

The chlorophyll content was determined spectrophotometrically. 10 μl of chloroplast suspension was added to 5 ml acetone (80 %). The solution was centrifuged with 2000 g for 5 min to suspend small scattering particles. Absorption was measured and chlorophyll content calculated according to Porra and co–workers [137]:

$$\begin{aligned} Chl_a(\mu g/ml) &= 501 \cdot (12.25 \cdot A_{663.6} - 2.55 \cdot A_{646.6}) \\ Chl_b(\mu g/ml) &= 501 \cdot (20.31 \cdot A_{646.6} - 4.91 \cdot A_{663.6}) \end{aligned} \tag{3.1}$$

3.2.4 Electron microscopy with the TEM

Isolated thylakoids of spinach and tobacco, embedded in agar, were embedded in EPON (EPON 812, Serva, Feinbiochemica Heidelberg), a synthetic epoxide–resin. After embedding the samples were examined with the transmission electron microscope.

Preparation

Thylakoids from tobacco and chloroplasts from spinach were isolated as descibed in Section 3.2.3. After the determination of the chlorophyll content the samples were stored in Eppendorf tubes on ice. From each sample a small amount was stored in a separate tube to measure the PS II activity and the whole chain electron transport. Spinach chloroplasts for the embedding were shocked osmotically as described in 3.2.3 and centrifuged with 630 g. Afterwards thylakoids were resuspended in ca. 0.5 ml solution D (hypertonic) mixed with 0.5 ml solution D (hypotonic). Thylakoids from both samples were spun down with an Eppendorf centrifuge. The supernatant was removed and the pellets embedded in 1.5% agar. The agar was allowed to cool down as much as possible to avoid damage to the thylakoids.

Fixation of pellets

The agar blocks containing the pellet were fixed in 4% glutaraldehyde to stabilize the cell structure and fix proteins[a]. After one hour the agar blocks were washed

[a]Many enzymes are fixed at their position during the fixation with glutaraldehyde but do not denature [127]

four times for 20–50 minutes in Sörensen buffer. Then the pellets were treated for one hour with 2% potassium permanganate ($KMnO_4$)to contrast membranes. Afterwards, the pellets were washed three times for 20 minutes in buffer.

Embedding of the samples

In the presence of water the polymerisation is disturbed. Therefore, prior to the embedding in EPON, the samples (agar blocks with the embedded pellet) have to be dehydrated. Dehydration was carried with ethanol in successive steps.

30% ethanol	15 min,
50% ethanol	15 min,
70% ethanol	over night,
80% ethanol	20 min,
90% ethanol	20 min,
abs. ethanol	2× 20 min,
propylenoxide	2× 20 min,

During each washing step ethanol was replaced in the middle of the washing time. After the dehydration successive addition of EPON started. Ca. 10 drops of EPON were added and the samples stored at 4°C. After 2 hours ca. 20 drops of EPON were added, and after 21 hours another 20 drops of EPON were added and the samples stored at room temperature in the fume hood. Three hours later the EPON–propylenoxide mixture was removed and pure EPON was added. On the next day the samples were filled in forms and allowed to polymerise for 27 hours at 70°C.

Staining of the ultra–thin sections

The atomic numbers of the most abundant elements in biological objects is relatively low. Therefore, due to the low electron deflection, sections often have a very poor contrast. To amplify the contrast the sections were treated with uranylacetate ($UO_2(CH_3COO)_2 \cdot 2\ H_2O$, 3%, in aqua dest.). Uranylacetate binds preferably to carboxyl–groups and phosphate–residues of the nucleic acids. After 40 minutes the grids were rinsed carefully with aqua dest. for several minutes followed by a treatment with lead–citrate. Lead–citrate reacts with phosphate, carboxyl, and sulfur–residues. After 5 minutes the grids were again carefully rinsed with distilled water.

3.2.5 Titration of the number of active PS II centres using DCMU

DCMU is a highly specific inhibitor of the Q_B binding site at PS II [46]. The number of active centres can be gradually inhibited by addition of subsaturating amounts of DCMU. The remaining number of active centres was determined polarographically in the presence of DMBQ and nigericin. Under the assumption that DMBQ accepts electrons from beyond the DCMU–binding site, the rate of oxygen evolution is taken to be proportional to the number of uninhibited PS II. The ratio of the oxygen evolution with added DCMU to that without DCMU gives the relative amount of blocked centres.

3.2.6 Polarographic determination of oxygen evolution — determination of steady–state electron transport rates

Oxygen concentration was measured with a Clark type electrode. A schematic diagram of the measuring system is shown in Figure 3.2. A Clark type electrode consists of a silver and a platinum electrode connected via an electrolyte (1 M KCl). An oxygen–permeable teflon membrane separates the cuvette with the thylakoid suspension from the electrodes. Oxygen can diffuse through the membrane. A voltage of 700 mV between the two electrodes is sufficient for the reduction of the oxygen at the platinum electrode (cathode) leading to the formation of hydroxide (OH^-) (see Figure 3.2). At the anode silver is oxidised and precipitates with the chloride of the electrolyte to form AgCl. Together electrons are taken up at the silver electrode and released at the platinum electrode. The current is proportional to the diffusing oxygen which in turn is proportional to the difference of the oxygen partial pressure on each side of the teflon membrane. The samples in the cuvette were well stirred to avoid an oxygen gradient. The measured current was converted to voltage and amplified. The voltage signal was recorded with an x-t–recorder. The cuvette was kept constantly at 20 °C with the help of a water bath.

For calibration the oxygen content of well stirred de–ionised water was measured. The water was saturated with oxygen i.e. 0.284 μmol_{O_2}/ml (at 20 °C). To gain a second well–defined value sodium dithionite ($Na_2S_2O_4$) was added. This is a very strong reducing compound and therefore removes all the oxygen from the solution. The voltage difference of both these values represents 0.284 μmol_{O_2}/ml.

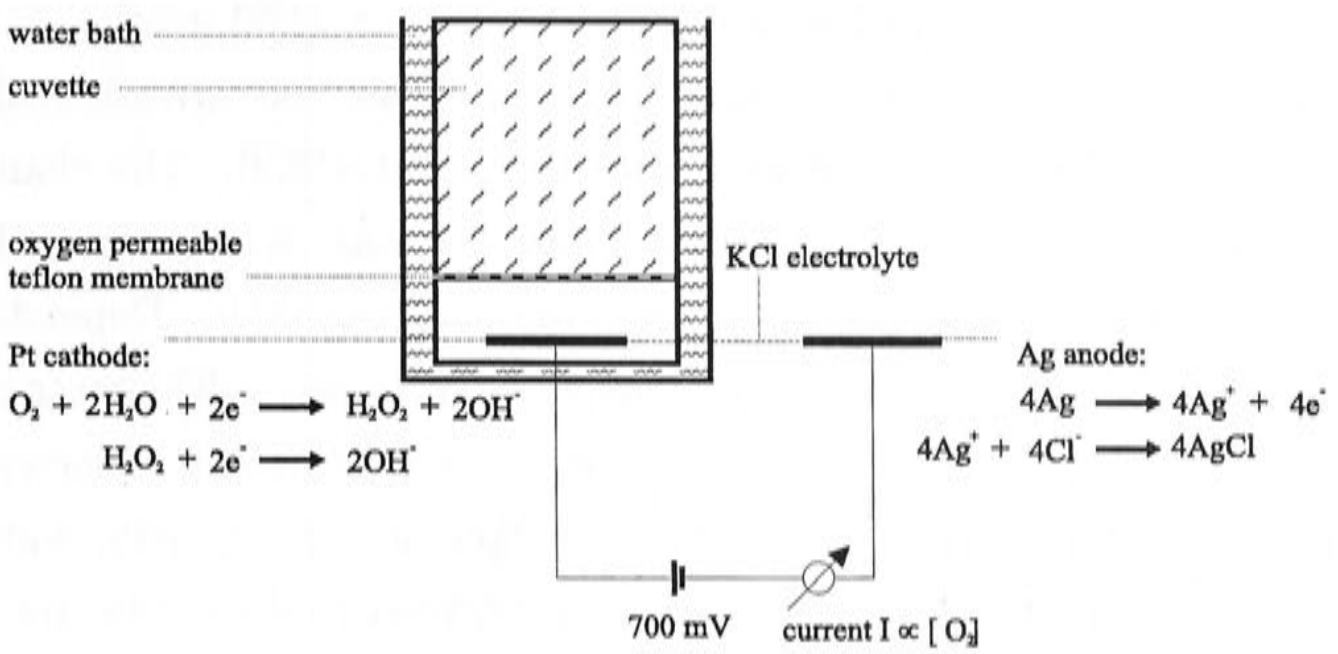

Figure 3.2: *Schematic diagram showing the principle of polarographic oxygen measurements with a Clarke–type electrode.*

part of the electron transport chain	**donor**	**acceptor**	**other chemicals**	**stoichiometry** O_2/e^-
whole chain electron transport	H_2O (natural)	MV (100 μM)	sodium azide (1 mM) nigericine (1 μM)	-1 O_2/4 e^-
electron transport through PS II	H_2O (natural)	DMBQ (1.1 mM)	nigericine (1 μM)	+1 O_2/4 e^-

Table 3.2: *Chemicals used for polarographic measurements of the steady–state electron transport.*

In order to measure stady state electron transport rates of a thylakoid suspension the sample was illuminated with saturating light (ca. 6000 $\mu mol_{quanta}\ m^{-2}\ s^{-1}$). According to which part of the electron transport chain was investigated artificial electron donors and/or acceptors were added (see Table 3.2). The changing oxygen concentration caused by the electron transport was recorded and the rate of oxygen evolution determined using the units $\mu mol_{e^-}/(mg_{Chl} \cdot h)$. Depending on the part of the electron transport chain being explored different stoichiometries between electron flux and oxygen evolution can occur. This relationship is shown in Table 3.2. All measurements are carried out in the presence of nigericin, which uncouples the pH gradient. Uncoupled conditions are chosen to avoid changes in the pH value in the lumen during the course of the experiments, which would influence the photosynthetic behaviour (e.g. by non–photochemical quenching).

3.3 Results

3.3.1 PS II titration at 20°C

A large number of PS II titration experiments was carried out with stacked thylakoids from different plants. When plotting whole chain electron transport versus PS II activity, it turns out that the shape of the resulting curves (control curves) is variable. Apart from more or less linear control curves (as an example see Figure 3.3), s–shaped functions are found (Figure 3.4 and 3.5). The s–shape can be more or less pronounced as can the curvature. Usually, curves of pea and spinach are more linear while those from tobacco exhibit more curvature, but some variability is also seen for different plants from one species. It may reflect physiological adaptation of the thylakoid structure. It should be noted that tobacco is grown in a glass house and hence under slightly varying irradiance and temperature.

To examine if the unexpected curves are caused by rearranged thylakoids due to the isolation, samples were embedded in an epoxide–resin and investigated with the transmission electron microscope.

Although the activities of the embedded samples were slightly below the usual values, the thylakoids nevertheless appear to be well stacked and intact as shown in Figure 3.6 and 3.7.

Each series is started without DCMU, followed by samples with increasing DCMU concentration. Measurements are also carried out in the opposite order (DCMU

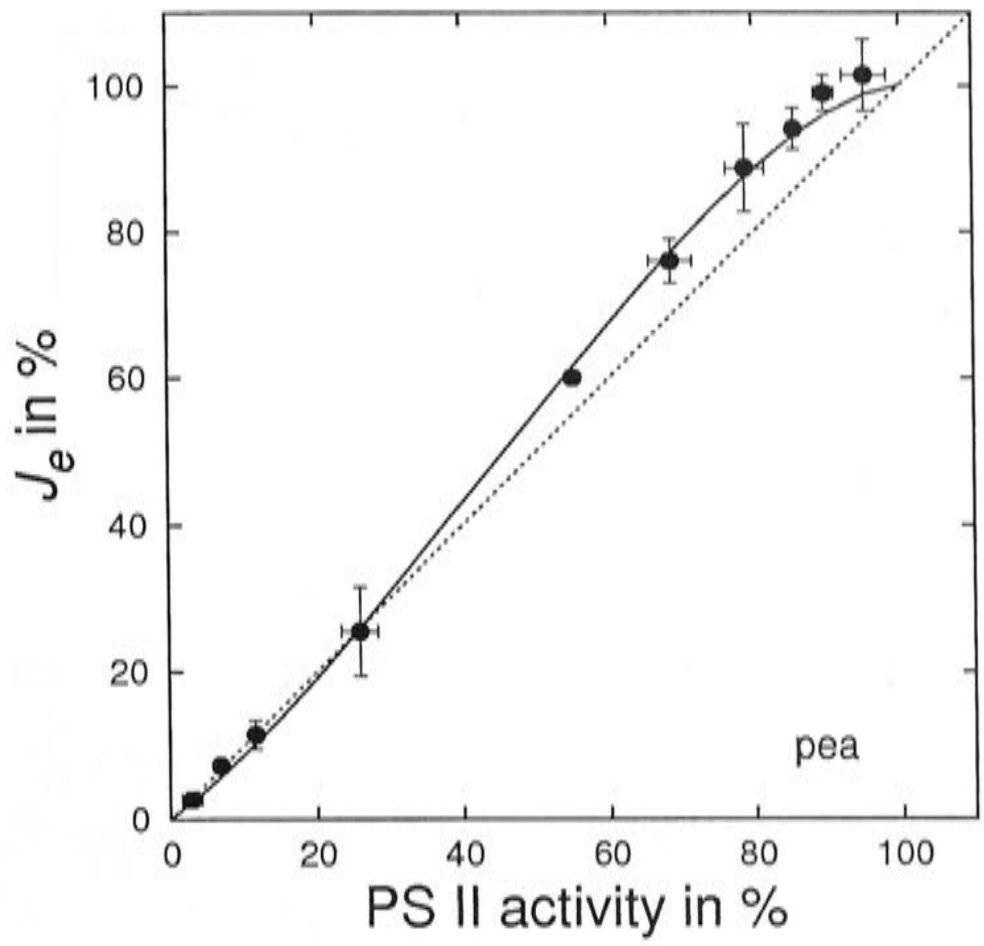

Figure 3.3: *Nearly linear flux control curve from Pisum sativum. 100% relates to the rates in the absence of DCMU. The solid line shows a fitted curve ($n = 1.6$, $r = 0.49$). For explanation see Appendix 3.5. The dotted line represents a 1:1 relationship.*

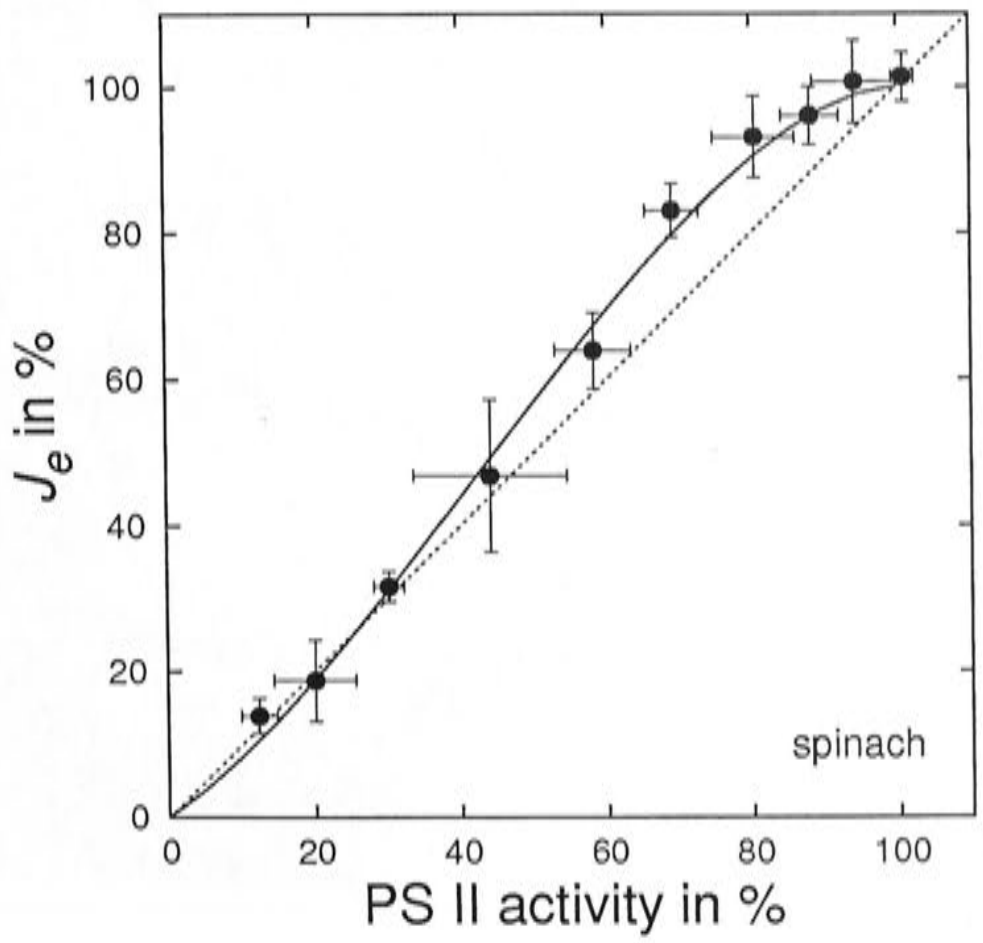

Figure 3.4: *Complex flux control curve from Spinacea oleracea. The solid line shows a fitted curve ($n = 1.7$, $r = 0.40$). For explanation see Appendix 3.5. The dotted line represents a 1:1 relationship.*

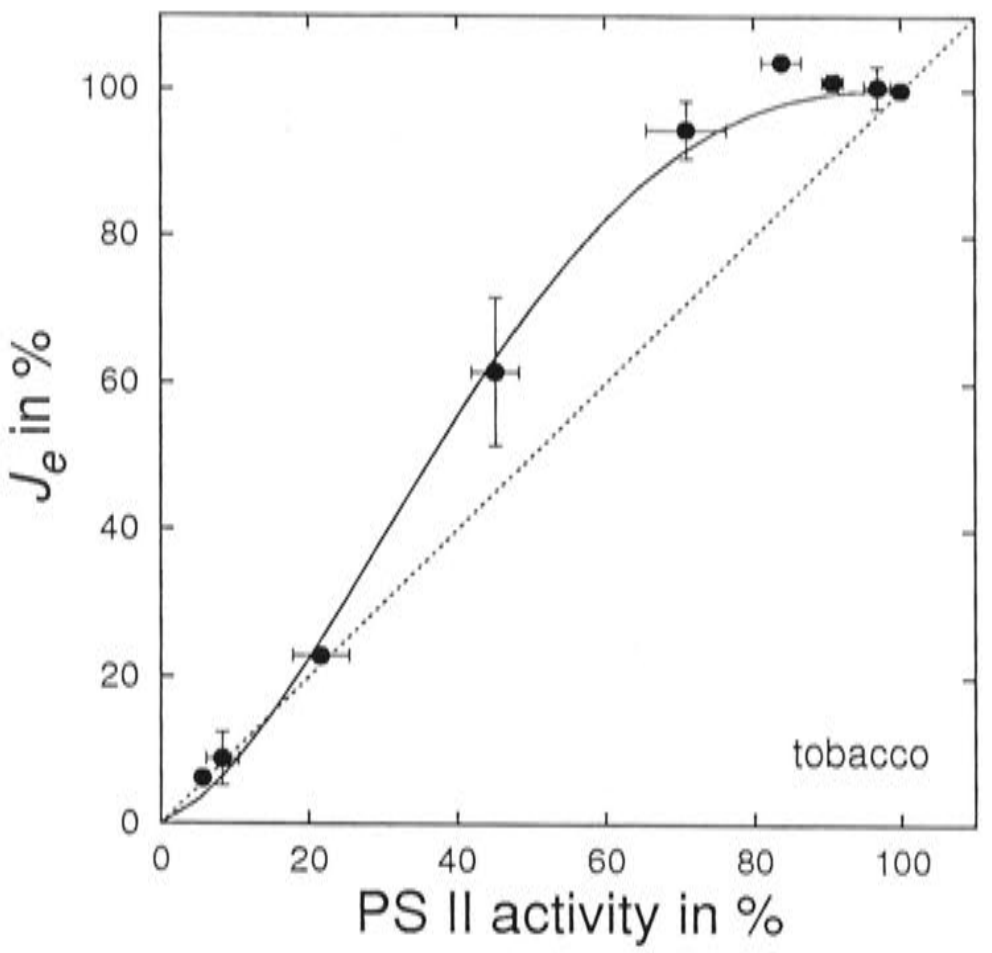

Figure 3.5: *Complex flux control curve from Nicotiana tabacum. As Figure 3.4,* $(n = 2.5,\ r = 0.17)$.

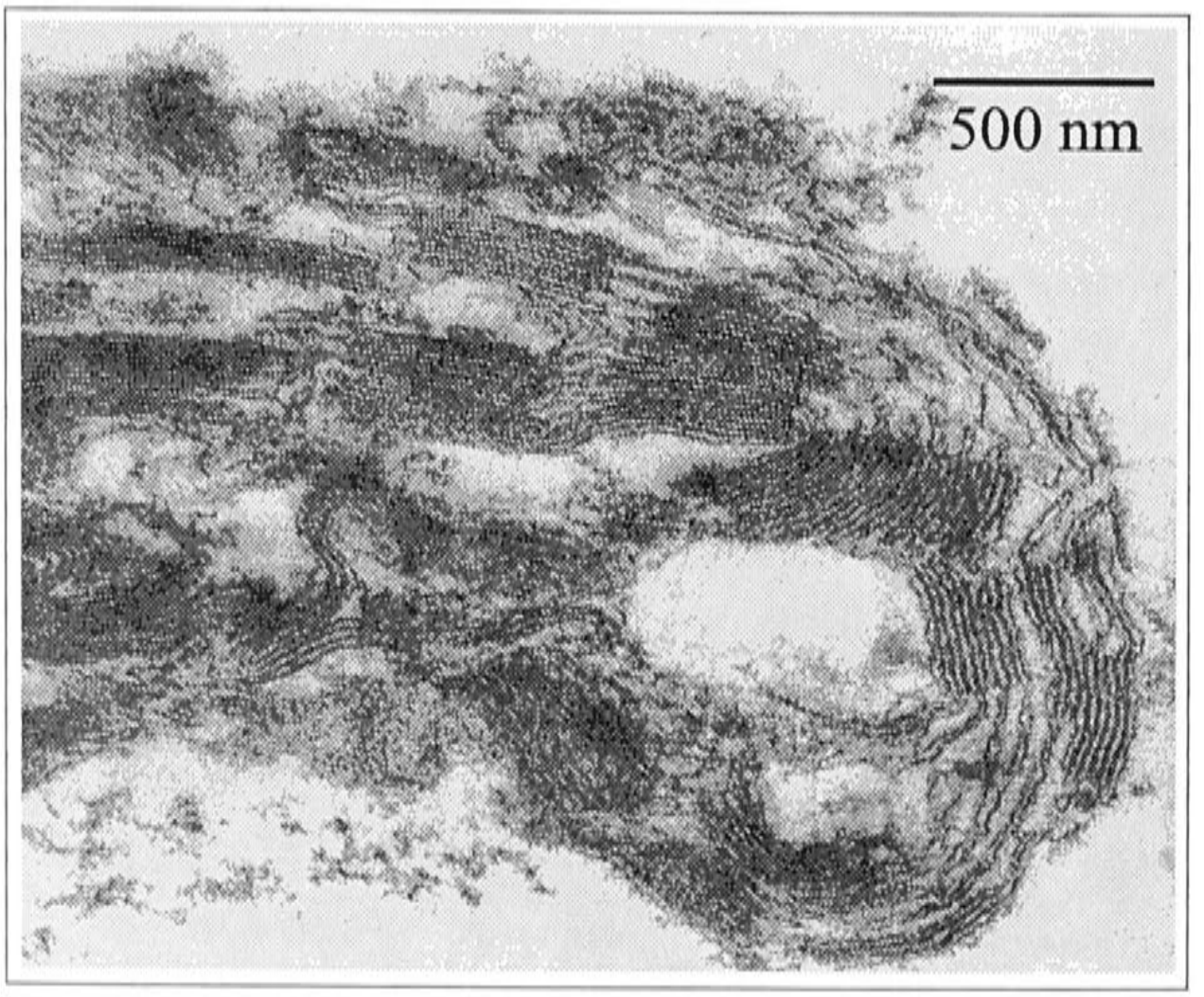

Figure 3.6: *Micrograph from isolated spinach thylakoids. PS II activity of the sample was 2319* $\mu mol_{e^-}\ h^{-1}\ mg_{Chl}^{-1}$ *(578* $mmol_{e^-}\ s^{-1}\ mol_{Chl}^{-1}$*) and the rate of whole chain electron transport was 832* $\mu mol_{e^-}\ h^{-1} mg_{Chl}^{-1}$ *(207* $mmol_{e^-}\ s^{-1}\ mol_{Chl}^{-1}$*).*

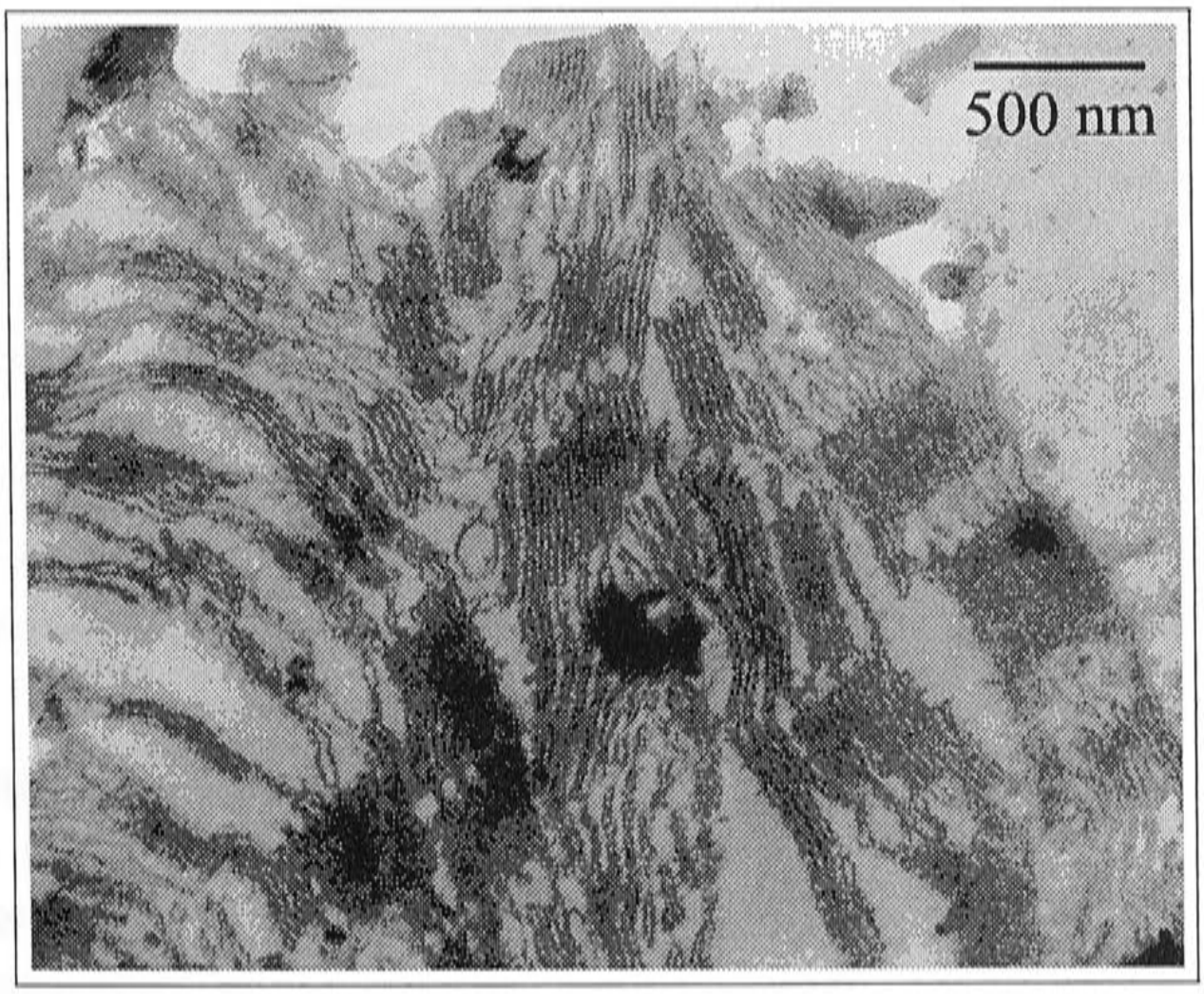

Figure 3.7: *Micrograph from isolated tobacco thylakoids. PS II activity of the sample was 1911 $\mu mol_{e^-}\ h^{-1}\ mg_{Chl}^{-1}$ (476 $mmol_{e^-}\ s^{-1}\ mol_{Chl}^{-1}$) and the rate of whole chain electron transport was 579 $\mu mol_{e^-}\ h^{-1}\ mg_{Chl}^{-1}$ (144 $mmol_{e^-}\ s^{-1}\ mol_{Chl}^{-1}$).*

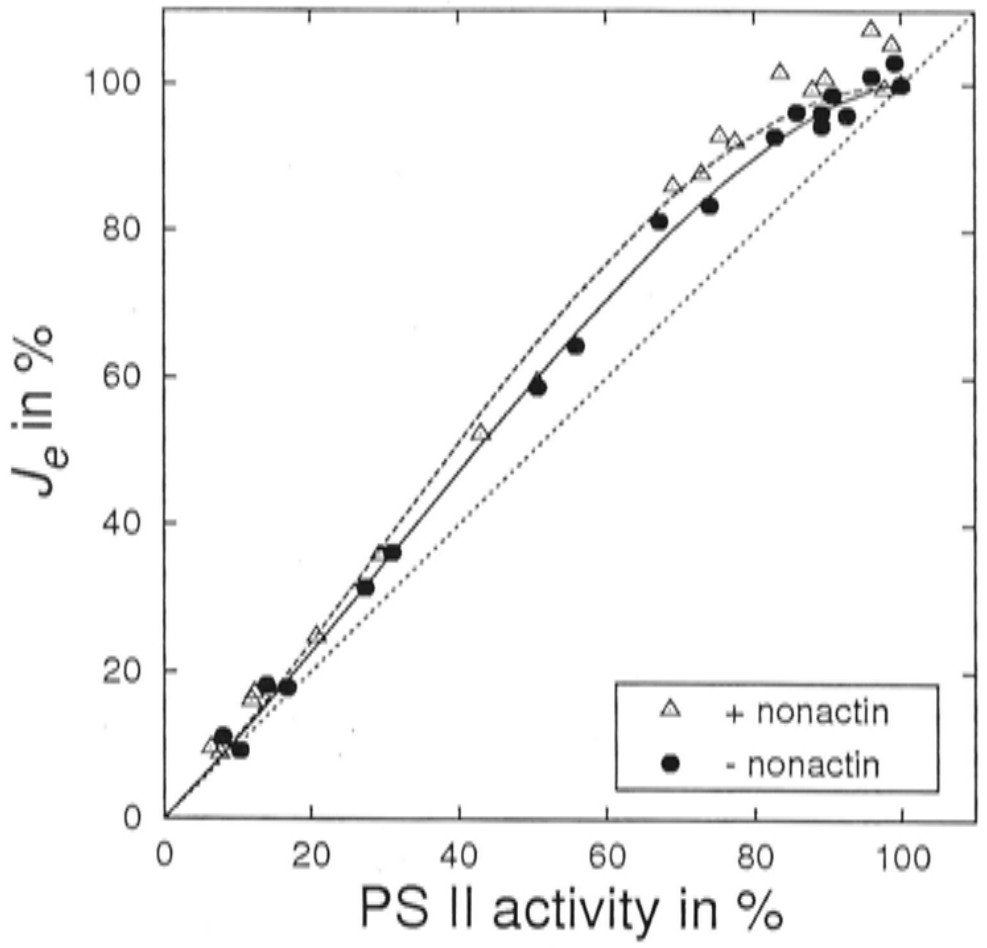

Figure 3.8: *Flux control curve from Nicotiana tabacum in the presence (triangles) and absence (circles) of nonactin, respectively. Lines show the best fits. Solid line:* $n = 1.61$, $r = 0.64$; *dashed line:* $n = 1.91$, $r = 0.53$.

concentration: high → low) to exclude the possibility that aging of the thylakoids caused the s–shape of the control curves (data not shown).

The light induced transmembrane electrochemical potential may influence the kinetics of electron transfer steps at cyt *bf* where the chemical gradient may mainly influence the reactions at the Q_o site and the electrical gradient may influence the reactions at the Q_r site [59, 18]. In the experiments presented here the proton gradient was uncoupled by nigericin but the electrical gradient was not[b]. This might lead to the situation that the poise between the reactions at the Q_o site and the Q_r site is disturbed thus leading to an unexpected control of whole chain electron transport. Therefore the influence of a developing electrical membrane potential on the complex control curves was tested. For this purpose, measurements are carried out in the presence of nonactin (0.5 μM), which uncouples the electrical potential across the membrane. As can be seen in Figure 3.8 the s–shape is found with or without addition of nonactin.

[b]Nigericin is a H^+/K^+–exchanger [37] and therefore uncouples the proton gradient but not the electrical gradient.

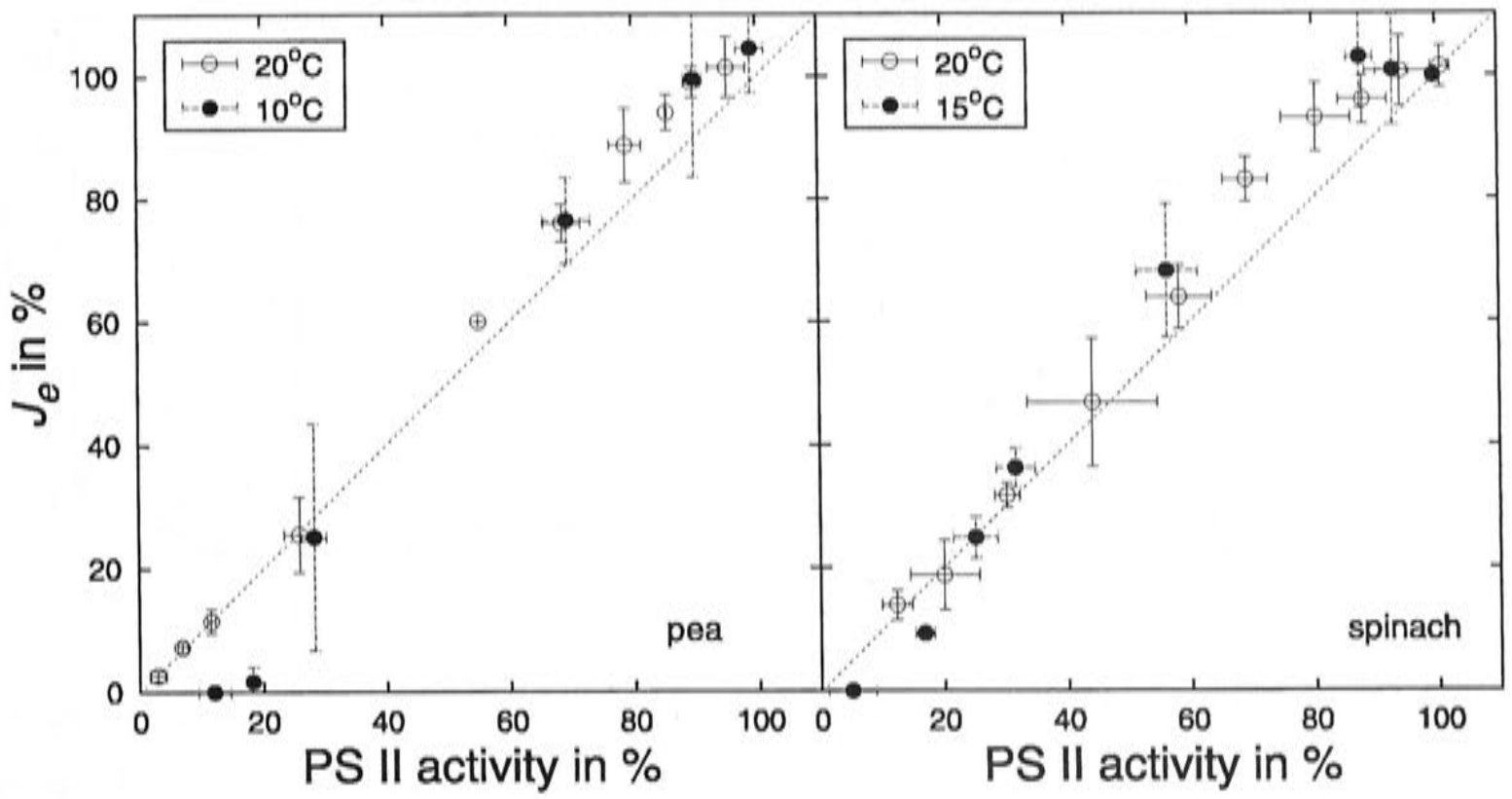

Figure 3.9: *Flux control curves from pea and spinach at different temperatures. Left: pea, right: spinach.*

Thus the complex curves cannot be explained simply by artifacts or simply assuming that PQ diffusion is restricted to small micro–domains, that would rather lead to a more or less linear flux control.

3.3.2 Influence of temperature

The temperature dependence of the complex shape of the control functions was investigated. Therefore, the same type of titration measurements was carried out with pea, spinach and tobacco at varied temperatures.

It can be seen in Figure 3.9 that the characteristics of the control curves for pea and spinach are not temperature dependent when the majority of PS II is active. The same holds for tobacco (data not shown). As this result is somewhat unexpected the Q_{10} (between 10 and 20°C) of PS II activity and the whole chain transport is investigated. Because pea and spinach are very similar in their control curves and activities, data of both are taken together to determine the Q_{10} values (see Figure 3.10). The Q_{10} of PS II activity is significantly lower than that for the whole chain transport J_e.

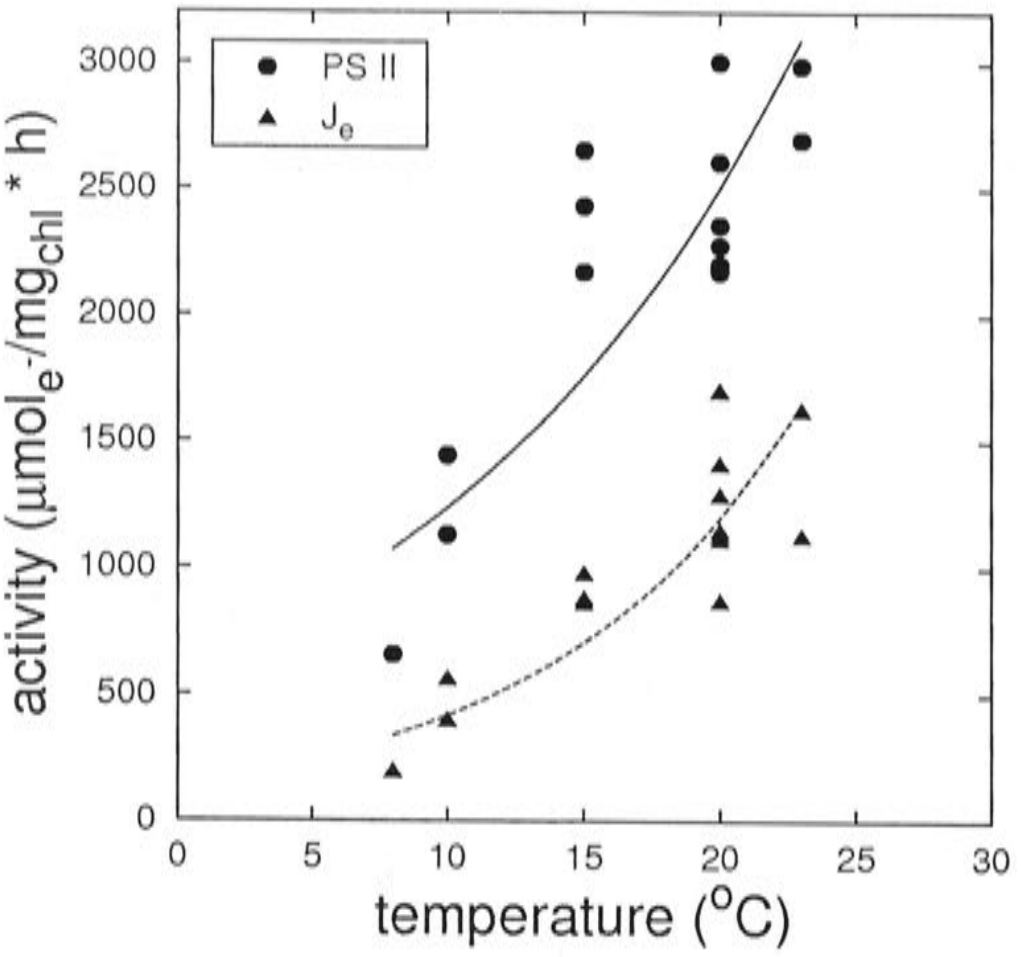

Figure 3.10: *PS II and J_e activity as a function of the temperature. Pea and spinach are taken together. The Q_{10} (between 10 and 20° C) of the PS II activity is around 2 whereas that for J_e is around 3.*

3.4 Discussion

The curves shown here do not show the dependency predicted by the models described in Chapter 2 which assume a shared plastoquinone pool (see Figure 2.13). However, these models do not account for any organisational features. Therefore another approach incorporating the arrangement of the integral proteins within the membrane was chosen.

The control curves were fitted with a mathematical model incorporating interacting adjacent plastoquinone diffusion domains that are functionally coupled by dimeric cytochrome *bf* complexes (see Appendix 3.5). So far, the control curves have been interpreted assuming a linear sequence of reactions within the electron transport chain [96]. The complex, s–shaped control behaviour may reflect a non–linear sequence of reactions. It is often discussed that cyt *bf* activity might be controlled by the redox state of PQ. Such a control would lead to a non–linear sequence of reactions, as the cyt *bf* activity would depend on the PS II activity.

Two parameters were introduced to characterise the domain size (n) and the redox control of cyt *bf* (r). The parameter n reflects how many PS II share a PQ pool with access to cyt *bf*. It should be stressed, however, that n may not simply

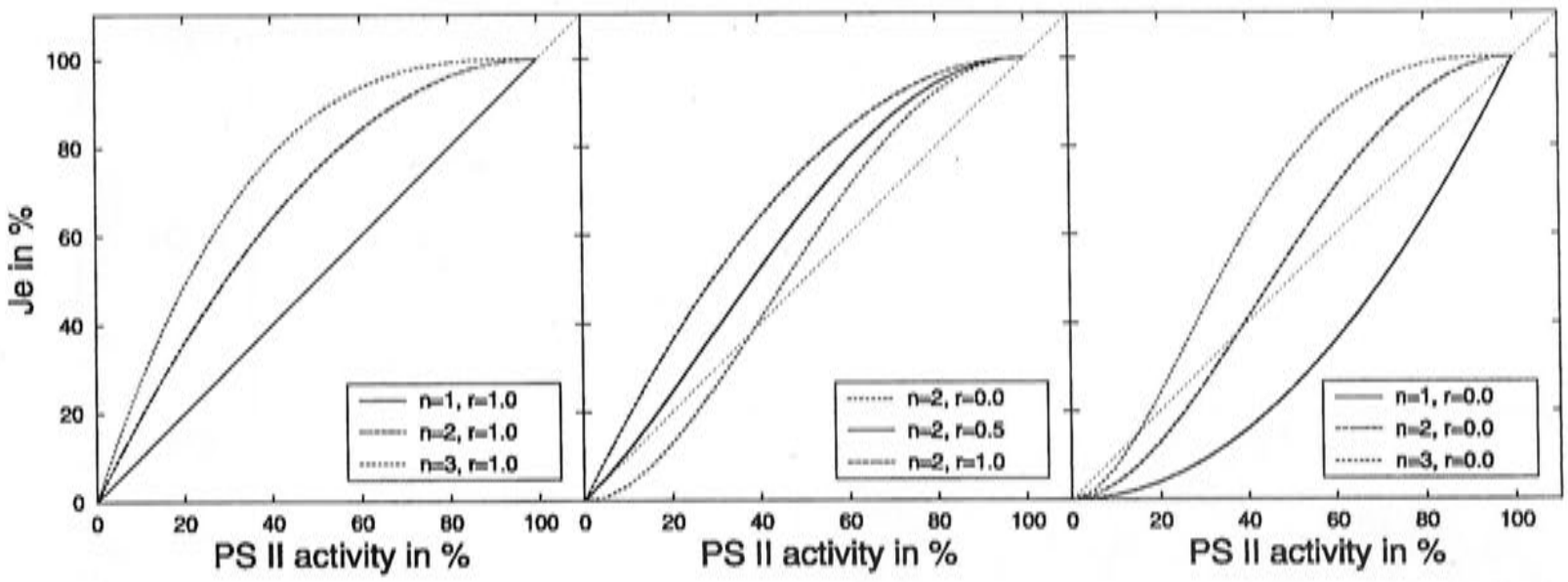

Figure 3.11: *Calculated curves according to the model. Two fit–parameters are varied: The number, n, of PS II accessing the same diffusion domain over a certain time period, and the 'residual activity', r, of cytochrome bf. Some of the theoretically possible combinations (e.g. $n = 1$ together with $r = 0$) are not found in experiments.*

be interpreted as a stoichiometric number. Micro–domains should be regarded as a temporal structure and each domain will rearrange. Thus a micro–domain only reflects the local and temporal stochiometry of proteins functionally connected to each other. It can be regarded as relatively stable if its turnover time exceeds that of fast electron transport (10 to 15 ms). As the stability decreases, the relative PQ diffusion space increases and a larger number of PS II share a pool with access to cyt *bf*. To some extent lateral PQ exchange may also be influenced by the relative density of cyt *bf*: if cyt *bf* is located in the close vicinity of PS II centres, photo–reduced PQ is rapidly trapped by cyt *bf* binding sites and consequently the exchange area for PQ decreases. This might smooth out local PQH_2 gradients somewhat and reduce lateral PQH_2/PQ exchange. In this sense n should be taken as a general exchange parameter. It reflects the probability for each individual PS II centre to share a diffusion domain for rapid access to cyt *bf* with other PS II centres. For $n = 1$ there is no lateral PQ exchange. Each PS II has separate access to cyt *bf*, and consequently the control function becomes more linear than for higher n (Figure 3.11). A linear flux control relates to a strong control by PS II of J_e. With increasing n the curvature increases and hence flux control by PS II decreases.

More s–shaped control curves could be obtained by introducing a second fit–parameter, r (with $0 \leq r \leq 1$) (Figure 3.11, middle and right). r describes a negative co–operativity between domains, as could be mediated by cyt *bf*. It is now generally assumed that cyt *bf* occurs as a dimer (see e.g. [38]). The functional significance

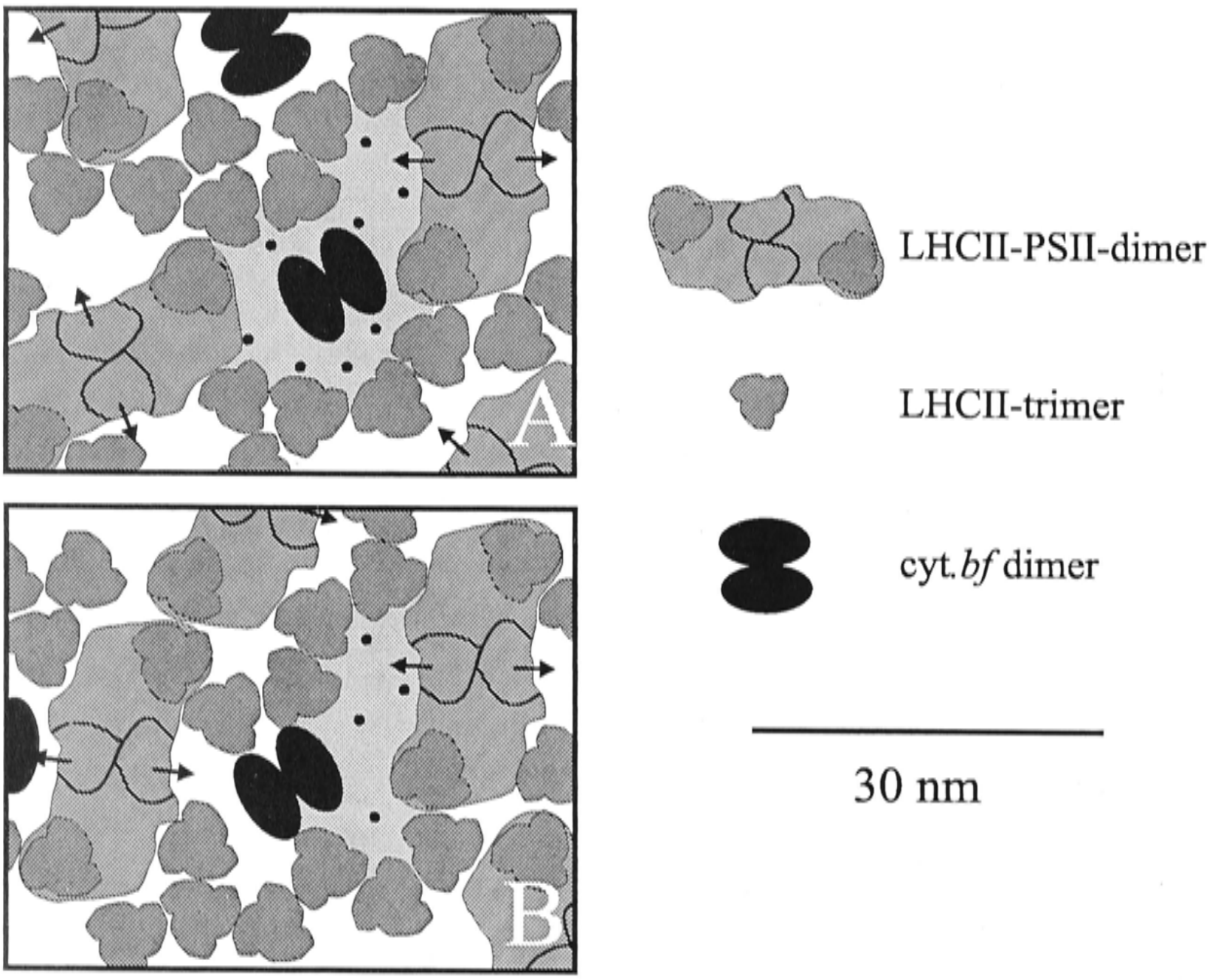

Figure 3.12: *Tentative representation of assembly of proteins in the thylakoid membrane according to the micro domain concept. A: a cyt bf dimer associated with one micro–domain, according to Kirchhoff et al. [96], modified. B: Extended micro–domain concept. A cyt bf monomer is associated with one micro–domain while the other monomer is associated with the adjacent micro–domain. Compare also Figure 3.1.*

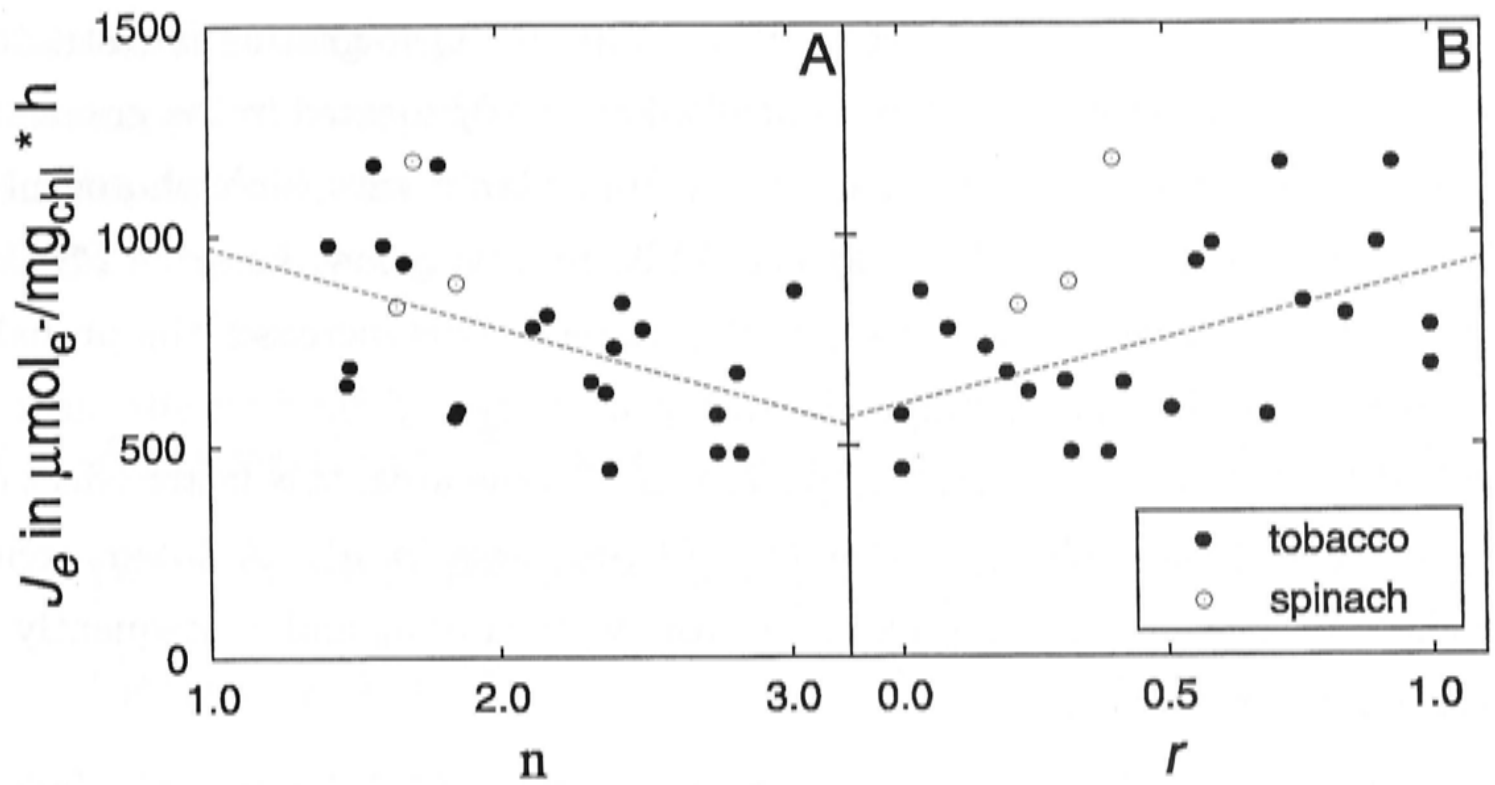

Figure 3.13: *A and B: relationship between J_e and the fitted parameters n and r, respectively.*

of the dimer is not yet clear. In a manner similar to that assumed for dimeric PS II complexes (compare Figures 3.1B and 3.12), the two monomers of a dimeric cyt *bf* complex could temporarily participate in different PQ diffusion domains, as depicted in Figure 3.12B. With partially inhibited PS II, the PQH_2 binding sites of the cyt *bf* dimer could then be occupied non–equally. A value of $r = 1$ means that both monomers of the cyt *bf* dimer operate independently. In this case inactivation of one monomer (PQH_2 site not occupied) does not influence PQH_2 oxidation on the other monomer. In contrast $r < 1$ means that the two monomers of a dimer operate in a co–operative way (see for example [66, 133, 65]). Thus inactivation of one monomer leads to complete ($r = 0$) or partial ($0 < r < 1$) inhibition of the other monomer ($r =$ **residual activity**). This kind of a co–operativity leads to a negative curvature of the control function (Figure 3.11, middle). It should be pointed out that n and r derived from data fitting represent average values. Inhomogeneous distribution of these parameters throughout the membrane is likely, but is not described by the model. Best fits for data from different experiments are shown in Figures 3.3, 3.4, 3.5, and 3.8 (see legends).

In Figure 3.13A and B, the light–saturated, whole chain electron transport rate is plotted against the parameters n and r obtained as best fits for individual flux control experiments. Only trends can be detected as there is considerable scatter in the data. Interestingly, despite the scatter, there seems to be a negative correlation between n and J_e, indicating that the relative size of domains decreases in plants

with high electron transport capacity. If fast lateral PQ migration is restricted to the grana, the capacity of J_e may be controlled by cyt *bf* located in the grana stacks (close to PS II) only [96]. Hence, in grana from plants with high photosynthetic fluxes (low n), the ratio PS II/cyt *bf* should be relatively low, i.e. each PS II may be located in the close vicinity of a cyt *bf* complex. This increases the probability of photo–reduced PQ being trapped rapidly by a cyt *bf* binding site near each individual PS II centre. In a densely packed membrane area, this latter effect could further decrease the exchange radius of PQ (decrease in n). A lower exchange radius in turn would lead to a greater control by PS II of J_e and consequently be of adaptational significance.

It has to be noted, however, that the measurements of PS II activity include both PS II_α and PS II_β but only PS II_α are located in the grana core and can consequently influence the structure of the micro–domains (see also Sections 1.1.2 and 1.2.1). There is also a slight tendency for r to increase with J_e, but this correlation is less significant. No significant correlation is seen between the fit–parameters and Chl a/b (not shown).

Temperature effects

Interestingly, for PS II activities above 40% the shapes of the control functions did not change significantly with temperature. As the Q_{10} of PS II activity is lower than that for J_e the PS II over–capacity is greater at lower temperatures. Nevertheless its control over the whole chain electron transport is not lower at lower temperatures. It seems that the chemical over–capacity does not in fact play an important role in controling photosynthetic electron transport. This may further point to the importance of the protein organisation within the thylakoids. For PS II activities below 40% the decrease of J_e with PS II activity seems to be steeper at low temperatures. This might point to a low r (see Figure 3.13).

At lower temperatures the viscosity of membranes is greater. This should lead to decreased diffusion coefficients. However, no difference in the control functions is found for different temperatures when the majority of PS II is active. This may indicate that diffusion processes do not influence the control of PS II on photosynthetic electron transport. However, the data shown here scatter a lot and should only be considered as preliminary experiments.

In summary it can be seen from the experiments shown above that the generally accepted assumption that all PS II share a common PQ pool may be an over–

simplification. In contrast, the way that the integral proteins are organised may have a strong influence on the photosynthetic electron flux. To investigate the relationship between the spatial organisation of the proteins and electron flux, a Monte Carlo simulation is developed and presenteed in the next Chapter.

3.5 Appendix: Model of how whole chain transport decreases with increasing PS II inhibition by DCMU

J_e = whole chain electron flux in relation to the uninhibited control,

c = number of cyt *bf* monomers in a micro–domain,

n = number of PS II in a micro–domain,

r = residual cyt *bf* activity,

PS = proportion of active PS II,

I = proportion of inhibited domains with all contributing PS II inhibited,

i = number of inhibited domains with which a considered domain is sharing a cyt *bf* complex,

$P(i)$ = probability of a domain having as neighbours i inhibited domains with which it is sharing a cyt *bf* complex,

It is assumed that J_e is limited by cyt *bf* activity. Each micro–domain contains c cyt *bf* monomers, connected to another monomer in a neighbouring domain. Thus, $J_{e,i}$ from a domain with i inhibited neighbours is:

$$J_{e,i} = \left(\frac{(c-i)}{c} + \frac{r \cdot i}{c} \right), \tag{3.2}$$

where the first term describes the activity by those cyt *bf* that are connected to a monomer in an uninhibited domain. The second term accounts for the activity of those cyt *bf* that form a dimer with a monomer in an inhibited domain, with r being a measure of the activity of such a cyt *bf*.

Consequently J_e from all micro–domains adds to:

$$J_e = \sum_{i=0}^{c} P(i) \cdot \left(\frac{(c-i)}{c} + \frac{r \cdot i}{c} \right) \tag{3.3}$$

with,

$$P(i) = (1-I) \cdot I^i \cdot (1-I)^{c-i} \cdot \frac{c!}{(c-i)! \cdot i!} \quad , \tag{3.4}$$

$$I = (1-PS)^n \quad . \tag{3.5}$$

In the equation for $P(i)$, the first term takes into account that only domains that are active themselves are contributing to J_e. The following two terms describe the probabilities for the neighbours to be in a certain state. One term desribes the probabilty that a neighbour is inhibited, and the other describes the probability that a neighbour is uninhibited.

Inserting equation (3.4) into equation (3.3) leads to:

$$J_e = \sum_{i=0}^{c} I^i \cdot (1-I)^{c-i+1} \cdot \frac{c!}{(c-i)! \cdot i!} \cdot \left(\frac{2(c-i)}{2c} + \frac{2r \cdot i}{2c} \right) \quad , \tag{3.6}$$

$$J_e = (1-I)^2 \cdot \sum_{i=0}^{c-1} I^i (1-I)^{(c-1)-i} \frac{(c-1)!}{((c-1)-i)!i!} + \ldots \tag{3.7}$$

$$\ldots + (1-I) \cdot rI \cdot \sum_{i=1}^{c} I^{(i-1)} (1-I)^{c-i} \frac{(c-1)!}{(c-i)!(i-1)!},$$

which simplifies when using the binomial theorem:

$$J_e = (1-I) \cdot [(1-I) + r \cdot I] \quad . \tag{3.8}$$

Inserting eq. 3.5 leads to:

$$J_e = (1-(1-PS)^n) \cdot [(1-(1-PS)^n) + r \cdot (1-PS)^n] \quad . \tag{3.9}$$

Chapter 4

Dependence of plastoquinol diffusion on the shape, size, and density of integral thylakoid proteins

Contents

The diffusion of plastoquinol in the chloroplast thylakoid membrane is modelled using Monte Carlo techniques. The integral proteins are seen as obstacles to diffusion, and features of percolation theory emerge. Thus the diffusion coefficient diminishes with increasing distance and there is a critical threshold of protein concentration, above which the long–range diffusion coefficient is zero. The area occupied by proteins in vivo is assessed and appears to be around this threshold, as determined from calculations assuming randomly distributed non–interacting proteins. Slight changes in the protein arrangement lead to pronounced changes in diffusion behaviour under such conditions. Mobility of the proteins increases the protein occupancy threshold, while boundary lipids impermeable to PQ diffusion decrease it. Further, the obstruction of plastoquinone/plastoquinol binding sites in a random arrangement is evaluated.

4.1 Introduction

Thylakoids are the site of photosynthetic electron transport. In higher plants they are highly structured by densely packed integral proteins, the latter being photosystem (PS) II, light–harvesting complexes (LHC) II, cytochrome (cyt) *bf*, and PS I associated with LHC I. In higher plants functional PS II is located in appressed membranes of the grana core, whereas PS I is only found in non–appressed thylakoids, the stroma lamellae and grana margins [14, 11, 164, 20, 1, 2]. The distribution of cyt *bf* complexes is less certain. It has been suggested that cyt *bf* complexes are almost homogeneously distributed [1, 8, 131]. Lateral electron flow between the integral proteins is managed by two mobile electron carriers: plastoquinol and plastocyanin. The hydrophilic plastocyanin diffuses in the lumen space and mediates electron transport between cyt *bf* and PS I whereas electron transport between PS II and cyt *bf* is mediated by plastoquinol diffusion within the lipid bilayer.

However, electrons liberated at PS II in the grana core must diffuse over the relatively large distance of up to 300 nm to cyt *bf* in the grana margins. In the thylakoids the protein density is very high. Using published data on protein structures and lipids, Kirchhoff et al. [97] calculated an area occupation by proteins of between 60 and 70%. Thus the proteins are densely packed and it has been argued that integral proteins may act as obstacles to PQ diffusion. There is indeed good evidence for restricted diffusion. The plastoquinone diffusion coefficient in thylakoids was found to be two orders of magnitude less than in protein free liposomes [24].

When diffusion of a mobile particle in a homogeneous medium is considered, the diffusion coefficient D, often referred to as the 'diffusion constant', is only dependent on the characteristics of the diffusing particle and the medium. This changes in the presence of obstacles when the medium becomes inhomogeneous and the apparent diffusion coefficient becomes more complex. The effects of obstacles on the diffusion of a mobile species can be described by percolation theory. According to this theory (see e.g. [166, 58]) the apparent diffusion coefficient is strongly dependent on the travelled distance being considered r and the concentration c of obstacles, so that we write $D_{app}(r, c)$ to signify that there is this dependence. For diffusion without obstacles $c = 0$ the diffusion coefficient $D_{app}(r, 0)$ is constant and independent of the distance travelled. This corresponds to the diffusion coefficient D in a homogeneous medium. For simplicity, from here on the subscript '*app*' will be omitted and we will refer to the apparent diffusion coefficient $D_{app}(r, c)$ as the diffusion coefficient $D(r, c)$. The diffusion coefficient in the absence of obstacles, i.e. in an homogeneous medium, will be referred to as $D(0)$.

When obstacles are introduced, the diffusion coefficient $D(r, c)$ decreases with increasing distance travelled, r, over a certain range, dependent on c, and then levels off. Over short distances, a diffusing particle is unlikely to encounter an obstruction, and the diffusion coefficient is similar to that without obstacles. With growing distances the particle must take a tortuous path through the obstructions. As a consequence the diffusion coefficient decreases with the travelled distance, r. This effect increases dramatically for higher area occupation, c. At low concentrations of obstacles, all vacancies are connected by some unbroken path and thus the mobile particle can eventually diffuse to any vacant site on the lattice. As the concentration of obstacles increases, some isolated clusters of vacancies appear. A tracer that starts in one of these finite clusters of vacancies is trapped, while other tracers that start on the infinite cluster of vacancies can still diffuse to infinite r. At still higher obstacle concentrations, only isolated clusters of vacancies are present. Each tracer is trapped on some cluster, and no long range diffusion is possible. This critical concentration is called the percolation threshold (c_p) and is defined as the highest concentration of obstacles at which an infinite cluster of vacancies exists. It means that the long range (large r) diffusion coefficient of the mobile species (e.g. plastoquinone) declines to zero when the fraction c of obstacles is greater than the percolation threshold, c_p.

Lavergne & Joliot observed the lack of rapid equilibration between plastoquinone and QA (the primary acceptor of PS II) throughout the membrane and they ex-

plained this by suggesting that PQ diffusion is restricted to small clusters of vacancies (micro–domains) within the membrane [111, 93, 109, 92]. PQ would diffuse freely within such a micro–domain but would not migrate rapidly across domain borders, which are formed by densely packed integral proteins (obstacles). Kirchhoff et al. [96] extended this concept by assuming that these clusters of vacancies (micro–domains) are formed by a hierarchy of interactions between PS II and LHC II.

In our investigation plastoquinol diffusion is simulated using the Monte Carlo method. The Monte Carlo algorithm was first introduced by Metropolis et al. [120] as a sampling algorithm to calculate properties of substances that may be considered as composed of interacting individual molecules. Today the name 'Monte Carlo' stands for numerical algorithms using random numbers to find an approximate solution of a complex system. It is often used for stochastic problems that are too complex to be solved analytically. The Monte Carlo method has been extended to a broad range of physical and biological systems. It has also been applied to diffusion in biomembranes (as examples see [150, 151, 124, 48, 79]). Saxton has investigated the effect of mobile obstacles on lateral diffusion in an archipelago [150]. In a subsequent paper [151] he investigated the distance dependence of the diffusion coefficient of mobile tracers in the presence of immobile obstacles. He found that long–range diffusion can be severely restricted by a high concentration of obstacles. Saxton discussed his results in a broad range of biological contexts. Mitchell and co–workers used the Monte Carlo method to study electron transport in thylakoids [124]. Their model combined a deterministic simulation of reaction kinetics with a Monte Carlo approach to the diffusion of plastoquinol. They compared different mechanisms of plastoquinol oxidation; a collisional mechanism that implies an immediate oxidation of plastoquinone on a succesful encounter with cyt *bf* and a tight binding mechanism that includes an irreversible binding of PQ to the Q_o side of the cyt *bf* complex before its slow oxidation takes place. For both mechanisms, comparisons were made between diffusion limited and a non–diffusion limited reaction of plastoquinol. With their model they obtained best fits to experimental data on P700 reduction kinetics when assuming either a very rapid tight–binding step for PQH_2 oxidation and a diffusion coefficient $\geq 3 \cdot 10^{-7}$ cm^2/s or a non–diffusion limited collision mechanism and a low diffusion coefficient of $\geq 2 \cdot 10^{-8}$ cm^2/s. The diffusion of phosphorylated light–harvesting complexes in thylakoid membranes has been investigated by Drepper et al. [48]. From their results Drepper and co–workers suggested a diffusion coefficient of $4.4 \cdot 10^{-13} - 1.9 \cdot 10^{-12}$ cm^2/s for unphosphorylated LHC II and $1.9 \cdot 10^{-12} - 4.4 \cdot 10^{-12}$ cm^2/s for phosphorylated LHC II, respectively. Move-

ment of the integral proteins according to these diffusion coefficients was suggested by Drepper and co–workers to prevent the formation of isolated diffusion domains. However, this is not consistent with the suggestion of Lavergne et al. and Joliot et al. [111, 93, 109, 92] that the plastoquinone pool within the grana membrane is composed of substantially isolated smaller pools that equilibrate slowly within that time.

Most published simulations of diffusion between obstacles are restricted to circular or hexagonal obstacles or differ in some other manner from the situation in thylakoids. Here, we present a Monte Carlo approach to the simulation of domain formation for plastoquinone diffusion in grana incorporating more realistic protein shapes. The complexes consist of PS II with tightly bound LHC II [74], cyt *bf* [31], and LHC II [105]. The aim is to investigate whether the high protein density in the thylakoids is sufficient to lead to the formation of diffusion domains if the distribution of the proteins is random. The obstruction of plastoquinone/plastoquinol binding sites in a random arrangement is considered. Based on the results from the previous sections we examine the influence of protein shape, boundary lipids and protein mobility on plastoquinone diffusion.

4.2 The simulation

The Monte Carlo calculations are carried out for a square lattice. Initially, tracers and immobile obstacles are distributed randomly on the lattice at the required concentrations. Then at each time step the tracers are allowed to move to an immediately adjacent unoccupied site by a random walk (diagonal movements are not considered). A move by a tracer can be blocked by an obstacle but not by another tracer. Tracers can occupy the same vacancy. Hence the tracers are not influencing each other and consequently one run with 1000 tracers equals 1000 runs with one tracer in the same arrangement of proteins. This is chosen to save computing time. On the other hand it means neglecting the size of the plastoquinone molecules. However, for an occupied area fraction (obstacles) of circa 75% and a stoichiometry of 6 plastoquinone per PS II the area occupied by PQ would be below 1%.

The mean square displacement $\langle r(t)^2 \rangle$ of the tracers is obtained as a function of time, and the diffusion coefficient $(D(r,c))$ is obtained according to Einstein's equation for diffusion in two dimensions: $4 \cdot D(r,c) = \langle r(t)^2 \rangle / t$ [54, 55].

The algorithm used to place the obstacles randomly on the lattice is as follows. A random site and a random orientation of the particle is chosen. If the site is vacant the obstacle is placed at this site, otherwise another random site is chosen. If no vacant site is found after a given number of tries all obstacles already placed on the lattice are moved to a random nearest–neighbour site (if the site is not vacant the obstacle remains in place). After this rearrangement the procedure of finding a free site for the particle to be placed is repeated. This goes on until the particle eventually is placed on the lattice (for computational simplicity for investigations with LHC II with boundary lipids the procedure is slightly different: Here if no vacant site for a particle is found after a given number of tries the procedure is started again instead of moving the particles already being placed on the grid).

A similar procedure is used for the movement of the tracers. At each time step all tracers are moved, but the move for each tracer is chosen independently. In each move, the particle attempts to move to a randomly chosen nearest–neighbour site. If the site is vacant, the particle moves to that site; if the site is blocked by an obstacle, the particle remains in place. This is in contrast to the algorithm used to place the obstacles on the lattice where the search for a free site is continued until a vacant site is found. The algorithm for the movement of the tracers is in principle the same as the algorithm used by Saxton (1987, [150]). The pseudo–random numbers generator used produces more than $2 \cdot 10^{18}$ random numbers [139].

For the movement of the mobile obstacles a similar procedure is used. In the case of mobile point obstacles the diffusion coefficient for the obstacles is chosen to be the same as for the tracers, corresponding to their similar size. For mobile circles, the diffusion coefficient for LHC II and cyt *bf* is assumed to be three orders of magnitude lower than that for plastoquinone diffusion. The diffusion coefficient of PS II is scaled according to the different areas the proteins occupy on the grid. The different diffusion coefficients for individual complexes are modelled by reducing the number of random steps of these complexes relative to that of the tracers. After all tracers have been moved each complex is moved with the probability $p = D_{obstacle}/D_{tracer}$.

The lattice is modelled with periodic boundary conditions, i.e. the actual shape of the lattice corresponds to a torus. Consequently, a particle that is positioned at one edge of the lattice is continued at the opposite side. The lattice spacing is chosen as 1 nm. This is related to the typical size of lipids. Thus at each time step a tracer travels 1 nm.

Each simulation is carried out for a maximum of 10^5 timesteps. All diffusion coefficients are normalised $[D_n(r,c)]$ to one in the absence of obstacles (here D(0) = $3.5{\cdot}10^{-7}$ cm^2/s, corresponding to the diffusion coefficient measured in pure phosphatidylcholine vesicles [25]). Using the Einstein equation $\langle r(t)^2 \rangle = 4 \cdot D(0)\, t$ one time step relates to $7.14 \cdot 10^{-9}$ s.

The simulation is written in C++ and runs under Windows and Linux on a personal computer. The program allows interactive selection of the structural parameters of the membrane model under graphic control. Parameters that can be chosen interactively are:

- display of the graphical control (on or off),
- size of the grid with periodical boundary conditions in nm × nm,
- diffusion coefficient of the tracer in the absence of obstacles, $D(0)$,
- shape of the proteins (given as a file with the affine coordinates),
- the stoichiometry between the three different proteins (relative to cytochrome *bf*),
- the fraction of occupied grid points,
- number of runs (that is the number of different initial distributions)
- number of tracers
- number of timesteps
- timepoint for measuring the distance (e.g. every time step or every 10th time step)
- for the boundary lipids, the type of occupation (e.g. none, permeable or impermeable to PQ diffusion)

4.2.1 Summary of the assumptions and approximations

lattice constant:	1 nm
lattice size:	200 nm×200 nm with periodic boundary conditions
time step:	7.14 ns
number of tracers:	1000
configurations:	500 initial configurations (200 for mobile obstacles)

Consequences of using a lattice:

A lipid bilayer is a discrete medium. Therefore it seems resonable to use a lattice in the simulation. Due to the discrete nature of the lattice the continuum diffusion is replaced by latttice diffusion. However, this does not appear to be a major limitation (see e.g. [153]; for more information concerning lattice geometry and continuum see e.g. [9]).

Percolation threshold:

The diffusion coefficients $D_n(r, c)$ obtained are used to determine the percolation threshold. However, it has to be mentioned here that the percolation threshold thus obtained is an apparent value, defined as the concentration at which the diffusion coefficient $D_n(r, c)$ goes to zero. To find the true threshold, one would need to analyse the long–range connectedness rather than $D_n(r, c)$ and plot the probability of connectedness versus the concentration and extrapolate to infinite system size (see e.g. Saxton [153]). However, in the present work the geometry is very specialized and therefore the apparent percolation threshold is used instead.

Obstacle geometry:

The average area occupied by a particle (depending on its orientation) is as follows:

particle	**number of occupied lattice sites**
PQ	1
point obstacles	1
PS II realistic	268
LHC II realistic	33
cyt *bf* realistic	32
sphere corresponding to PS II	265
sphere corresponding to LHC II	33
sphere corresponding to cyt *bf*	33

Interaction:

A pure hard–core interaction between obstacles or between obstacles and tracers is assumed. Further, the perturbation of the lipid matrix by proteins is neglected (for more detail on treatment of perturbation see 'dynamic boundary layer' models as mentioned e.g. in [176, 9] or Marcelja [114]).

4.3 Results

We start our considerations with the determination of the stoichiometry of the integral proteins and the area that they occupy in grana thylakoids. This is followed by the simulation of plastoquinone diffusion between obstacles exhibiting a realistic shape, derived from structural analysis of the integral photosynthetic proteins (PS II with tightly bound LHC II [74], cyt *bf* [31], and LHC II [105], Figure 4.1). The integral proteins are assumed to be randomly distributed. Different protein densities are investigated and plastoquinone diffusion in such an arrangement is examined. Thirdly, we show the influence of the obstacle (protein) size and shape, which is of importance for evaluating possible consequences of the formation of photosynthetic supercomplexes. Next the influence of boundary lipids surrounding light–harvesting complexes, the most abundant integral proteins, is described. Finally the influence of obstacle mobility on the plastoquinone diffusion coefficient is described.

4.3.1 Estimation of the stoichiometry of the integral proteins in the grana core and of the area covered by these proteins

The exact area that proteins occupy in the thylakoids is not known and differing values can be found in the literature. Kirchhoff et al. [97] calculated from available structural data an area of between 60 and 70%. However, in the grana core the area covered with protein might differ somewhat from the average value for the whole thylakoids. Therefore an estimation of the area covered with proteins in the grana core is carried out similar to that in [97].

For the estimation of the protein densities in the grana core and the protein stoichiometries, the following data from the literature are used:

(a) 1.7 mmol cyt *bf*/mol Chl [188],

(b) 230 Chl molecules/PS II [116] corresponding to 4.35 mmol PS II/mol Chl,

(c) 90–100 molecules Chl/PS II monomer without LHC II trimer [89],

(d) 36 molecules Chl/LHC II trimer [106],

(e) 1601 $\pm$ 151 nmol lipid/mg Chl, Chl a = 68%, Chl b = 32% [52].

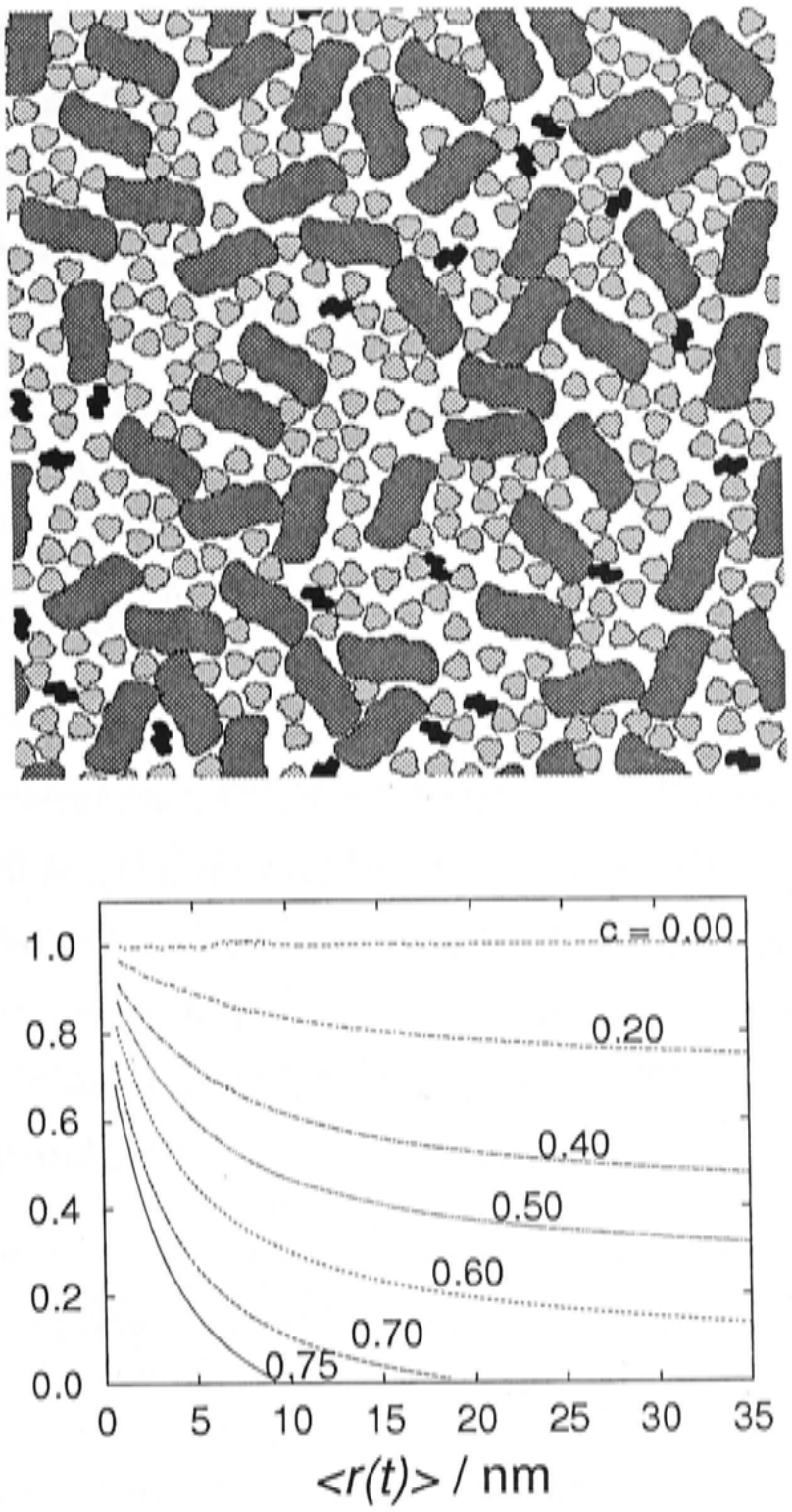

Figure 4.1: *Random distribution of photosynthetic proteins on a square lattice, 200×200 nm. Dark grey: Photosystem II dimers, black: cyt bf dimers, light grey: free light–harvesting trimers. The stoichiometry of the complexes PS II : cyt bf : LHC II is 2.6 : 1 : 14.1. The occupied area fraction is 0.6. Below: Distance dependence of the normalised diffusion coefficient $D_n(r, c)$ of a point tracer on a square lattice in the presence of immobile obstacles exhibiting a realistic shape. Curves are for different occupied area fractions. 1000 tracers were used, and 500 different initial distributions of the obstacles (see Section 4.2). The slight deviation of the diffusion coefficient $D_n(0)$ from one reflects statistical errors. Another indication of the statistical error is the occasional discontinuity in the curves, representing the transition between separate runs. For c=0 for 217 data points $D_n(0) = 1.0012 \pm 0.0042$. No specific interaction between proteins was assumed.*

component	concentration (mmol/mol Chl)	area per molecule (nm^2)	nm^2 component per molecule Chl	stoichiometry
[a](PS II–LHC $II_3)_2$	2.17	285	0.620	2.56
[b]cyt bf_2	0.85	51	0.043	1.00
[c]LHC II_3 (free)	11.35–12.57	34	0.39–0.43	13.35–14.78
[d]lipids	720 ± 68	0.54±0.05	0.319–0.465	847.06
total			1.37–1.56	

Table 4.1: *Occupied area fraction and protein stoichiometries in the grana core. The shapes of the super complexes are derived from the following publications: [a][31], [b][74], [c][105], [d][97].*

concentration of free LHC II trimers per PS II monomer: Assuming that in the grana core only PS II and LHC II contain chlorophyll [1], it follows from (b) and (c) that 130–140 molecules Chl per PS II monomer are associated with LHC II trimers. Using (d) 3.61–3.89 LHC II trimers per PS II are calculated. Given one tightly bound LHC II trimer per PS II monomer [74], it follows that there are 2.61–2.89 free LHC II per PS II monomer. This leads to 11.4–12.6 mmol free LHC II/mol Chl.

concentration of lipids per mol Chl: A lipid concentration of 1.43 ± 0.14 mol lipids / mol Chl follows from (e). As the lipids are organized as a bilayer this leads to 0.72 ± 0.07 mol lipids / mol Chl.

The relationship between the occupied area fraction and the stoichiometries is illustrated in Table 4.1.

The results shown in Table 4.1 lead to an occupied area fraction of 0.70 to 0.77.

4.3.2 Diffusion between randomly distributed, immobile photosynthetic proteins

Figure 4.1 illustrates the model of the thylakoid membrane used in the simulation. It depicts the shape of the photosynthetic proteins and their random arrangement in the membrane. The dependence of the normalised diffusion coefficient $D_n(r, c)$ on the protein concentration and the distance travelled is shown in Figure 4.1. In accordance with percolation theory the diffusion coefficient in the absence of obstacles $D(0)$ is constant and independent of the travelled distance. For diffusion in the presence of obstacles it can be clearly seen that the diffusion coefficient becomes distance

dependent and decreases with increasing distance travelled (r). As expected from percolation theory this effect becomes more significant for higher area occupation. Finally, the percolation threshold c_p is reached at an occupied area fraction between 0.6 and 0.7. Beyond this point, the tracers are trapped within diffusion domains.

In thylakoids, proteins may well cover an area close to 70% (i.e. an occupied area fraction of 0.7) (see above and [97]). For the protein shapes investigated (immobile, and without specific protein–protein interactions) this is around the percolation threshold. Thus rapid plastoquinone (PQ) diffusion is expected to be restricted. Under the given conditions, free PQ exchange can probably not occur for distances over 20 nm for an occupied area fraction of 0.7 (9.4 nm for a fraction of 0.75).

The average distance (centre to centre) from one cytochrome *bf* complex to the closest photosystem II is about 15 nm at protein densities of 60% (c=0.6) to 75% (c=0.75) (Figure 4.2). Accordingly a cyt *bf* in an average diffusion domain is expected to be accompanied by at least one PS II. Analysing the distribution of the distances from cyt *bf* complexes to PS II it is found that for an occupied area fraction of 0.7, about 1.77 PS II are located within the distance of 20 nm (47 different protein distributions were analysed each with 23 cyt *bf* and 60 PS II). For an occupied area fraction of 0.75 only 0.11 PS II per cyt *bf* are located within a radius of 9.4 nm (40 different protein distributions were analysed each with 25 cyt *bf* and 64 PS II). This illustrates the huge effect that a slightly increased area occupation has if the area covered with proteins is near the percolation threshold.

Conversely, for many PS II there is no cyt *bf* complex in close vicinity (see Figure 4.1), i.e. these centres are isolated, at least within the time frame of rapid electron flux. For an occupied area fraction of 0.7 about 50.2%($\pm$5.2%) of the PS II complexes are at a distance larger than 20 nm from the next cyt *bf* (200 different protein distributions are analysed). For an occupied area fraction 0.75, as much as 95.9%($\pm$2.8%) are located at a distance greater than 9.4 nm, that would allow free plastoquinone diffusion.

However, if the occupied area fraction is below the percolation threshold PQ may travel over a fairly large distance during the time course of photosynthetic electron transport. In Figure 4.3 it is shown how tracers (plastoquinol) spread out from a randomly chosen site (e.g. a binding site on PS II) within a few ms. The occupied area fraction is chosen to be 0.6, which is close to domain formation but still below the percolation threshold. Plastoquinone diffusion is very fast compared to the time for photosynthetic electron transport. Therefore if it is not trapped in a diffusion

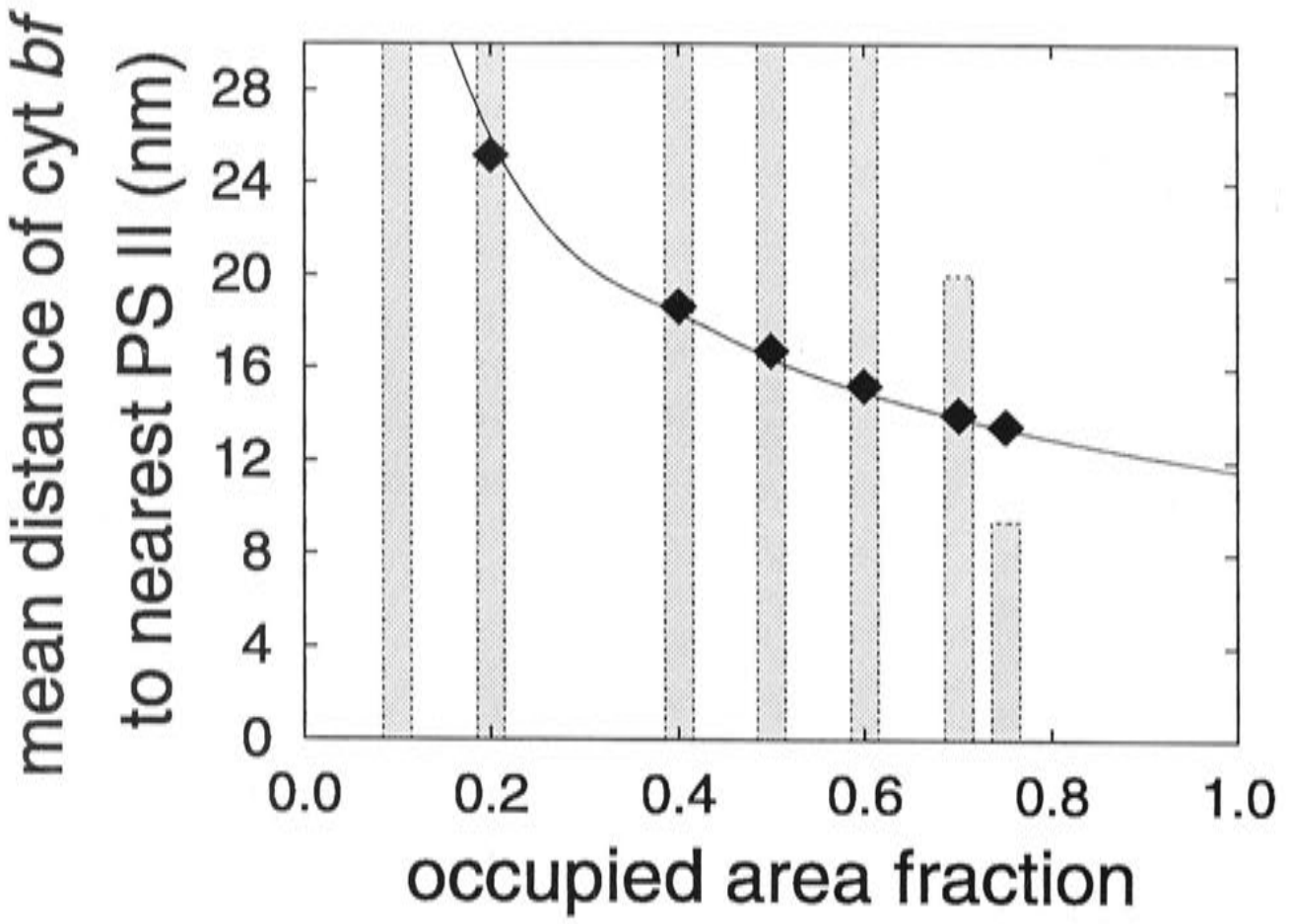

Figure 4.2: *Average distance (nm) from a cyt bf complex to the next PS II versus the ratio of occupied lattice points. Line: data fitted with* $y = 11.6 \cdot x^{-0.5}$. *Columns show the distance plastoquinone is allowed to travel.*

domain, PQ could migrate within a few milliseconds over a large area and visit a large number of cytochrome *bf* complexes. In this scenario PQ diffusion certainly would not limit electron flux (turnover time $\approx$ 10–15 ms).

Obstruction of binding sites in a random distribution

A random arrangement results in a certain fraction of binding sites on PS II or that are obstructed by other proteins. Assuming a size and position of the binding sites as shown in Figure 4.4 the percentages of obstructed binding sites are as shown in Table 4.2.

For all occupied area fractions, the percentage of obstructed Q_B binding sites on PS II is very similar to that of Q_r binding sites on cyt *bf*. In contrast to these binding sites the fraction of obstructed Q_o binding sites on cyt *bf* is relatively low as it is less exposed (see Figure 4.4). Obviously the differential obstruction of different binding sites is highly dependent on their exact position at the protein. In this respect, realistic shapes may play a major role and should be taken into consideration.

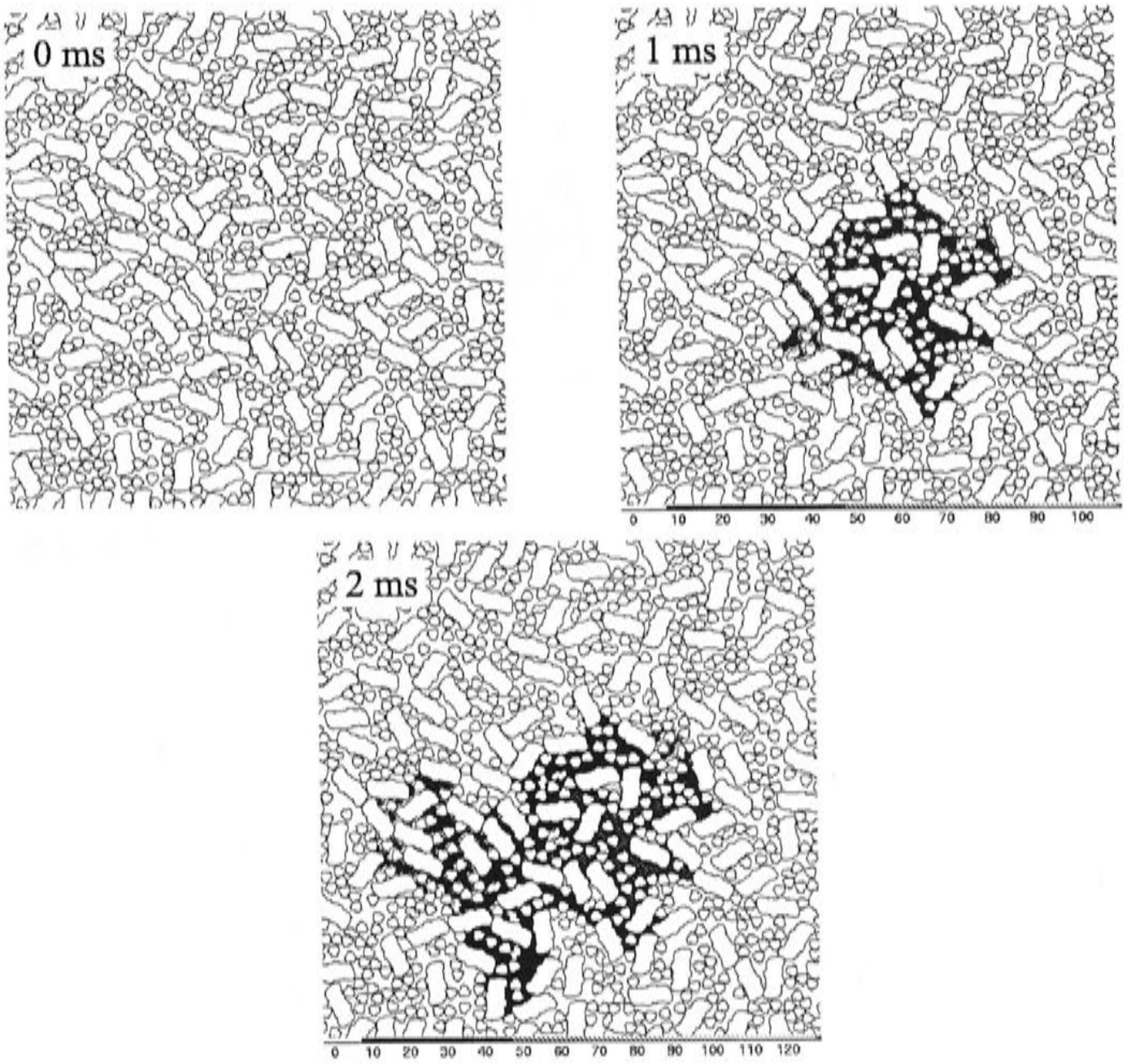

Figure 4.3: *Shows the distance plastoquinone may travel on a millisecond time scale if the occupied area fraction is 0.6 (i.e. below the percolation threshold). The grid is 300 × 300 nm. 1000 tracers were placed at a randomly chosen Q_B–binding site on PS II and their journey was recorded. The grey scale represents the frequency of visits of a certain lattice site. Numbers indicate how many times (on average) a tracer has occupied a lattice point drawn in the corresponding shade. E.g. the black spots show the sites on the grid that a tracer has occupied between 10 and 19 times. This can be interpreted as a measure of the probability for plastoquinone to have travelled a certain distance.*

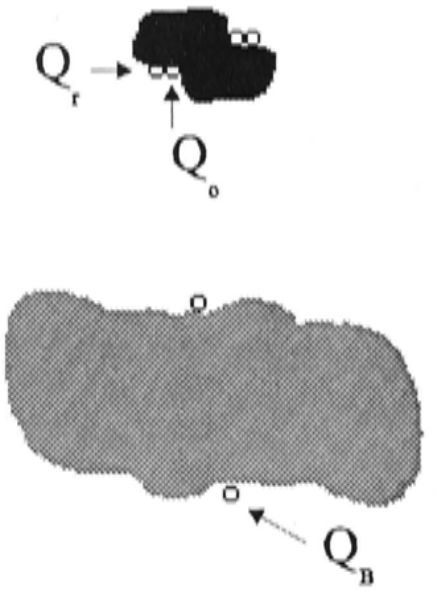

Figure 4.4: *Proteins with binding sites, grey: PS II, black: cyt bf. The shapes shown here were used to determine the percentage of occupied binding sites in Table 4.2.*

Occupied area fraction	Percentage of obstructed bindingsites		
	Q_B	Q_o	Q_r
0.0	0.0	0.0	0.0
0.2	0.8	0.2	0.7
0.4	2.1	0.6	2.2
0.5	3.4	0.8	3.7
0.6	6.7	1.8	7.0
0.7	13.2	4.2	13.2

Table 4.2: *Obstructed binding sites in a random protein arrangement as affected by the occupied area fraction. The values represent the average of 500 different random arrangements, and the matrix is 200×200 nm. The size and position of the binding sites are assumed to be as shown in Figure 4.4. It should be noted that only binding sites directly blocked by a protein are counted.*

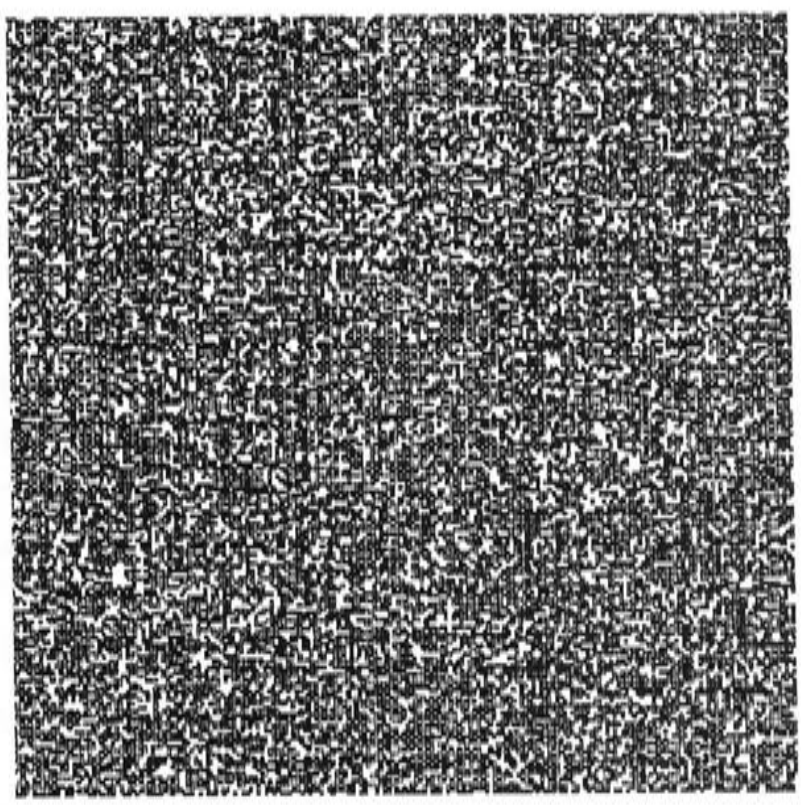

Figure 4.5: *As Figure 4.1 but with point obstacles.*

4.3.3 Relationship between the shape of the obstacles and the diffusion coefficient $D_n(r, c)$

The diffusion of a mobile particle (e.g. plastoquinone) between immobile obstacles is highly dependent on the size and shape of the latter. To elucidate this dependency different types of obstacles are compared: (1) point obstacles (Figure 4.5) and (2) circular obstacles of a size comparable to that of the photosynthetic proteins (Figure 4.6).

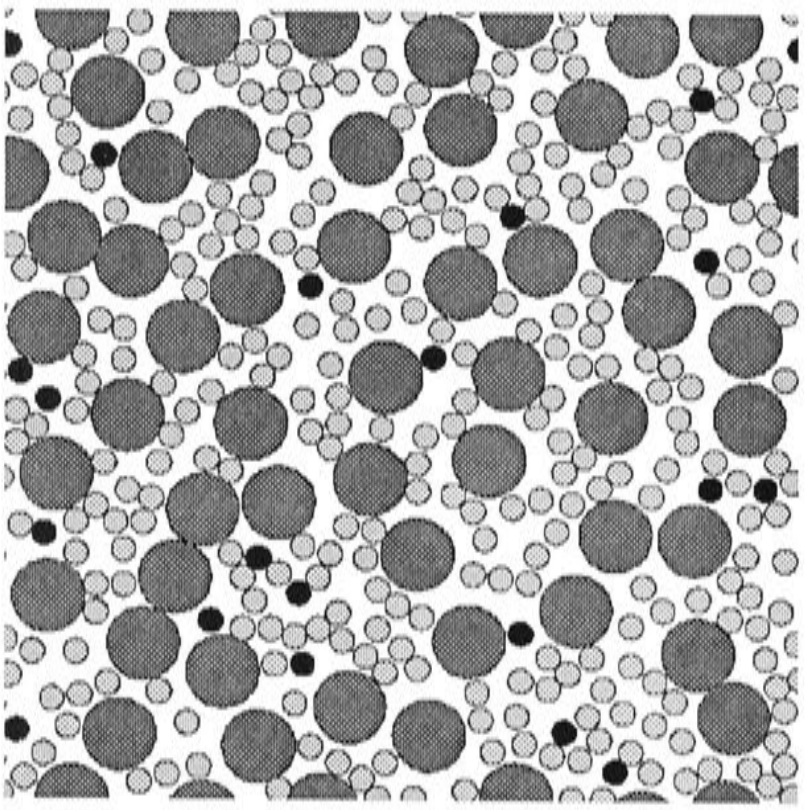

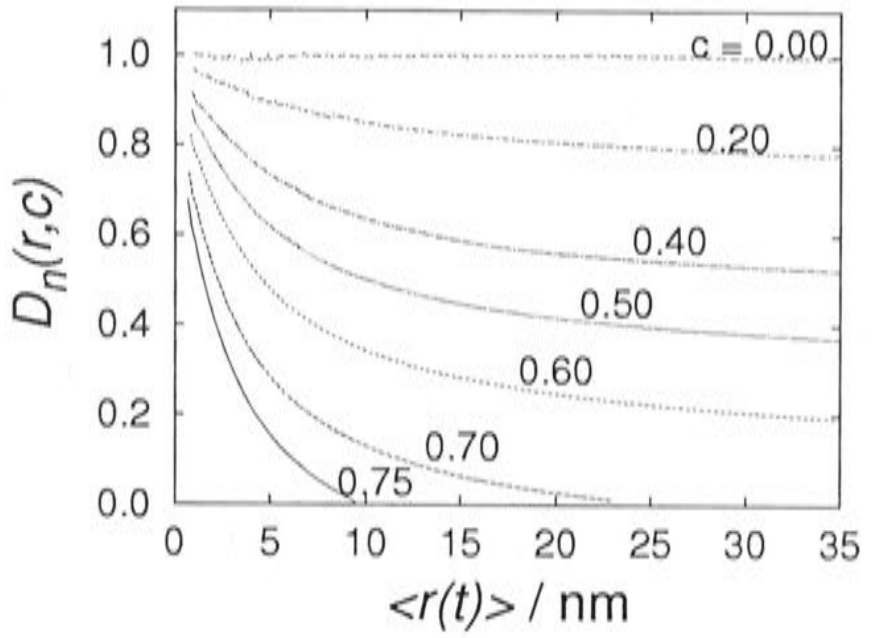

Figure 4.6: *As in Figures 4.1 and 4.5 but with circular obstacles of a size corresponding to the obstacles in Figure 4.1. The radius of the obstacles corresponding to PS II (dark grey) is 9.23 nm, the radius for those corresponding to cyt bf (black) and LHC II (light grey) is 3.13 nm. This leads to about the same number of occupied lattice points as for the obstacles of realistic shapes.*

Figure 4.5 shows the distance dependency of the normalised diffusion coefficient $D_n(r, c)$ of mobile particles diffusing between immobile point obstacles. The percolation threshold c_p is reached at an occupied area fraction between 0.4 and 0.5. This is in accordance with the expected value of 0.41 for a square lattice (triangular lattice: 0.50, continuum: 0.332 [166, 150, 149]).

In principle, effects similar to those seen for realistic protein shapes can be seen for circles (Figure 4.6. Compare also Figure 4.1 showing the results for realistic shapes). However, point obstacles (Figure 4.5) are much more efficient in hindering particle diffusion than are more compact obstacles. For immobile point obstacles the percolation threshold at which diffusion domains are formed is around $c_p = 0.4$. For circles and the protein shapes it is above 0.6.

As can be seen by comparing Figures 4.1 and 4.6 the percolation threshold c_p for circles is slightly higher than for realistic shapes of comparable size. Overall, however, the effect of realistic protein shape, compared to shapes of equal size on PQ migration, is relatively small.

4.3.4 Influence of boundary lipids on plastoquinone diffusion

There is some evidence that protein complexes in grana stacks are surrounded by lipids (boundary lipids) preventing direct protein contact. Ivancich and co–workers [88] found a heterogeneity in the boundary lipid fraction in grana stacks. About 2/3 of the boundary lipids exchange rapidly with bulk lipids whereas 1/3 exchanges very slowly or not at all with bulk lipids. It is likely that the latter fraction represent lipids localized in the protein contact zones.

In our model boundary lipids are regarded as an additional layer surrounding the LHC II (see also [9]). It is further assumed that boundary lipids can be shared by neighbouring LHC complexes, i.e. that there may be as little as one common layer of lipids between two neighbouring LHC II (see Figures 4.7 and 4.8). The boundary lipids are not assumed to interact with the other proteins. Although other proteins have boundary lipids too, it seems sufficient to consider here the boundary lipids of LHC II as it is the most abundant protein in the grana core and here the boundary lipids may be of particular structural importance (see discussion).

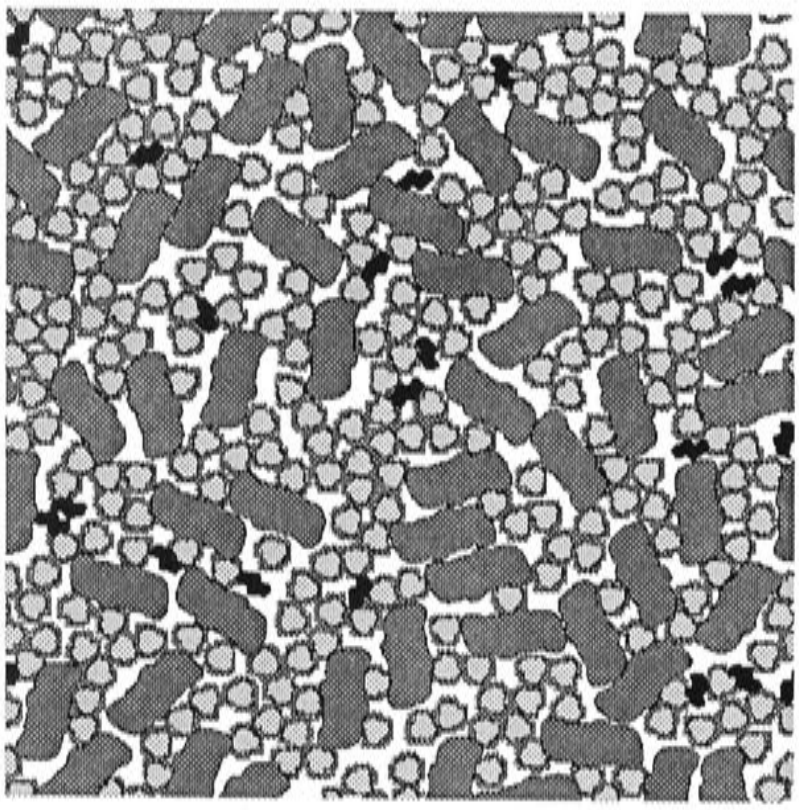

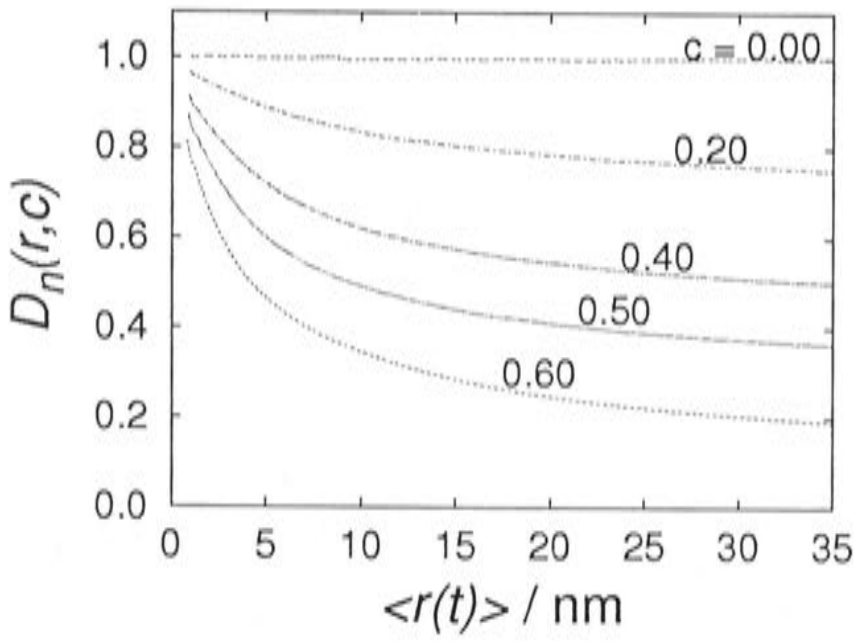

Figure 4.7: *As in Figure 4.1 but here a layer of boundary lipids is surrounding the LHC II complexes. Below: distance–dependent normalised diffusion coefficient* $D_n(r, c)$ *for the case where boundary lipids are assumed permeable to plastoquinone. That means plastoquinone can exchange easily with the lipids and thus travel unobstructed through the sites occupied by boundary lipids. Due to the layer of boundary lipids the size of the proteins to fit in the lattice is increased (independent of the nature of the lipids, i.e. permeable to PQ or impermeable). Therefore it takes a long computing time to find a free site on the lattice if the occupied area fraction is very high. For that reason calculations for occupied areas larger than 0.6 were not carried out.*

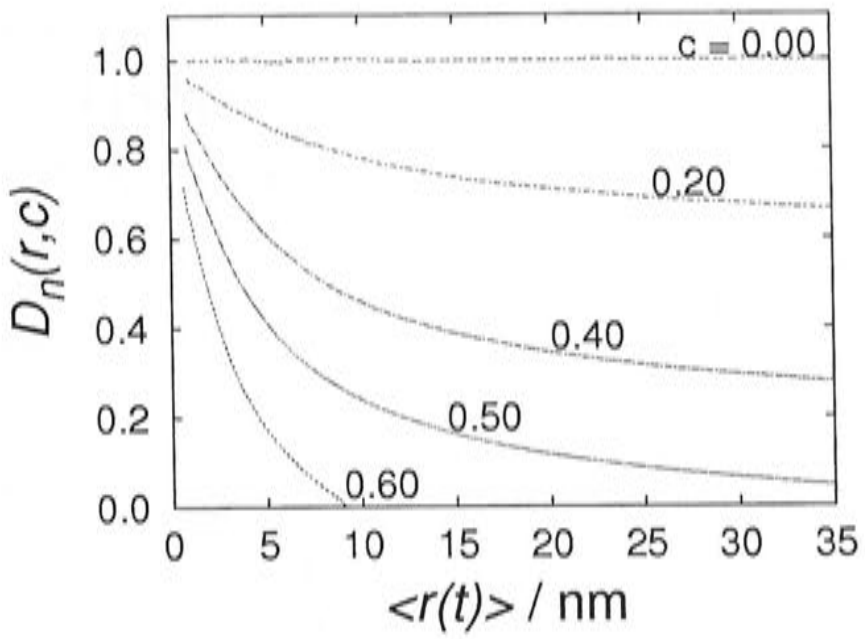

Figure 4.8: *As in Figure 4.7 but here the boundary lipids are assumed to be impermeable to plastoquinone. A plastoquinone cannot travel to a site blocked by a boundary lipid.*

Two extreme cases are investigated:

(1) all boundary lipids are permeable to plastoquinone diffusion. Thus, PQ can diffuse through 'boundary lipid channels' (Figure 4.7).

(2) All boundary lipds are impermeable to plastoquinone (Figure 4.8).

As can be seen from Figures 4.7 and 4.8 the diffusion behaviour for the two scenarios is quite different. For permeable boundary lipids (case (1)) PQ diffusion is facilitated (Figure 4.7). In this case the boundary lipids act as a spacer preventing the formation of closed diffusion domains. For case (2) the simulation predicts a drastically obstructed PQ diffusion (Figure 4.8) compared with the situation in the absence of boundary lipids (see Figure 4.1). Impermeable boundary lipids increase the apparent size of the LHC II by circa 35% and hence lead to a drastically obstructed PQ diffusion.

Overall, boundary lipids may play an important role in plastoquinone diffusion in grana stacks and be of considerable significance, physiologically.

4.3.5 Effect of mobile obstacles

In Figures 4.9 and 4.10 the normalised diffusion coefficient for tracers diffusing between mobile obstacles is shown. It can be seen that the diffusion coefficient approaches a constant (concentration dependent) value as r, the distance travelled, increases.

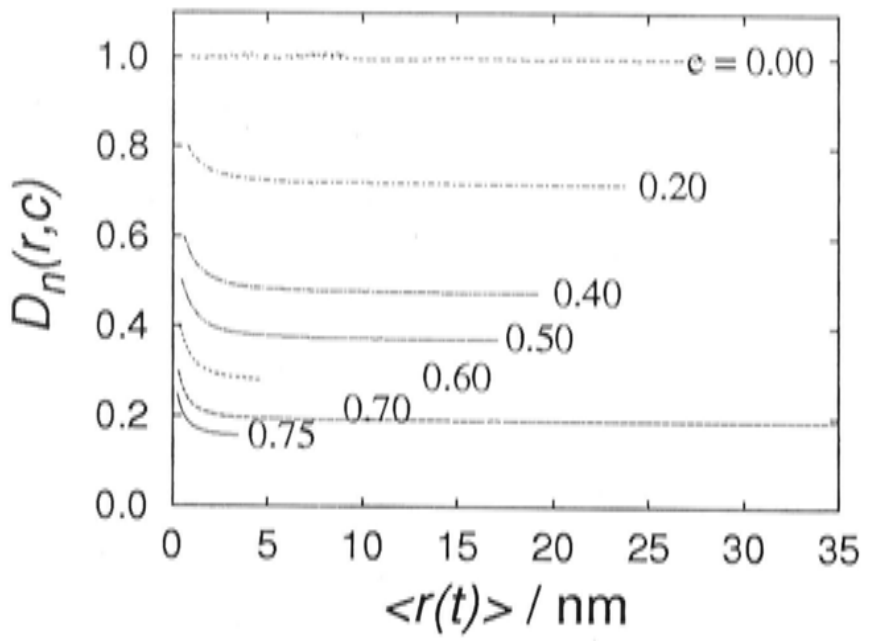

Figure 4.9: *Similar to Figure 4.5 but this Figure shows the normalised diffusion coefficient of the tracer in the presence of mobile point obstacles. The diffusion coefficient of the point obstacles was assumed to be the same as that of the tracer. Area occupation as indicated.*

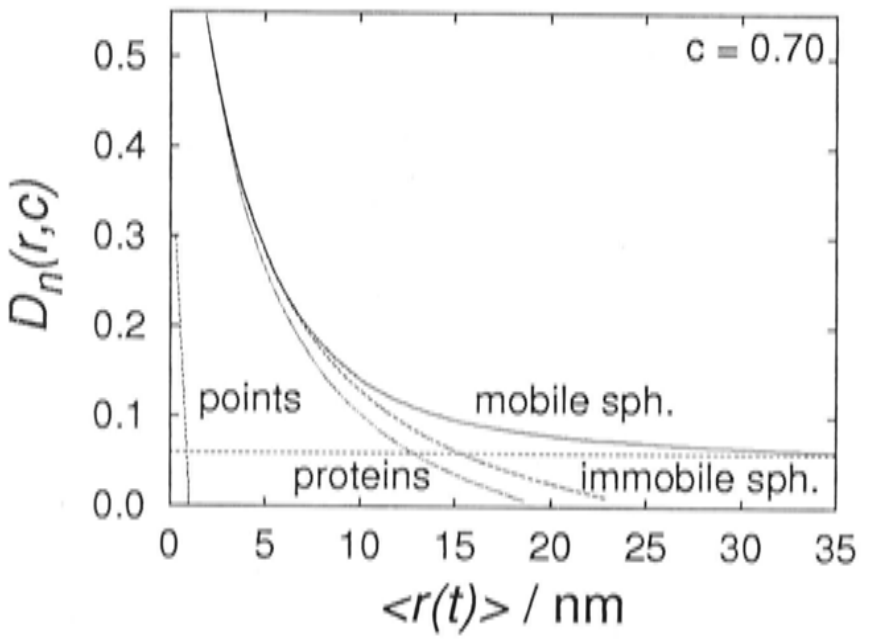

Figure 4.10: *As Figure 4.9. The solid line shows the diffusion coefficient for the case of mobile spherical obstacles whereas the dashed line shows that for the case of immobile spherical obstacles. The dotted horizontal line shows the value of 0.06 that the solid line approaches for large r. The radius of the circles was chosen to match the obstacle area to that of photosynthetic proteins as shown in Figure 4.1. The diffusion coefficient of LHC II and cyt bf was assumed to be three orders of magnitude lower than that of the tracer. PS II occupies an area that covers 265 grid points, whereas LHC II occupies an area that covers 33 grid points. Accordingly the diffusion coefficient of PS II was assumed to be 33/265 times that of LHC II. For comparison curves for immobile point obstacles and protein shapes are also shown. The occupied area fraction used was 0.7.*

As point obstacles and tracers are of comparable size, each is given the same diffusion coefficient. In this case, no percolation threshold exists and long–range diffusion can occur at all concentrations, see Figure 4.9. This is in accordance with previous simulations [150, 135, 176].

Figure 4.10 shows the effect of mobile, circular obstacles, corresponding in size to the photosynthetic proteins. The diffusion coefficient for LHC II and cyt *bf* is assumed to be three orders of magnitude lower than that for plastoquinone diffusion ($D(0) = 3.5 \cdot 10^{-7}$ cm^2/s). A diffusion coefficient of $4 \cdot 10^{-10}$ cm^2/s was determined for the cytochrome bc_1 complex in mitochondria [68]. The diffusion coefficient of PS II is scaled according to the different areas the proteins occupy on the grid.

In Figure 4.10 the normalised diffusion coefficient for diffusion between mobile and immobile circular obstacles is shown for an occupied area fraction of 0.7. The area fraction investigated is above the percolation threshold found for an arrangement with immobile obstacles. It can be seen in Figure 4.10 that in the case of mobile obstacles the normalised diffusion coefficient approaches a value of 0.06 for large r (dotted line). This corresponds to a diffusion coefficient of $2.1 \cdot 10^{-8}$ cm^2/s. Accordingly a PQ could travel farther than 290 nm within 10 ms. How effective mobile obstacles are in hindering plastoquinone diffusion certainly depends on the diffusion coefficients of the obstacles [176]. In our simulation a diffusion coefficient for LHC II of the same order of magnitude as for cyt *bf* is assumed, corresponding to their similar sizes. It has to be noted, however, that the LHC II diffusion coefficient *in vivo* is expected to be much lower due to protein–protein interaction and interaction between LHC II complexes in adjacent grana discs.

4.4 Discussion

The diffusion of plastoquinone in the thylakoid membrane was studied by a Monte Carlo simulation. The diffusion coefficient for plastoquinone was determined assuming that randomly distributed integral proteins obstruct lateral plastoquinone diffusion.

First we will discuss the situation of plastoquinol diffusion between immobile obstacles exhibiting a realistic shape. Next, the influence of the shape of the obstacles will be examined. In a third part the influence of boundary lipids will be discussed followed by the last part, which deals with the diffusion between mobile obstacles.

4.4.1 Diffusion between immobile obstacles of the shape of photosynthetic proteins

It was found that the diffusion coefficient decreases strongly with increasing protein densities and distance travelled. This is in agreement with percolation theory [151, 176, 9] and the observation that plastoquinone diffusion in thylakoids is much slower than in pure liposomes [24]. It shows that any experimental determination of the diffusion coefficient in the presence of obstacles needs to take into account its distance dependency. Differing experimental setups will involve measurements of different travelled distances leading to different estimates of $D(r, c)$, e.g. in measurements by fluorescence photobleaching recovery typically $r \approx 1$ μm, whereas in measurements by eximer formation or fluorescence quenching $r \approx 1$–10 nm (see e.g. [151, 56, 180]).

With increasing protein densities the diffusion is further obstructed. Finally, the long range (large r) diffusion coefficient declines to zero when the area fraction c of obstacles is greater than the percolation threshold c_p. This raises the question of how close thylakoid membranes are to the percolation threshold beyond which fast long range PQ migration is disrupted. For randomly distributed, non–interacting, immobile proteins an occupied area fraction between 0.6 and 0.7 leads to the formation of diffusion domains (Fig. 4.1). Interestingly, a critical re–evaluation of the protein density has led to the conclusion that the occupied area fraction could be as high as 0.64–0.74 in thylakoids (see [97] and references therein) and 0.70–0.77 in grana (see Table 4.1).

The simulation presented here shows that despite the retarding effect of protein density, below the percolation threshold PQ can equilibrate throughout the membrane. Plastoquinone diffuses extremely quickly compared to electron transport, and thus reduced plastoquinone, PQH_2, could travel the distance from each PS II to a cytochrome *bf* complex to deliver electrons within an appropriate time (see Figure 4.2 and 4.3). The situation is very different for an occupied area fraction of 0.7 where domains are formed under the conditions used in the simulation. Here PQ is trapped in diffusion domains. Within such a domain it can diffuse freely but it cannot leave its domain. The average greatest pathlength for PQ diffusion is approximately 20 nm at this occupancy of 0.7 (Fig. 4.1). Correspondingly, cyt *bf* in a certain diffusion domain can only contribute to linear electron flux when at least one PS II complex is closer than 20 nm. This seems to be the case in an average domain: a mean centre–centre distance of about 15 nm between cyt *bf* and the next PS II is estimated for an area occupation of 0.6–0.75 (see Fig. 4.2). A different

picture emerges for PS II. More than 50% of the PS II are separated from cyt *bf* by a distance of more than 20 nm and hence, are located in 'cyt *bf* free' domains, at least within the time scale of rapid electron transport (10–15 ms).

Since thylakoids are highly covered with proteins, possibly very close to the percolation threshold, slight changes in the protein arrangement could lead to pronounced changes in the diffusion behaviour. In the following we discuss several factors that could influence the percolation threshold and shift it one way or another.

4.4.2 Obstacle size and shape

The retarding effect of obstacle density decreases with increasing obstacle size (compare Fig. 4.5 with Figs. 4.1 and 4.6). This is an important observation and in accordance with the results of Saxton [151, 176]). It indicates that aggregation of proteins to larger 'supercomplexes' could facilitate the migration of small molecules like PQ within the membrane (see also [35]). Large electron transport supercomplexes have been found for bacterial systems [94] and in higher plants large PS II–LHC II supercompexes have been observed [28, 186]. The formation of such aggregates may lead to more compact obstacles and thus minimise obstruction of PQ diffusion (i.e. increase the percolation threshold). Interestingly, although high protein concentrations reduce PQ mobility, macromolecular crowding on the other hand favors associations of proteins in macromolecular structures [35, 57, 122] which are in turn less efficient in hindering PQ diffusion.

For realistic shapes the ratio of circumference to area is higher than for circles of equal size. Correspondingly circles are more compact and less efficient as obstacles than realistic shapes (see e.g. Xia and Thorpe[a] and Almeida and Vaz [185, 176, 9]). This explains the slightly higher percolation threshold found for circles. However, the difference in their percolation thresholds is not very pronounced. Thus, for simulations of PQ diffusion the assumption of circular shapes is a good approximation. This may not necessarily be the case for investigations of electron transfer at protein binding sites. If one regards more specific features of PQ turnover, e.g. the accessibility of PQ binding sites and binding probability, then the protein shape

[a]Xia and Thorpe have studied the percolation properties of ellipses in a continuum as a function of their aspect ratio [185, 9]. Their results can be summarized by the formula $p_c = (1/3)^{4/(2+y)}$ with $y = b/a + a/b$, where a and b are the major and minor semiaxes.

may well play a role. Table 4.2 suggests that the probability that binding sites are obstructed by other proteins depends on the shape of the protein and on the position of the binding site. Furthermore, the shape of the proteins may be important for the formation of cavities that affect the accessibility of binding sites.

4.4.3 Boundary lipids

It was shown that lipids play an important role in the aggregation of LHC II [158] and there is evidence that phosphatidylglycerol (PG) stabilizes the trimeric form of LHC II [178] and promotes the formation of PS II dimers [103]. Boundary lipids can exert a strong influence on the functionality and mobility of integral proteins [156].

From spin label studies, it is known that lipid mobility in thylakoids is reduced compared to a protein–free lipid membrane [180]. This suggests that a large number of proteins and protein complexes are surrounded by more or less tightly bound boundary lipids. Little is known about boundary lipids in thylakoids. Depending on the degree of their immobilisation, these lipids could be more or less 'permeable' to PQ. Figures 4.7 and 4.8 show possible effects of boundary lipids on PQ diffusion. In our simulation two extreme cases are considered. In the first case all boundary lipids are assumed to be completely permeable to PQ diffusion. I.e. PQ can rapidly exchange with the boundary lipids. This would lead to the formation of lipid channels and prevent the formation of diffusion domains. In the second case it is assumed that the boundary lipids are tightly bound and cannot rapidly exchange with plastoquinone and thus impede PQ diffusion. Accordingly this kind of immobile boundary lipids would lead to a much lower percolation threshold. The two extreme cases have opposite effects and most likely boundary lipids in the real membrane are neither completely permeable nor completely impermeable. Rather one might expect a mixture of both. Furthermore, different proteins could be surrounded by different lipid boundaries. How boundary lipids influence plastoquinone diffusion will certainly depend on the composition and position of the lipids on the proteins. We know too little about boundary lipids in the thylakoids, but we demonstrate here that they may be an important feature of thylakoid structure[b].

[b]For other treatments of lipids surrounding proteins see also the 'dynamic boundary layer model' mentioned in [176, 9] or Marcelja [114].

4.4.4 Mobility of the integral proteins

In the previous sections diffusion of small tracers between immobile obstacles was discussed. In the following we discuss diffusion between mobile obstacles.

Lateral migration of integral proteins is a basic feature of membrane function, regulation, and biosynthesis. For biosynthesis, function, and acclimation of the photosynthetic apparatus in plants, lateral transport of proteins between stroma lamellae and grana thylakoids is essential [12, 15]. Figure 4.9 shows that the obstacle mobility counteracts the formation of diffusion domains. If the obstacles are mobile, no diffusion domains are formed, and long–range diffusion can occur at all obstacle concentrations, as previously shown by Pink [135, 176]. The key question is whether the obstacles are mobile or immobile on the time scale of the process under consideration (e.g. photosynthetic electron transport).

Figure 4.10 shows a simulation of plastoquinone diffusion, assuming that the mobility of the obstacles (circular obstacles of a size comparable to that of grana proteins) is three orders of magnitude lower than that of PQ. This corresponds to the diffusion coefficient measured for cyt *bf* [68]. Under these conditions the diffusion coefficient for PQ approaches $2.1 \cdot 10^{-8}$ cm^2/s ($0.06 \cdot 3.5 \cdot 10^{-7}$ cm^2/s). Consequently PQ could travel farther than 290 nm in 10 ms, suggesting that under such conditions electron transport may not be limited by PQ migration. Drepper and co–workers [48] came to a similar conclusion.

However, the mobility of LHC II is probably restricted by lateral interaction and transverse interaction across adjacent grana membranes. Drepper and co–workers suggest a diffusion coefficient of $4.4 \cdot 10^{-13} - 1.9 \cdot 10^{-12}$ cm^2/s for unphosphorylated LHC II (see [48] and references therein). This is two to three orders of magnitude lower than that used in our calculations. Furthermore a fraction of LHC II is known to form large supercomplexes with PS II [28, 186]. No information exists about the mobility of such aggregates. It is likely that they are highly immobile because of their size and multiple lateral and cross–membrane interactions. Therefore, the diffusion coefficient of LHC II *in vivo* may be not large enough to prevent domain formation. Clearly, the influence of protein mobility on PQ diffusion is an important factor in understanding PQ percolation in thylakoids. More information about protein mobility in thylakoids is thus required.

4.4.5 Diffusion domains in thylakoids

Mitchell and co–workers concluded from their simulation of plastoquinone diffusion that electron transport is not limited by plastoquinone diffusion [124]. However, in their model an occupied area fraction around 0.35 was assumed, which is well below the percolation threshold estimated in the simulation presented here. In a later publication [48] their model was further developed and included a possible mobility of obstacles and an occupied area fraction of 0.5–0.7. In this paper they conclude that if movement of the obstacles occurs, long–range diffusion of a tracer is not prevented, but only retarded. Of course the extent certainly depends on the diffusion coefficient of the obstacles. On the other hand, from their observation that no global redox equilibrium between the mobile plastoquinone pool and QA on PS II is achieved, Lavergne and Joliot concluded that plastoquinone is restricted to small domains. They regard this kind of microstructure as the result of a free random distribution of proteins without specific protein–protein interactions.

However, for occupied area fractions near the percolation threshold a random arrangement results in a considerable fraction of domains lacking cyt *bf* [92, 109] (see also the discussion above) and of obstructed binding sites [111, 109] (see also Table 4.2). According to the simulation presented here, more than 50% of the PS II complexes are isolated on the time scale of rapid electron transfer. Furthermore, the reactions at the Q_o binding site are generally assumed to be the rate limiting step of photosynthesis, and thus obstruction of these binding sites seems wasteful. Random high–density distribution of proteins in the membrane could lead to an inefficient microstructure, where electron transport is hindered. On the other hand, tight packing of LHC II and PS II is required for optimal transfer of excitation energy between chlorophyll binding proteins. This suggests that the random arrangement might be structured by such factors as protein–protein interactions, as suggested by Kirchhoff and co–workers [96]. They measured the control of electron transport and the redox equilibrium between QA and cyt *bf* complexes. Their results support the micro–domain concept of Lavergne and co–workers but they suggest that the micro–domains are formed by a hierarchy of specific PS II–LHC II interactions rather than by free random distribution.

Chapter 5

Protein–protein interactions

Contents

5.1 Introduction

The density of photosynthetic proteins in the thylakoids is very high [126, 97] (see also Chapter 4). Due to the high protein density plastoquinone diffusion may be severely restricted, depending on the organisation of the integral proteins. However, the exact nature of the protein organisation is an open question. Lavergne and co–workers [109] suggest a random organisation which, taking into account the results of Chapter 4 (e.g. the likely obstruction of binding sites), seems rather unlikely. Kirchhoff and co–workers [96] propose a structure that is more ordered because of protein–protein interactions.

Although LHC II appears as individual particles in freeze–fracture electron micrographs[a], within a grana membrane LHC II complexes may be tightly associated with neighbouring LHC II complexes and PS II complexes [107]. During the last two decades a number of experiments have shown that multisubunit proteins (e.g. LHC II, PS I, PS II, cyt *bf*) can associate to produce higher aggregation forms. These constitute homo- or hetero–oligomeric assemblies (often referred to as 'supercomplexes'). Examples for homo–oligomers are the trimeric form of LHC II ($(\text{LHC II})_3$) [89, 105] and the cyt *bf* dimer [80, 85, 38]. Hetero–oligomers exist for the majority of PS II (PS II_α, $(\text{PS II}_\alpha\text{–LHC II})_2$) [74] and PS I ($\text{PS I–(LHC I)}_8$) [89, 27]. While it seems a common feature that proteins tend to form oligomers, there are others that do not: PS II_β and the ATP–ase do not form higher aggregation states.

The functional role of these supercomplexes may be to increase the efficiency of energy transduction in the photosynthetic process or stabilize proteins or parts of them. For example it is thought that the formation of cyt *bf* dimers stabilises the Rieske centre [85].

Recent evidence supports the existence of an even higher level of protein assemblage, located mainly in the grana region. Firstly, heptameric LHC II-trimers [40] as well as complexes formed by $(\text{LHC II})_3$ and $(\text{PS II}_\alpha\text{–(LHC II)}_3)_2$ supercomplexes [29, 186] have been isolated by fast solubilization of grana stacks, followed by single particle analysis using electron microscopy. The authors conclude that these aggregates also exist in the native membrane. Secondly, the analysis of light–induced changes in circular dichroism of thylakoids indicates the existence of a long-range

[a]It should be noted that plastic deformations during freeze–fracturing can reduce particle sizes [160].

chiral order. These signals are interpreted as indicating a macro–domain structure in grana stacks [87, 63].

The segregation and aggregation of protein–assemblies is of functional significance. Phosphorylation of the LHC II proteins results in a segregation from PS II and lateral migration of the complexes, which is regarded as an essential mechanism for the regulation of the energy distribution between the two photosystems in plants [7, 6]. The modification of LHC II by the negatively charged phosphate group is likely to decrease protein–protein interactions. On the other hand the most likely explanation for the well–established phenomenon of energy–transfer between PS II_α units (cooperativity) [102] is that several PS II_α centers share a common antenna bed mediated by LHC II complexes. To facilitate energy transfer, close contact between several of these complexes must occur. Furthermore, using a functional analysis of electron transport reactions, a micro–domain hypothesis was developed by Joliot, Lavergne, and co–workers [93, 109] and extended by others [24, 96] (see also Sections 1.2.5 and 3.4). According to the extended micro–domain hypothesis, (PS II_α–LHC $II_3)_2$ and LHC II_3 build up a network–like arrangement, within which plastoquinone molecules are temporarily trapped. The participation of cyt *bf* complexes in these networks is unclear. In contrast to supercomplexes, it is expected that micro–domains are less stable structures with a finite lifetime [96, 92].

In this Chapter the role of protein–protein interactions in the organisation of proteins in a membrane is investigated, starting with interacting spheres corresponding to the size of LHC II trimers. Different energies for the interactions are considered. The arrangement of the particles is then investigated by a nearest neighbour analysis and pair correlation analysis. Investigations are carried out for different particle densities to get a basic understanding of the influence of protein–protein interactions on pattern formation. In the second Section the influence of non–interacting ('disturbing') spheres on the organisation of the particles is investigated. This Section relates to the cytochrome *bf* complexes in the thylakoids, that may not interact with other proteins. Finally, proteins with shapes corresponding to photosynthetic proteins are considered. LHC II particles are assumed to interact with each other, cyt *bf* is considered to be non–interacting while PS II is assumed to contain integral, tightly bound LHC II complexes that interact in the same manner as free LHC II.

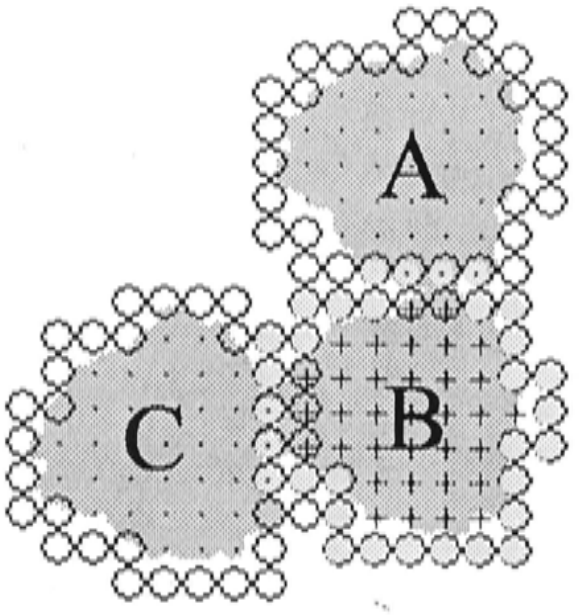

Figure 5.1: *Binding sites on LHC II. Binding sites are shown as open circles, binding sites belonging to LHC II (B) are shaded in light grey. Lattice points occupied by LHC II labelled with 'A' and 'C' are shown as black points, those occupied by the LHC II labelled with 'B' are shown as crosses. Two of the binding sites of LHC II labelled with 'A' come to lie on lattice points occupied by LHC II (B) (discernible as circles around the black crosses (lattice sites)). Therefore LHC II (A) is considered to have two bound sites. LHC II (B) has three binding sites bound to LHC II (A) and three bound to LHC II (C) (light grey circles with a black point in it), which adds up to six bound sites. Finally, LHC II (C) has three bound sites (crosses in circles). It has to be noted that the grey shapes of the LHC II are only for visualisation.*

5.2 The simulation

The particles were placed randomly (corresponding to E = 0 kT) on the lattice as described in Chapter 4.

5.2.1 LHC II

The number of attributes of the LHC II are extended by an additional layer of grid points surrounding them. These grid points reflect the binding sites. If another LHC II comes to lie on these grid points (from here on referred to as binding sites) each occupied point is counted as a bound site (see also Figure 5.1)[b].

[b]It has to be noted here that 'bound sites' are also counted if E = 0 kT. In this case unbinding always occurs.

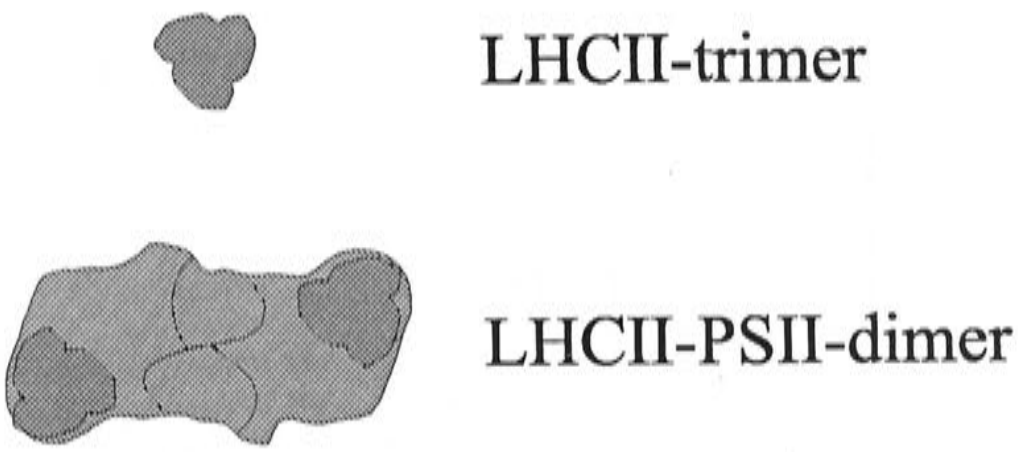

Figure 5.2: *Schematic diagram of a LHC II trimer and a (PS II–LHC II_3) dimer. The positions of the tightly bound LHC II trimers are illustrated.*

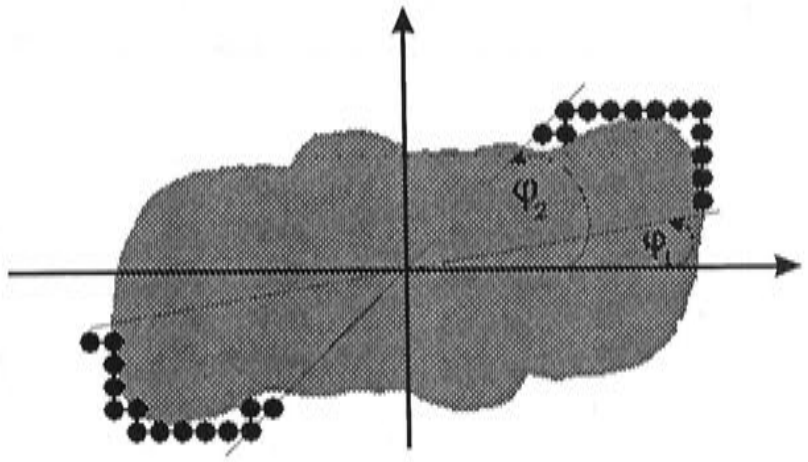

Figure 5.3: *Binding sites on PS II. Binding sites are shown as filled circles. The angles φ_1 and φ_2 (here 10° and 45°) determine the position of the binding sites.*

5.2.2 PS II

PS II usually forms oligomers consisting of two PS II monomers and two LHC II trimers (see Figure 5.2). It is assumed that the LHC II trimers that are tightly bound to PS II interact with free LHC II and other LHC II tightly bound to PS II. Accordingly, those parts of the (PS II–$(LHC\ II)_3)_2$ (from now on referred to as PS II) where the LHC II is bound should interact with other LHC II complexes.

Due to the rotational symmetry of the complexes the position of the binding sites can be defined by two angles relative to the particle (φ_1 and φ_2, see also Figure 5.3). Between these angles all nearest and next nearest neighbouring lattice sites of a PS II are considered as binding sites. Trigonometric calculations are slow to process, and therefore a geometrical approach was chosen to find the binding sites for all orientations of the PS II on the lattice.

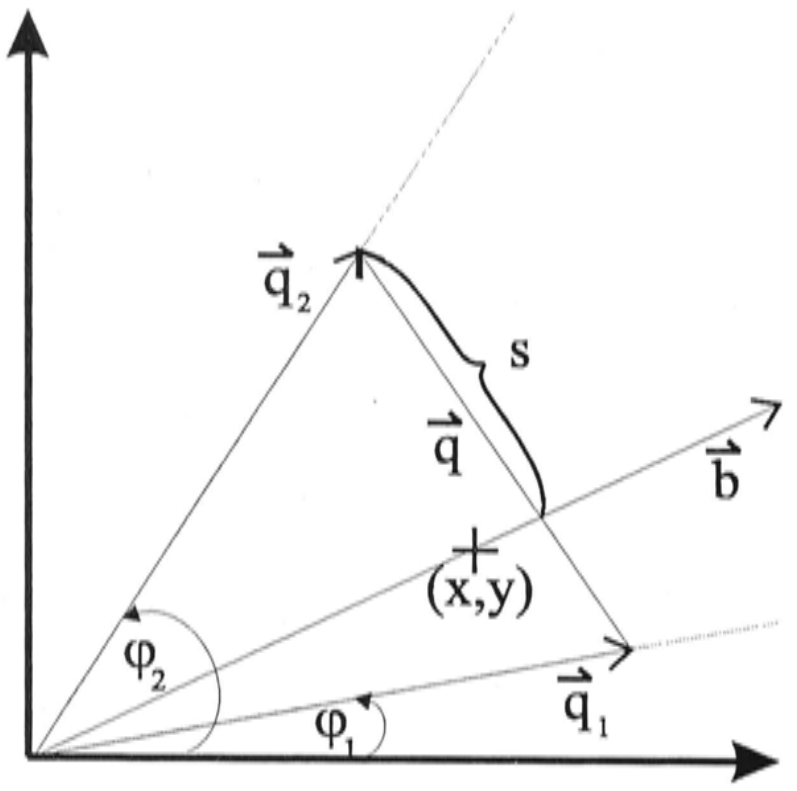

Figure 5.4: *Schematic diagram of the vectors used to find the binding sites on PS II. (x,y) is the lattice point under test as to whether it is a binding site or not. φ_1 and φ_2 determine the interacting segment. The length of $\vec{q}_1$ and $\vec{q}_2$ is chosen to be unity. $\vec{q}$ is $\vec{q}_2 - \vec{q}_1$. $\vec{b}$ is the vector from the origin through (x,y) extending through the whole lattice. s is the distance between the ending point of $\vec{q}$ and the intersection of $\vec{b}$ with $\vec{q}$. See also Figure 5.3*

Finding the binding sites on the (PS II–(LHC II)$_3$)$_2$ supercomplexes

The aim is to find whether a certain lattice point (x,y) surrounding PS II is between the two angles φ_1 and φ_2 that determine the binding sites and is therefore considered to be a binding site.

The vector $\vec{b}$ is defined to be the vector from the origin through the lattice point (x,y) and spanning the whole lattice (see also Figure 5.4). If (x,y) lies between the two given angles φ_1 and φ_2 it follows that $\vec{b}$ intersects with the vector ($\vec{q}$) connecting the vectors $\vec{q}_1$ and $\vec{q}_2$ as defined in Figure 5.4.

Let $\vec{q}$ be:

$$\vec{q} = \vec{q}_2 - \vec{q}_1, \tag{5.1}$$

$$= \begin{pmatrix} \cos\varphi_2 \\ \sin\varphi_2 \end{pmatrix} - \begin{pmatrix} \cos\varphi_1 \\ \sin\varphi_1 \end{pmatrix}. \tag{5.2}$$

From Figure 5.4 it follows that the lattice site (x,y) is between the two given angles φ_1 and φ_2 if $0 < s/q < 1$ (q being the length of $\vec{q}$). The question arises of how to express s/q in terms of φ_1 and φ_2.

Define the vector $\vec{n}$, normal to vector $\vec{b}$, as:

$$\vec{n} = \begin{pmatrix} -b_y \\ b_x \end{pmatrix} \tag{5.3}$$

According to the theorem of intersecting lines

$$\frac{s}{q} = \frac{\vec{n} \cdot \vec{q}_2}{\vec{n} \cdot \vec{q}} \tag{5.4}$$

$$= \frac{n_x \cos\varphi_2 + n_y \sin\varphi_2}{n_x(\cos\varphi_2 - \cos\varphi_1) + n_y(\sin\varphi_2 - \sin\varphi_1)}. \tag{5.5}$$

This procedure is carried out for all nearest and next nearest neighbours of a PS II. If, for the lattice point under consideration, $0 < s/q < 1$ the point is considered to be a binding site.

The information obtained is then stored as a (static) particle attribute in the form of an array of vectors. The index of the array corresponds to the orientation of the particle in the lattice, while each vector contains the coordinates of all binding sites for a certain orientation of the particle within the lattice.

The advantage of this procedure is that instead of calculating trigonometric functions for each lattice site considered, a trigonometric function ($\cos\varphi_1$, $\sin\varphi_1$, $\cos\varphi_2$, and $\sin\varphi_2$) needs to be calculated only four times. The results of these four functions are stored and re–used thus saving much computing time.

5.2.3 Interaction

Short range, nearest neighbour, attractions between the LHC II complexes are introduced. No long range attractive force is assumed–but rather a Lennard–Jones potential with very short range (minimum at the distance of the lattice spacing). Correspondingly, only direct contact with the binding site leads to a binding event. The binding energy of a particle (e.g. PS II or LHC II) is considered to be the sum of bound sites the particle is involved with (see Figure 5.1) times the assumed energy (E, in units of kT). When two particles collide they stick together until a particle unbinds. Because of its thermal energy a particle can unbind from its neighbours with the probability $e^{-\Delta E/kT}$. T is the temperature and ΔE is the energy change due to the unbinding[c]. It is assumed that $\Delta E = nE$, where n is the number of

[c]Since only attractive forces are considered here, ΔE resulting from binding is negative, whereas ΔE resulting from unbinding is positive.

bound sites of a particle. At each step a randomly chosen particle is tested whether it is unbinding. To test for unbinding a random number between zero and 1 is chosen. If $e^{-nE/kT}$ is larger than this random number, the transition is accepted or otherwise rejected. This is similar to the procedure used by Shih and co–workers [155]. Correspondingly the higher the binding energy (E), the lower the probability for unbinding. When the procedure is repeated as often as there are particles on the grid, this corresponds to one timestep.

5.2.4 Movement of a particle

A particle that undergoes an unbinding transition is moved to a random nearest neighbour site on the lattice. If the site is occupied another neighbouring site is tried. Particles bound to others are considered to be stationary because of their larger weight. This corresponds to a form of the Multicentre Diffusion Limited Aggregation (standard aggregation models like Multicenter Diffusion Limited Aggregation are summarized e.g. in Saxton [152] and [153]) with a high concentration of immobile seeds. The assumption of immobility of clusters is a simplification. However, cross membrane interactions between proteins in adjacent grana discs are expected to restrict the mobility of clusters much more than that of single particles.

For non–spherical particles, e.g. particles with the shape of photosynthetic proteins, the exact calculation of their translation and rotation in a membrane is very difficult, and therefore some simplifications are needed. Accordingly, it is assumed that translation in all dimensions is equally probable. Furthermore, it is assumed that at each time step each particle rotates either -10° or +10°. That is, forces tangential to the body surface (viscosity of the matrix molecules) and forces normal to the surface (pressure–forces caused by momentum transfer between the particles and the matrix molecules) are not addressed directly but subsumed into the ratio of rotational energy/translational energy. This is somewhat arbitrary but the exact degree of rotation should not influence the general outcome.

Due to the long computing time required for all conditions only 2–3 different runs are averaged for each condition. However, a large lattice is used with many particles. Therefore the variability of different runs is not very pronounced. To illustrate the variability, the single results of the particle pair correlation function for the conditions showing the most variability are shown in Figure 5.5. This illustrates that the variability is reasonably small compared to the effects observed.

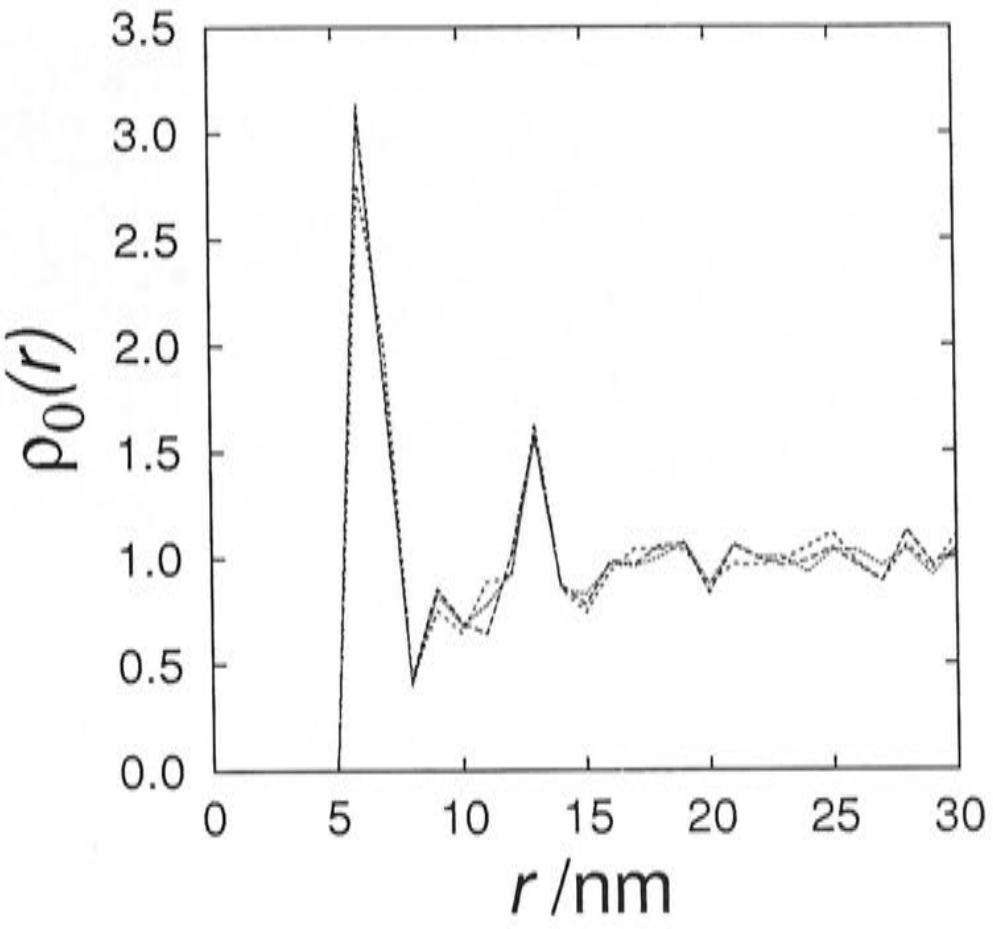

Figure 5.5: *Single (non–averaged) results showing the variability of different runs. The results of the three single runs are plotted. Runs under those conditions that show the most variability are shown. ρ_0 is the relative density of particles at distance r (for more detailed description of the axes see Section 5.3).*

5.3 Results and Discussion

5.3.1 Interacting spheres of the size of LHC II

The arrangement of homogeneous interacting spheres is investigated for different particle densities. Figure 5.6 shows the distribution of randomly placed spheres (corresponding to E = 0 kT) on a 200×200 square lattice. The diameter of a sphere is 6.25 nm.

In this investigation different interaction energies are examined. When two particles collide, they stick together until a particle unbinds. Because of its thermal energy a particle can unbind from its neighbours with the probability $e^{-\Delta E/kT}$. Particles placed randomly (E = 0 kT) on a lattice will thus rearrange until a steady–state is reached where the frequency of binding equals that of unbinding. This binding and unbinding leads to different patterns of arrangements according to the interaction energy. In Figure 5.7 particle arrangements are shown that result from the same initial distribution but using different interaction energies. From Figure 5.7 it can be seen that higher interaction energies lead to more ramified patterns whereas

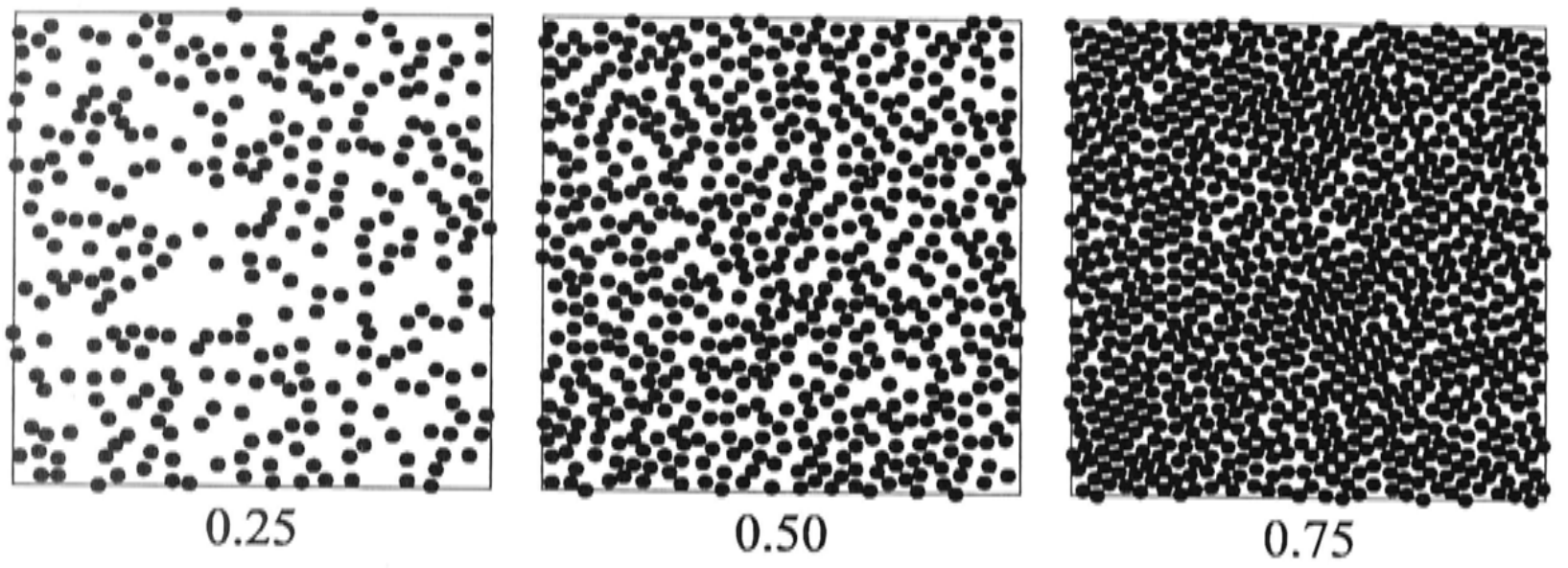

Figure 5.6: *Random distribution ($E = 0$ kT) of homogeneous spheres on a square lattice. The occupied area fraction is 0.25, 0.50 or 0.75. The diameter of the spheres is 6.25 nm and the lattice size is 200×200 nm.*

lower interaction energies result in more clustered patterns. This is in agreement with the results of Shih and co–workers [155] (see also [152] and references therein).

However, the human visual system tends to recognize order in any distribution. Therefore it is not a good referee for deciding if the particles are ordered in a certain way or more randomly distributed. Objective criteria are required for the analysis of particle distributions[d]. Typical approaches to distribution analysis are the nearest neighbour distribution analysis (NNDA) and the pair correlation analysis (PCA) [104]. The NNDA is computed for a given sample by determining the distance between a particle and its nearest neighbour for each of the particles. From the list of nearest neighbour distances the (accumulated) probability ($P_{acc}(r)$) of finding the nearest neighbour within the distance r is calculated and plotted versus r. Aggregated particles (attractive interaction forces) show a relative excess of small nearest neighbour distances while repelled particles with the same average particle density show a relative deficiency of small nearest neighbour distances. The NNDA is of course dependent on the particle density. Figure 5.8 shows that the higher the particle density the smaller the distance to the nearest neighbour. The diameter of a sphere is 6.25 nm, and so particles closer than 6 nm (c.f. the resolution of the lattice is 1 nm) cannot be found.

Figure 5.9 shows the influence of attractive forces between the particles. It can be seen that the probability of finding a neighbour in the close vicinity of the

[d]Experimental data have to be corrected for edge effects but the periodic characteristics of the lattice used in the simulation did not show edge effects.

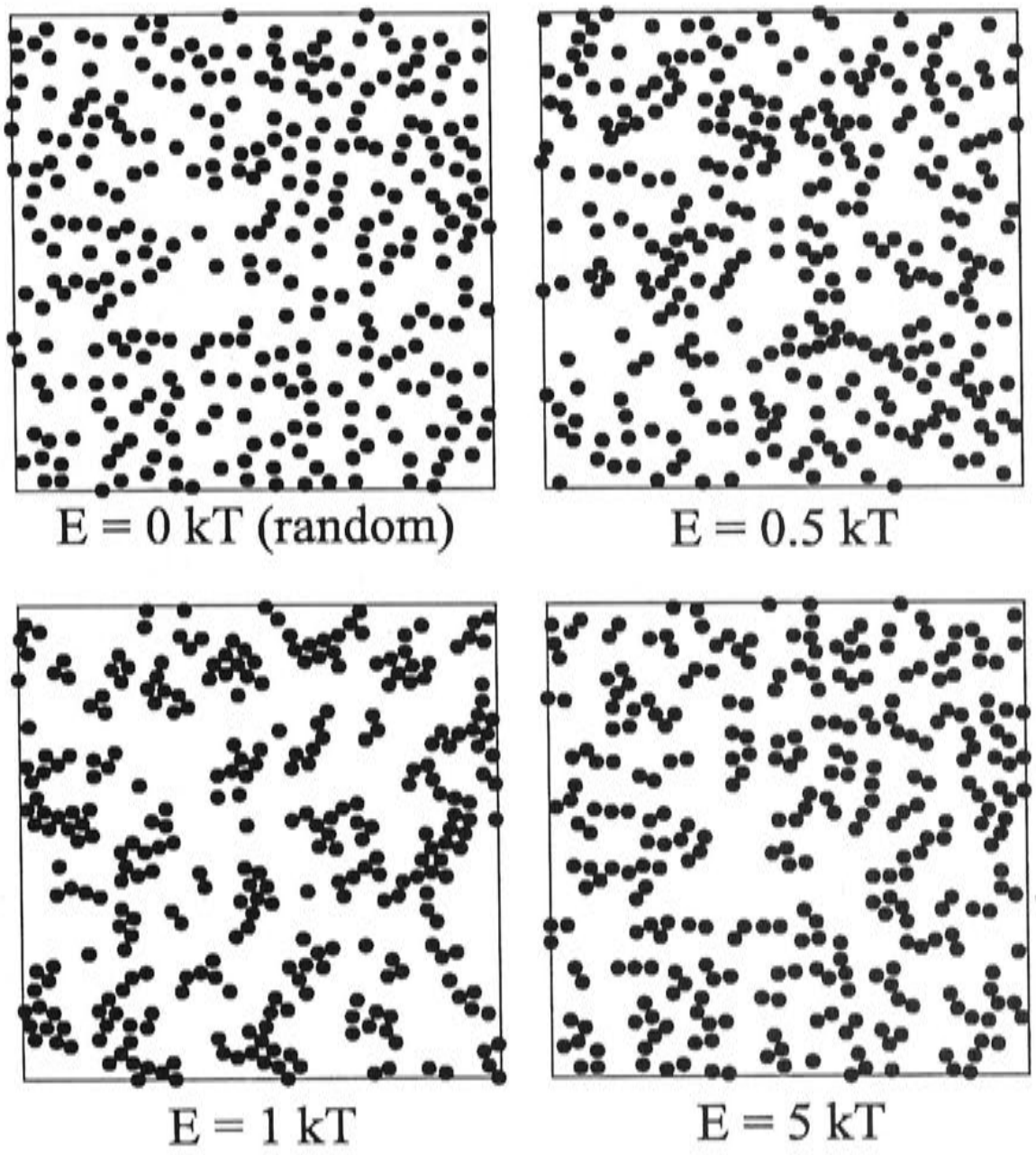

Figure 5.7: *Steady–state distribution of interacting spheres according to different interaction energies. The area fraction is 0.25 and the energies resulting in the arrangements shown are 0 kT (random), 0.5 kT, 1 kT, and 5 kT.*

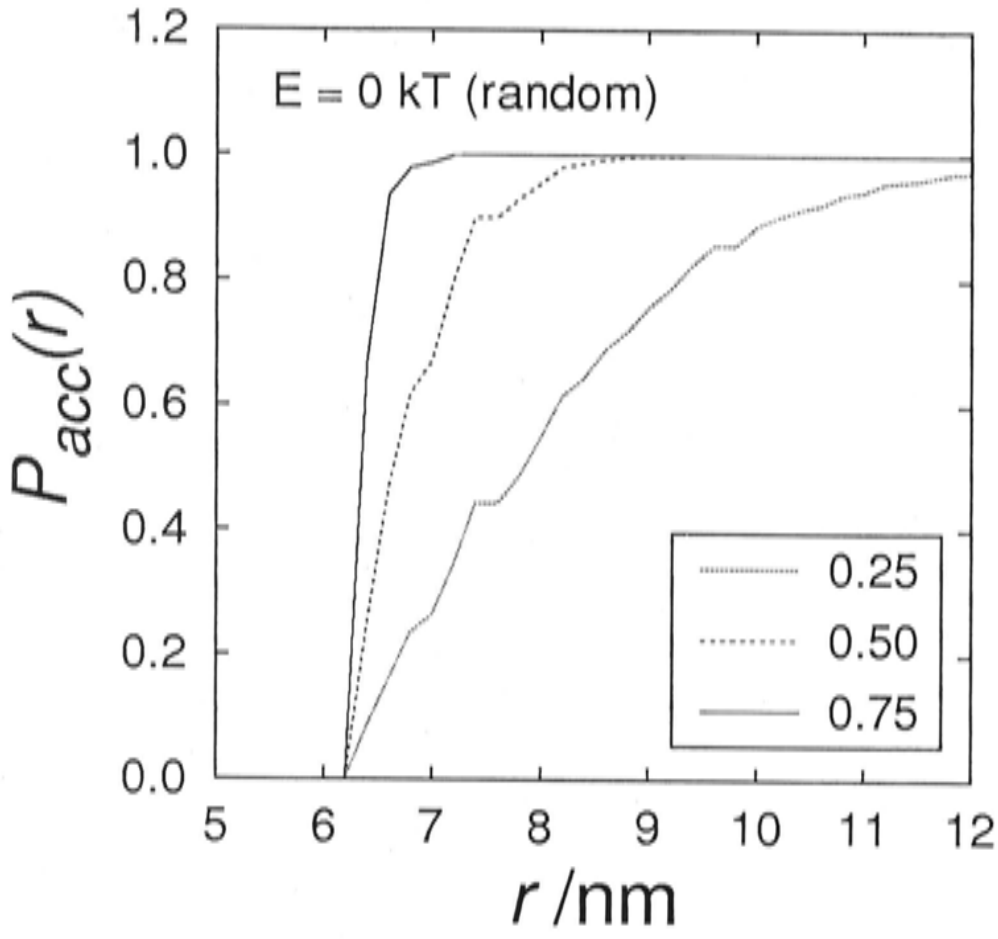

Figure 5.8: *Nearest neighbour distribution analysis (NNDA) for $E = 0\ kT$ (randomly distributed particles) with different particle densities. The y–axis shows the accumulated probability $P_{acc}(r)$ of finding the nearest neighbour within the distance r. The higher the occupied area fraction, the higher is the probability of finding a nearest neighbour in close vicinity. Because of the long computing time only 2 runs are averaged. However, due to the relatively large number of particles runs differ little from each other.*

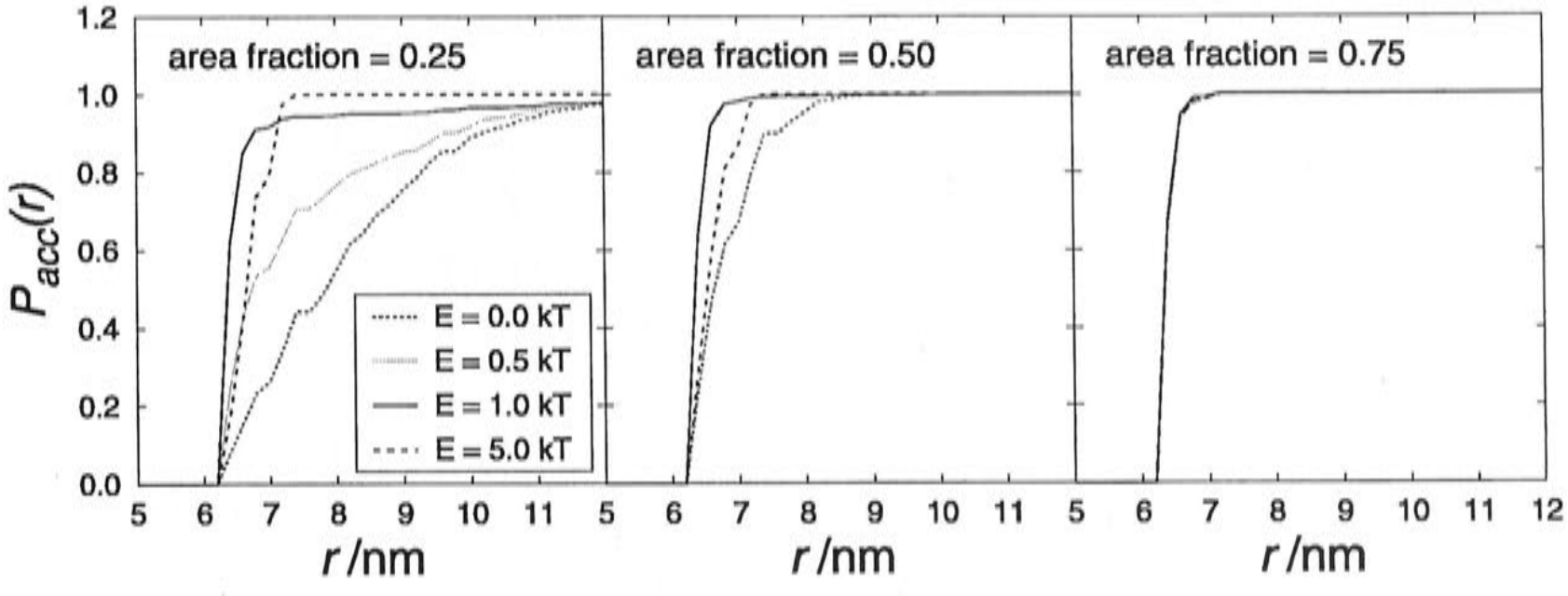

Figure 5.9: *Similar to Figure 5.8 but here the nearest neighbour distribution analysis (NNDA) is shown for interacting particles with different interaction energies and different particle densities.*

particle is increased for interacting particles reflecting more clustered arrangements. Interestingly, 5 kT and 10 kT (not shown) are less efficient than 1 kT in increasing the probability of finding a neighbour in a small distance. The difference between random distribution (E = 0 kT) and arrangements due to interaction becomes less pronounced for higher particle densities. For an occupied area fraction of 0.75 (see Figure 5.9, right) no difference can be seen between a random distribution and the distribution of interacting particles.

While the NNDA gives information about the distance of a particle to its nearest neighbour, the PCA allows the analysis of the relative densities, ρ_0, of particles in the vicinity of one particle. The PCA is computed for a given sample of particles by determining the mean number of particles ($n(r)$) found in a shell of radii $r - dr$ and $r + dr$ around an average particle. In other words, the resulting function $\rho_0(r)$ describes the deviation of the local particle density from the average density. ρ_0 is calculated in the following way (similar to the function described by McQuarrie [117]):

$$\rho_0(r) = \frac{n(r)}{\rho\pi((r+dr)^2 - (r-dr)^2)}, \tag{5.6}$$

with ρ = particle density

dr = 0.5 nm (lattice spacing = 1.0 nm)

Figures 5.10–5.15 show the PCA for different particle densities and varied interaction energies.

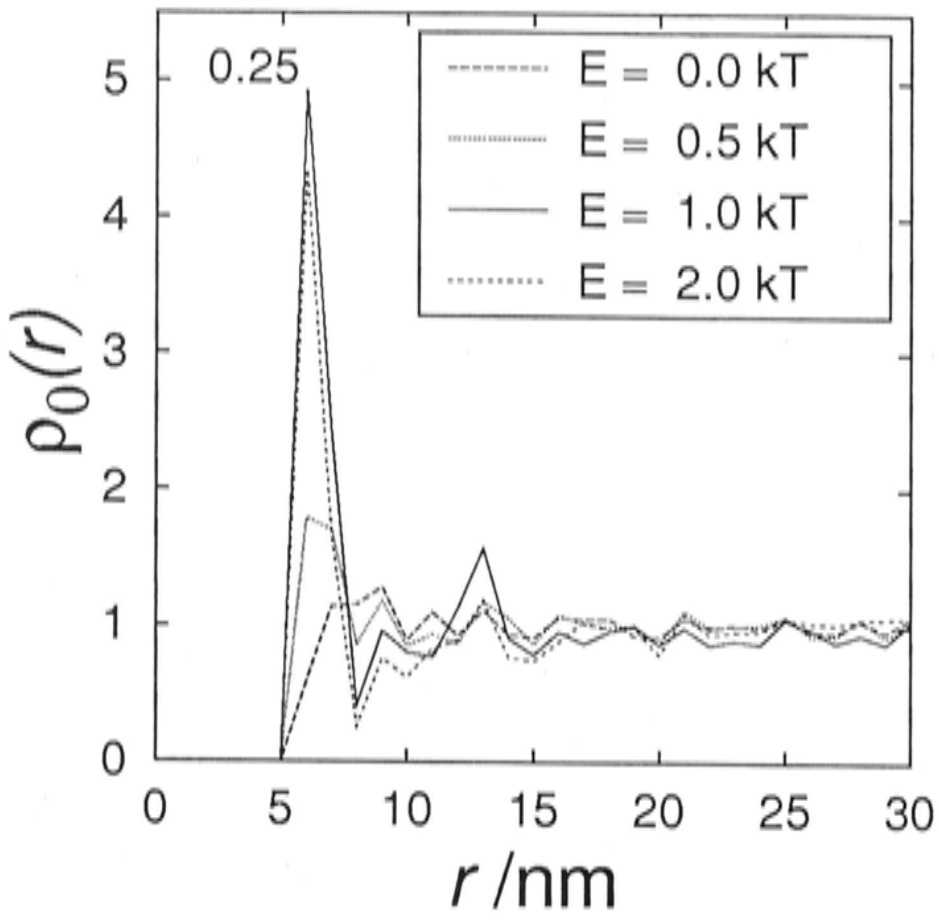

Figure 5.10: *Pair correlation analysis (PCA) for 0.25 area occupation. $E = 0$ kT (random) compared to energies of interaction of $E = 0.5$ kT, $E = 1$ kT and $E = 2$ kT. The y–axis shows the relative particle density $\rho_0(r)$.*

In Figure 5.10 it can be seen how interaction energies lead to a strong increase in particle density in the close vicinity of a particle. There is a pronounced maximum at 6 nm. The effect is less pronounced for 2 kT than for 1 kT. Once a particle is bound to another particle the probability for a particle to move is lower for higher interaction energies than for low interaction energies. Consequently, for higher interaction energies the probability of being trapped in a local minimum of the potential is higher than for lower interaction energies. Therefore low interaction energies are expected to lead to more clustered arrangements while higher energies are expected to lead to more ramified arrangements (local minimum) [155]. This effect can also be seen in Figure 5.7.

Figure 5.11 is similar to Figure 5.10 but shows the PCA for higher interaction energies (5 kT and 10 kT). For high interaction energies (5 kT, 10 kT) the increase in particle density near to other particles is much less pronounced. This is in accordance with the effect described above that lower energies lead to more clustered arrangements. Interestingly, the pronounced maximum (6 nm for 1 kT and 2 kT) is shifted to 7 nm. In Figure 5.12 three spheres are shown illustrating the two possible smallest distances to the nearest neighbour. In the linear position (upper left sphere to lower left sphere) the distance is 7 nm, due to the resolution of the lattice

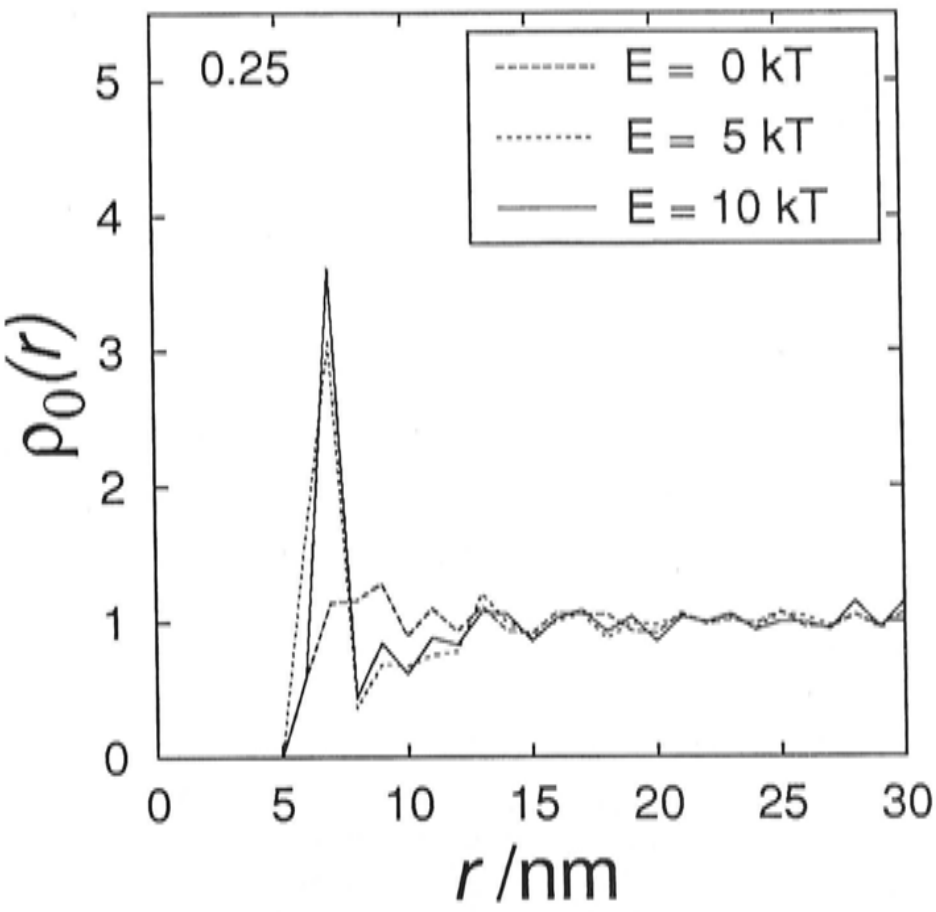

Figure 5.11: *Pair correlation analysis (PCA) for 0.25 area occupation, as Figure 5.10. $E = 0\ kT$ (random) compared to $E = 5\ kT$ and $E = 10\ kT$.*

(diameter: 6.25 nm, lattice spacing: 1 nm). In the angular arrangement (upper left sphere to upper right sphere) the minimal distance is 6.08 nm. Thus the shift in the maximum indicates that for higher energies particles are arranged in rather linear chains, whereas for lower energies particles are arranged in oblique angles.

It has to be noted here that the smaller distance in the case of angular orientation compared to linear orientation not only leads to a denser packing but also to a higher number of bound sites. If the particles are linearly arranged, only one binding site is occupied. In contrast, for an angular arrangement the nearest neighbour will occupy more than one binding site. Accordingly the algorithm used (together with the grid geometry) leads to a preferential orientation of the particles at an angle oblique to the square lattice. In the case of lower interaction energies the probability of a particle to 'find' this more optimal orientation is higher than for high interaction energies. Thus the lattice characteristics used may enhance the effect of low interaction energies compared to the effect of high interaction energies. Nevertheless, the principal behaviour is expected to be the same as for continuous areas[e].

---

[e]For square lattices using points instead of spheres and allowing interaction only between nearest neighbours, the preference of oblique angles will not occur.

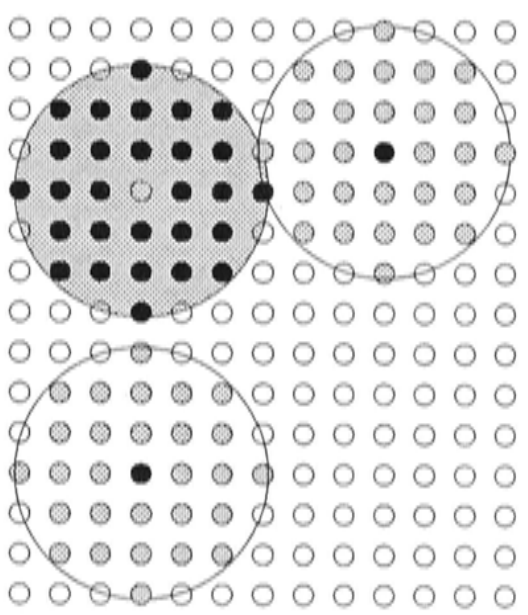

Figure 5.12: *Possible arrangement of nearest neighbours on a square lattice. Filled circles denote occupied lattice sites. The considered sphere is grey and lattice sites occupied by it are black. The lattice spacing is 1 nm and the diameter of the spheres is 6.25 nm. The distance in the linear arrangement (upper left sphere to lower left sphere) is 7 nm while in the angular arrangement (upper left sphere to upper right sphere) the distance is 6.08 nm.*

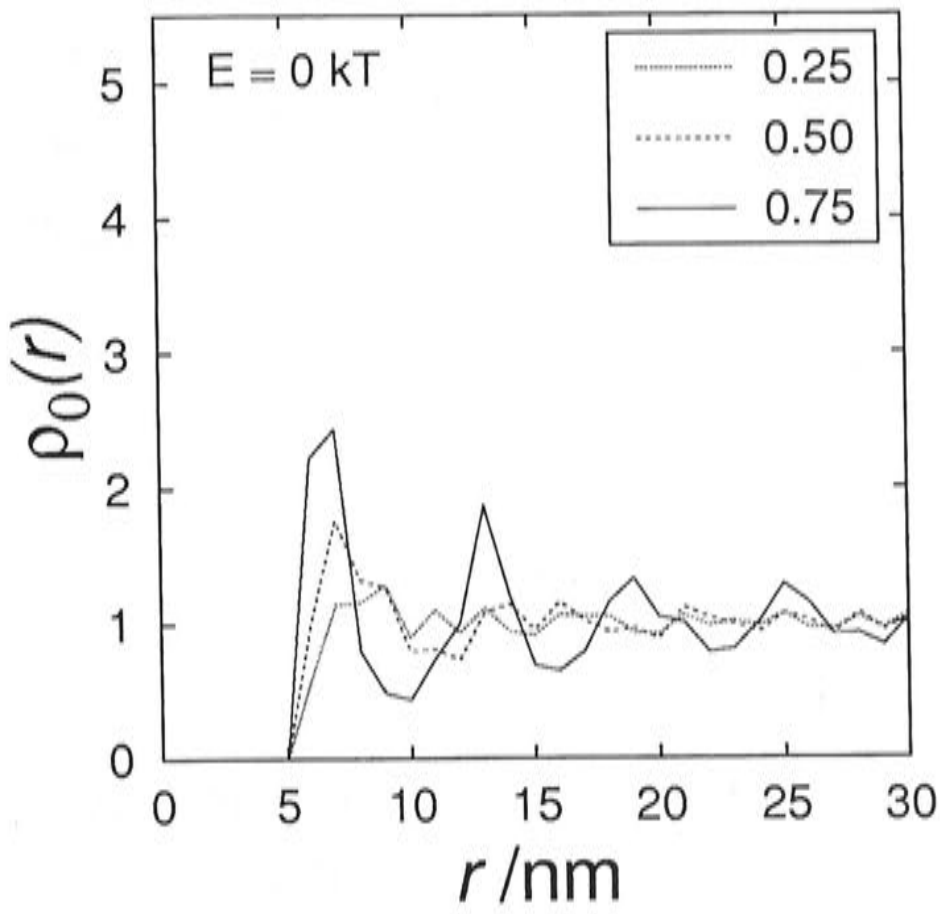

Figure 5.13: *Pair correlation analysis (PCA) for E = 0 kT (random distribution) with different area occupation.*

For 10 kT the effect of decreasing the nearest neighbour distance appears to be stronger than for 5 kT (see higher maximum for small r for 10 kT compared to 5 kT in Figure 5.11). This may, however, be attributed to the fact that in the present simulation clusters of particles are considered to be immobile. Immobile once bound to another particle, the particles will stay in their place instead of moving and forming longer chains. The artifact caused by the assumption of immobility of clusters is more significant for high interaction energies because unbinding becomes a rare event. Then small clusters will remain in place instead of forming larger chains. For high densities this artifact is less because unbinding does not often lead to movement e.g. if all neighbouring sites are occupied an unbinding particle cannot move.

It is interesting to investigate the density dependence of the PCA of randomly distributed particles (E = 0 kT). The results are shown in Figure 5.13. It can be seen that a high density without interaction energy may also have the effect of cluster formation. This reflects the 'organising effect of entropy'. As discussed earlier (see e.g. Section 1.2.4) entropy may lead to higher levels of organisation [132, 44, 35]. For an area occupation of 0.75, due to the high particle density, there are more possibilities to arrange the spheres in the lattice when they are ordered. For 0.75 occupied area fraction, oscillation around the mean density occurs. This reflects the

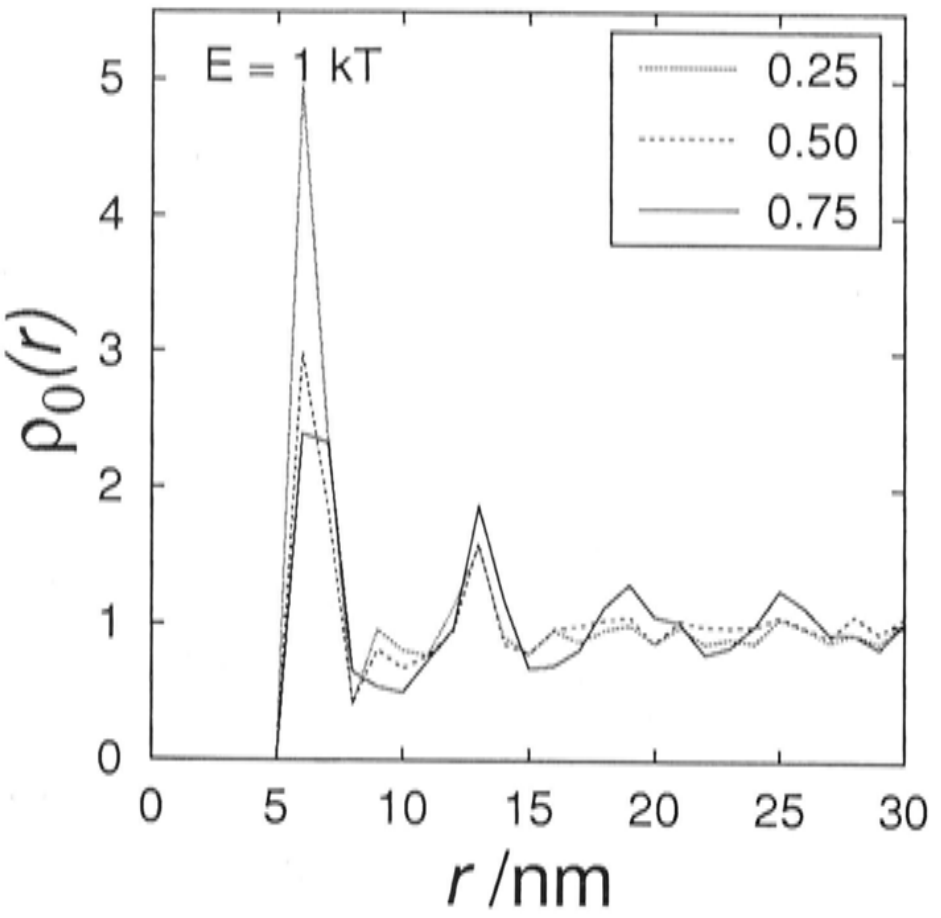

Figure 5.14: *Pair correlation analysis (PCA) for interacting particles (1 kT) for different particle densities.*

tendency of the spheres to be arranged in an ordered way, due to the high particle density. The most compact packing of spheres (hexagonal closest packing) in a continuous area is expected to result in an oscillating PCA. For larger distances, r, disturbances in the packing will become more probable and thus the oscillations will become broader and less extreme. On the other hand, the oscillations also reflect the periodic nature of the lattice. Due to the square characteristics, two different positions of a nearest neighbour are possible (6.08 nm and 7 nm, see also Figure 5.12). In a continuous area the the closest distance to a particle is simply its diameter (here 6.25 nm). Therefore the square nature of the lattice leads to broader peaks. For large r on the other hand, the grid nature of the simulation will have less effect as more and more combinations of possibilities occur for a particle to occupy sites oblique to the considered particle. However, comparing Figures 5.10 and 5.11 with Figure 5.13 shows that without interaction the peaks are relatively broad, whereas interaction energy leads to clearly distinct optima.

To illustrate the effect of the particle density, together with the interaction energy, the PCA for different densities and 1 kT interaction energy is shown in Figure 5.14, while Figure 5.15 shows the same for 5 kT.

For 1 kT (Figure 5.14) the clustering is most pronounced for an occupied area fraction of 0.25. For 0.50 area fraction the effect is smaller. For 0.75 area frac-

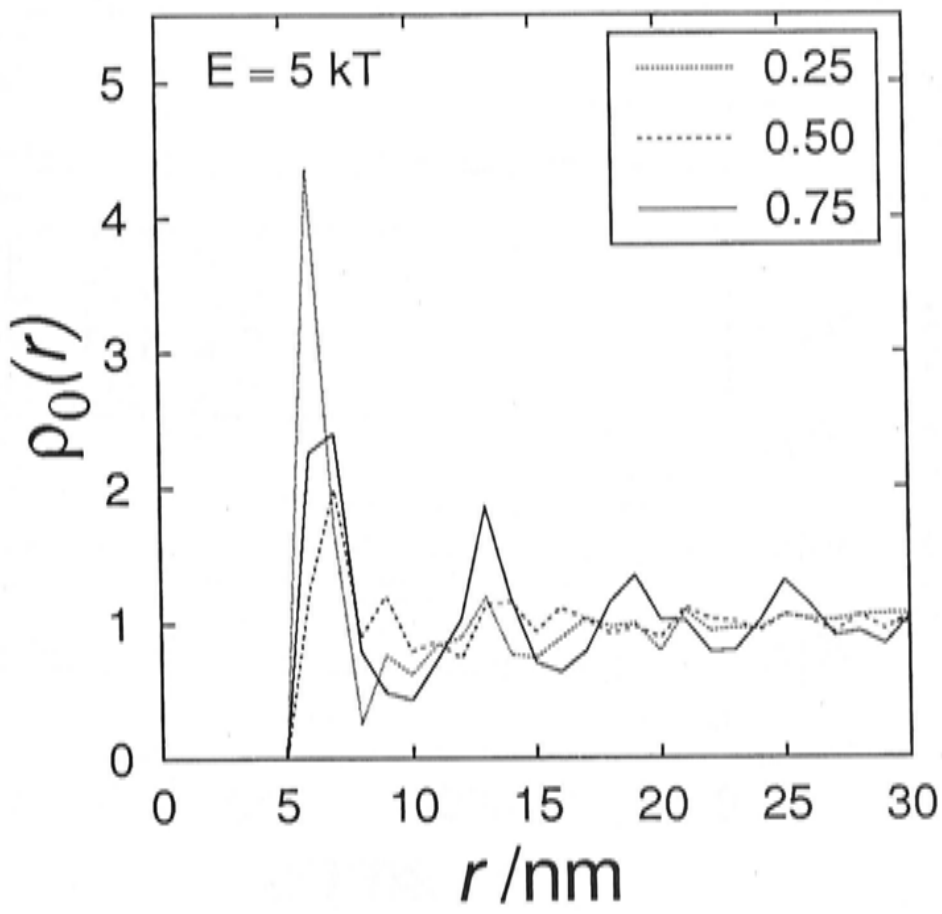

Figure 5.15: *Pair correlation analysis (PCA) for interacting particles (5 kT) for different particle densities.*

tion there is still clustering but it equals that for non–interacting spheres of the same density.

For 5 kT (Figure 5.15) the clustering is most pronounced for an occupied area fraction of 0.25 as is the case for 1 kT. However, for 0.50 area fraction the maximum of PCA at low r is less pronounced than for 0.75 area fraction. For 0.75 area fraction the PCA cannot be distinguished from that for random distribution (E = 0 kT) or for E = 1 kT.

In Figure 5.16 the number of bound sites (see also Figure 5.12) is plotted versus the number of Monte Carlo steps. All investigated particle densities are shown (0.25, 0.50 and 0.75). In accordance with the NNDA–analysis and the PCA–analysis the Figure shows that for an occupied area fraction of 0.75 the arrangement is rather similar, independent of the interaction energy. For an occupied area fraction of 0.50 and 0.25 Figure 5.16 shows that for higher interaction energies (2 kT, 5 kT, and 10 kT) less bound sites are formed than for E = 1 kT. In Figure 5.17 the number of bound sites in the equilibrium relative to that for E = 0 kT is plotted versus the interaction energy leading to the respective arrangement. In this Figure it can be seen clearly that the importance of interaction decreases with increasing particle density. Further the introduction of particle interaction with 1 kT results in many more bound sites, but further increase of the interaction energy leads to a decreased effect.

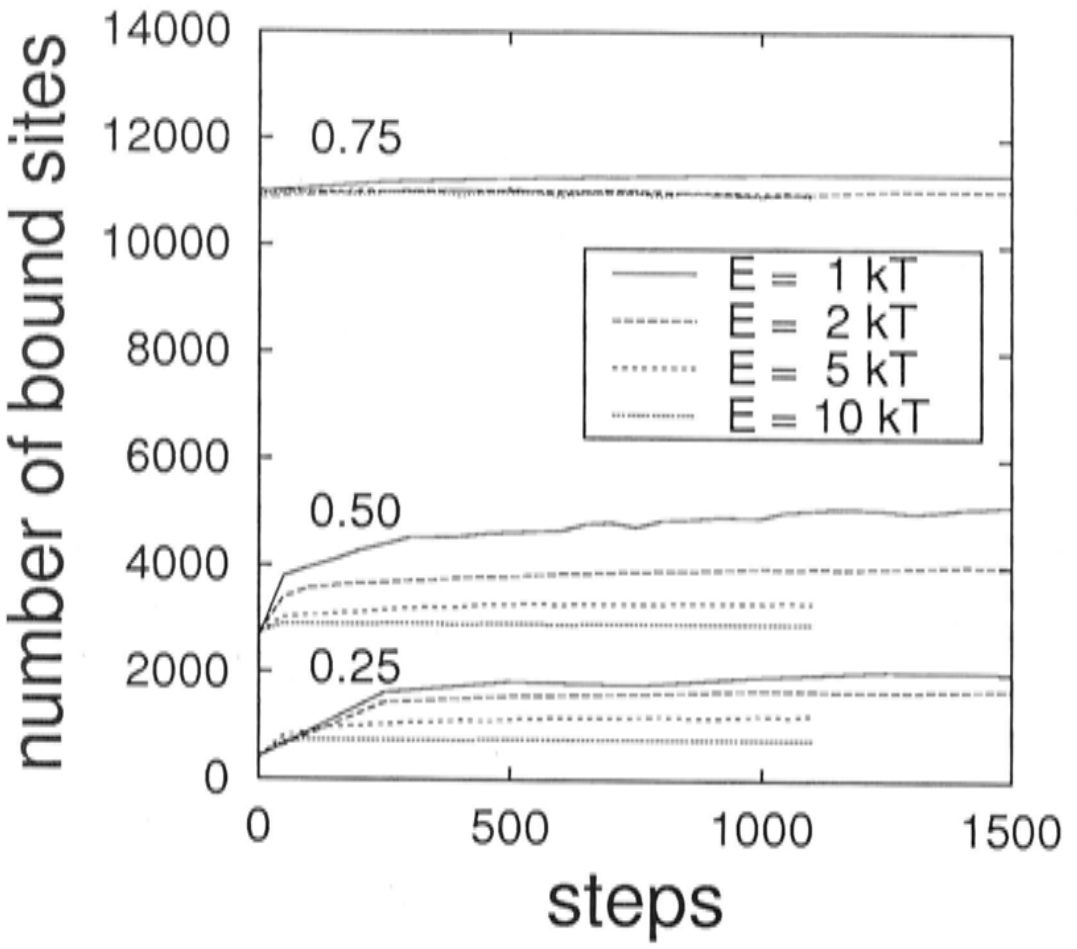

Figure 5.16: *Kinetics of the number of bound sites. Different interaction energies are considered and also different particle densities.*

5.3.2 Interacting and non–interacting spheres corresponding to LHC II and cyt *bf*

While there is some evidence that LHC II complexes interact with each other and with (parts of) PS II complexes it is unclear if cyt *bf* also interacts with other proteins. Therefore the influence of non–interacting spheres on the arrangement of interacting spheres is investigated. The investigations are carried out for an occupied area fraction of 0.50. The ratio of interacting : non–interacting spheres = 4:1. The arrangement of the particles for the random state (E = 0 kT) and E = 1 kT interaction energy is shown in Figure 5.18.

Figure 5.19 illustrates the effect of interaction energy on the PCA of both interacting spheres (top) and non–interacting spheres (bottom). For the PCA only particles of the same sort (e.g. interacting compared with other interacting spheres) are taken into account. Figure 5.19 shows that the behaviour of interacting spheres in the presence of non–interacting spheres is very similar to that in the absence of non–interacting spheres. The introduction of interaction energies leads to a higher density of interacting particles close to other interacting particles (low r). In contrast to that, the introduction of attractive forces between the interacting spheres leads to a shift of the peak of the PCA of non–interacting spheres to larger r. This shows that while interacting spheres tend to form clusters, the non–interacting spheres

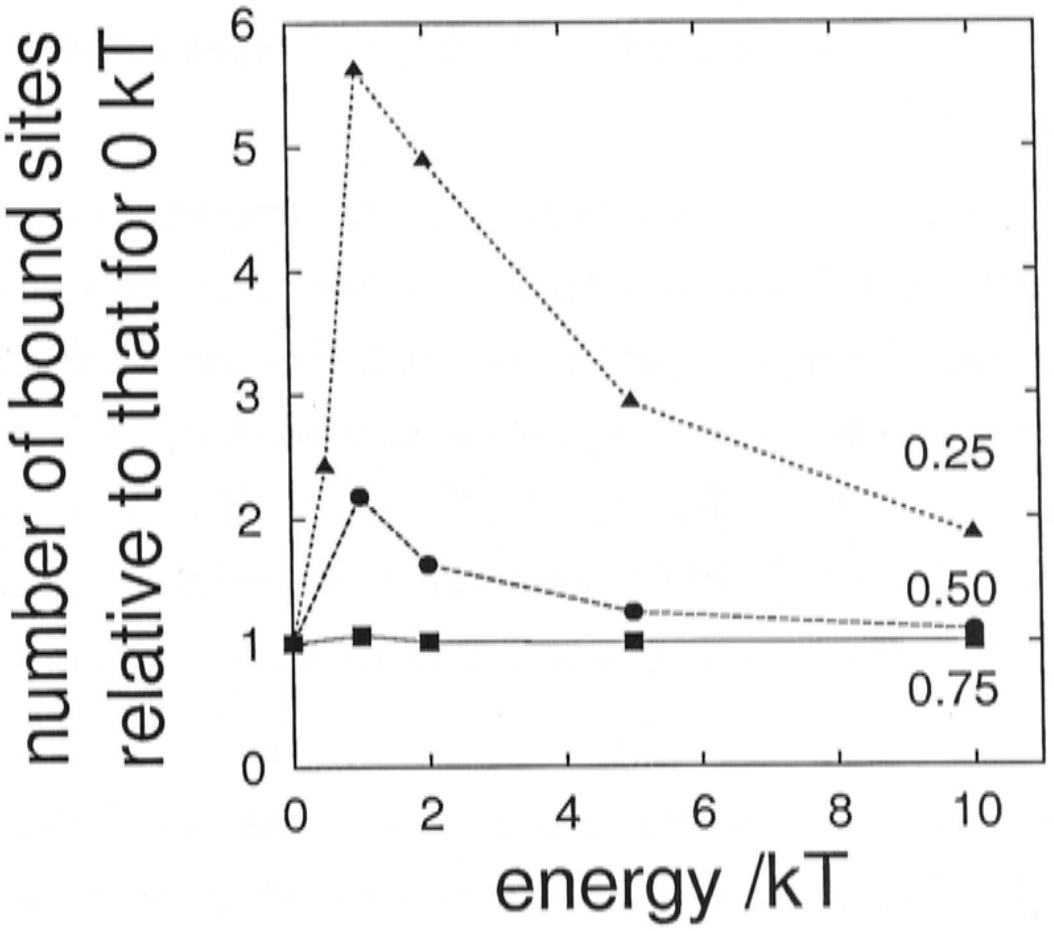

Figure 5.17: *Number of bound sites relative to that in for $E = 0$ kT. Numbers of bound sites are determined after the system has reached steady–state.*

tend to be kept apart by the interacting spheres.

As discussed above, for lower interaction energies the interacting particles form denser clusters. More compact clustering of the interacting spheres in turn leads to more free space for the non–interacting spheres. This may explain why the non–interacting particles show less tendency to be close together and the PCA is shifted towards higher r. The effects of interacting forces are less pronounced for higher interaction energies.

5.3.3 Influence of protein–protein interactions on photosynthetic electron transport

In this Section the influence of protein–protein interactions on particles exhibiting the shape of photosynthetic proteins is examined. An occupied area fraction of 0.65 is chosen. This is slightly below the value of 0.70–0.77 estimated in Chapter 4 for grana thylakoids. However, 0.65 is chosen because it is expected to be very close to the percolation threshold for immobile obstacles of the shape of photosynthetic proteins if no protein interactions are assumed (see also Chapter 4).

A random (E = 0 kT) arrangment of the particles is shown in Figure 5.20 together with the steady–state arrangement resulting from protein–protein interactions with

E = 5 kT. Due to the high protein density not much re–organisation of the particles is found (see Figure 5.20).

NNDA is carried out for closer examination of the arrangement of the particles. For the analysis only particles of the same sort are taken into account, i.e. for LHC II only other LHC II complexes are considered. The same holds for cyt *bf* and PS II. The examination with the help of NNDA revealed that, similar to interacting spheres, the accumulated probability ($P_{acc}(r)$) for a LHC II to have another LHC II in its vicinity is shifted towards lower distances r by protein–protein interactions (see Figure 5.21). For cytochrome *bf* and PS II no difference in $P_{acc}(r)$ is found (data not shown).

However, as the chosen area occupation is close to the percolation threshold for plastoquinone (PQ) diffusion it was investigated if PQ diffusion in the steady–state arrangement (shown in Figure 5.20 right) differs from that in randomly distributed proteins (Figure 5.20 left). In addition to the importance of PQ diffusion within thylakoids, the lateral diffusion of an inert tracer obstructed by the clusters is a sensitive probe of the aggregation [152]. The results are shown in Figure 5.22. It can be seen that the diffusion coefficient of PQ is slightly but significantly lower when interactions are introduced. Due to the long calculation time only three runs are averaged but PQ mobility was decreased to a significant extent in all single runs.

Perhaps a more important effect is illustrated in Table 5.1. In this Table the percentage of obstructed binding sites is shown. Clearly, protein–protein interactions

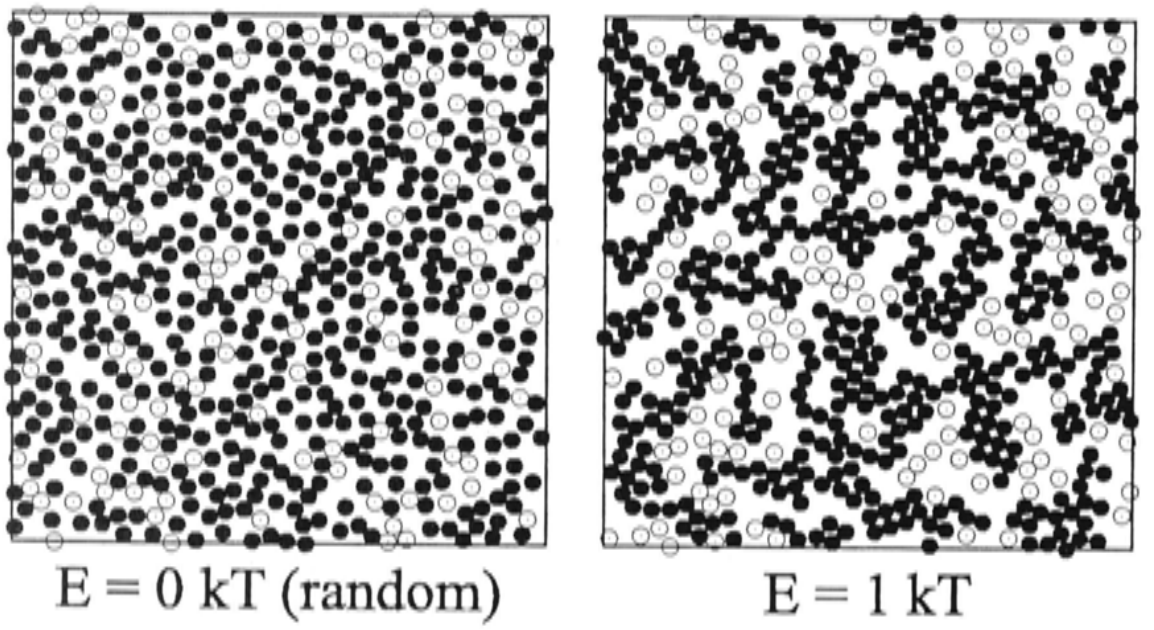

Figure 5.18: *Random ($E = 0\ kT$) and steady–state distribution of non–interacting spheres (open circles) and spheres interacting with $E = 1\ kT$ (black circles). The area fraction is 0.50.*

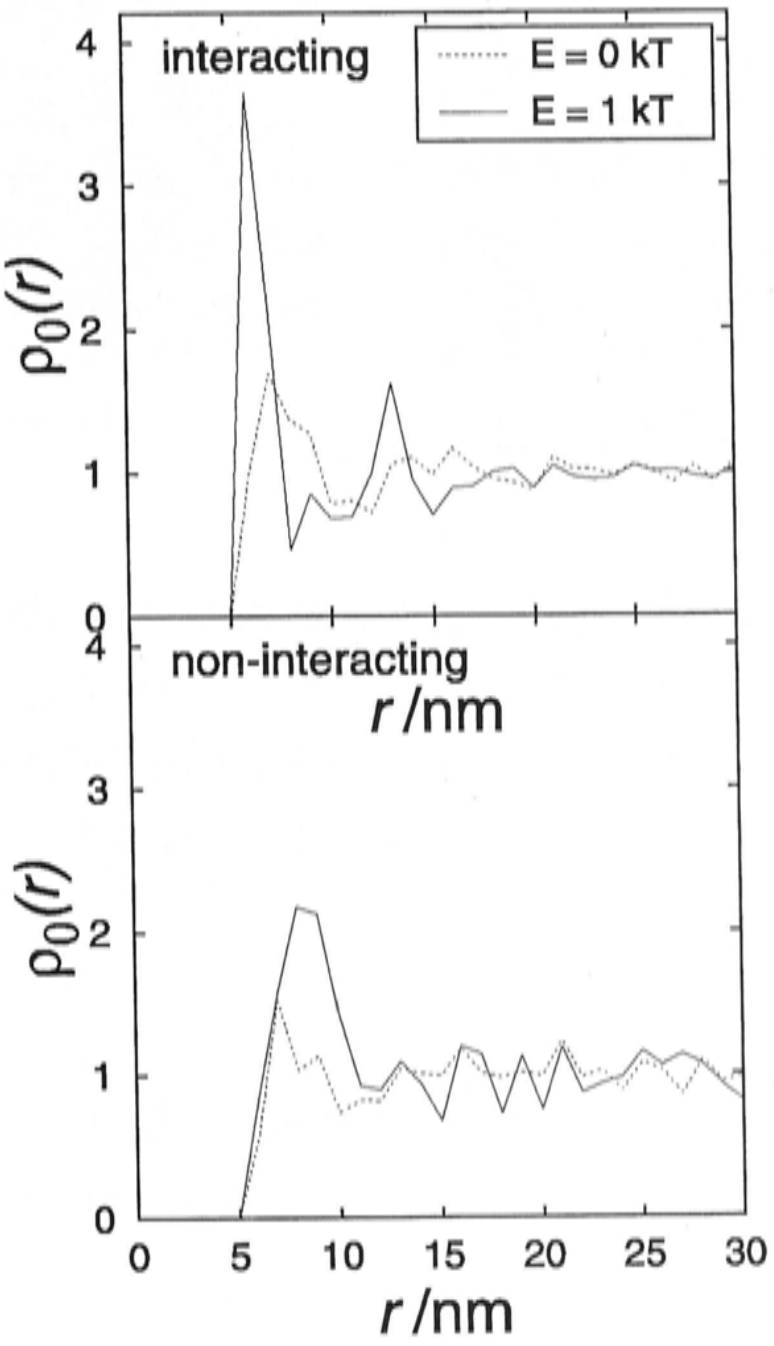

Figure 5.19: *Influence of non–interacting spheres on the arrangement of particles in the membrane. The area occupation is 0.50 and 20% of the particles are non–interacting. The PCA for $E = 0$ kT and the arrangement resulting from 1 kT interaction energy is shown. Top: interacting spheres (LHC II). Below: non–interacting spheres (cyt bf).*

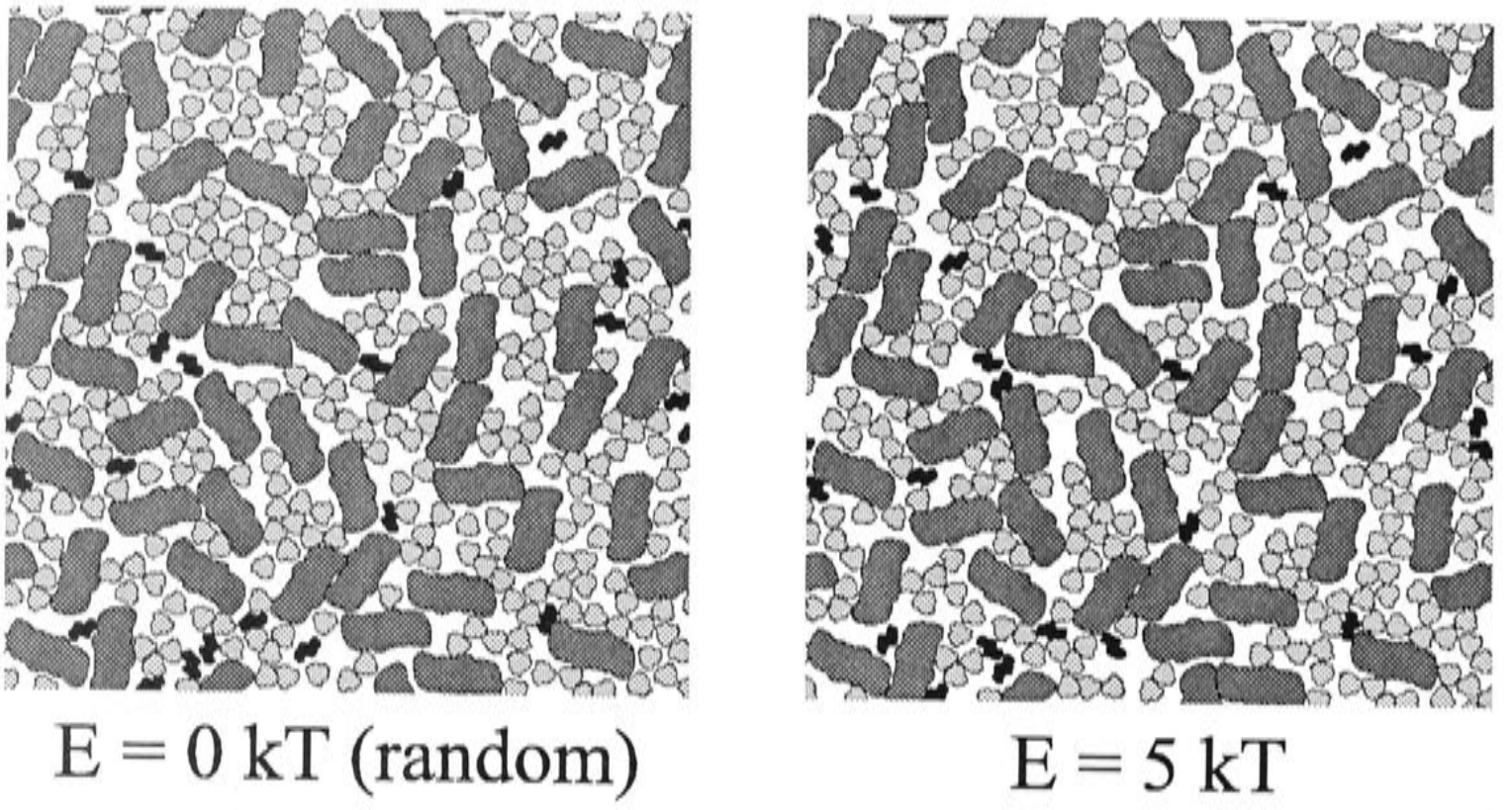

Figure 5.20: *Random (E = 0 kT) and steady–state distribution of photosynthetic proteins (E = 5 kT). Dark grey: PS II dimers, black: cytochrome bf dimers, light grey: free LHC II trimers. The stoichiometry of the complexes is PS II : cyt bf : LHC II is 2.6 : 1 : 14.1 and the occupied area fraction is 0.65.*

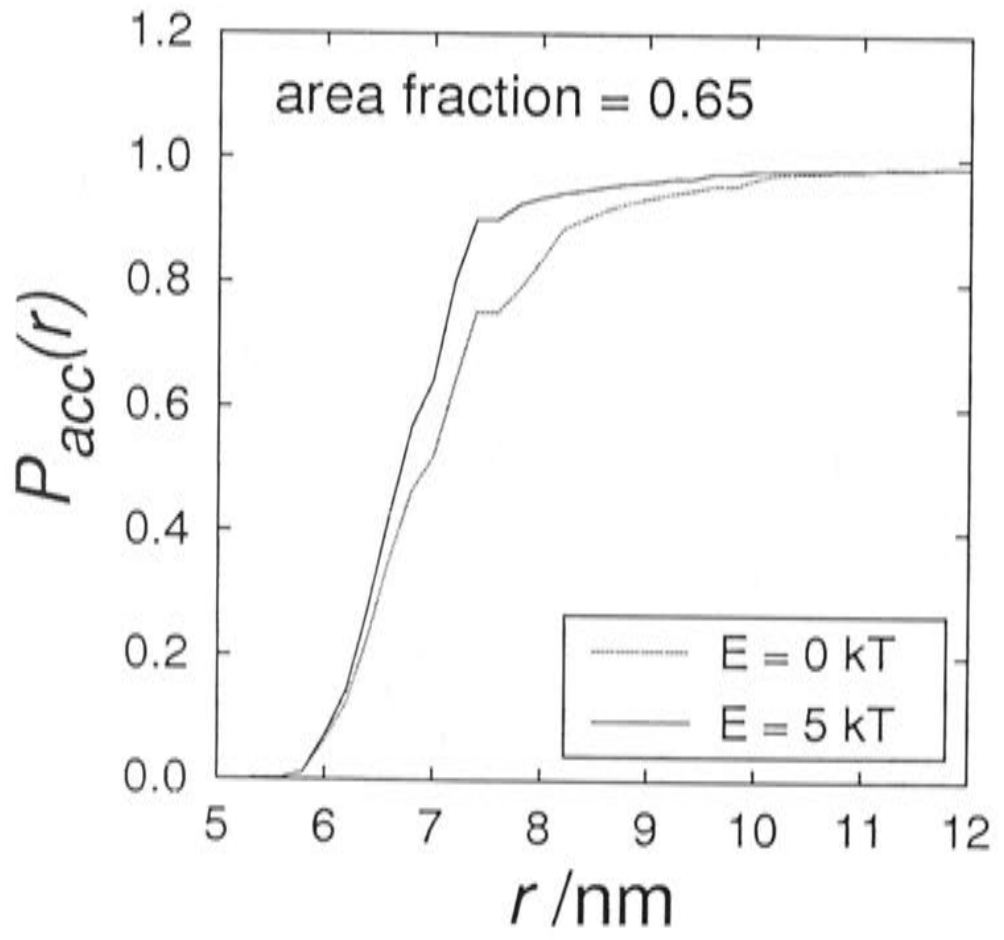

Figure 5.21: *Nearest neighbour distribution analysis (NNDA) for photosynthetic proteins. E = 0 kT and E = 5 kT. The occupied area fraction is 0.65.*

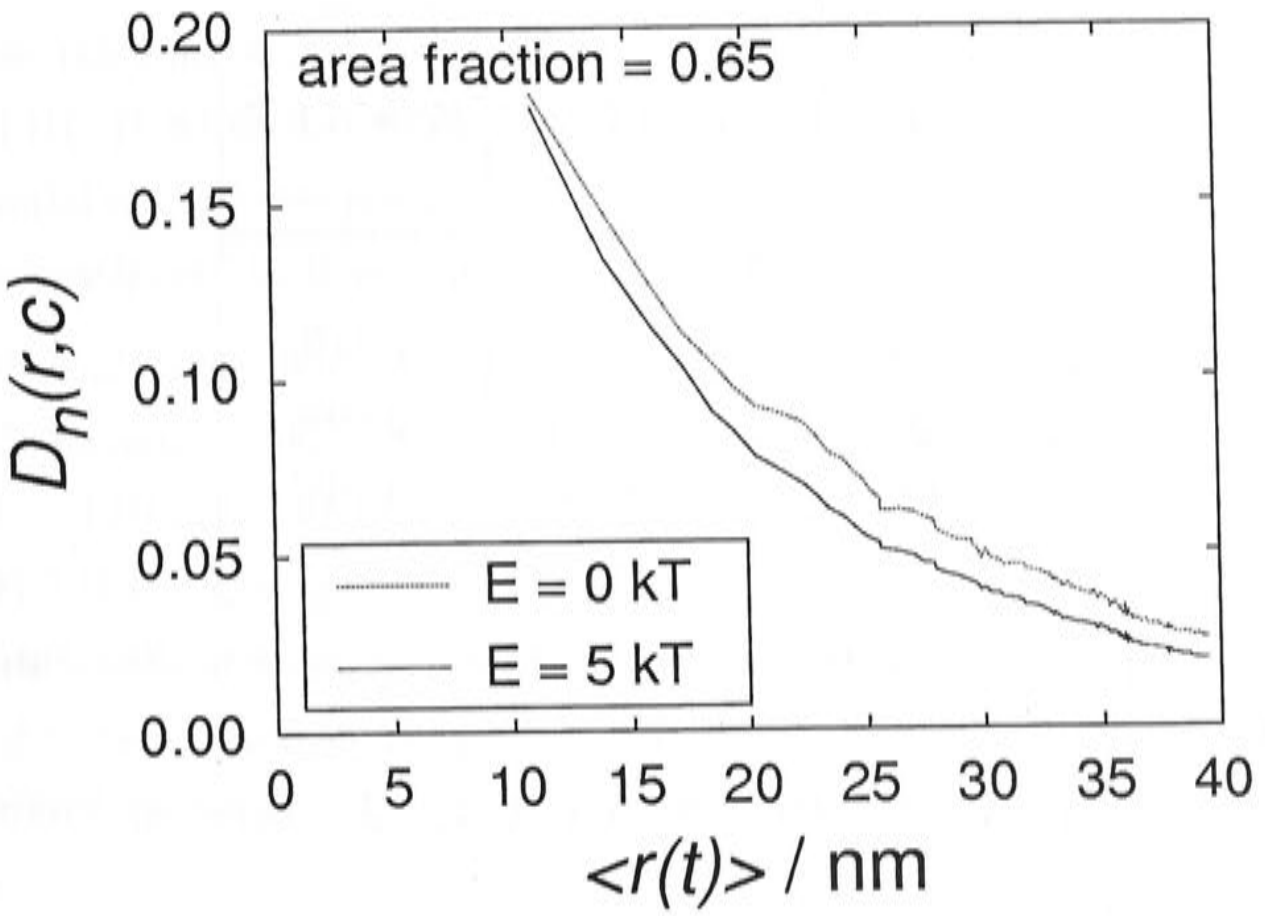

Figure 5.22: *Diffusion coefficient of PQ diffusing between randomly distributed (E = 0 kT) photosynthetic proteins and between photosynthetic proteins arranged as a result of protein–interactions (E = 5 kT). The occupied area fraction is 0.65.*

decrease the obstruction of binding sites.

5.4 Summary and Conclusion

The arrangement of interacting particles was studied. The nearest neighbour distribution analysis (NNDA) and the pair correlation analysis (PCA) were examined. The effect of interaction energies between particles on their organisation is of interest in the context of thylakoid architecture which in turn may have a pronounced influence on photosynthesis (see also Chapter 4). The arrangement of LHC II in the thylakoid membrane is of importance in understanding efficient energy–transfer between LHC II complexes. Furthermore, it was suggested by Kirchhoff and co–workers [96] that protein–protein interactions may lead to the formation of diffusion domains for plastoquinone. Therefore in this Chapter effects of interaction between particles (proteins) are investigated.

Firstly, the effects of different interaction energies and particle densities on the arrangement of interacting spheres are discussed. Secondly, the influence of non–interacting particles 'disturbing' the organisation of interacting particles is considered. Finally, it is examined how LHC II–LHC II and (PS II–$(\text{LHC II})_3)_2$–LHC II

binding site	E = 0 kT	E = 5 kT
Q_B	13.10%	7.74%
Q_o	2.27%	0.00%
Q_r	9.85%	3.79%

Table 5.1: *Percentage of obstructed binding sites in a random distribution and in a distribution resulting from $E = 5$ kT. Occupied area fraction: 0.65. Q_B: binding site on PS II, Q_o: oxidising binding site on cyt bf, Q_r: reducing binding site on cyt bf.*

interaction may influence plastoquinone diffusion and thus electron transport.

The results of Section 5.3.1 show that the arrangement of interacting particles is highly dependent on the interaction energy (see Figures 5.7, 5.9–5.11, 5.16, and 5.17). Lower interaction energies (1 kT, 2 kT) lead to a more clustered particle distribution whereas higher energies (5 kT, 10 kT) result in ramified chains. This is in accordance with the results of Shih and co–workers [155].

However, the arrangement of the particles is not only dependent on the interaction energy but also on the particle density (see Figures 5.6, 5.8, 5.13–5.15). The ordering effect of high particle densities is very similar to that of interaction energies. Both lead to a steeper increase in the NNDA and higher PCA at low r, i.e. generally a higher probability for one particle to be close to another. The higher the particle density the lower is the effect of interaction[f]. For occupied area fractions of 0.75 the arrangement of the spheres is independent of the interaction energy. This is interesting because in thylakoids the area occupied by proteins is around 0.7. Therefore interaction energies may not have a strong influence on the thylakoid architecture. However, using only homogeneous interacting spheres with binding sites all around the surface is a very crude simplifying assumption for the modelling of thyalkoids

[f]It has to be noted here that Saxton showed another effect of density on the distribution of interacting particles. In his (irreversible) cluster–cluster aggregation model he showed that clusters forming at low densities are more extended than those formed at high density as reflected by the higher fractal dimension of the latter [152]. However, in his investigations much lower particle densities were investigated than in the model presented here.

and further refinement is needed. The interacting spheres used in the simulation resemble LHC II which is rather spherical and of similar size to the spheres used in the simulation. Consequently these simulations are more suited to describing LHC II reconstituted in liposomes than in thylakoids.

In thylakoids not all photosynthetic proteins may be modelled by interacting spheres of the same size. Among the photosynthetic proteins, PS II is very large compared to LHC II. Therefore, using the same area fraction, more space may be left for LHC II to take the tortuous path between non–interacting proteins until it binds to an interacting protein (compare also Chapter 4). In addition not all photosynthetic proteins may interact with other proteins. For example for cytochrome *bf* nothing is known about interactions with other proteins. Furthermore the largest complexes, here referred to PS II, are in fact PS II with tightly bound LHC II (((PS II)–(LHC II)$_3$)$_2$). Therefore they are expected to interact with free LHC or other LHC II tightly bound to PS II. However, ((PS II)–(LHC II)$_3$)$_2$ probably does not interact on its whole surface but rather where the LHC II is located.

Therefore the simulation is refined step by step. First the simulation is extended to account for non–interacting particles. The results are shown in Section 5.3.2. The non–interacting spheres are assumed to be of the same size as the interacting spheres. This is assumed because the sizes of LHC II (interacting) and cyt *bf* (probably non–interacting) are in the same range. It has to be noted that the ratio interacting : non–interacting spheres used in the simulations does not reflect the stoichiometries of the photosynthetic proteins. In this Section the principal effects are investigated and the relatively large proportion of non–interacting spheres is chosen because it was expected to lead to clearer effects. As can be seen in Section 5.3.2 non–interacting spheres do not alter qualitatively the behaviour of interacting spheres. In contrast non–interacting spheres are influenced by interacting spheres. The relative density of non–interacting particles becomes higher at larger distances from each other (larger r). This shows that while interacting spheres tend to form clusters, the non–interacting spheres tend to be kept apart by the interacting spheres. In thylakoids this could lead to a more homogeneous distribution of the non–interacting cyt *bf*. This may be of importance because cyt *bf* is involved in the rate limiting step of photosynthesis, the PQH_2 oxidation. In thylakoids densely packed with proteins PQH_2 diffusion may be severely restricted (see also Chapter 4). Therefore the distribution of cyt *bf* in the thylakoids may be of importance.

As a second step the influence of interaction between LHC II and parts of PS II

is examined taking into account the realistic shape of the proteins. Due to the high density of proteins in the thylakoids the introduction of protein–protein interactions does not exert a strong effect on the arrangement of the proteins. However, PQ diffusion is influenced by the interactions: compared to the diffusion in randomly arranged proteins the diffusion coefficient of PQ is decreased when protein–protein interactions are introduced. On the other hand the percentage of binding sites obstructed by proteins is significantly reduced in the presence of protein–protein interactions. Since cyt *bf* is not likely to interact with other proteins, it is expected to be much more mobile than interacting proteins. Accordingly the probability for a binding site on cyt *bf* to be obstructed permanently is low. PQH_2 oxidation at cyt *bf* is considered to be the rate–limiting step in electron transport. Taking that into account, interaction energies resulting in a more homogeneous distribution of cyt *bf* and an increased accessibility of the binding sites may play an important role in electron flux. This holds particularly if PQ diffusion is restricted. On the other hand protein–protein interactions may indeed increase the retarding effect of the high protein density in thylakoids.

5.4.1 Outlook

As described above, each particle was required to unbind (according to the probability $e^{-nE/kT}$) before it was allowed to move to a random neighbouring site. However, it may be that after such a movement the particle is actually bound tighter than it was before. Therefore it may be a useful refinement to calculate the binding energy, then in a second step search for a site to which the particle could move and thirdly evaluate the probability for this step to occur according to $e^{-n(E_{after}-E_{before})/kT}$. On the other hand such a refinement might only lead to a faster approach to steady–state, but not change the basic characteristics.

Another refinement could be to allow the clusters to move. However, as discussed together with the results, this should not alter the result significantly (especially for high protein densities and/or high interaction energies).

Chapter 6

Monte Carlo simulation of electron flux

Contents

6.1 Introduction

Photosynthetic electron flow involves the integral complexes of photosystem II, cytochrome *bf*, and photosystem I which operate in series via the mobile plastoquinone and plastocyanin. In principle the problem of electron transport between PS II and cyt *bf* is equivalent to that of ubiquinol diffusion and its oxidation at the cytochrome bc_1 complex in bacterial and mitochondrial electron transport. However, in thylakoids of higher plants the two photosystems are laterally separated. PS II is located in the grana core whereas PS I is located in the grana margins and the stroma lamellae ([14, 11, 164, 20, 1, 2], see also Section 1.2). As a consequence diffusing electron carriers, mediating electrons between the photosystems and cyt *bf*, are required to travel the distance of ca. 200–250 nm between the centre of the grana and the margins. There is no general agreement on which of the two mobile carriers, plastoquinone or plastocyanin, is responsible for long range electron transport (see also Section 1.2.5).

Most published models on electron transport assume a common plastoquinone pool shared by all PS II[a]. A shared plastoquinone pool implicitly assumes fast plastoquinone exchange throughout the membrane. In Chapter 4 it is shown that long range diffusion of plastoquinone in thylakoids may be severely restricted by the integral proteins. Therefore in this Chapter electron transport is modelled using a Monte Carlo approach incorporating realistic protein shapes (without protein–protein interaction). The complexes consist of PS II with tightly bound LHC II [74], cyt *bf* [31], and free LHC II [105] randomly distributed within the membrane (see also Chapter 4). Plastoquinone diffuses between these integral proteins.

However, the contribution of the diffusion to reaction kinetics of the electron transport is not only determined by the diffusion coefficient of plastoquinol but also by the binding mechanism. Therefore two different binding mechanisms are investigated: tight binding and a collisional mechanism. The tight binding mechanism includes an irreversible binding of PQ to the Q_o site of cyt *bf* before its slow oxidation takes place. The collisional mechanism implies immediate electron transfer after a successful encounter. Both mechanisms lead to an exponential decay with the same rate constant k when diffusion processes are not limiting. In thylakoids however, where diffusion may be highly restricted, the two mechanisms are expected to

[a]The model of Mitchell and co–workers [124] is one model considering possible consequences of thylakoid architecture on electron transport.

lead to a different behaviour. Therefore both mechanisms are tested with the model and the results compared.

The experimental approach to the role of the diffusion of plastoquinol is to follow the reduction of P700, the reaction centre chlorophyll of PS I, by electrons induced by a flash at PS II. This is a convenient method of accurately measuring whole–chain electron transport. The rate constant of the sigmoidal reduction kinetics and the initial lag give information about the rate–determining oxidation of plastoquinol [167] and reactions preceeding this step [70], respectively.

The experimental data obtained are then compared with the results of the simulation. An attempt is made to match the measured data by varying rate constants used in the simulation. A similar approach was chosen by Mitchell and co–workers [124]. Electron transfer at cyt *bf* is modelled according to an obligatory Q–cycle as described in Section 6.2.

6.2 Methods

6.2.1 P700 re–reduction

Monitoring the oxidation state of the primary donor P700 of photosystem I (PS I) via near infra–red absorption spectroscopy provides valuable information on PS I–driven photosynthetic electron transport in vivo (see [98] and references therein). Detection of the redox changes of P700 in the region of the $P700^+$ cation radical absorption band peaking at 820 nm has basically three advantages: (1) measuring light > 800 nm is not absorbed by thylakoids, (2) near infra–red has no actinic effect on photosynthesis of green plants and (3) there is no interference from chlorophyll fluorescence. Near infra–red measuring light allows the application of high intensity with the advantage of a high signal/noise ratio. In order to discriminate the measuring light from continuous background light the former usually is modulated.

Thylakoids are isolated as described in Section 3.2. The flash–induced kinetics of P700 re–reduction were measured with the Dual–Wavelength Emitter–Detector Unit (ED–P700DW, Heinz Walz GmbH, Effeltrich, Germany) in combination with a standard PAM Chlorophyll Fluorometer (PAM 101, Heinz Walz GmbH, Effeltrich, Germany) (see also Figure 6.1). Saturating light flashes are applied with a single turnover flash lamp (XST-103, Heinz Walz GmbH, Effeltrich, Germany). Continuous weak far–red light of ca. 17 W/m^2 ensured that all the components between

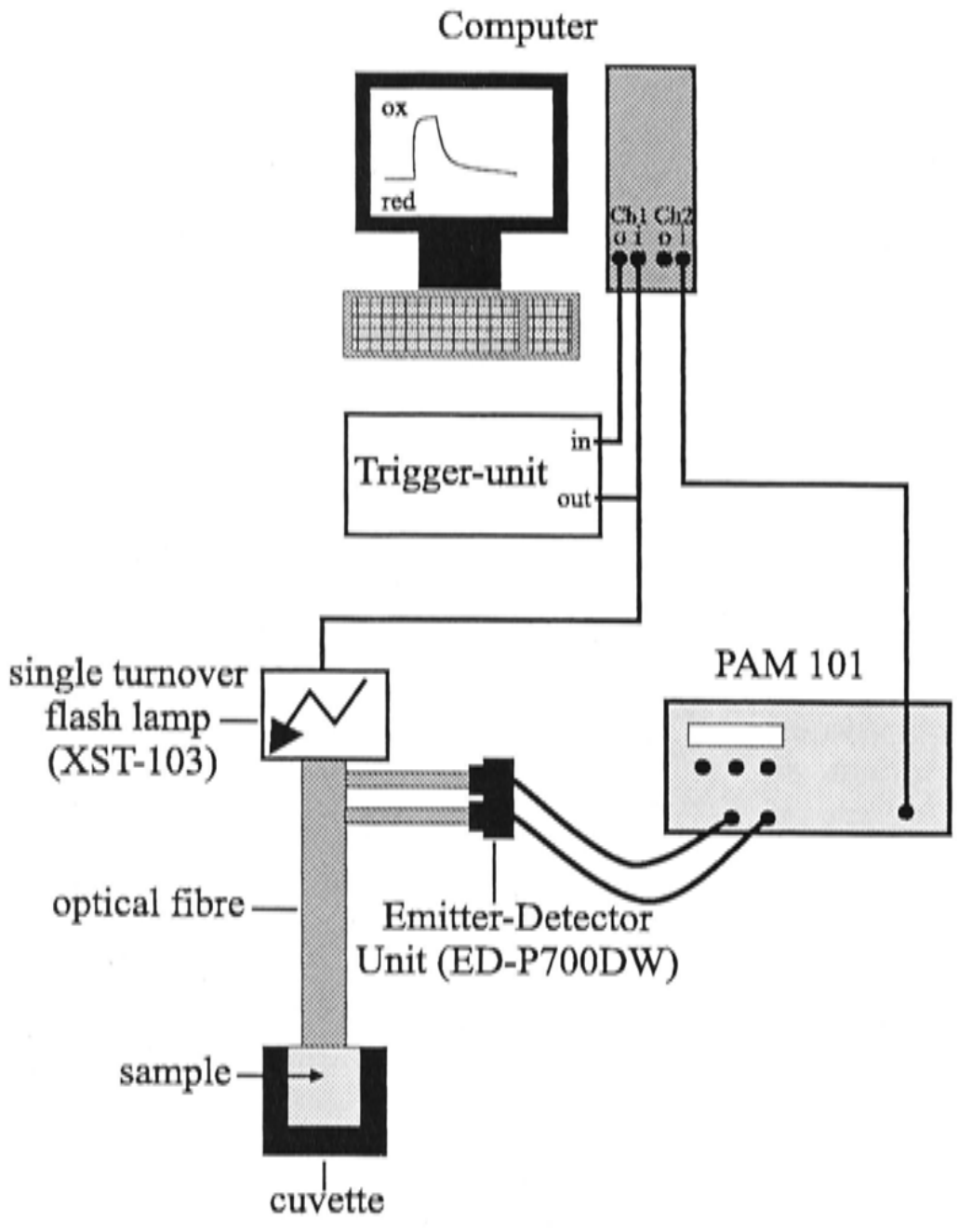

Figure 6.1: *Schematic diagram of the experimental setup.*

the two photosystems were oxidised between flashes. The background light was checked to ensure that it did not measurably increase the amount of oxidised P700. Twenty flashes were applied on the same sample and averaged. This was repeated with the same sample 6–7 times (e.g. 120–140 flashes). A time of 5 s between two measurements allowed for relaxation of the samples. The averaged 20 flashes were then checked for ageing effects. Usually measurements of up to 100 flashes did not show significant ageing. The measurements were repeated with a fresh sample and another series of flashes applied. To obtain the data that are matched with the model the kinetics of three different samples are averaged. The frequency of data acquisition was 25000 Hz.

The data acquisition and triggering was carried out with the help of a LabVIEW–program (**Lab**oratory **V**irtual **I**nstrument **E**ngineering **W**orkbench, version 6.1, Copyright 2000 National Instruments Corporation). For the measurements a commercially developed program (von Kruedener und Danckwerts Meß– und Prüfsysteme, Kürten, Germany) was modified to run on another computer. It was further

tailored for the measurements described in this Chapter. A delay between trigger signal and data acquisition was incorporated to allow for the timing of trigger signal and acquisition. Additional modifications involved the hardware control (triggering) and file handling. At the start of the progam a trigger signal is sent to a trigger–unit. After the chosen delay the data acquisition is started. After receiving the trigger signal from the program, the trigger–unit sends a trigger signal to the flashlamp and to the computer. A delay between the trigger signal from the program and the trigger–output of the trigger–unit can be chosen. This together with the ability to choose a delay in the program, enables fine–tuning of the timing between trigger signal and data acquisition. Hence it is possible (1) to send the trigger signal from the program to the trigger–unit, (2) to start the data acquisition and (3) to trigger the flash light. This ensures that the very first data of the P700 re–reduction can be measured.

A problem occurred with the triggering of the light flash. It turned out that the commissioned program showed inaccuracies of ca. 2 ms. This is far too great for the highly time–resolved measurements presented here. Therefore the trigger pulse is measured with a second channel and the offset between the trigger–time of different measurements is calculated with a cross correlation [86]. The offset so obtained is then substracted from the actual measurements. The method of cross correlation works well with the trigger signal as it has a very simple rectangular shape[b].

6.2.2 The simulation

The basic simulation is similar to that described in Chapter 4. However, the protein–objects are now extended to include binding sites for redox reactions. Similarly the plastoquinone (PQ)–objects are extended to have a state, reflecting their redox state.

6.2.3 The protein–objects

Accounting for the dimeric character of PS II and cyt *bf* each protein–object has two binding sites. Each binding site can be in two states: oxidised or reduced. Due to the grid character of the simulation, the resolution is restricted to the distance between two grid points (i.e. 1 nm). Therefore the binding sites may be shifted somewhat

[b]It was attempted to do the cross correlation with the actual data but then a change in the sign of the measured data caused problems.

relative to the body of the protein for the different orientations of the protein. To avoid a binding site becoming located within the protein itself (inaccessible to PQ) the binding site was calculated as a floating point parameter for each orientation of the protein[c]. Given this floating point number, the next neighbouring grid point not occupied by the protein itself was chosen to present the binding site. The Q_o and Q_r binding site are very close to each other. Therefore, the determination of binding sites in this manner may lead to a situation where both binding sites, Q_o and Q_r, are placed on the same site of the grid. This is avoided by choosing the second nearest neighbour on the grid to represent the binding site if the determination of a Q_r binding sites results in a grid point that is already occupied by another binding site.

6.2.4 The plastoquinone–objects

The plastoquinone–objects are similar to the tracers used in Chapter 4. Unlike the tracers, PQ cannot occupy the same vacant site on the grid. Furthermore the PQ–objects are extended by the attribute 'state' that accounts for the different redox states of PQ. Each PQ can be in three states: oxidised, one–fold reduced and two–fold reduced. Only oxidised and two–fold reduced plastoquinone are allowed to move. This takes into account that no free semiquinone is found in thylakoids. It reflects the finding that the dissociation constant of oxidised PQ as well as that of PQH_2 (i.e. two–fold reduced) is ca. three orders of magnitude higher than that of the singly reduced semiquinone [43] (see also Section 1.1.2). This may be caused by Coulomb interactions that stabilize the semiquinone at the Q_B site, whereas the neutral forms (PQ and PQH_2) may leave the binding site easily.

6.2.5 Modelling electron transport

At each encounter between PQ and a binding site of PS II or cyt *bf* first a test is carried out to ascertain whether PQ and the binding site are both in the right redox state (e.g. PQ oxidised at an encounter with Q_B, and Q_B carrying an electron). The next test is for whether the electron is then actually transported. The rate constants of the single reactions were taken as the probability, p, for a reaction to take place. At an encounter between PQ and a binding site (both in the right

[c]As PQ travels on the grid floating point coordinates are not accessible for PQ.

redox state) a random number, r, between zero and one was chosen. If $r < (1 - p)$, the electron is not transferred. Consequently, the smaller the value of p, the higher the probability of choosing a number that satisfies the condition and thus the electron is not transferred. A probability $p = 0$ always satisfies the condition and electron transport is not carried out. In turn, a probability $p = 1$ does not fulfill the condition and the transfer is always carried out. Assuming high availability of the reactants and no diffusion limitations, as is the case for ideal *in vitro* experiments, this behaviour results in an exponential decay corresponding to the rate constant (p).

As long as the sample is illuminated, the Q_A is assumed to always carry electrons ready for transfer at a successful encounter (i.e. saturating light conditions).

For the electron transfer at the cyt *bf* an obligatory Q–cycle is assumed [123, 174, 100, 101, 80] (see also Section 1.1.3). If FeS is oxidised and PQ two–fold reduced, electron transfer to FeS at the Q_o binding site is carried out after a successful encounter. After successful electron transfer to FeS the transfer of the second electron of the plastoquinol to cyt b_l follows immediately if the latter is oxidised [81, 112]. If cyt b_h is oxidised, the electron is immediately transferred from cyt b_l to cyt b_h [81]. For the sake of simplicity the oxidation of PQH_2 at the Q_o site is assumed to have the same rate constant regardless of whether there is reduced cyt b on the cyt *bf* complex.

If an oxidised PQ encounters the Q_r site, an electron is transferred from cyt b_h to PQ if the encounter is evaluated to be successful. The now singly reduced PQ is not allowed to move and it stays at the Q_r binding site until the second electron transfer takes place. This will be the case when cyt b_h is reduced again and if the encounter is evaluated to be successful according to the rate constant for electron transfer at the Q_r site. The rate constant for both electron transfers is assumed to be the same, regardless whether PQ is oxidised or singly reduced.

Electron transport between the Rieske–centre (FeS) and P700 is treated as a 'black–box' and one equilibrium constant is used to describe the redox state of FeS and P700.

6.2.6 Data fitting

The simulation allows certain parameters to vary in order to match experimental data on redox experiments. Parameters that can be varied are the rate constants of the following reactions:

$$
\begin{array}{rcll}
QA^- + QB & \xrightarrow{k_0} & QA + QB^- & \text{transfer of first electron} \\
QA^- + QB^- & \xrightarrow{k_1} & QA + QB^{2-} & \text{transfer of second electron} \\
QB^{2-} + 2H^+ & \xrightarrow{k_2} & PQH_2 & \text{protonation and dissociation} \\
PQH_2 + FeS_{ox} & \xrightarrow{k_3} & PQ^- + FeS_{red} + 2H^+ & \text{oxidation of } PQH_2 \text{ at } Q_o \\
PQ + \text{cyt } b_h^- & \xrightarrow{k_4} & PQ^- & \text{reduction of PQ at } Q_r \\
FeS_{red} + P700^+ & \xleftrightarrow{k_5} & FeS_{ox} + P700 & \text{equilibrium}
\end{array}
$$

The rates of electron transfer at the Q_B binding site are reasonably well known. Therefore the rate constants for the first (k_0) and the second electron transfer (k_1) at PS II were chosen to be 6670 and 2500 s^{-1}, respectively. These values are within the range of those given by Diner and co–workers [42]. Assuming free plastocyanin diffusion the equilibrium constant k_5 can in principle be calculated from the equilibrium constants for the following reactions:

$$
\begin{array}{rcl}
FeS_{red} + \text{cyt } f_{ox} & \xleftrightarrow{K_a} & FeS_{ox} + \text{cyt } f_{red} \\
\text{cyt } f_{red} + PC_{ox} & \xleftrightarrow{K_b} & \text{cyt } f_{ox} + PC_{red} \\
PC_{red} + P700^+ & \xleftrightarrow{K_c} & P700 + PC_{ox}.
\end{array}
$$

However, values for K_a, K_b, and K_a vary greatly in the literature. For K_a values can be found between 3.2 [76] and 18 [39]. Values for K_b vary between 1.0 [130] and 10 [82, 81]. Finally, values for K_c range from 5 [91] to 87 [49]. A collection of references to these rate constants can be found in Berry and Rumberg [22]. However, the redox state of P700 only declines to ca. 80% during the first 10 ms. Therefore electrons will be always transferred from the Rieske centre to P700 if the equilibrium constant is larger than 150.

The remaining free parameters (k_2, k_3, k_4) are varied to find the function that leads to the least sum of errors squared when compared with the experimental data. Two different algorithms are used to vary the parameters: a genetic algorithm and an algorithm according to Powell [138]. Genetic algorithms, when properly implemented, are capable of both exploration (broad search) and exploitation (local search) of the search space. Genetic algorithms are particularly useful if the function to be optimised has several optima. In this case a classical algorithm such as Powell's may get trapped in a local optimum instead of finding the global optimum. However, genetic algorithms are relatively slow. Thus it is convenient to combine both approaches.

Algorithm to do optimization according to Powell

The Powell algorithm is described by Powell 1964 [138]. It is an optimization algorithm. The algorithm assumes that the behaviour near the optimum is quadratic. A quadratic behaviour can be described by a parabola that is determined by three points. Given a certain point in the parameter space, two additional points are evaluated. One point is obtained by using a value lower than the parameter considered while the other is obtained by using a value above the parameter considered. These three points are used to determine a parabola. The optimum of the parabola is with some luck a step to the desired optimum of the considered function. If the obtained point in the parameter space is closer to the optimum the procedure is repeated with that point. Otherwise another parabola is sought.

The algorithm determines the direction for the next step to be perpendicular to the last step. This assumption leeds to a faster convergence to the minimum/maximum. Powell's algorithm requires continuous functions. Derivatives are not used. However, due to its iterative nature the algorithm is somewhat sensitive to starting values. The implementation of this routine is described in [140].

In the present work an algorithm was used that enabled the choice of intervals within which the varied parameters are changed[d].

Genetic Algorithm to do optimisation

A genetic algorithm creates a population of solutions based on the fitting–parameters. The algorithm then operates on the population to evolve the best solution. All

[d]This extention of Powell's algorithm was developed by Thomas Strauß.

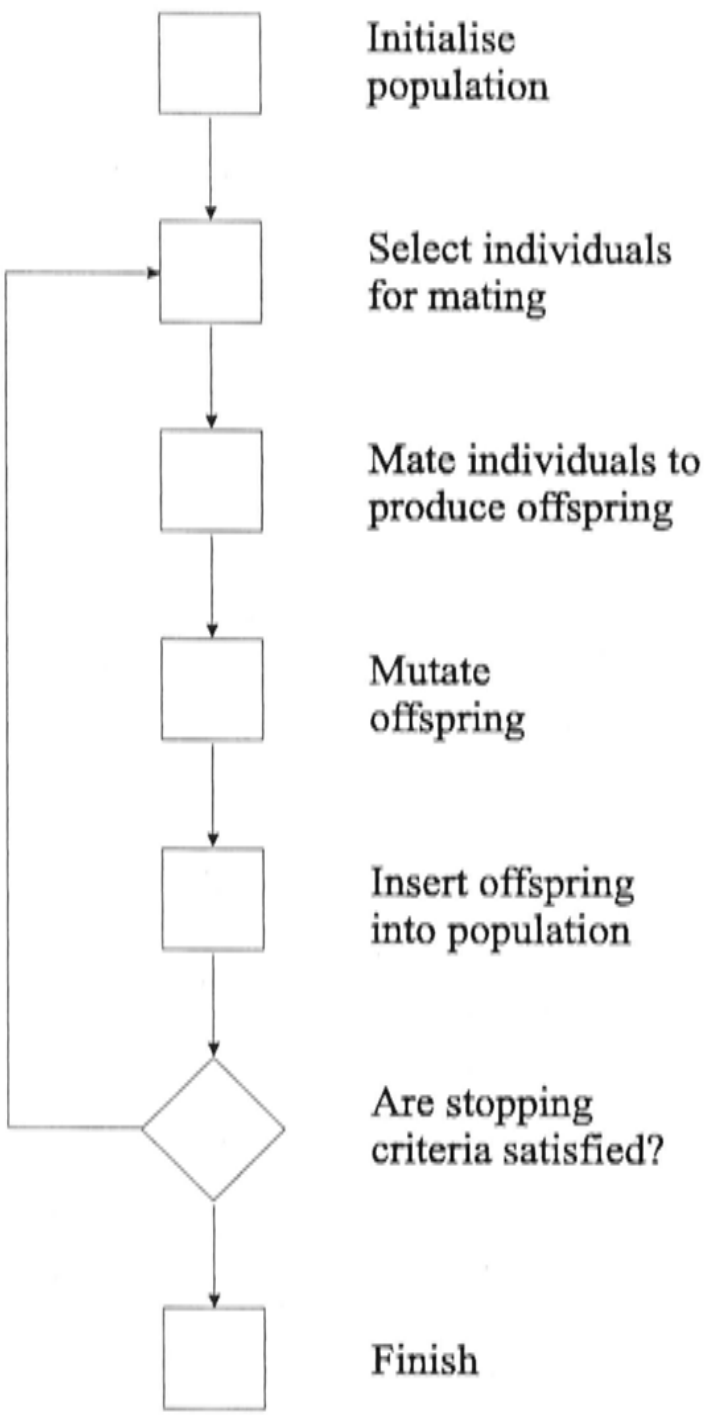

Figure 6.2: *Schematic diagram of the genetic algorithm.*

fitting–parameters together build a chromosome where each single fitting–parameter relates to a gene. The genetic algorithm determines which individuals should survive, which should reproduce, and which should die (see Figure 6.2). This relates to the fitness of an individual, which in turn corresponds to the sum of errors squared (the larger the sum of the errors squared the less fit). Typically a genetic algorithm has no obvious stopping criterion. Often the number–of–generations is used as a stopping measure. Other typical stopping criteria are the fitness–of–best–individual or convergence–of–population.

The library used here allows four varieties of genetic algorithms: (1) the 'simple genetic algorithm' described by Goldberg [64] uses non–overlapping populations, (2) a 'steady–state genetic algorithm', (3) an 'incremental genetic algorithm', in which each generation consists of only one or two children, and (4) the 'deme genetic algorithm' which evolves multiple populations (with exchanging individuals) in parallel using a steady–state algorithm.

For the problem addressed here the 'steady–state genetic algorithm' has been chosen. It uses overlapping populations with a user–specifiable amount of overlap. The algorithm creates a population of individuals. In each generation the algorithm creates a temporary population of individuals, adds these to the previous population, then removes the worst individuals in order to return the population to its original size. The amount of overlap between generations can be chosen by specifying a replacement parameter (either in percent or in numbers of individuals). Newly generated offspring are added to the population, then the worst individuals are destroyed (so the new offspring may or may not make it into the population, depending on whether they are better than the worst in the population).

Acknowledgement: The software for this work used the GAlib genetic algorithm package, written by Matthew Wall at the Massachusetts Institute of Technology. Copyright ©1995–1996 Massachusetts Institute of Technology.

6.2.7 Starting conditions and settings

The stoichiometries used are the ones calculated in Section 4.3: PS II : cyt *bf* : LHC II = 2.56 : 1 : 14.12. Additionally two PS I (monomers) per PS II (dimers) are assumed. The acceptors of PS II function as a two–electron gate. Therefore under steady–state conditions one half of the acceptors will stay as a semiquinone at the Q_B site on PS II after a saturating light flash while the other half produces PQH_2. Accordingly every second Q_B site (randomly chosen) has a bound PQH_2 that is released after dissociation has taken place. No free diffusing oxidised PQ is modelled to save computing time. However, free, diffusing PQ is not expected to act as an obstacle to PQH_2 migration or have any other significant influence. For cyt *bf* it is assumed that the state with one reduced cyt *b* is stable within the measuring time. This is in agreement with the observation that one quarter of cyt *b* is reduced in the steady–state (note that each cyt *bf* contains two cyt *b*) [145]. The other components are oxidised before the flash [69].

6.3 Results and Discussion

To obtain quantitative information about rate constants involved in photosynthetic electron transport, rate constants used in the model were varied to match the experimental data. Two different mechanisms at the Q_o site on cyt *bf* are compared in the next two Sections: tight binding and a collisional mechanism.

Parameters that are varied are k_2 (dissociation of PQH_2 from PS II), k_3 (PQH_2 oxidation at Q_o), and k_4 (PQ reduction at Q_r) (as described in Section 6.2.6). Other rate constants involved are reasonably well known and therefore these values were not varied but taken from the literature.

6.3.1 Tight binding mechanism

Assuming there is a tight binding mechanism, a good fit to the measured data could be obtained (see Figure 6.3). An area fraction of 0.70 was chosen corresponding to the value estimated for grana thylakoids in Section 4.1. For the conditions used in the simulation, this area fraction is above the percolation threshold and hence diffusion domains where PQ is trapped are formed.

The parameters resulting in the best fit are well within the range of published data (see Table 6.1). The lattice size is chosen to be 400 nm×400 nm (with periodical boundary conditions). This size corresponds to the size of the grana core. The lattice size is relatively large and inhomogeneities caused by the random distribution of the proteins should be minimised. However, the exact values of the rate constants depend on the configuration of the proteins. Three different protein configurations were chosen and parameters varied to match the measured data (see Table 6.2).

Interestingly the different parameters vary to a different extent. Whereas k_3 is within a small range for all configurations investigated k_4 varies to a great extent. This is not entirely unexpected since k_3 describes the oxidation of PQH_2 at the Q_o site on cyt *bf* which is agreed to be the rate–limiting step of whole chain electron transfer. Thus electron flux is expected to be very sensitive to this parameter. k_4 describes the reduction of PQ at the Q_r binding site on cyt *bf*. It does not seem to play a major role in determining the measured curve. This is probably due to the low probability for a PQ to find a cyt *bf* carrying two electrons when only one saturating light flash is applied. Consequently the simulation is not expected to be very sensitive to this parameter.

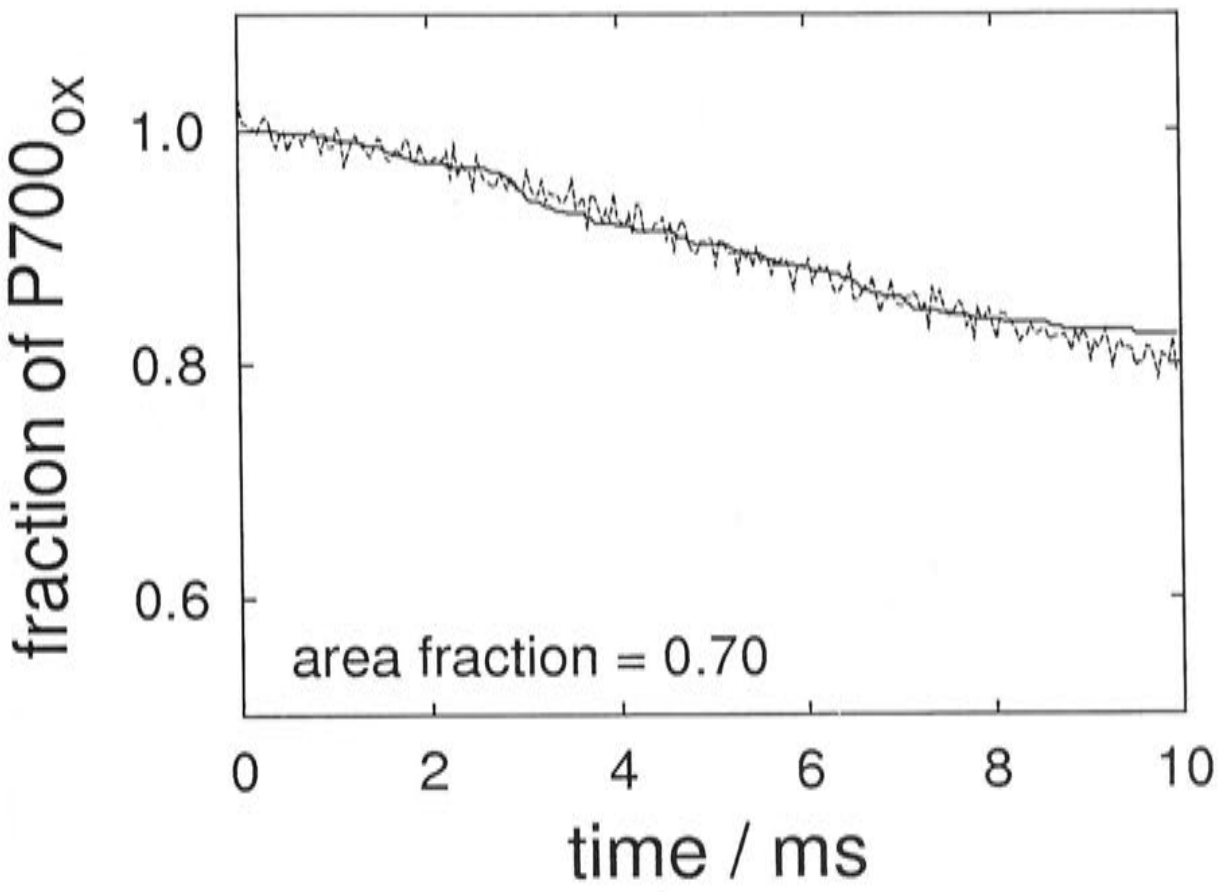

Figure 6.3: *Comparison of the simulation (solid line) with the observed P700 re-reduction (dashed line) for a tight binding mechanism. An occupied area fraction of 0.70 (i.e. above the percolation threshold) is assumed. Rate constants are* $k_2 = 1206.1\ s^{-1}$, $k_3 = 294.9\ s^{-1}$, *and* $k_4 = 335.2\ s^{-1}$ *(nomenclature as described in Section 6.2.6).*

rate constant in s^{-1}	**literature**	**area occupation** 0.70	0.60	0.70 (permeable)
k_2	495–2310 [124] 1000 [84]	1206.1	1641.4	242.9
k_3	305 [81] 200–330 [78, 38]	294.9	100.0	100.0
k_4	400 [81]	335.2	250.0	368.8

Table 6.1: *Rate constants for several electron transfer steps from literature and obtained from simulations.*

k_2	1206.1	725.2	1298.1
k_3	294.9	329.1	288.6
k_4	335.2	543.6	100.3

Table 6.2: *Rate constants resulting from best fits for different random protein distributions with an area fraction of 0.70.*

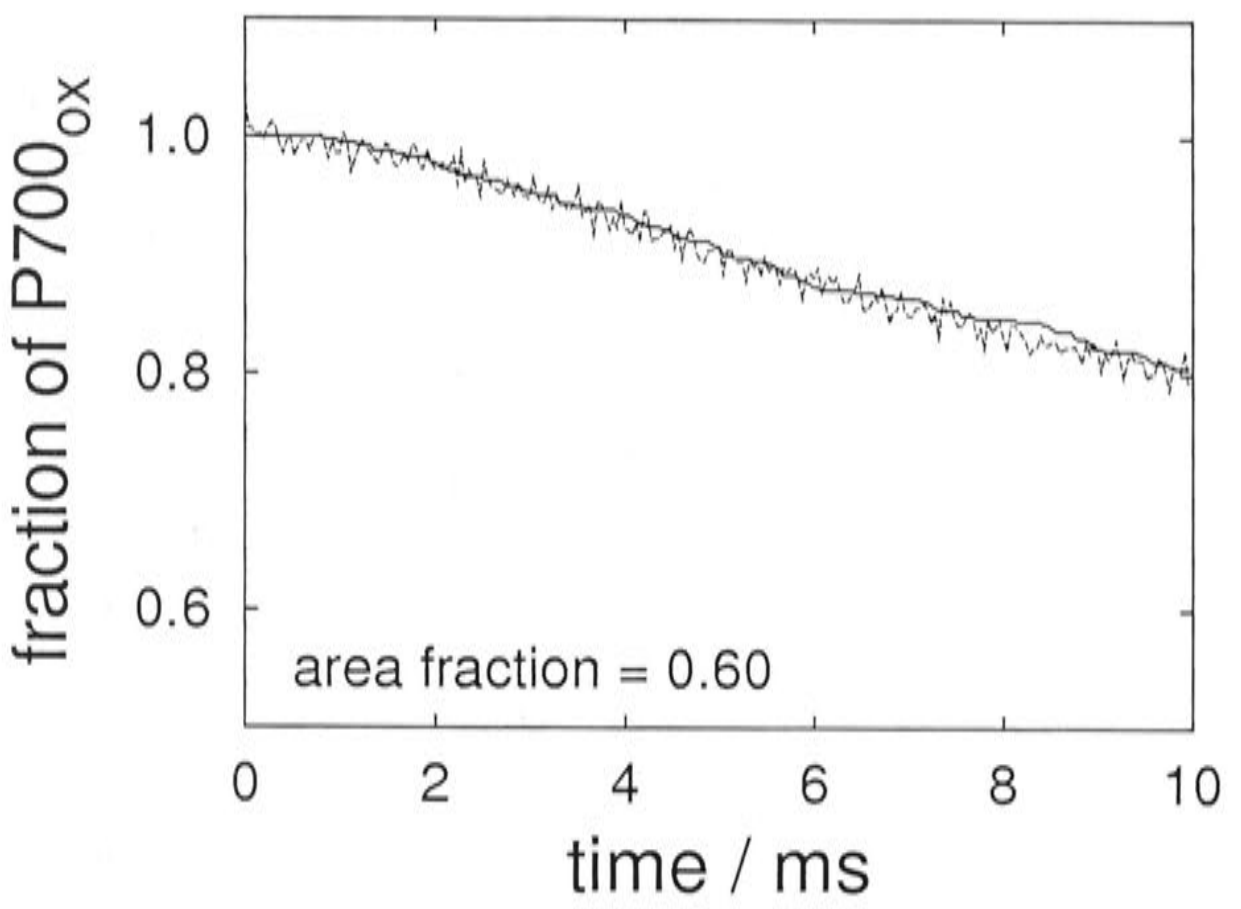

Figure 6.4: *As Figure 6.3 but assuming an occupied area fraction of 0.60 (i.e. below the percolation threshold). Rate constants are* $k_2 = 1641.4\ s^{-1}$, $k_3 = 100.0\ s^{-1}$, *and* $k_4 = 250.0\ s^{-1}$ *(nomenclature as described in Section 6.2.6).*

To investigate the influence of the protein density and hence the retardation of PQ migration, the simulation was repeated for an occupied area fraction of 0.60 which is below the percolation threshold.

As with an area fraction of 0.70 good fits are obtained (see Figure 6.4). However, the rate constants obtained are not in good agreement with published data. To match the experimental data the reaction at the Q_o site would need to be very slow ($k_3 = 100\ s^{-1}$). This is probably to compensate for the much faster 'finding' of the binding site due to the less restricted diffusion of PQ.

To elucidate the effect of restricted PQH_2 diffusion a hypothetical extreme case is investigated: an area occupation of 0.70 is chosen but it is assumed that the proteins do not interfere with PQ diffusion (i.e. being permeable to PQ). For PQH_2 oxidation the same rate constant (k_3) is obtained as for 0.60 area occupation. Additionally a

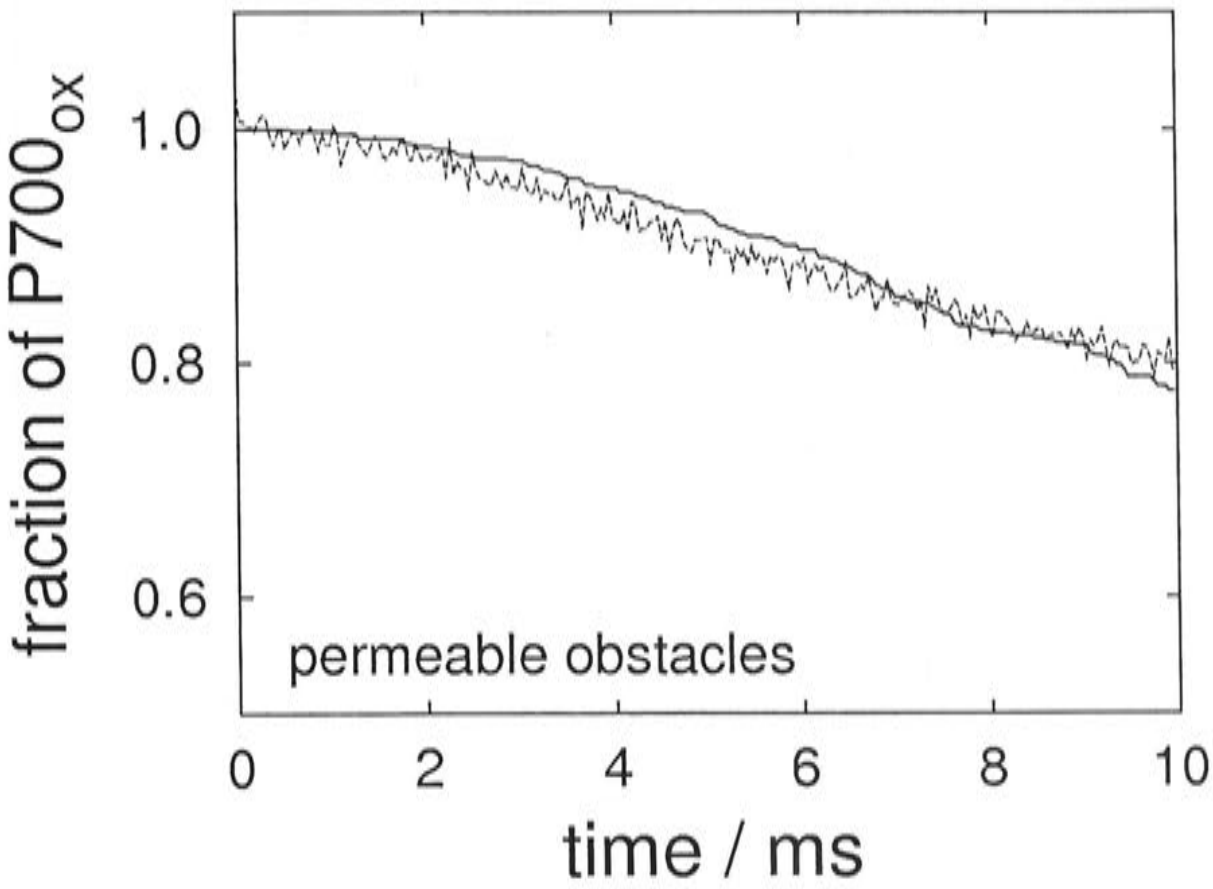

Figure 6.5: *As Figure 6.3 but here the proteins are assumed to be permeable for PQ. Rate constants are* $k_2 = 242.9\ s^{-1}$, $k_3 = 100.0\ s^{-1}$, *and* $k_4 = 368.8\ s^{-1}$ *(nomenclature as described in Section 6.2.6).*

slow dissociation from PS II (> 4 ms) is obtained to account for the measured slow decline in the amount of oxidised P700. However, as can be seen in Figure 6.5, the simulation does not match the experimental data well. At short times the simulated curve declines too slowly. This is probably due to the slow dissociation constant found. The initial lag (about 2 ms) before the steeper decline in the amount of oxidised P700 starts, may be caused by reactions proceeding the oxidation of PQH_2 [124] (i.e. dissociation and diffusion of PQH_2 and possibly time spent at the Q_o site before being oxidised). Figure 6.5 illustrates that this initial lag is much too pronounced if the dissociation constant is as low as the one obtained if proteins do not restrict PQ migration.

In summary the experimental data are best matched when restriction of plastoquinone diffusion is pronounced (area fraction 0.70). This clearly points out the importance of structural characteristics of thylakoids in models of electron transport. An influence of diffusion processes on reaction rates is also reported for the activation of transducin by rhodopsin [154]. Higher concentrations of reactants are expected to lead to an increased reaction rate by the law of mass action. However, they also lead to a decreased rate of reaction by lowering the diffusion coefficient of the reactants (here only PQH_2 is considered to be mobile but this does not alter the principal results).

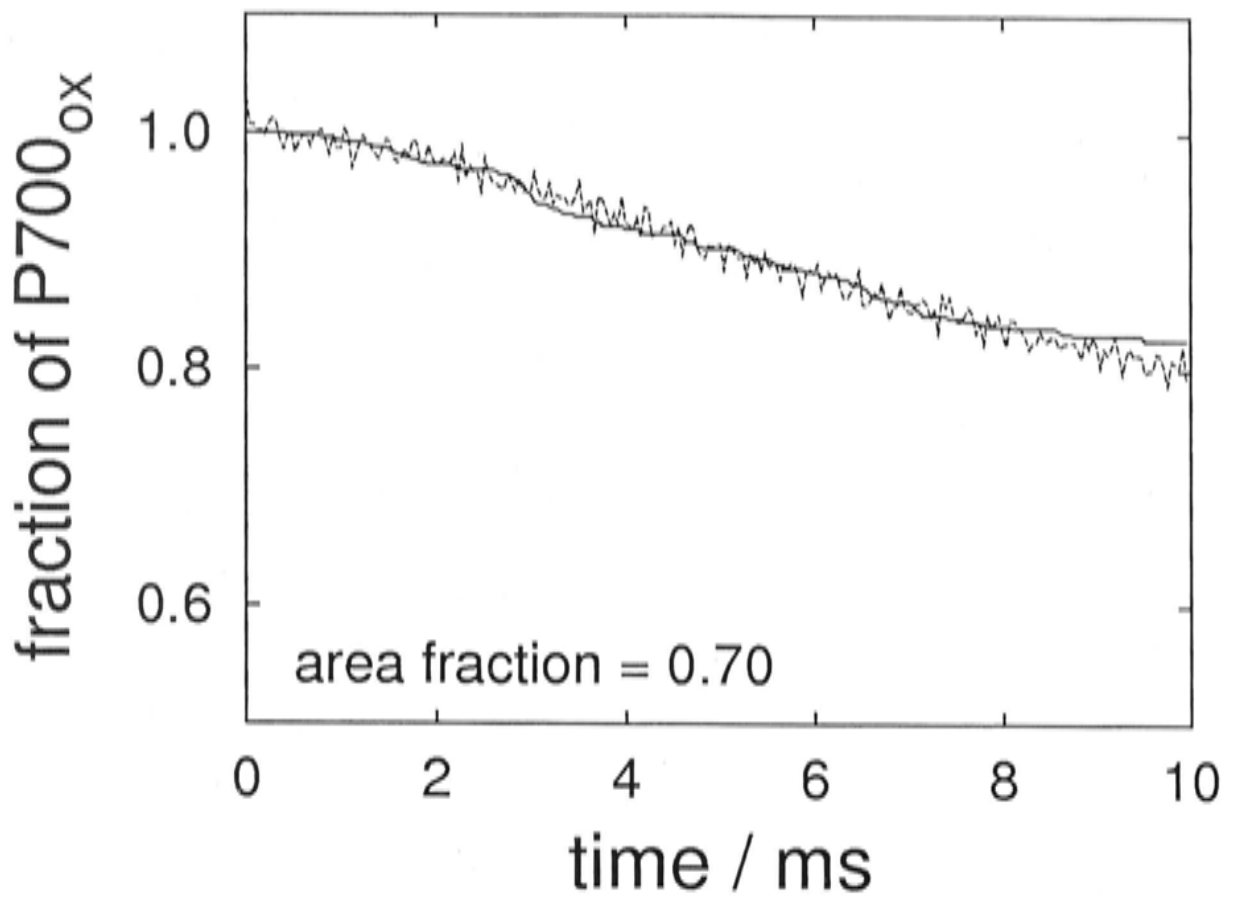

Figure 6.6: *Comparison of the simulation (solid line) with the observed P700 re–reduction (dashed line) for a collisional mechanism. An occupied area fraction of 0.70 (i.e. above the percolation threshold) is assumed. Rate constants are* $k_2 = 1352.1\ s^{-1}$, $k_3 = 48806.2\ s^{-1}$, *and* $k_4 = 49561.5\ s^{-1}$ *(nomenclature as described in Section 6.2.6).*

6.3.2 Collisional mechanism

In this Section a collisional mechanism is assumed instead of the tight binding mechanism. As can be seen in Figure 6.6 good fits are obtained. However, the resulting rate constant for oxidation of PQH_2 at the Q_o site is more than two orders of magnitude higher than that found in the literature (see Table 6.1).

This could be explained by the diffusion limitation. In the case of diffusion limitation the rate constant is composed of the probability of finding a binding site (diffusion limited) and the probability for an electron transfer to take place (see also [176, 122]). Accordingly the rate constant found in the simulation will then refer to the rate of the actual electron transfer. To match the rate constants found in the literature (305 s^{-1}) this requires a probability of about 1:160 for a PQH_2 to meet a Q_o binding site. To test for the probability of finding a binding site, the simulation is repeated with the same configuration but this time the number of successful encounters and the total number of encounters are counted. A probability of 1:2840 is found for an encounter to be successful. This would be commensurate with an apparent electron transfer rate of 48806.2/2840 s^{-1} which is much too low.

Further, if a collisional mechanism were indeed the case, it is expected that the rate constant found here (48806.2 s^{-1}) equals that measured *in vitro* where no diffusion limitation occurs. This however is not the case. The rate constant found in *C. reinhardtii* is 250–300 s^{-1} [134] and thus is within the same order of magnitude as the *in vivo* rates. Equal rates *in vivo* and *in vitro* would fit better with the tight binding mechanism.

It should be noted that in the case of a collisional mechanism the resulting rate constants are much more sensitive to the protein configurations. A factor of two has been found for different starting conditions (not shown). Due to the diffusion limitation it is important whether or not a PQH_2 has good access to a Q_o binding site. However, rate constants resulting from other configurations are still not satisfying.

In summary it seems that a collisional mechanism is not suitable to describe the measured data on P700 re–reduction kinetics while a tight binding mechanism leads to good fits with rate constants in agreement with the literature.

It should be noted, that the tight binding mechanism and the collisional mechanism are both simplifications. More generally reactions should be described by the rates of binding (k_{on}), unbinding (k_{off}) and the internal electron transfer rate (k_3). However, no firm figures exist for plant cyt *bf* complexes. Therefore the simplifications of a tight binding and a collisional mechanism are introduced, reflecting two extreme cases.

Chapter 7

Summary and Outlook

Contents

7.1 Summary

The present thesis is aimed at gaining a better understanding of whole chain photosynthetic electron transport by examining linear electron flow with the aid of mathematical models.

In the second Chapter a 'classical' mathematical model of electron transport, based on differential equations, is developed. In this model thylakoid structure is not taken into account. The model was used to investigate the pH dependency of P700 re–reduction. Rate constants of the most important electron transfer steps were varied to match experimental data from the literature [147]. Different pH–dependencies of the reactions at the Q_r site on cyt *bf* were tested. Good fits to the experimental data were obtained resulting in reasonable time constants with values well within the published range. However, although the model is able to explain some of the features of electron transfer, it is not able to explain others.

In Chapter 3 measurements are shown that illustrate the limits of models neglecting organisational aspects of thylakoids. PS II was titrated with DCMU and whole chain transport was measured. Since the oxidation of PQ at cyt *bf* is accepted to be the rate limiting step of photosynthetic electron flow, titration of only a small number of PS II is not expected to result in a significantly decreased electron flux if a shared PQ pool is assumed. However, if the measured whole chain transport is plotted versus PS II activity an unexpected s–shaped curve is obtained. This cannot be explained when a shared PQ pool is assumed (see e.g. the model in Chapter 2).

In the last decade experimental evidence arose that the diffusion of plastoquinol may be restricted [26, 24] and therefore a shared plastoquinol pool may be an over–simplification. Lavergne, Joliot and co–workers have observed that there is no rapid redox equilibration between free plastoquinone and QA, the primary quinone acceptor at PS II. From their results they developed the micro–domain concept, described in Section 1.2.5. This model accounts for the high protein density in thylakoids assuming that PQ diffusion may be severely restricted by randomly distributed integral proteins [111, 93, 109, 92]. The micro–domain concept was extended by Kirchhoff and co–workers [96]. They suggest that diffusion domains may be the result of a hierarchy of specific protein–protein interactions.

In most mathematical models of electron transport the organisation of proteins in thylakoids is severely neglected. Although a variety of structural data of the photosynthetic proteins and their aggregation in thylakoids is available, little is known

about the functional consequences. To fill this gap a mathematical model describing organisational characteristics of thylakoids according to the micro–domain concept was developed in Chapter 3. However, the published micro–domain concepts cannot explain the complex s–shaped curves resulting from PS II titration. Therefore the previous models of thylakoid architecture were further extended. The measured data were matched with the model that was developed in this Chapter. Although only two varied parameters were employed, good fits to the measured data were obtained for several different species. It was shown that the combination of both functional and spatial aspects can strongly influence electron transport. The model assumed a dimeric Q–cycle. Such a dimeric Q–cycle was suggested by Gopta and co–workers [65]. Whether the two monomers of cyt *bf* are indeed functionally interacting is still under discussion and a dimeric Q–cycle is not commonly accepted. Further, the model developed in Chapter 3 uses average numbers for stoichiometries and spatial aspects. Inhomogeneities or protein–protein interactions are not taken into account. Nevertheless the model shows clearly that thylakoid architecture may strongly influence electron transport.

To further elucidate the organisation of proteins within thylakoids and its influence on photosynthetic electron transport, a Monte Carlo simulation was developed (see Chapters 4–6). With this simulation the influence of integral photosynthetic proteins on the diffusion of plastoquinone/plastoquinol was examined in Chapter 4. An occupied area fraction of 0.70 in grana thylakoids was determined using available structural data on the photosynthetic proteins. For an occupied area fraction as high as 0.70 it was found that a random distribution of proteins could indeed lead to the formation of diffusion domains within which PQ is trapped. This is in accordance with the micro–domain concept of Lavergne and Joliot. In the case of a random distribution PS II may be isolated from cytochrome *bf* complexes for the time relevant for photosynthetic electron transport (also discussed e.g. in [111]). Additionally, random distribution may lead to obstruction of binding sites. Particularly in the case of the Q_o site, which is considered to be the site of the rate limiting reaction, this seems wasteful. The degree of obstruction depends on the geometry of the protein and the exact position of the binding site on the protein (see Section 4.3, Table 4.2). Altogether, random distribution, although often assumed, may not be a favorable arrangement. Instead, the organisation of the proteins may be influenced by additional factors.

investigated factor	**preventing domain formation**	**enhancing domain formation**
obstacle shape boundary lipids mobility of obstacles	compact exchange with PQ highly mobile	ramified tightly bound to proteins immobile
protein–protein interactions	clustering (low energies?)	ramified (high energies?)

Table 7.1: *Factors influencing the percolation threshold.*

The value of 0.70 is very close to the percolation threshold from which closed diffusion domains are formed. Therefore slight changes in the arrangement may shift the percolation threshold one way or the other and thus prevent or enhance domain formation. Several factors which could influence the percolation threshold were investigated (see Table 7.1).

Obstacle shape: Most integral proteins in the thylakoids form oligomers [89, 105, 80, 85, 38]. Even higher aggregates of integral photosynthetic proteins were found in grana thylakoids [89, 27]. The formation of compact oligomers may lead to a decreased percolation threshold and hence facilitate PQ migration, while formation of ramified aggregates would have the opposite effect.

Boundary lipids Little is known about boundary lipids. They might strongly influence thylakoid architecture and the formation of protein aggregates [178, 158, 63, 103].

Mobility of obstacles: Lateral migration of the integral proteins is important for function, regulation and biosynthesis. However, protein mobility within thylakoids is expected to be highly restricted, firstly because of the abundance of proteins acting as obstacles for their diffusion and secondly due to protein–protein interactions. Accordingly relatively low protein mobility is expected.

In the next Chapter (Chapter 5) protein–protein interactions were introduced into the simulation. The most abundant proteins in thylakoids are LHC II complexes. They are assumed to interact with other free LHC II and with LHC II tightly bound to PS II.

It was found that low interaction energies (about 1 kT) lead to more clustered arrangements while high interaction energies (E = 5 kT or higher) result in ramified chains. However, the effect of protein–protein interactions decreases with increasing protein density. In thylakoids the protein density is very high and hence the effect of interaction energies may not be very pronounced. Having a mixture of interacting and non–interacting protein may have interesting effects: It was found that mobility of cyt *bf* may reduce the number of its binding sites being obstructed (see Table 5.1). In addition, interaction between proteins may further decrease the percolation threshold for PQ diffusion by the formation of more ramified chains of obstacles.

In Chapter 6 bindings sites on the proteins were introduced and electron transfer was modelled. Two different routines were introduced that allow optimisation (one according to Powell and the other a genetic optimisation routine). P700 re–reduction kinetics were measured and rate constants of some involved electron transfer steps were varied to match the experimental data. Two different binding mechanisms at the Q_o site on cyt *bf* were investigated: a tight binding mechanism which implies irreversible binding at the Q_o site and a collisional mechanism that involves immediate electron transfer after a succesful encounter. The latter involves the need for several encounters until transfer finally takes place. Consequently, in a diffusion limited electron transport chain it may take a long time until transfer occurs. Since the protein density in thylakoids is very high - around the percolation threshold - it is expected that PQ diffusion is severely restricted.

For the tight binding mechanism, assuming an area occupation of 0.70, good fits were obtained resulting in rate constants that are in good agreement with published data. Reducing the restriction of PQ diffusion (lowering the area fraction to 0.60 or assuming permeability of the proteins) leads to a rate constant for PQH_2 oxidation that is rather low and not in good agreement with the literature. Similarly, the assumption of a collisional mechanism only leads to good fits when unrealistic rate constants are used. Here, the rate constant for PQH_2 oxidation would need to be too high. This may be to compensate for the long time required to 'find' the binding site and reflects the somewhat opposite situation compared to lowering the restriction of PQ migration described above.

In summary it is observed that best fits are obtained when diffusion restriction is severe and a tight binding mechanism is assumed.

7.2 Outlook

As summarized above, it was found in the present investigations that the structure and organisation of thylakoids may have a large impact on photosynthetic electron transport. However, little is known about the thylakoid architecture. The work here points out the need for more experiments in several fields. Particularly the following factors require deeper knowledge for a better understanding of photosynthetic electron transport:

- The role of boundary lipids in the organisation and aggregation of integral proteins. Here spin label studies and examinations of reconstituted proteins in liposomes may prove as valuable tools for examination.
- The mobility of obstacles. Fluorescence recovery after photobleaching has already provided useful data [68] but more data are needed. Particularly data are required concerning the mobility of unphosphorylated LHC II and PS II.
- protein–protein interactions. They may play an important role but not much is known about the extent of interaction between the different proteins involved in photosynthetic electron transport.

The diffusion coefficient of PQ within the thylakoids is expected to be distance dependent. Therefore it would be interesting to compare different estimates of $D(r, c)$ involving different distances (see also Section 4.4). The values obtained may give interesting information about the structure of thylakoids. The obtained data could be compared with the distance dependent diffusion coefficient determined with the model assuming randomly arranged proteins. If the experimental data decline steeper with increasing distance than the diffusion coefficient obtained from the simulation it can be concluded that in thylakoids factors occur enhancing domain formation. A slower decline of the measured data on the other hand would indicate factors counteracting domain formation in thylakoids (such as the formation of more compact supercomplexes).

Another approach may be to further investigate the temperature dependence of the experiments described in Chapter 3. Diffusion processes are temperature dependent as are interactions. Therefore it may be enlightening to examine if temperature influences the control of electron transport.

The magnitude of protein–protein interactions can be investigated by the analysis of particle distribution from micrographs obtained by atomic force microscopy. The resolution is not high enough to distinguish between cyt *bf* and LHC II. However, BBY preparations [23] do not contain cyt *bf*. The resulting micrographs only show PS II and LHC II. Accordingly it is possible to analyse the distribution of PS II and compare the distribution obtained with results from the simulation using different interaction energies.

Investigating whole chain electron transport, different reaction mechanisms could be tested. For example the influence of a dimeric Q–cycle could be examined. Data from other experiments that could be matched are P700 re–reduction in the presence of DCMU, fluorescence relaxation or cyt *bf* reduction kinetics. Furthermore it could be investigated if the Monte Carlo simulation is able to explain the complex s–shaped curves found in plots where whole chain transport is plotted versus PS II activity (as described in Chapter 3). An attempt could be made to match the experimental data so obtained with the model, using random protein distribution and distributions resulting from different interaction energies.

Bibliography

[1] P-Å. Albertsson. The structure and function of the chloroplast photosynthetic membrane – a model for the domain organization. *Photosynthesis Research*, 46:141–149, 1995.

[2] P-Å. Albertsson. The domain structure and function of the thylakoid membrane. *Recent Res. Devel. Bioener*, 1:143–171, 2000.

[3] P-Å. Albertsson. A quantitative model of the domain structure of the photosynthetitc membrane. *Trends in Plant Science*, 6:349–354, 2001.

[4] P-Å. Albertsson, E. Andreasson, and P. Svensson. The domain organization of the plant thylakoid membrane. *FEBS Lett*, 273(1,2):36–40, 1990.

[5] J. F. Allen. How does protein phosphorylation regulate photosynthesis? *Trends Biochem. Sci.*, 17:12–17, 1992.

[6] J. F. Allen. Protein phosphorylation in regulation of photosynthesis. *Biochim. Biophys. Acta*, 1098:275–335, 1992.

[7] J. F. Allen, J. Benett, K. E. Steinback, and C. J. Arntzen. Chloroplast protein phosphorylation couples plastoquinone redox state to distribution of excitation energy between photosystems. *Nature*, 291:25–29, 1981.

[8] D. R. Allred and L. A. Staehelin. Spatial organization of the cytochrome b_6-f complexe within chloroplast thylakoid membranes. *Biochim. Biophys. Acta*, 849:94–103, 1986.

[9] P. F. F. Almeida and W. L. C. Vaz. *Handbook of Biological Physics*, chapter 6. Lateral Diffusion in Membranes, pages 305–357. Elsevier Science B. V., Amsterdam, 1995.

[10] J. M. Anderson. The significance of grana stacking in chlorophyll *b* containing chloroplasts. *Photobiochemistry and photophysics*, 3:225–241, 1982.

[11] J. M. Anderson. Insights into the consequences of grana stacking of thylakoid membranes in vascular plants: a personal perspective. *Aust. J. Plant Physiol.*, 26:625–639, 1999.

[12] J. M. Anderson, W. S. Chow, and D. J. Goodchild. Thylakoid membrane organisation in sun/shade acclimation. *Aust. J. Plant Physiol.*, 15:11–26, 1988.

[13] J. M. Anderson and A. Melis. Localization of different photosystems in seperate regions of chloroplast membranes. *Proc Natl Acad Sci USA*, 80:745–749, 1983.

[14] B. Andersson and J. M. Anderson. Lateral heterogeneity in the distribution of chlorophyll-protein complexes of the thylakoid membranes of spinach chloroplasts. *Biochim. Biophys. Acta*, 593:427–440, 1980.

[15] B. Andersson and S. Styring. Photosystem ii: molecular organization, function and acclimation. *Curr. Top. Bioenerg*, 16:1–81, 1991.

[16] E. Andreasson and P-Å. Albertsson. Heterogeneity in photosystem I - the larger antenna of photosystem I is due to functional connection to a special pool of LHC II. *Biochim. Biophys. Acta*, 1141:175–182, 1993.

[17] P-O. Arvidson and C. Sundby. A model for the topology of the chloroplast thylakoid membrane. *Aust. J. Plant Physiol.*, 26:687–694, 1999.

[18] R. P. Barbagallo, C. Breyton, and G. Finazzi. Kinetic effects of the electrochemical proton gradient on plastoquinone reduction at the Qi site of the cytochrome b_6f complex. *J. Biol. Chem.*, 34:26121–26127, 2000.

[19] J. Barber. Influence of surface charges on thylakoid structure and function. *Annu. Rev. Plant Physiol.*, 33:261–295, 1982.

[20] J. Barber. *Encyclopedia of Plant Physiology, New Series, Photosynthesis III.*, chapter Surface electrical charges and protein phosphorylation., pages 653–664. Springer Verlag, Berlin, 1986.

[21] S. Berry and B. Rumberg. Proton to electron stoichiometry in electron transport of spinach thylakoids. *Biochim. Biophys. Acta*, 1410:248–261, 1999.

[22] S. Berry and B. Rumberg. Kinetic modeling of the photosynthetic electron transport chain. *Biochemistry*, 53:35–53, 2000.

[23] D. A. Berthold, G. T. Babcock, and C. F. Yocum. A highly resolved oxygen–evolving photosystem II preparation from spinach thylakoid membranes. EPR and electron transport properties. *FEBS Lett.*, 134:231–234, 1981.

[24] M. F. Blackwell, C. Gibas, S. Gygax, D. Roman, and B. Wagner. The plastoquinone diffusion coefficient in chloroplasts and its mechanistic implications. *Biochem. Biophys. Acta*, 1183:533–543, 1994.

[25] M. F. Blackwell, K. Gounaris, Zara S. J., and J. Barber. A method for estimating lateral diffusion coefficients in membranes from steady-state fluorescence quenching studies. *Biophysical Journal*, 51:735–744, 1987.

[26] M. F. Blackwell and J. Whitmarsh. Examination of plastoquinone diffusion in lipid vesicles. *Biophysical Journal*, 58:1259–1271, 1989.

[27] E. J. Boekema, A. F. Boonstra, J. P. Dekker, and M. Rögner. Electron microscopic structural analysis of photosystem I, photosystem II and the cytochrome b_6/f complex from green plants and cyanobacteria. *J. Bioenerg. Biomembr.*, 26:17–29, 1994.

[28] E. J. Boekema, J. F. L. van Breemen, H. van Roon, and J. P. Dekker. Arrangement of photosystem ii supercomplexes in crystalline macrodomains within the thylakoid membrane of green plant chloroplasts. *J. Molo. Biol.*, 301:1123–1133, 2000.

[29] E. J. Boekema, H. van Roon, F. Calkoen, R. Bassi, and J. P. Dekker. . *Biochemistry*, 38:2233–2239, 1999.

[30] U. Brandt and J. Okun. Role of deprotonation events in ubihydroquinone:cytochrome c oxidoreductase from bovine heart and yeast mitochondria. *Biochemistry*, 36:11234–11240, 1997.

[31] C. Breyton. Conformational changes in the cytochrome b6f complex induced by inhibitor binding. *J. Biol. Chem.*, 275:13195–13201, 2000.

[32] R. D. Britt. *Oxygenic photosynthesis: The light reactions*, chapter 9. Oxygen evolution., pages 137–164. Kluwer Academic Publishers, 1996.

[33] S. R. Broadbent and J-M. Hammersley. Percolation processes I. Crystals and mazes. *Proc. Cambr. Phil. Soc.*, 53:629–641, 1957.

[34] D. J. Chapman and J. Barber. Analysis of plastoquinone-9 levels in appressed and non-appressed thylakoid membrane regions. *Biochim. Biophys. Acta*, 850:170–172, 1990.

[35] W. S. Chow. Grana formation: entropy-assisted local order in chloroplasts. *Aust. J. Plant Physiol.*, 26:641–647, 1999.

[36] G. Cornic, N. G. Bukhov, C. Wiese, R. Bligny, and U. Heber. Flexible coupling between light-dependent electron and vectorial proton transport in illuminated leaves of C_3 plants. role of photosystem I-dependent proton pumping. *Planta*, 210:468–477, 2000.

[37] W. A. Cramer and D. B. Knaff. *Energy Transduction in Biological Membranes: A Textbook in Bioenergetics*, pages 79–138. Springer–Verlag New York Inc., New York, 1989.

[38] W. A. Cramer, G. M. Soriano, M. Ponomarev, D. Huang, H. Zhang, S. E. Martinez, and J. L. Smith. Some new structural aspects and old controversies concerning the cytochrome *b6f* complex of oxygenic photosynthesis. *Annu. Rev. Plant Physiol. Plant Mol. Biol.*, 47:477–508, 1996.

[39] A. R. Crofts and C. A. Wraight. The electrochemical domain of photosynthesis. *Biochimica et Biophysica Acta*, 726:149–185, 1983.

[40] J. P. Dekker, H. van Roon, and E. J. Boekema. Heptameric association of light-harvesting complex II trimers in partially solubilized photosystem II membranes. *FEBS Lett.*, 449:211–214, 1999.

[41] B. Deryagin and L. Landau. A theory of the stability of strongly charged lyophobic sols and the coalescence of strongly charged particles in electrolytic solution. *Acta Physicochim. URSS*, 14, 1945.

[42] A. B. Diner and G. T. Babcock. *Oxygenic photosynthesis: The light reactions*, chapter 12. Structure, dynamics, and energy conversion efficiency in photosystem II., pages 213–247. Kluwer Academic Publishers, 1996.

[43] A. B. Diner, V. Petrouleas, and J. J. Wendoloski. The iron-quinone electron-acceptor complex of photosystem II. *Physiol. Plant.*, 81:423–436, 1991.

[44] A. D. Dinsmore, A. G. Yodh, and D. J. Pine. Entropic control of particle motion using passive surface microstructures. *Nature*, 383:239–242, 1996.

[45] G. C. Dismukes. Splitting water. *American Association for the Advancement os Science*, 292:447–448, 2001.

[46] V. W. Draber, J. F. Kluth, K. Tietjen, and A. Trebst. Herbizide in der Photosyntheseforschung. *Angew. Chemie*, 103:1650–1663, 1991.

[47] F. Drepper. *Linearer Elektronentransport der Photosynthese: Beiträge von lateraler Diffusion, Dynamik der Protein-Protein-Wechselwirkungen und Elektronentransferreaktionen.* PhD thesis, Universitaet Freiburg i. Br., 1994.

[48] F. Drepper, I. Carlberg, B. Andersson, and W. Haehnel. Lateral diffusion of an integral membrane protein: Monte Carlo analysis of the migration of phosphorylated light-harvesting complex II in the thylakoid membrane. *Biochemistry*, 32:11915–11922, 1993.

[49] F. Drepper, M. Hippler, W. Nitschke, and W. Haehnel. Binding dynamics and electron transfer between plastocyanin and photosystem I. *Biochemistry*, 35:1282–1295, 1996.

[50] A. Yu. Dubinskii. A model of electron transfer in chloroplasts with allowance for Mitchell's Q-cycle: Numerical simulation. *Biophysics*, 45(2):262–268, 2000.

[51] A. Yu. Dubinskii and A. N. Tikhonov. Regulation of electron and proton transport in chloroplasts. *Biophysics*, 42(3):644–661, 1997.

[52] S Duchene and P. A. Siegenthaler. Do glycerolipids display lateral heterogeneity in the thylakoid membrane? *Lipids*, 35(7):739–744, 2000.

[53] U. Eberl, A. Ogrodnik, and M. E. Michel-Beyerle. Vom Licht zum Leben – Physik und Photosynthese. *Phys. Blätter*, 50(3):215–220, 1994.

[54] A. Einstein. Zur Theorie der Brownschen Bewegung. *Annalen der Physik*, 19:371–381, 1906.

[55] A. Einstein. *Investigations on the Theory of the Brownian Movement.* Dover Publications, Inc., New York, 1956.

[56] J. Eisinger, J. Flores, and W. P. Petersen. A milling crowd model for local and long–range obstructed lateral diffusion. *Biophys. J.*, 49:987–1001, 1986.

[57] R. J. Ellis. Macromolecular crowding: obvious but underappreciated. *Trends in Biochem. Sci.*, 26:597–604, 2001.

[58] J. Feder. *Fractals.* Plenum Publishing Corp., New York, 1988.

[59] G. Finazzi and F. Rappaport. In vivo characterization of the electrochemical proton gradient generated in darkness in green algae and its kinetic effects on cytochrome b_6f turnover. *Biochemistry*, 37:9999–10005, 1998.

[60] P. J. Flory. Molecular size distribution in three dimensional polymers. I, II, III. *J. Am. Chem. Soc.*, 63:3083–3100, 1941.

[61] R. C. Ford, S. S. Stoylova, and A. Holzenburg. An alternative model for photosystem II/light harvesting complex II in grana membranes based on cryo-electron microscopy studies. *Eur. J. Biochem.*, 269:326–336, 2002.

[62] S. Galamand and A. Mauger. Universal formulae for percolation thresholds. *Phys. Rev. E*, 53:2177, 1996.

[63] G. Garab and L. Mustárdy. Role of LHC II containing macrodomains in the structure, function and dynamics of grana. *Aust. J. Plant Physiol.*, 26:649–658, 1999.

[64] D. Goldberg. *Genetic Algorithms in Search, Optimization and Machine Learning.* Addison–Wesley, 1989.

[65] O. A. Gopta, B. A. Feniouk, W. Junge, and A. Y. Mulkidjanian. The cytochrome bc_1 complex of *Rhodobacter capsulatus*: ubiquinol oxidation in a dimeric Q-cycle? *FEBS Letters*, 431:291–296, 1998.

[66] T. Graan and D. Ort. Quantitation of 2,5-dibromo-3-methyl-6-isopropyl-*p*-benzoquinone binding sites in chloroplast membranes: Evidence for a functional dimer of the cytochrome b_6f complex. *Archives of Biochemistry and Biophysics*, 248(2):445–451, 1988.

[67] E. L. Gross. *Oxygenic Photosynthesis: The Light Reactions*, chapter 21. Plastocyanin: structure, location, diffusion and electron transfer mechanisms., pages 413–429. Kluwer Academic Publishers, 1996.

[68] S. Gupte, E.-S. Wu, L. Hoechli, M. Hoechli, K. Jacobson, A. Sowers, and C. R. Hackenbrock. Relationship between lateral diffusion, collision frequency,

and electron transfer of mitochondrial inner membrane oxidation-reduction components. *Proc. Natl. Acad. Sci.*, 81:2606–2610, 1984.

[69] W. Haehnel. Electron transport between plastoquinone and chlorophyll a_I in chloroplasts. *Biochim. Biophys. Acta*, 305:618–631, 1973.

[70] W. Haehnel. The reduction kinetics of chlorophyll a_I as an indicator for proton uptake between the light reactions in chloroplasts. *Biochim. Biophys. Acta*, 440:506–521, 1976.

[71] W. Haehnel. Photosynthetic electron transport in higher plants. *Ann. Rev. Plant Physiol.*, 35:659–693, 1984.

[72] W. Haehnel, A. Pröpper, and H. Krause. Evidence for complexed plastocyanin as the immediate electron donor of p-700. *Biochim. Biophys. Acta*, 593:384–399, 1980.

[73] W. Haehnel, R. Ratajczak, and H. Robenek. Lateral distribution and diffusion of plastocyanin in chloroplast thylakoids. *The Journal of Cell Biology*, 108:1397–1405, 1989.

[74] B. Hankammer, J. Barber, and E. J. Boekema. Structure and membrane organization of photosystem II in green plants. *Annu. Rev. Plant Physiol. Plant Mol. Biol.*, 48:641–671, 1997.

[75] G. Hastings, S. Hoshina, A. N. Webber, and R. E. Blankenship. Universality of electron and energy transfer processes in photosystem one. *Biochemistry*, 34:15512–15522, 1995.

[76] G. Hauska, G. Herold, C. Huber, W. Nitschke, and D. Sofrova. Stigmatellin affects both hemes of cytochrome *b* in cytochrome *b6f/bc1*–complexes. *Z. Naturforsch.*, 44c:462–467, 1989.

[77] G. Hauska, E. Hurt, N. Gabellini, and W. Lockau. Comparative aspects of quinol-cytochrome *c*/plastocyanin oxidoreductases. *Biochim. Biophys. Acta*, 726:97–133, 1983.

[78] G. Hauska, M. Schütz, and M. Büttner. *Oxygenic Photosynthesis: The Light Reactions*, chapter 19. The Cytochrome b_6f Complex-Composition, Structure and Function., pages 377–398. Kluwer Academic Publishers, 1996.

[79] T. Heimburg. Monte carlo simulations of lipid bilayers and lipid protein interactions in the light of recent experiment. *Current Opinion in colloid and Interface Science*, 5:225–232, 2000.

[80] A. B. Hope. The chloroplast cytochrome *bf* complex: a critical focus on function. *Biochim. Biophys. Acta*, 1143:1–22, 1993.

[81] A. B. Hope, R. R. Huligol, M. Panizza, M. Thompson, and D. B. Matthews. The flash induced turnover of cytochrome *b*-563, cytochrome *f* and plastocyanin in chloroplasts. Models and estimation of kinetic parameters. *Biochim. Biophys. Acta*, 1100:15–26, 1992.

[82] A. B. Hope, J. Liggins, and D. B. Matthews. The kinetics of reactions in and near the cytochrome **b/f** complex of chloroplasts. II. cytochrome *b*-563 reduction. *Aust. J. Plant Physiol*, 16:353–64, 1989.

[83] A. B. Hope, P. Valente, and D. B. Matthews. Effects of pH on the kinetics of redox reactions in and around the cytochrome *bf* complex in an isolated system. *Photosynthesis Research*, 42:11–120, 1994.

[84] B.-D. Hsu. A theoretical study on the fluorescence induction curve of spinach in the absence of DCMU. *Biochim. Biophys. Acta*, 1140:30–36, 1992.

[85] D. Huang, R. M. Everly, R. H. Cheng, H. Heymann, J. B. amd Schägger, V. Sled, T. Ohnishi, T. S. Baker, and W. A. Cramer. Characterization of the chloroplast cytochrome b_6f complex as a structural and functional dimer. *Biochemistry.*, 33:4401–4409, 1994.

[86] E. C. Ifeachor and B. W. Jervis. *Digital Signal Processing.* Addison–Wesley, 1993.

[87] A. Istokovics, I. Simidjiev, F. Lajkó, and G. Garab. Characterization of the light–induced reversible changes in the chiral macro–organization of the chromophores in chloroplast thylakoidmembranes. temperature dependence and effect of inhibitors. *Photosynth. Res.*, 54:45–53, 1997.

[88] A. Ivancich, L. I. Horwáth, M. Droppa, G. Horwáth, and T. Farkas. Spin label esr study of lipid solvation of supramolecular photosynthetic protein complexes in thylakoids. *Biochim. Biophys. Acta*, 1196:51–56, 1994.

[89] S. Janson. The light-harvesting chlorophyll a/b binding proteins. *Biochim. Biophys. Acta*, 1184:1–19, 1994.

[90] A. Joliot and P. Joliot. *Photosynthesis: Mechanisms and Effects*, chapter Proton-Pumping within Cytochrome *bf* Complex., pages 1573–1576. Kluwer Academic Publishers, 1998.

[91] P. Joliot and A. Joliot. Electron transfer between the two photosystems: II. equilibrium constants. *Biochim. Biophys. Acta*, 765:219–226, 1984.

[92] P. Joliot and A. Joliot. Electron transfer between photosystem II and the cytochrome *bf* complex: mechanistic and structural implications. *Biochem. Biophys. Acta*, 1102:53–61, 1992.

[93] P. Joliot, J. Lavergne, and D. Béal. Plastoquinone compartmentation in chloroplasts. I. evidence for domains with different rates of photo-reduction. *Biochim. Biophys. Acta*, 1101:1–12, 1992.

[94] P. Joliot, A Verméglio, and A. Joliot. Supramolecular membrane protein assemblies in photosynthesis and respiration. *Biochem. Biophys. Acta*, 1141:151–174, 1993.

[95] H. Kirchhoff. *Kontrolle des photosynthetischen Elektronentransportes in Thylakoiden höherer Pflanzen: Argumente fuer eine Mikrodomänenorganisation zwischen PS II und Cyt.b_6f Komplex.* PhD thesis, Westfaelische Wilhelms–Universitaet Muenster, 1998.

[96] H. Kirchhoff, S. Horstmann, and E. Weis. Control of the photosynthetic electron transport by PQ diffusion microdomains in thylakoids of higher plants. *Biochim. Biophys. Acta*, Bioenergetics 1459 (1):148–168, 2000.

[97] H. Kirchhoff, U. Mukherrjee, and H.-J. Galla. Molecular architecture of the thylakoid membrane: lipid diffusion space for plastoquinone. *Biochemistry*, 41:4872–4882, 2002.

[98] C. Klughammer and U. Schreiber. *Photosynthesis: Mechanisms and Effects*, chapter Measuring P700 absorbance changes in the near infrared spectral region with a dual wavelength pulse modulation system., pages 4357–4360. Kluwer Academic Publishers, 1998.

[99] D. B. Knaff. *Oxygenic Photosynthesis: The Light Reactions*, chapter 17. Ferredoxin and ferredoxin-dependent enzymes., pages 333–361. Kluwer Academic Publishers, 1996.

[100] D. M. Kramer and A. R. Crofts. *Current Research in Photosynthesis, Vol III*, chapter A Q–cycle mechanism for electron transfer in chloroplasts, pages 283–286. Kluwer, 1990.

[101] D. M. Kramer and A. R. Crofts. *Research in Photosynthesis, Vol II*, chapter A Q-cycle-type model for turn-over of the bf complex under a wide range of redox conditions., pages 491–494. Kluwer, 1993.

[102] G. H. Krause and E. Weis. Chlorophyll fluorescence and photosynthesis: the basics. *Annu. Rev. Plant Physiol. Plant Mol. Biol.*, 42:313–349, 1991.

[103] O. Kruse, B. Hankamer, C. Konczak, C. Gerle, E. Morris, A. Radunz, G. H. Schmid, and J. Barber. Phosphatidylglycerol is involved in the dimerization of photosystem II. *J. Biol. Chem.*, 275:6509–6514, 2000.

[104] U. Kubitscheck and R. Peters. Localization of single nuclear pore complexes by confocal laser scanning microscopy and analysis of their distribution. *Meth. Cell Biol.*, 53:79–98, 1998.

[105] W. Kühlbrandt and D. N. Wang. Three-dimensional structure of plant light-harvesting complex determined by electron crystallography. *Nature*, 350:130–134, 1991.

[106] W. Kühlbrandt, D. N. Wang, and Y. Fujiyoshi. Atomic model of plant light-harvesting complex by electron crystallography. *Nature*, 367:614–621, 1994.

[107] D. J. Kyle, L. A. Staehelin, and C. J. Arntzen. Lateral mobility of the light–harvesting complex in chloroplast membranes controls excitation energy distribution in higher plants. *Arch. Biochem. Biophys.*, 222:527–541, 1983.

[108] H. Laasch. Non-photochemical quenching of chlorophyll *a* fluorescence in isolated chloroplasts under conditions of stressed photosynthesis. *Planta*, 171:220–226, 1987.

[109] J. Lavergne, J.-P. Bouchaud, and P. Joliot. Plastoquinone compartmentation in chloroplasts. II. theoretical aspects. *Biochim. Biophys. Acta*, 1101:13–22, 1992.

[110] J. Lavergne and J.-M. Briantais. *Oxygenic Photosynthesis: The Light Reactions*, chapter 14. Photosystem II Heterogeneity., pages 265–287. Kluwer Academic Publishers, 1996.

[111] J. Lavergne and P. Joliot. Restricted diffusion in photosynthetic membranes. *TIBS*, 16:129–134, 1991.

[112] T. Link. The role of the 'Rieske' iron sulfur protein in the hydoquinone oxidation (Q_P) site of the cytochrome bc_1 complex. The proton gated mechanism. *FEBS Letters*, 412:257–264, 1997.

[113] R. Malkin. *Oxygenic Photosynthesis: The Light Reactions*, chapter 16. Photosystem I electron transfer reactions – components and kinetics., pages 313–332. Kluwer Academic Publishers, 1996.

[114] S. Marcelja. Towards a realistic theory of the interaction of membrane inclusions. *Biophysical Journal*, 76:593–594, 1999.

[115] R. A. Marcus and N. Suttin. Electron transfer in chemistry and biology. *Biochim. Biophys. Acta*, 811:265–322, 1992.

[116] S. W. McCauley and A. Melis. Quantification of photosystem ii in spinach thylkaoids. *Biochim. Biophys. Acta*, 849:175–182, 86.

[117] D. A. McQuarrie. *Statistical Mechanics*. Harper Collins, New York, 1976.

[118] A. Melis. *Oxygenic Photosynthesis: The Light Reactions*, chapter 29. Excitation energy transfer: functional and dynamic aspects of Lhc (cab) proteins., pages 523–538. Kluwer Academic Publishers, 1996.

[119] A. Menikh and M. Fragata. Fourier-transform infrared spectroscopic study of ion-binding and intramolecular interactions in the polar head of digalactosyldiacylglycerol. *Eur. Biohys. J.*, 22(6):249–258, 1993.

[120] N. Metropolis, A. W. Rosenbluth, M. N. Rosenbluth, and A. H. Teller. Equation of state calculations by fast computing machines. *The Journal of Chemical Physics*, 21(6):1087–1092, 1953.

[121] N. Metropolis and S. Ulam. The Monte Carlo method. *J. Am. Statist. Ass.*, 44:335–341, 1949.

[122] A. P. Minton. The influence of macromolecular crowding and macromolecular confinement on biochemical reactions in physiological media. *The Journal of Biological Chemistry*, 276(14):10577–10580, 2001.

[123] P. Mitchell. Possible molecular mechanisms of the protonmotive function of cytochrome systems. *J. Theor. Biol.*, 62:327–367, 1976.

[124] R. Mitchell, A. Spillmann, and W. Haehnel. Plastoquinol diffusion in linear photosynthetic electron transport. *Biophys. Journ.*, 58:1011–1024, 1990.

[125] N. Murata. Control of excitation transfer in photosynthesis. II. magnesium ion dependent distribution of excitation energy between two pigment systems in spinach chloroplasts. *Biochim. Biophys. Acta*, 189:171–181, 1969.

[126] D. J. Murphy. The molecular organisation of the photosynthetic membranesw of higher plants. *Biochim. Biophys. Acta*, 864:33–94, 1986.

[127] W. Nagl. *Elektronenmikroskopische Laborpraxis.* Springer Verlag, Berlin, Heidelberg, New York, 1981.

[128] W. Nitschke, G. Hauska, and A. R. Crofts. Fast electron transfer from low- to high-potential cytochrome b_6 in isolated cytochrome b_6 complex. *FEBS Lett*, 232:204–208, 1988.

[129] J. H. A. Nugent and D. S. Bendall. Functional size measurements on the chloroplast cytochrome *bf* complex. *Biochim. Biophys. Acta*, 893:177–183, 1987.

[130] D. P. O'Keefe. Structure and function of the chloroplast cytochrome *bf* complex. *Photosynth. Res.*, 17:189–216, 1988.

[131] J. Olive, O. Vallon, Wollman F.-A., M. Recouvreur, and P. Bennoun. Studies on the cytochrome b6-f complex. II. localization of the complex in the thylakoid membranes from spinach and chlamydomonas reinhardtii by immunocytochemistry and freeze-fracture analysis of b6-f mutants. *Biochim. Biophys. Acta*, 851:239–248, 1986.

[132] L. Onsager. The effects of shape on the interaction of colloid particles. *Annals of the New York Academy of Science*, 51:627–659, 1949.

[133] R. S. Pan, L. F. Chien, M. Y. Wang, M. Y. Tsai, R. L. Pan, and B. D. Hsu. Functional size of photosynthetic electron transport chain determined by radiation inactivation. *Plant Physiol.*, 85:158–163, 1987.

[134] Y. Pierre, C. Breyton, C. Tribet, D. Kramer, J. Olive, and Popot J. L. Purification and characterization of the cytochrome b_6f complex from *Chlamydomonas reinhardtii*. *J. Biol. Chem.*, 270:29342–29349, 1995.

[135] D. A. Pink. Protein lateral movement in lipid bilayers. simulation studies of its dependence upon protein concentration. *Biochim. Biophys. Acta*, 818:200–204, 1985.

[136] M. V. Ponamarev and W. A. Cramer. *Photosynthesis: Mechanisms and Effects*, chapter Non-Concerted Reduction of Cytochromes f and b_6 in Mutants Affecting the Cytochrome f Internal Water chain. Kluwer Academic Publishers, 1998.

[137] R. J. Porra, W. A. Thompson, and P. E. Kriedemann. Determination of accurate extinction coefficient and simultaneous equations for essaying chlorophylls a and b extracted with four different solvents: verification of the concentration of chlorophyll standards by atomic absorption spectroscopy. *Biochim. Biophys. Acta*, 975:384–394, 1989.

[138] M. J. D. Powell. An efficient method for finding the minimum of a function of several variables without calculating derivatives. *Comput. J.*, 7:155–163, 1964.

[139] W. H. Press, B. P. Flannery, S. A. Teukolsky, and W. T. Vetterling. *Numerical Recipes in C, The Art of Scientific Computing*, chapter 7.1, pages 205–214. Cambridge University Press, 1988.

[140] W. H. Press, B. P. Flannery, S. A. Teukolsky, and W. T. Vetterling. *Numerical Recipes in C, The Art of Scientific Computing*, chapter 10.5, pages 309–317. Cambridge University Press, 1988.

[141] P. J. Randall and D. Bouma. Zinc deficiency, carbonic anhydrase, and photosynthesis in leaves of spinach. *Plant. Physiol.*, 52:229–232, 1973.

[142] M. Rathenow and D. Rumberg. Stoichiometry of proton translocation during photosynthesis. *Ber. Bunsenges. Phys. Chem.*, 84:1059–1062, 1980.

[143] K-H Rhee, E. P. Morris, J. Barber, and W. Kühlbrandt. Three-dimensional structure of the plant photosystem II reaction centre at 8-Å resolution. *Nature*, 396:283–286, 1998.

[144] K-H Rhee, E. P. Morris, D. Zheleva, B. Hankamer, W. Kühlbrandt, and J. Barber. Two-dimensional structure of plant photosystem II at 8-Å resolution. *Nature*, 389:522–526, 1997.

[145] P. R. Rich, P. Heathcote, and D. A. Moss. Kinetic studies of electron transfer in a hybrid system constructed from the cytochrome *bf* complex and photosystem I. *Biochim. Biophys. Acta*, 892:138–151, 1987.

[146] P. R. Rich, S. A. Madgwick, and D. A. Moss. The interactions of duroquinol, DBMIB and NQNO with the chloroplast cytochrome *bf* complex. *Biochim. Biophys. Acta*, 1058:312–328, 1991.

[147] D. Rumberg and U. Siggel. pH changes in the inner phase of the thylakoids during photosynthesis. *Naturwissenschaften*, 56(3):130– 132, 1969.

[148] K. Sauer. *Encyclopedia of Plant Physiology 19*, chapter 2. Photosynthetic Light Reactions – Physical Aspects., pages 85–97. Pirson, A. and Zimmermann, M. H., 1986.

[149] M. J. Saxton. Lateral diffusion in an archipelago. the effect of impermeable patches on diffusion in a cell membrane. *Biophysical Journal*, 39:165–173, 1982.

[150] M. J. Saxton. Lateral diffusion in an archipelago. the effect of mobile obstacles. *Biophysical Journal*, 52:989–997, 1987.

[151] M. J. Saxton. Lateral diffusion in an archipelago. distance dependence of the diffusion coefficient. *Biophysical Journal*, 56:615–622, 1989.

[152] M. J. Saxton. Lateral diffusion and aggregation. *Biophysical Journal*, 61:119–128, 1992.

[153] M. J. Saxton. Lateral diffusion in an archipelago. dependence on tracer size. *Biophysical Journal*, 64:1053–1062, 1993.

[154] M. J. Saxton and J. C. Owicki. Concentration effects on reactions in membranes: rhodopsin and transducin. *Biochim. Biophys. Acta*, 979:27–34, 1989.

[155] W. Y. Shih, I. A. Aksay, and R. Kikuchi. Reversible–growth model: Cluster–cluster aggregation with finite binding energies. *Physical Review A.*, 36:5015–5019, 1987.

[156] M. Shinitzky (ed.). *Biomembranes, Physical aspects.* VCH Verlagsgesellschaft mbH, Weinheim, 1993.

[157] I. Simidijev, V. Barzda, L. Mustárdy, and G. Garab. Role of thylakoid lipids in the structural flexibility of lamellar aggregates of the isolated light-harvesting chlorophyll a/b complex of photosystem II. *Biochemistry*, 37:4169–4173, 1998.

[158] I. Simidijev, S. Stoylova, A. Holzenburg, H. Amenitsch, P. Laggner, T. Jávorfi, L. Mustárdy, and Garab G. *Photosynthesis: Mechanisms and Effects*, chapter Reconstitution of membranes using non-bilayer forming lipids and plant LHC II., pages 1799–1803. Kluwer Academic Publishers, 1998.

[159] D. J. Simpson. Freeze-fracture studies on barley plastid membranes III. Location of the light-harvesting chlorophyll-protein. *Carlsberg Res. Commun.*, 44:303–336, 1979.

[160] D. J. Simpson. Freeze–fracture studies on barley plastid membranes IV. Analysis of freeze–fracture particle size and shape. *Carlsberg Res. Commun.*, 45:201–210, 1980.

[161] C. H. Snyder, E. B. Gutierrez-Cirlos, and B. L. Trumpower. Evidence for a concerted mechanism of ubiquinol oxidation by the cytochrome bc_1 complex. *The Journal of Biological Chemistry*, 275(18):13535–13541, 2000.

[162] G. L. Soriano, M.V. Ponamarev, C. J. Carell, D. Xia, J. L. Smith, and W. A. Cramer. Comparison of the cytochrome bc(1) complex with the anticipated structure of the cytochrome b(6)f complex: De plus ça change de plus c'est la même chose. *J. of Bioenergetics and Biomembranes*, 31(3):201–213, 1999.

[163] L. A. Staehelin. *Photosynthesis III: Photosynthetic membranes and light-harvesting systems*, chapter Chloroplast structure and supramolecular organization of photosynthetic membranes., pages 1–84. Springer-Verlag Berlin, 1986.

[164] L. A. Staehelin and M. DeWitt. Correlation of structure and function of chloroplast membranes at the supramolecular level. *J. Cell. Biochem.*, 24:261–269, 1984.

[165] L. A. Staehelin and G. W. M. van der Staay. *Oxygenic Photosynthesis: The Light Reactions.*, chapter 2. Structure, composition, functional organization and dynamic properties of thylakoid membranes., pages 11–30. Kluwer Academic Publishers, 1996.

[166] D. Stauffer and A. Aharony. *Introduction to Percolation Theory.* Taylor and Francis, London, 1992.

[167] H. H. Stiehl and H. T. Witt. Quantitative treatment of the function of plastoquinone in photosynthesis. *Z. Naturforsch.*, 24:1588–1598, 1969.

[168] W. H. Stockmayer. Theory of molecular size distribution and gel formation in branched chain polymers. *J. Chem. Phys.*, 11:45, 1943.

[169] D. Stys. Stacking and separation of photosystem I and photosystem II in plant thylakoid membranes: A physico-chemical view. *Physiol. Plant.*, 95:651–657, 1995.

[170] P. Svensson, E. Andreasson, and Albertsson P.-Å. Heterogeneity among photosystem I. *Biochim. Biophys. Acta*, 1060:45–50, 1991.

[171] F. Sykes and Essam J. W. Exact critical percolation probabilities for site and bond problems in two dimensions. *J. Math. Phys.*, 5:1117, 1964.

[172] H-W. Trissl and J. Lavergne. Fluorescence induction from photosystem II: Analytical equations for the yields of photochemistry and fluorescence derived from analysis of a model including exciton-radical pair equilibrium and restricted energy transfer between photosynthetic units. *Aust. J. Plant Physiol.*, 22:183–93, 94.

[173] H.-W. Trissl and C. Wilhelm. Why do membranes from higher plants form grana stacks? *Trends Biochem. Sci.*, 18:415–419, 93.

[174] B. L. Trumpower. The protonmotive Q cycle: coupling of proton translocation to electron transfer by the cytochrome bc1 complex. *J. Biol. Chem.*, 265:11409–11412, 93.

[175] R. Van Grondelle, J. P. Dekker, T. Gillbro, and V. Sundstrom. Energy transfer and trapping in photosynthesis. *Biochimica et Biophysica Acta*, 1187:1–65, 1994.

[176] W. L. C. Vaz and Almeida P. F. F. Phase tolopogy and percolation in multi–phase lipid bilayers: is the biological membrane a domain mosaic? *Curr. Opinion Struct Biol.*, 3:482–488, 1993.

[177] E. J. W. Verwey and J. Th. G. Overbeek. *Theory of the stability of lyophobic colloids.* Elsevier, 1948.

[178] M. S. Webb and B. R. Green. Biochemical and biophysical properties of thylakoid acyl lipids. *Biochim. Biophys. Acta*, 1060:133–158, 1991.

[179] M. S. Webb, C. P. S. Tilcock, and B. R. Green. Salt-mediated interactions between vesicles of the thylakoid lipid digalactosyldiacylglycerol. *Biochim. Biophys. Acta*, 938:323–333, 1988.

[180] W. P. Williams. *Lipids in Photosynthesis: Structure, Function and Genetics*, chapter The physical properties of thylakoid membrane lipids and their relation to photosynthesis., pages 103–118. Kluwer Academic Publishers, 1998.

[181] H. T. Witt. *Oxygenic Photosynthesis: The Light Reactions*, chapter 18. Structure analysis of single crystals of photosystem I by X-ray, EPR and ENDOR: a short status report., pages 363–375. Kluwer Academic Publishers, 1996.

[182] L. Wollenberger, H. Stefansson, S-G. Yu, and P-Å. Albertsson. Isolation and characterization of vesicles originating from the grana margins. *Biochim. Biophys. Acta*, 1184:93–102, 1994.

[183] F.-A. Wollmann and B. Diner. Cation control of fluorescence emission, light scatter, and membrane stacking in pigment mutants of *chlamydomonas reinhardii*. *Arch. Biochem. Biophys.*, 201:646–658, 1980.

[184] D. Xia, H. Kim, C-A. Yu, A. Kachurin, L. Zhang, and J. Deisenhofer. A novel electron transfer mechanism suggested by crystallographic studies of mitochondrial cytochrome *bc1* complex. *Biochem. Cell Biol*, 76:673–679, 1998.

[185] W. Xia and M. F. Thorpe. Percolation properties of random ellipses. *Phys. Rev. A*, 38:2650, 1988.

[186] A. E. Yakushevska, P. E. Jensen, W. Keegstra, H. van Roon, H. V. Scheller, E. J. Boekema, and J. P. Dekker. Supermolecular organization of photosystem II and its associated light-harvesting antenna in *arabidopsis thaliana*. *Eur. J. Biochem.*, 268:6020–6028, 2001.

[187] C. A. Yu, D. Xia, H. Kim, J. Deisenhofer, L. Zhang, A. M. Kachurin, and L. Yu. Structural basis of functions of the mitochondrial cytochrome *bc1* complex. *Biochim. Biophys. Acta*, 1365:151–158, 1998.

[188] S.-G. Yu, G. Björn, and P.-A. Albertson. Characterization of a non- detergent PSII - cytochrome *bf* preparation (bs). *Photosyn. Res.*, 37:227–236, 1993.

[189] H. Zhang, J. P. Whitelegge, and W. A. Cramer. Ferredoxin:$NADP^+$ oxidoreductase is a subunit of the chloroplast cytochrome b_6f complex. *Journal of Biological Chemistry*, 276(41):38159–38165, 2001.

[190] A. Zouni, H.-T. Witt, J. Kern, P. Fromme, N. Krauß, W. Saenger, and P. Orth. Two-dimensional structure of plant photosystem II at 8-Å resolution. *Nature*, 389:522–526, 1997.